A *cw*-ENDOR investigation of metal-ligand interactions in solution

Submitted in canditure for the degree of
Doctor of Philosophy

By

Richard James Tucker, M.Chem

Department of Chemistry
University of Wales, Cardiff

September 2005

ProQuest LLC
789 East Eisenhower Parkway
P.O. Box 1346
Ann Arbor, MI 48106-1346

Declaration

This work has not previously been accepted in substance for any degree and is not being concurrently submitted in candidature for any degree.

Signed ..... (candidate)

Date 17-2-06

This thesis is the result of my own investigations, except where otherwise stated. Other sources are acknowledged by footnotes giving explicit references. A bibliography is appended.

Signed ..... (candidate)

Date 17-2-06

I hereby give consent for my thesis, if accepted, to be available for photocopying and for inter-library loan, and for the title and summary to be made available to outside organisations.

Signed ..... (candidate)

Date 17-2-06

Summary

Electron Nuclear DOuble Resonance (ENDOR) spectroscopy has been employed in this Thesis to study a range of paramagnetic metal-ligand complex systems. The investigations focussed on the observation of conformational changes, solvatochromic effects and weak diastereomeric interactions of the complexes in frozen solution. Using a combination of angular selective ENDOR spectroscopy and DFT calculations, the structure and conformations of the $[V^{IV}=O(acac)_2]$ complex in coordinating and non-coordinating solvents was examined. In the non-coordinating solvent (CD_2Cl_2) the complex was found to adopt the expected square pyramidal structure, where the VO.....H_{lig} distances and coordinates obtained by DFT and ENDOR were in excellent agreement with each other confirming the expected structure. More importantly, in coordinating solvents (such as pyridine) two different stereoisomers of the resulting $[V^{IV}=O(acac)_2(C_5D_5N)]$ adduct, which differed in energy by only 3 $kJmol^{-1}$, were readily identified and discriminated by ENDOR (*PCCP* ***2002***).

Subtle changes to metal-ligand structures by solvatochromic effects were also examined using $[V^{IV}=O(salen)]$ in both coordinating (DMF) and non-coordinating (CD_2Cl_2) solvents. In the non-coordinating solvent (CD_2Cl_2), the expected square pyramidal symmetry of the V=O ion above the NNOO plane of the ligand was confirmed both by ENDOR and DFT. However, in the coordinating solvent (DMF), a subtle perturbation from square pyramidal structure was observed suggesting than DMF coordinated *trans* to the vanadyl oxo-ligand, pulling $V^{IV}=O$ back into the ligand plane. This was evidenced through analysis of the VO....H_{lig} distances determined by ENDOR and confirmed by DFT (*Chem. Phys. Lett.* ***2003***).

ENDOR was also used to explore the weak enantioselective binding between vanadyl based chiral salen complexes (abbreviated to [VO(Jacobsen)]) and chiral propylene epoxide. Differences in epoxide binding by enatiomers of the complex was evidenced by changes to the ^1H epoxide derived peaks in the ENDOR spectra. These changes were assigned to the small structural differences between the diastereomeric metal-epoxide adducts. Simulation of the spectra revealed differences in the VO...$^1H_{epoxide}$ distances for the diastereomeric pairs, which was confirmed by DFT. While the epoxide molecule was very weakly coordinated, ENDOR measurements of the racemic complex in racemic epoxide nevertheless indicated the preferential coordination of the *R*-[VO(Jacobsen)] to *R*-epoxide. This demonstrates the unique power of the ENDOR technique to resolve weak chiral interactions for which EPR spectroscopy alone lacks sufficient resolution (*JACS* ***2004***).

Finally, the diastereomeric interactions between chiral amines and copper based chiral salen complexes (abbreviated to [Cu(Jacobsen)]) was investigated, as a comparison with the previous weak interactions in the VO(Jacobsen)-epoxide case. Diastereomeric discrimination was once again evidenced by ENDOR. The slight differences in the Cu-amine distances, constrained by the chirality of the anchoring site, resulted in subtle difference in the spin densities to the ligand nitrogens, which was detected in the ENDOR experiment.

Acknowledgments

There are many people to whom I am deeply indebted for their advice and continuous support in the preparation of this thesis and execution of this research. This acknowledgement seeks to provide my deepest thanks to these people.

Firstly, among these people are Dr. Damien Murphy and Dr. Ian Fallis, who were my supervisors during the project. They provided the highest level of support, encouragement, and guidance and scientific advice of the highest quality.

I would also like to thank Dr. Robert Farley who was a post doctoral research assistant in the department. Dr. Farley provided excellent technical assistance on both the EPR and ENDOR analysis.

I would like to acknowledge Dr. David Willock for his kind assistance in providing the DFT data.

Additionally, I would like to acknowledge my fellow postgraduates in both the EPR laboratory and the surface science department, as well as the postgraduates in the coordination chemistry laboratories.

Finally, I would like to thank my parents for their support and financial influence whilst undertaking this study.

Thank you all

"Nothing exists until it is measured"

Niels Bohr, 1930

"I am further inclined to think that when are views are sufficiently to enable us to reason with precision concerning the proportions of elementary atoms we shall find the arithmetical relation alone will not be sufficient to explain their mutual action and that we shall be obliged to acquire a geometrical conception of their relative arrangement in all three dimensions of solid extension"

William Hyde Wollison, 1808

Contents

Chapter 1

Introduction

1.0 Introduction

Homogeneous catalysis is an indispensable discipline in chemistry, and is quickly becoming an important process not only in the laboratory but also on an industrial scale, especially when applied to the production of enantioselective compounds. A concise understanding of the role and applications of homogeneous catalysts is needed by academia and industry, as new industrially important processes require transition metal complexes as active catalysts in homogeneous solutions. Delicate combinations of ligand steric and electronic effects of the catalyst in the homogeneous phase have been found to influence strongly the structure and reactivity of labile, catalytically active transition metal complexes. Before 1960 only a few homogeneous catalysts were used, intermittently, on an academic or an industrial scale. The past several years, however, have seen the emergence of a variety of novel, useful and important homogeneous catalyst systems and this rapid enrichment seems to be the beginning of further growth in this field.

The elucidation of the catalytic action of the majority of homogeneous catalystic systems can be easily examined along the reaction coordinate by non-destructive chemical analysis such as Nuclear Magnetic Resonance (NMR), Electron Paramagnetic Resonance (EPR), Infra-Red (IR) spectroscopy and Resonance Raman (RR) techniques, to name but a few techniques. This ease of investigation into the mechanism of homogeneous catalysts and their structural properties is a major advantage, opening new, novel ways to develop intriguing and industrially important catalysts.

Although X-ray and EPR have allowed us to understand the structural properties associated with the catalysts in a solid state form, there are few techniques which allow us to obtain structural information in solution (frozen). One such technique, namely Electron Nuclear DOuble Resonance (ENDOR) can be used to study paramagnetic metal ligand complexes, elucidating structural properties in frozen solution, comparable to those from X-ray structural analysis. The specific conformations and structure adopted by the ligands in solution, are crucial to the transfer of chiral information from the active metal centre to the achiral substrate in catalysis. To understand these processes (in solution), it is necessary to *elucidate the detailed molecular structure and geometry* of the metal ligand complexes themselves. EPR offers limited insight into the nature of the binding ligands or the geometry of

the ligands themselves. However, ENDOR spectroscopy can provide far greater detail on the weak couplings between the electron spin of the transition metal ion and the ligand nuclei. In this way, information on the *spatial arrangement of the ligand nuclei in the chiral catalyst and the achiral substrates can in principle be determined.*

To fully characterise the catalytic activity of the homogeneous catalyst, numerous studies can be carried out to elucidate structural information on the catalysts. Although there are many approaches to study homogeneous catalysis, this thesis will present the research from certain chemical disciplines. Therefore, the use of ligand design, molecular modelling and spectroscopic studies will be described in detail to characterise transition metal homogeneous catalysts, vanadyl (VO^{2+}) and copper (Cu^{2+}) type complexes. In the design and synthesis of paramagnetic metal ligand complexes, subtle electronic and structural changes were employed. Following the synthesis of these novel transition metal complexes, a comprehensive spectroscopic study was carried out using Nuclear Magnetic Resonance (NMR), Electron Paramagnetic Resonance (EPR), Infra Red (IR), UV-Vis (UV), Mass Spectrometry (Electrospray, APCI, EI) and most importantly Electron Nuclear DOuble Resonance (ENDOR) Spectroscopy.

Through ENDOR spectroscopy, a number of transition metal complexes were studied and characterised. The double resonance experiment (ENDOR) allowed information to be obtained on the distances between the transition metal and remote surrounding ligand nuclei. This information is important, as ENDOR has been employed to study the conformational changes of asymmetric homogeneous catalysts, eg., oxovanadium (IV) complex, and the solvatochromic effects, eg., vanadyl salen complexes, in frozen solution (Chapter 5 [6]). Due to the high sensitivity of the ENDOR technique, further applications are shown in the study of weak diastereomeric interactions, between a transition metal complex and a weak coordinating epoxide, ie., propylene oxide. The observation of weak diastereomeric interactions in frozen solution, demonstrates the ability of ENDOR spectroscopy to detect and quantify the exceedingly weak interactions in solution.

Although the spectroscopic analysis was the main focus of the research, a combined molecular modelling approach based on Density Functional Theory (DFT) was undertaken, in order to compliment the ligand coordinates extracted from the

ENDOR analysis, the results of which are shown to be in excellent agreement and will be presented herein.

This research is of broad interest to large areas of the chemistry community. For those interested in advanced spectroscopic techniques and modern applications of theoretical chemistry, this thesis aims to establish that ENDOR spectroscopy coupled with DFT analysis can be a powerful tool in understanding the subtleties of the interactions of substrates in solution. Perhaps more significantly the method allows exploration of weak interactions in paramagnetic systems which are inaccessible by NMR methods or too subtle for effective direct analysis *via* EPR.

1.1 Asymmetric Homogeneous Catalysts

The excellent success of the well-known Sharpless [1] epoxidation reaction helped inspire widespread efforts to identify more general catalytic systems which might be effective for the asymmetric epoxidation of unfunctionalised olefins. The question of whether substrate precoordination through a pendant functional group is required for a highly enantioselective catalytic reaction of a prochiral olefin has been answered in the negative with the discoveries of enantioselective cyclopropanation in the 1970's and dihydroxylation in the early 1980's. The quest for effective asymmetric epoxidation catalysts for simple olefins did not reach success until relatively recently [2, 3]. One of the first advances came with the discovery of chiral metal complexes that effect highly enantioselective oxo-transfer to un-fuctionalised olefins [4, 5]. Such catalysts [6, 7, 8], have stereoselective mimetic properties to those found in biological oxidation systems (Chapter 4). A detailed mechanistic understanding has begun to emerge that bears importance for both synthetic and enzymatic oxo-transfer catalyst systems. Such systems have addressed important questions regarding asymmetric epoxidation methodologies. This chapter aims to present an overview of some of the main strategies for asymmetric homogeneous catalysis, with emphasis on catalytic epoxidation of un-functionalised olefins with synthetically made catalysts.

1.2 Oxo-transfer mechanisms

Oxygen transfer from metal complexes to olefins results in a net two electron reduction at the metal centre. As a result, only metals capable of shuttling between oxidation states can be effective oxygen transfer catalysts. Among the most common are Iron, Manganese, Ruthenium and Chromium. These have been effective for catalytic epoxidation *via* oxo-transfer [9, 10] in synthetic systems. These metals are quite often coordinated by tetradentate porphyrin (Figure 1.1a) and salen (Figure 1.1b) ligand frameworks.

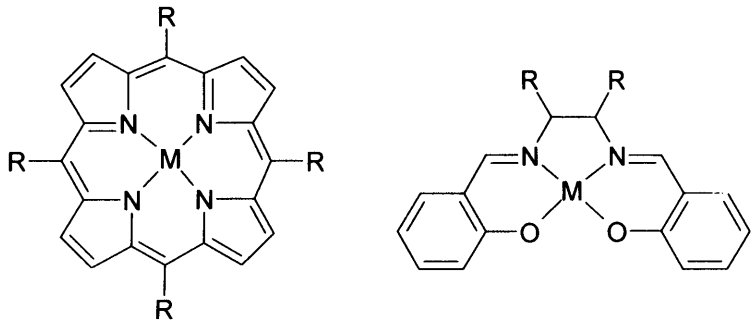

Figure 1.1: Examples of oxo-transfer catalysts; (a) tetradentate porphyrin and (b) *N,N'*-ethylenebis(salicylideneamine) - salen ligand frameworks.

There have been many proposals put forward for the mechanism of oxygen transfer from high valent metal oxo complexes. However one of the two main fundamental proposals involves substrate attack at both the metal and the oxo centers to generate an oxametallacycle intermediate (Figure 1.2a). This type of mechanism was first reported in the literature by Sharpless in 1977, in the context of chromyl chloride oxidations [11].

Olefin epoxidation reactions catalyzed by porphyrin and salen complexes [12, 13] have also attracted many proposals. However there is lack of substantial evidence, indicating that oxametallacycle intermediates do not participate in these reactions [14, 15, 16]. One of the most widely and now most commonly accepted mechanism, for oxo-transfer involves direct substrate attack at the oxo-ligand with concerted oxygen delivery, leading to C-O bond formation (Figure 1.2b,c). Groves *et al* [17] in 1985 proposed a mechanism or transition state geometry for epoxidation by porphyrin complexes, involving a perpendicular, side on approach of the olefin to the

metal-oxygen bond. This type of approach accounted for the relatively enhanced reactivity of *cis* over *trans* alkenes in porphyrin (Figure 1.1a) and other catalyst systems. A similar model also explained the observed enantioselectivites in asymmetric epoxidation reactions with successful chiral catalysts [18, 19]. The lack of complete stereospecificity in the epoxidation of certain olefin classes offers compelling evidence for a stepwise mechanism for oxo-transfer [20, 21].

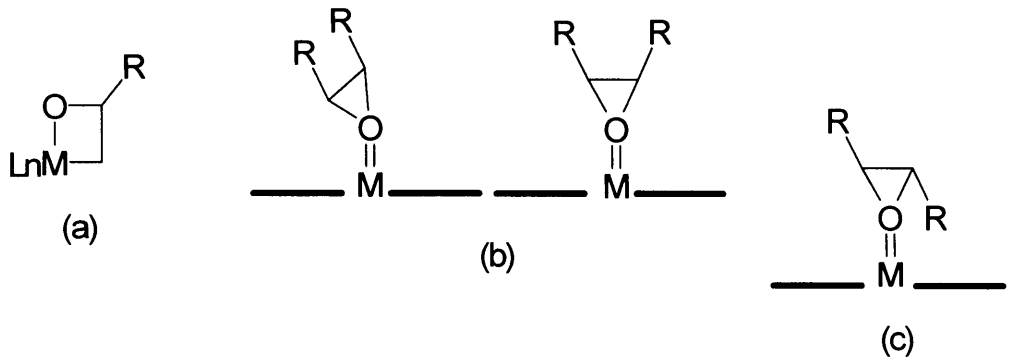

Figure 1.2: Postulated oxygen delivery intermediate; (a) oxametallocyne, (b,c) attack of olefin on double bond itself.

Alkyl substituted olefins generally undergo stereospecific epoxidation, with *cis*-olefins affording *cis*-epoxides (Figure 1.3a) [22]. In contrast, acyclic olefins conjugated to aryl, vinyl or alkynyl groups undergo nonstereospecific epoxidation, with *cis*-olefins affording mixtures of *cis* and *trans*-epoxide products. Experiments carried out with sensitive radical probes are found to be consistent with this type of mechanistic study [23, 24]. However, non-polar radical intermediates are implicated by the observation of electronic and reactivity trends in the case of non-concerted epoxidations with Mn(salen) catalysts (Figure 1.3b) [19, 25].

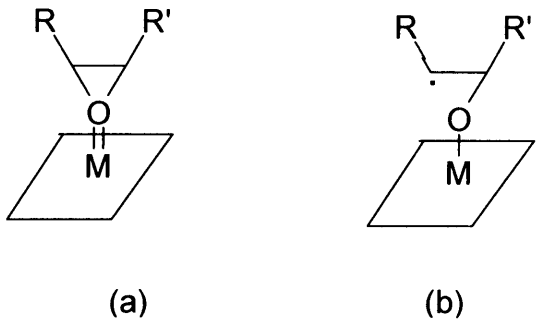

Figure 1.3: Representation of non-concerted oxygen delivery.

1.3 Stoichiometric oxidants

There are a wide variety of stoichiometric oxidants for effective oxygen atom donors in oxo-transfer reactions with (salen)-metal and (porphyrin)- metal catalysts. Such oxidants include NaOCl (sodium hypochlorite) [26, 27, 28], alkyl hydroperoxides [29, 30, 31], peroxy acids [32], amine *N*-oxides [33, 34], oxaziridines [35], ozone [36], potassium hydrogen persulfate (oxone) [37], hydrogen peroxide [38, 39], periodate [40, 41] and magnesium monoperoxyphthalate [42]. In addition to this, the use of molecular oxygen with and without a stoichiometric reductant has been reported in epoxidations employing synthetic heme mimics [43, 44, 45]. However, among all of these oxidants, NaOCl has been studied the closest and has widely been used in asymmetric catalytic epoxidations [46, 47, 48, 49]. The addition of a Lewis base capable of coordinating to the metal centre during the epoxidation process, has been found not only to be vitally important in the turnover rate, but also in epoxide yield.

1.4 Characterization of metal-oxo complexes

In the literature, there are a series of five and six-coordinate chiral [Mn^{III}(salen)] complexes, which are known to be highly effective in the asymmetric epoxidation catalytic processes and have been characterized by X-ray crystallography [50]. It is found that when a comparison is made between these complexes, the ligand geometry surrounding the metal centre and the chiral diamine backbone remained constant. However, salicylidene regions of the complexes adopted a wide range of conformations.

1.5 Ligand design

To obtain good enantioselectivities in olefin epoxidation of salen type complexes, two structural additions of the ligand framework are needed; (a) diimine bridge (dissymmetric) and (b) bulky substituents on the 3 and 3' positions of the salicylide ligand. The ligand shown in Figure 1.1b, is found to have the optimum structural properties, both steric and electronic, for the asymmetric epoxidation catalysis. However, due to the ease by which the complex shown in Figure 1.1b can

be prepared, it has made it the most widely used catalysis in this class of ligands (Figure 1.4).

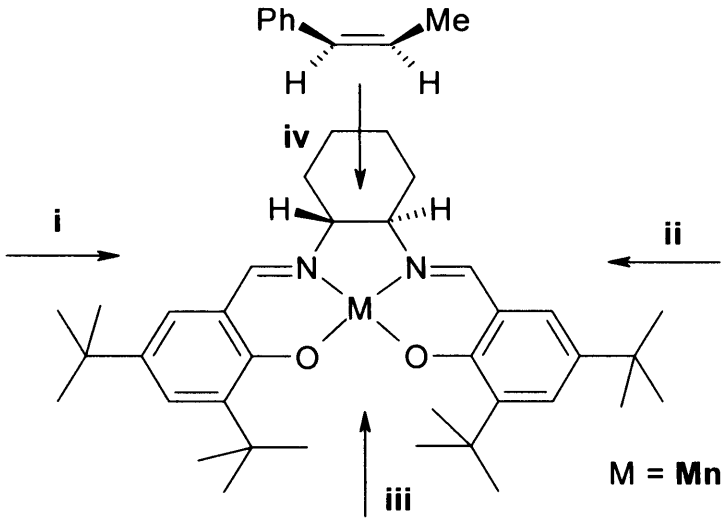

Figure 1.4: Systematic representation of the catalysts mode of action.

The epoxidation mechanism is found [51] to take place *via* a side on approach, whereby the bulky tertiary butyl groups are proposed to block attacks from the (**i-iii**) positions (Figure 1.4). This steric hinderence enforces approach (**iv**), increasing communication with the imine backbone. The catalyst in Figure 1.4 has showed applications not only in the laboratory, but also on industrial scales for the epoxidation of a range of olefins, namely *cis* di and trisubstituted olefins.

Table 1.1: Enantiomeric excess results illustrating different enantiomeric excesses with respect to altering the bulkiness of the ligand framework. e.e (%) represents the enantiomeric excess of epoxide formed on reaction completion. Associated Figure can be seen on previous page.

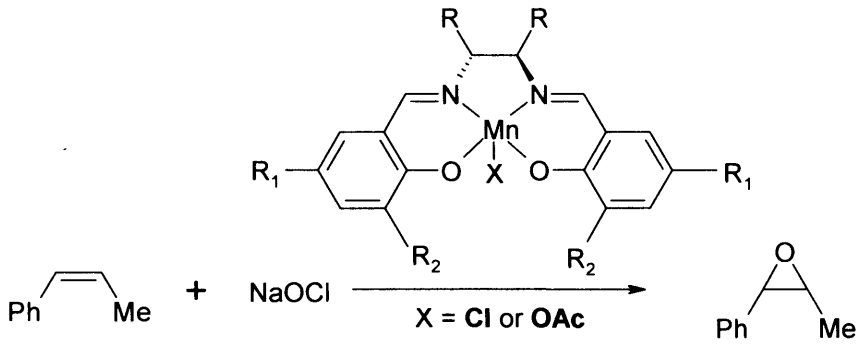

R,R	R_1	R_2	ee (%)
Ph, Ph	H	H	10
Ph, Ph	H	t-Bu	84
-$(CH_2)_4$-	Me	t-Bu	80
-$(CH_2)_4$-	t-Bu	t-Bu	90
-$(CH_2)_4$-	OMe	t-Bu	86
-$(CH_2)_4$-	NO_2	t-Bu	46
-$(CH_2)_4$-	OSi(i-Pr)$_3$	t-Bu	92

One of the most challenging substrate classes for asymmetric epoxidation oxo-transfer catalysts are *trans* olefins. Jacobsen and co-workers addressed this problem, through the synthesis of two novel Schiff base complexes [51]. The new complexes (Figure 1.5a), have an axially dissymmetric backbone, which replaces the more traditional 1,2-diamine backbone. This catalyst showed improved enantioselectivity in the epoxidation of methylstyrene (*trans*-β). The second novel Schiff base complex, consisted of a metal complex, with one of the salicylidene units replaced with a tropolone ring, affording the non C_2-symmetric salen complex (Figure 1.5b). X-ray crystallographic studies of the catalyst shown in Figure 1.5a reported that the complex was dramatically distorted, where the manganese metal was 0.38 Å above the ligand (*xy*) plane. This pyramidalisation of the ligand structure, permits the unhindered approach of substrates towards the reactive metal-oxo site and is a key step with

sterically demanding substrates such as *trans*-olefins. Therefore, the stereo-induction in the formation of these complexes, compared to the C_2 symmetric complexes, suggests a completely different mechanism for chiral recognition.

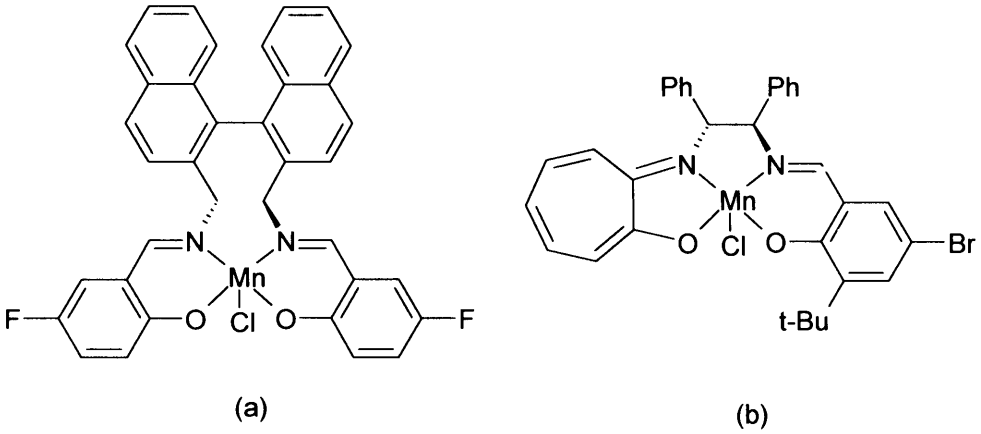

Figure 1.5: Asymmetric epoxidation oxo-transfer catalysts; (a) complex showing an axially dissymmetric backbone and (b) novel Schiff base salen complex.

1.6 Kinetic resolution in catalysis for asymmetric synthesis

1.6.1 *Chirality*

Similar to the well-known physical characteristics of most substances such as colour, hardness, texture, melting point and acidity, chirality is also a universally intrinsic property, which characterizes highly complex structures. A substance is known as 'chiral' when it can exist in nature in two structural forms (at least) in which the spatial arrangements of its atoms are non-superimposable mirror-images of each other, analogous to our right and left hands. Chiral compounds often exist as mixtures made up of these two twin-like mirror images of each other called 'enantiomers'. Enantiomers are chemically identical - being made up of the same number and type of atoms and have the same chemical and physical properties except for their molecular orientation in space and therefore in their interaction with other chiral substances.

Molecular chirality plays a vital part in nature and also in science and technology. This is important as life depends on the "molecular chirality", as many biological processes are asymmetric in nature. The difference between the

enantiomers (structurally) can be serious, with respect to the biological effects from the synthetically derived compounds.

Since 1848, when Louis Pasteur successfully separated the two enantiomers of tartaric acid, modern day chemists have developed a wide range of experimental techniques to produce enantiomerically pure compounds. Some of the most widely used chiral molecules include carbohydrates, alkaloids and amino acids.

1.6.2 *Hydrolytic Kinetic Resolution (HKR)*

Over recent years, the most common way to obtain enantiomerically pure asymmetric compounds is *via* the kinetic resolution of racemic mixtures as enantiomers react at different rates under asymmetric circumstances. In the asymmetric kinetic resolution process, a chiral catalyst or reagent is used to promote selectivity of one enantiomer over the other, resulting in a mixture of enantiomerically enriched starting materials and final products.

The hydrolytic kinetic resolution (HKR) of racemic terminal epoxides has emerged as a powerful method by which enantiomerically pure compounds can be prepared [52, 53, 54, 55, 56]. Today, the most widely used chiral catalyst for the hydrolytic kinetic resolution is a cobalt ligand complex. This complex was first reported in 1997 and has become the standard method by which enantiomerically pure epoxides and vicinal diols may be prepared (Figure 1.6)[57]. As can be seen from Figure 1.6, reaction of the racemic epoxide mixture with the corresponding HKR catalyst (Figure 1.6a,b), gave rise to one enantiomer of the epoxide and the alcohol.

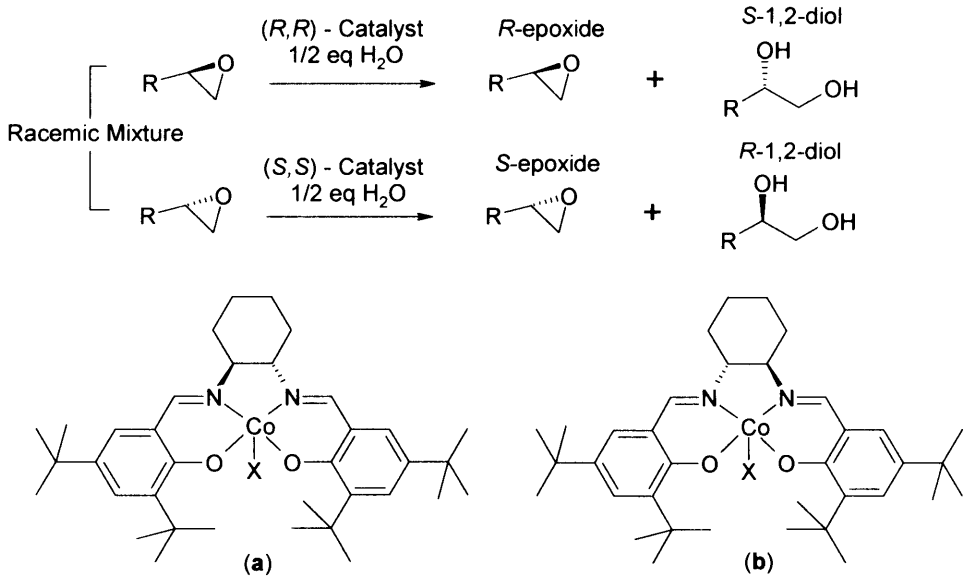

Figure 1.6: (a) (*S,S*)- and (b) (*R,R*)- enantiomers of a chiral cobalt salen complex. The process uses water as the only reagent and low loadings of a recyclable catalyst (a,b) [57].

Amongst some of the methods for the preparation of enantio-enriched epoxides, the previously mentioned Sharpless epoxidation (Figure 1.2b) has the most significant impact on asymmetric catalytic reactions. One of the most notable features of kinetic resolution is that the enantiomeric composition of an unreacted substrate can, in effect, be controlled by changing the conversion resulting in enantiopure compounds at significantly high conversions [58]. Some of the other features associated with hydrolytic kinetic resolution include high selectivity factors over a wide range of terminal epoxides and also the accessibility to a wide variety of racemic terminal epoxides, at an affordable cost [59, 60]. Therefore, the principal cost in the reaction process is the catalyst used and not the catalytic loadings, as only relatively small amounts of the catalyst are used, namely 0.2-2 mol% (1 mol% in the case of the cobalt (II) complex) [61, 62].

Jacobsen and Larrow [63], with an interest in obtaining a practical method for obtaining enantiomerically pure compounds (terminal epoxides), suggested that the following criteria must be fulfilled for a successful kinetic resolution experiment:

(a) The racemic substrates (epoxides) must be both cheaply and easily prepared from relatively cheap starting materials.

(b) Both enantiomers of the catalyst are needed for the full resolution of the epoxides.

(c) The nucleophile, in this case water, must be also relatively cheap and easy to obtain.

(d) Resolved epoxides, both (*R*) and (*S*), should be obtained in high yields and enantiomerically pure.

1.6.3 *Stereoselectivity in salen-type epoxidations*

A derivative of the salen type ligand, namely the 1994 "reagent of the year", Jacobsens catalyst, is found to convert achiral olefins to chiral epoxides with enantiomeric excesses greater than 90%. Jacobsen's catalyst is one of over approximately 75 epoxidation catalysts, based on a chiral salen ligand, complexed with Manganese (III). Jacobsen type catalyst is a convenient and efficient tool for the stereoselective synthesis, demonstrated by its applications in the synthesis of the key side chain in Taxol® (antitumour drug). The mechanism of the reaction process has two main steps involving oxygen transfer and the method of chiral induction.

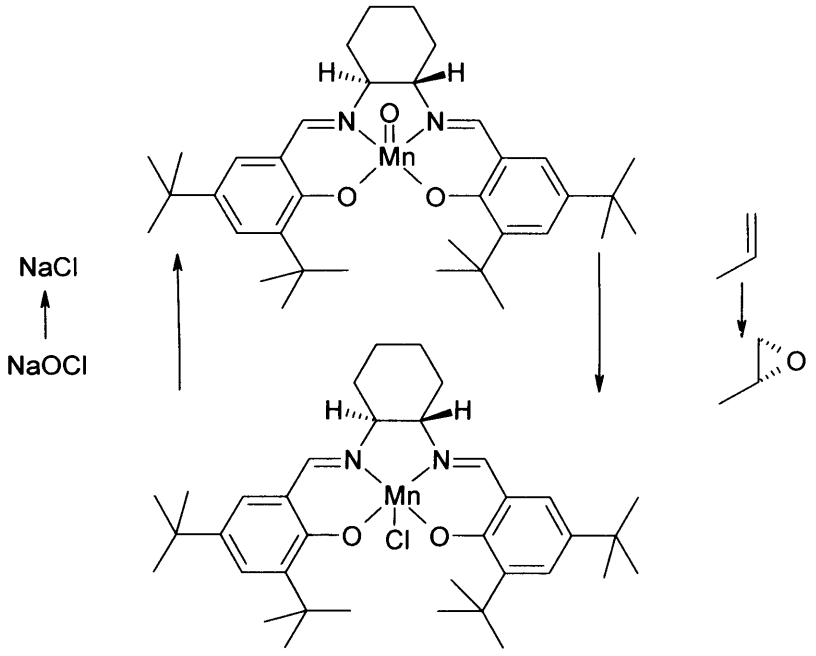

Figure 1.7: Catalytic process, showing oxygen transfer taking place *via* a two step cycle.

The oxygen transfer occurs through a two step catalytic cycle. Such mechanisms are found in metal porphyrin catalysed epoxidations. A relatively cheap

oxidant, such as bleach (NaOCl), transfers atomic oxygen to the Manganese (Figure 1.7). Oxygen transfer from the catalyst to the alkene has been thought to occur *via* several different mechanisms. Such intermediates include attack of an oxygen radical on the double bond itself, concerted oxygen delivery or the formation of a metallaoxetane intermediate (Figure 1.8). Norrby and co-workers [64] recently postulated a mechanism through which a metallaoxetane may occur as a reaction intermediate. However, Jacobsen showed that oxidation occurs *via* different mechanisms. Oxygen transfer to alkenes with radical stabilizing groups, occurs by an attack of an oxygen centred radical on the alkene. This mechanism is supported by the observation that *cis* alkenes result in both *cis* and *trans* epoxides.

Stereoselectivity in the reaction mechanism must occur in the second step of the catalytic cycle, where the oxygen is transferred from the complex to the epoxide.

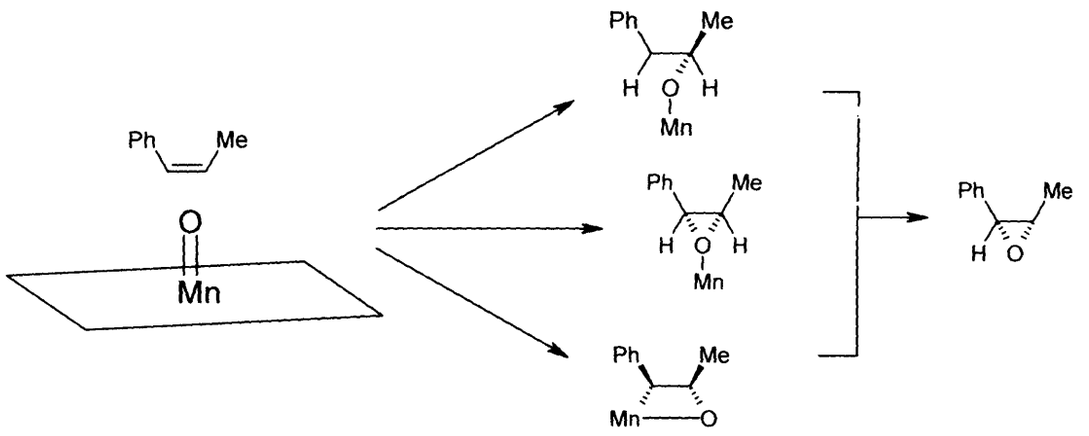

Figure 1.8: Postulated intermediates for the oxygen transfer from the catalyst to the alkene [57].

Jacobsen and co-workers recently reported [57] a new cobalt salen catalyst which has applications for the use in the hydrolytic kinetic resolution (HKR) of terminal epoxides and also for the enantioselective catalytic ring opening of *meso* epoxides. Catalytic amounts (1mol%) of Co(II) are used in the proposed reactions and the catalyst may be recycled. Excellent enantioselectivities and significantly high chemical yields are obtained using the Co(II)-*N,N'*-bis(3,5-di-*tert*-butylsalicylidine) complex for terminal epoxides. The chiral Co(II) complex is also effective for the asymmetric ring opening of *meso* epoxides, with benzoic acid.

1.7 Spectroscopic investigation of metal Schiff base complexes

1.7.1 *Paramagnetic cobalt complexes*

Cobalt (II) complexes have been widely studied due to their biological and chemical interest [65]. Cobalt (II) porphyrin complexes are of interest as models for Co-substituted hemo and myoglobin [66]. Also, cobalt and pyridine adducts have been studied by EPR and ENDOR spectroscopy as models for the heme unit in deoxygenated myoglobin and haemoglobin [67, 68].

A continuous wave (cw) and pulse electron paramagnetic resonance study of cobalt (II) alamin, diluted in hydroxo-cobalt (III) alamin was reported by Schweiger *et al* [69]. Hyperfine sublevel correlation spectroscopy (HYSCORE) was employed at X and Q-band frequencies to study the weakly coupled corrin nitrogens and the remote nitrogens of the DMBI (dimethyl benzimidazole) ligand. Hyscore measurements provided a unique set of data, allowing the A and Q tensors to be determined. At the higher Q-band frequency, interpretation of the HYSCORE spectra is simplified since the number of combinations is decreased. However, at X-band, the combined peaks between different corrin nitrogens are ambiguous, as hyperfine interactions are close to cancellation, causing strong mixing.

EPR has also been used to study long range magnetic ordering in very weak interacting solvent systems. EPR investigations were carried out on two bimetallic molecular magnets $(NBu_4)_2Co_2[Cu(opba)]_3.S$, where S = $3DMSO.3H_2O$ and $2H_2O$ [70].

A pulse EPR and ENDOR study of the electronic structure of a sigma-carbon bonded cobalt (IV) corrole was investigated by Schweiger *et al* [71]. They reported principal g values of $g_1 = 1.9670$, $g_2 = 2.1122$, $g_3 = 2.0043$, where the g_1 and g_2 axes point at the nitrogens of the corrole macrocycle. The cobalt hyperfine matrix, A, had values of $A_1 = 72$, $A_2 = 8$ and $A_3 = 10$ MHz. An excellent description of the electronic structure, consistent with the experimental data, was achieved using density functional theory simulations. Both the calculated data and experimental results showed that there is a significant amount of spin density on both the cobalt d_{yz} orbital and on the macrocycle itself.

Co(III) (salen) complexes studied by Baan [72] have been reported as important intermediates in reactions of Co(salen) derivatives, as in the reduction of (hydroxo)Co(III) (salen) with alcohols and aldehydes (Figure 1.9). it was found that air oxidation of the complex shown in Figure 1.9 gave a bridged (alkoxo)Co(III)(salen) complex, with a planar salen ligand. However, in the presence of MeOH, a monomeric bridged complex precipitates (Figure 1.9b), whereas in dichloromethane (CH_2Cl_2), another bridged complex is obtained with twisted-salen ligands (Figure 1.9c).

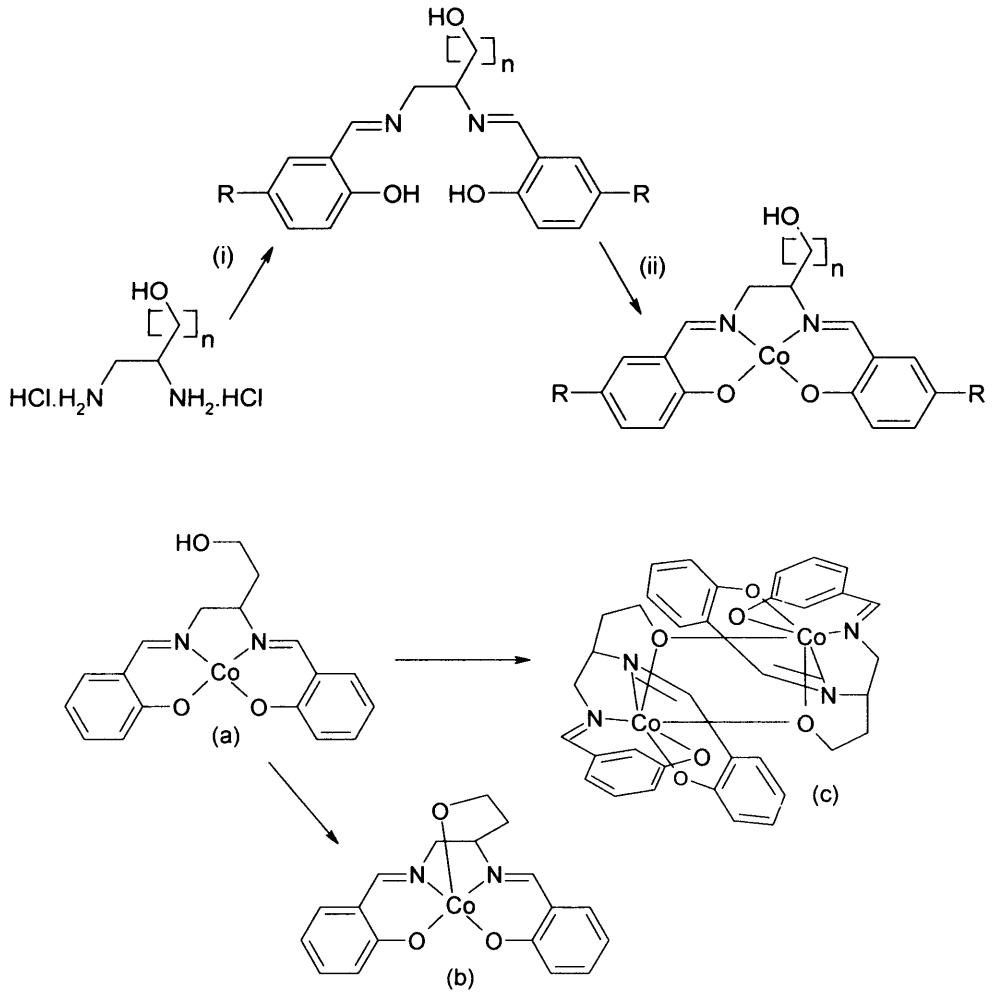

Figure 1.9: Series of (Alkoxo) Co(III) (Salen) complexes reported by *Baan*; (i) formation of salen ligand framework and (ii) complexation with cobalt acetate. $[\ ]_n$ represents repeating bonds [72].

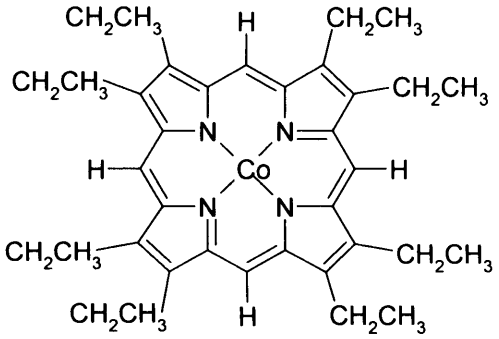

(a)

Figure 1.10: (**a**) dioxygen activation catalyst (oxyCo)TPP(L) [73].

ENDOR spectroscopy and pulsed ENDOR were used in order to resolve the interaction of the Cobalt metal and surrounding magnetic nuclei. The use of cw and pulsed multifrequency EPR and ENDOR, have formed the basis of many studies, such as that of Co(II) tetraphenylporphyrin complexes. The dioxygen storage and transport function of heme proteins, haemoglobin (Hb) and myoglobin (Mb), has been the subject of many different spectroscopic techniques. It is found that many planar Co(II) complexes can form 1:1 adducts with molecular oxygen since they possess a coordinated nitrogen base in the sixth position. Because of their unique features, Van Doorslaer and Schweiger [73] used cw EPR and ENDOR to study frozen solutions of (oxyCo)TPP(L) (TPP=tetraphenylporphyrin, L=pyridine, 1-methylimidazole) (Figure 1.10a). Using a combination of cw EPR at X, Q and W-band and Davies-ENDOR, the g and cobalt hyperfine matrices and their corresponding principal axes were determined for the first time in detail.

Cobalt salen type complexes have also been previously studied due to their catalytic ability for dioxygen activation in the oxidation of veratryl alcohol. The complexes were chosen to examine the influence of ligand structure on catalytic activity in basic aqueous conditions. Although Schweiger [74] probed the surroundings of a Co(II) porphyrin complex, Welker, Chapman and Day [75] reported the synthesis and enantioselective Diels-Alder reactions of two optically active Cobalt (III) salen-1,3-butadien-2-yl complexes. The synthesis of enantiomerically pure complexes is of utmost importance in organic chemistry, where the asymmetric Diels-Alder reaction is one of the most powerful synthetic methods for the control of stereochemistry.

Until recently, dienes such as 1,3-butadiene have not been used in enantioselective Diels-Alder reactions. However, Welker *et al* [75] developed an effective method for the preparation of cobalt (III) salen [Co(salen)]-1,3-butadien-2-yl complexes and showed their ability to react via Diels-Alder. Their findings showed evidence of the first chiral transition-metal substituted 1,3-dienes with sigma bonds from the transition metal to the dienyl fragment.

The chemical reduction of transition metal complexes of π-acceptor ligands such as those shown in Figure 1.11, are of interest, because of the possibility of forming either a metal reduced species or a metal-stabilized ligand radical [76]. Such redox properties are found to be highly dependent on the axial ligation. Anacona *et al* [77] studied the redox chemistry of cobalt(II) complexes of the macrocyle, in the presence of a series of axial ligand donors, determining whether or not, redox characteristics are observed. From cyclic voltammetry studies of the complex in DMSO, only one revesible reduction wave at -1.35 V *vs* Ag |$AgBF_4$ reference electrode was present. This was indicative of a diamagnetic species which was assigned as a mononuclear d^8 Co(I) species.

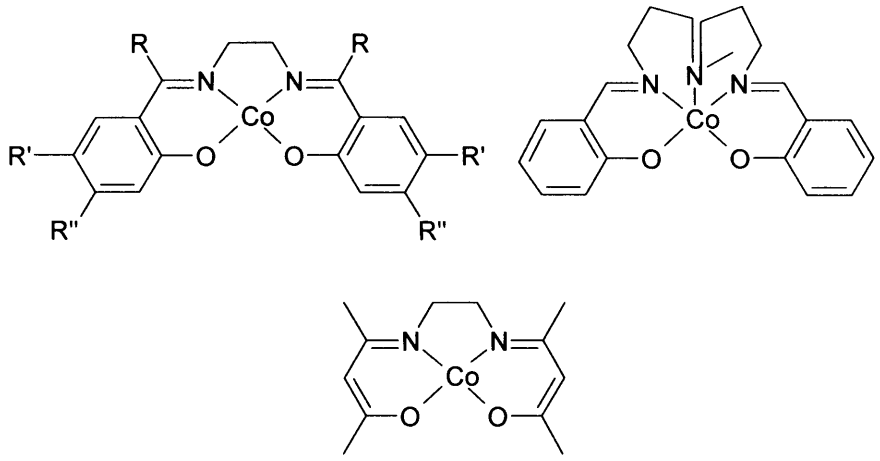

Figure 1.11: Transition metal complexes of π-acceptor macrocyclic ligands [76].

The axial ligation properties of macrocyclic cobalt complexes have also been reported by Reddy *et al* [78]. He studied the template synthesis using acetylacetone and various aromatic diamines (Figure 1.13), eg., 1,2-diaminobenzene and 3,4-diaminotoluene for the first time. These complexes were alkylated using CH_3I and C_2H_5Br in the presence of pyridine, therefore resulting in the macrocyclic organocobalt complexes. The complexes were characterized through spectral and electrochemical studies.

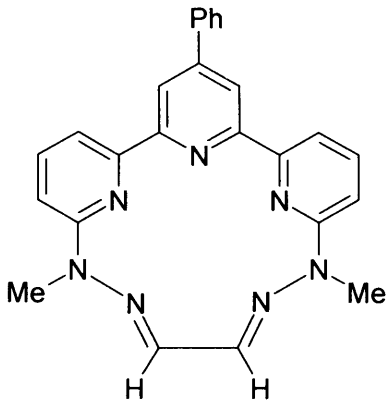

Figure 1.12: Example of a macrocyclic template ligand, as synthesised by Anacona *et al* [77].

When it comes to designing new catalysts, cobalt (II) salen and salophen complexes (Figure 1.13) are known to participate in a variety of chemically important reactions. The most common feature of these ligands is the square planar N_2O_2 arrangement (Figure 1.14) that stabilizes normally inaccessible oxidation states in the metal. Cobalt (II) and Nickel (II) complexes are known to undergo reversible or quasi-reversible reduction at solid electrodes, forming the cobalt (I) and nickel (I) species [77] [78]. Such reduced complexes behave as strong nucleophiles and are useful for the catalytic reduction of alkyl halides. One major drawback with regards to salen and other salen type complexes is the presence of imino moieties, which can cause instability in the metal complex. To overcome this Goken and Peters [79] synthesised a new class of catalyst. The catalyst, 6,6'-bis(2-hydroxyphenyl)-2,2'-bipyridine is highly stable and exhibits the same reduction characteristics as the salen and salophen complexes.

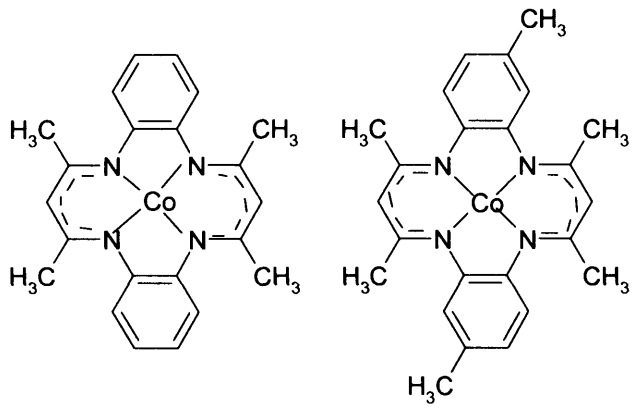

Figure 1.13: Cobalt (I) salen and salophen complexes, illustrating the square planar arrangement [78].

Branchaud and co-workers showed that vitamin B_{12} catalyzes the enantioselective desymmetrization of epoxides (*meso*), aziridines and activated cyclopropanes [80]. The mechanism postulated by Branchaud is shown below (Figure 1.14) for the desymmetrization of *meso* cyclic epoxides.

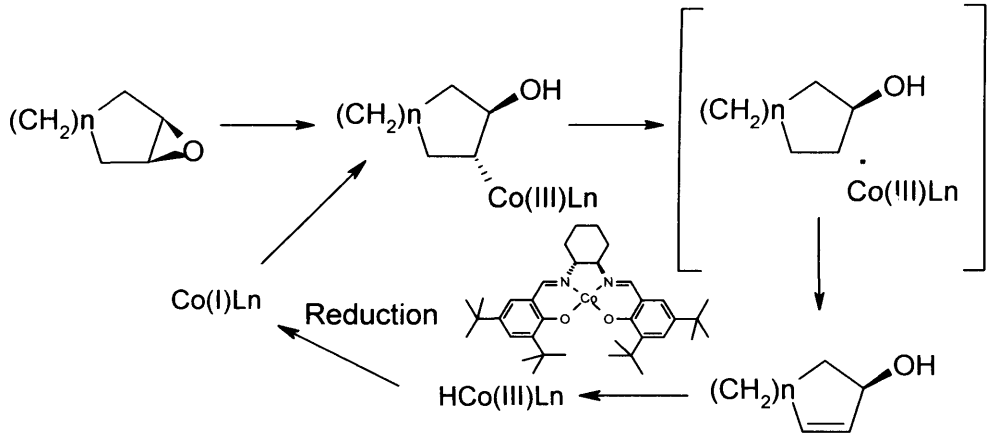

Figure 1.14: Mechanism for the desymmetrization of *meso* cyclic epoxides [80].

Although much of the emphasis has been on the study of cobalt(II) salen type complexes in catalytic processes, cobalt metal complexes have also found applications in biological studies, especially when encapsulated. This encapsulation process results in extremely high binding constants, resulting in a negligibly small release of the metal cations. An EPR study of high and low-spin Co(II) encapsulated complexes, having a hexadentate ligand was reported by *Symons* and *Taiwo* [81]. The hexadentate "Sar" ligands can be thought of as ethylene diamine complexes, which are capped at either end (Figure 1.15c) They found that the chemically prepared

cobalt(II) complexes had well defined EPR spectra at 4 K in the high spin, g = 9 region. However, when the cobalt centres were exposed with radiation at 77 K, a low spin species was initially formed with g values ~ 2.0023 and after annealing to 115 K, the corresponding high spin complex was formed. On warming, the features shown in Figure 1.15a broadened reversibly, establishing the high spin character of these complexes, also showing large axial distortion giving rise to a large zero field splitting and a minor rhombic distortion.

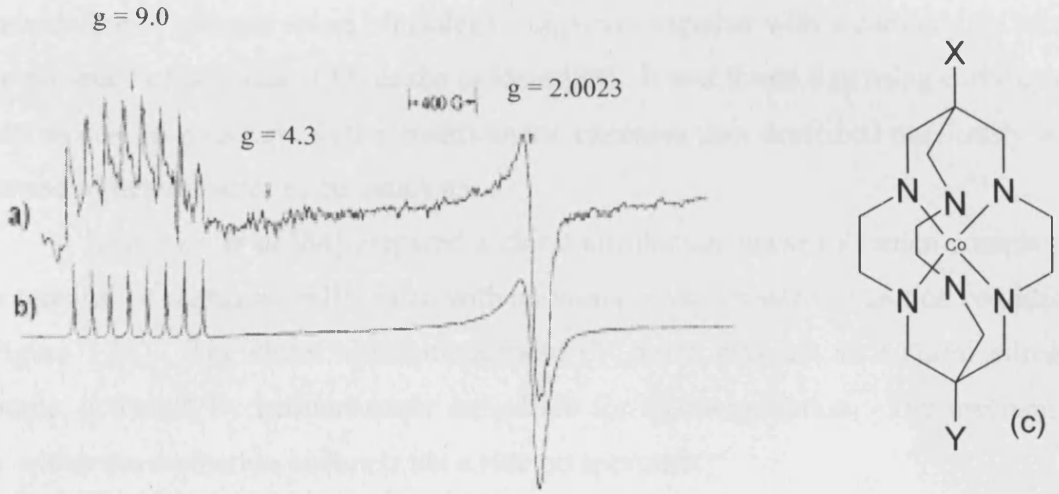

Figure 1.15: Co(II) encapsulated complex (c). EPR spectra recorded at 4K; (a) experimental and (b) simulation. EPR spectra recorded at 4 K in the high spin g = 9 region [81].

1.7.2 *Manganese salen-type complexes*

A major achievement recently in catalytic enantioselective oxidation is the epoxidation of prochiral unfunctionalised olefins, catalysed by Mn(salen) complexes. Two catalytic systems for the enantioselective epoxidation were developed by Talsi *et al* [82]. The first system involves a two-phase system with commercial aqueous buffered bleach phase and an organic phase, which is a solution of substrate and catalyst. The second catalytic system involved m-chloroperbenzoic acid (m-CPBA), N-methylmorpholine *N*-oxide (NMO) and a catalyst in DCM, which is effective in the enantioselective epoxidation of styrene. To study the mechanism of Mn(II) (salen) catalysts for oxidation, Talsi and co-workers used EPR spectroscopy to study complexes of (*R,R*)-(-)-*N,N'*-bis(3,5-di-*tert*-butylsalicylidene)-1,2-cyclohexane

diaminomanganese (III) chloride and *N,N'*-bis (salicylidene) ethylenediamino manganese(III) chloride.

Chiral (salen)Mn(III) complexes have become the most efficient and practical catalysts for the asymmetric epoxidation of unfunctionalised olefins. Very high yields of epoxides with high enantioselective excesses have been obtained with a variety of disubstituted *cis*-alkenes and a range of oxidants, eg., PhIO, NaOCl or per-acids. The salen epoxidation methodology also includes the enantioselective synthesis of certain mono, tri and tetrasubstituted epoxides. Pietikainen reported the asymmetric epoxidation of alkenes using Mn(salen) complexes together with a carboxylate salt in the presence of aqueous H_2O_2 as the oxidant [83]. It was found that using carboxylate salts as co-catalysts gave better enantiomeric excesses than described previously with the use of heterocycles as co-catalysts.

Jorgensen *et al* [84] prepared a chiral nitridomanganese (V) salen complexes, by reaction of manganese(III) salen with ammonia under oxidative reaction conditions (Figure 1.16). The chiral nitridomanganese (V) salen may act as a chiral nitrogen source, activated by trifluoroacetic anhydride for alpha-amination. The mechanism by which the amination occurs is *via* a side on approach.

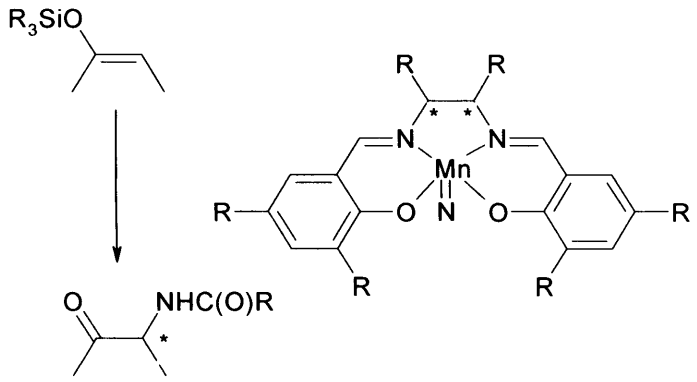

Figure 1.16: Chiral nitridomanganese (V) salen complex, prepared by the reaction of manganese (III) salen with ammonia under oxidative reaction conditions, * represents chiral centre [84].

Manganese (III) has also shown applications in porphyrin based systems, such as the use of metalloporphyrins, especially in the preparation of synthetic porphyrins. The enhanced activity of manganese(III) complexes make them ideal for epoxidation,

through supramolecular complexation. However, the use of these metalloporphyrin catalysts in synthesis has been limited by catalyst deactivation, which is thought to occur *via* two pathways, irreversible ligand oxidation and oxo dimer formation. Nguyen presented a novel supramolecular catalytic epoxidation system, where individual components can be altered to enhance the catalysts activity and induce selectivity. It had been found that pyridines bind to zinc porphyrins with binding constants of the order of 3×10^3 M^{-1} [85]. The binding of pyridine to magnesium porphyrins was also observed by Nguyen, with binding constants of $K_b = 2 \times 10^3$ M^{-1}. Nguyen showed that several manganese(III) porphyrins increased turnover numbers significantly for the catalytic epoxidation of styrene, with the addition of bulky Lewis acids such as ZnTPP and MnTPP (TPP=tetraphenylporphyrin) (Figure 1.17).

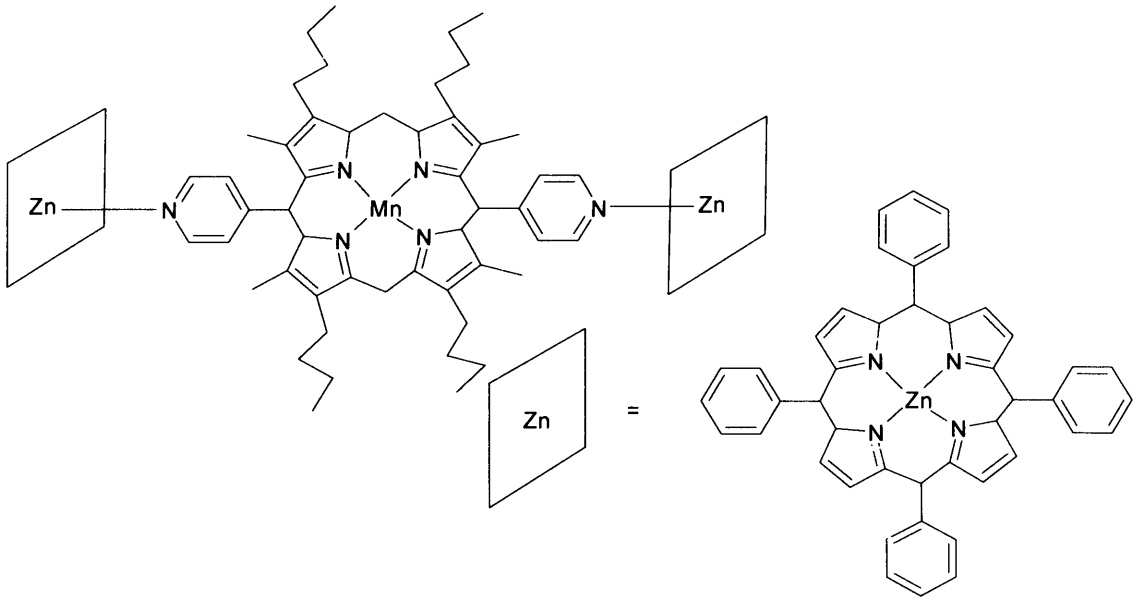

Figure 1.17: Manganese (III) porphyrin complex, for the catalytic epoxidation of styrene. Catalytic enhancement and selectivity can be introduced *via* the binding of Zinc porphyrins [85].

In the presence of the coordinating pyridines, less significant enhancement is observed, where the residual enhancement is ascribed to the protection of the manganese-oxo intermediate through catalytic site coordination. The addition of such bulky Lewis acids led to the reactivation of the deactivated catalysts and complete recovery of the original catalyst.

Magnetic resonance techniques have also been employed to study and probe the electronic structure of antiferromagnetically coupled dinuclear Manganese complexes (Mn^{III} Mn^{IV}) by Lubitz and Wieghardt [86]. They studied several exchange-coupled dinuclear manganese complexes using EPR and ENDOR spectroscopy. The complexes were divided into two classes, one containing two oxo-bridges and the other containing two oxo-bridges and an OAc bridge. The latter complexes are sterically hindered through joining the two macrocyclic ligands and *via* an exchange of the NH groups with NCH_3. On the basis of specifically deuterated complexes, and results from orientation selective ENDOR spectra, some hyperfine couplings in the proton region could be assigned to positions within the complex. They calculated all the dipolar hyperfine couplings, based upon point-dipole data and coordinates provided by x-ray crystallography.

Manganese complexes have been found as active sites in a number of metalloenzymes, examples of which, include [87] manganese catalase (MC) and oxygen-evolving complex (OEC) of oxygenic photosynthesis photosystem II. While no definitive structure has been determined for the OEC, the catalytic site of the oxygen evolution consists of a cluster of four manganese ions ligated by amino acid residues. Although Lubitz [86] studied the electronic structure of the dinuclear manganese complexes, Britt and Peloquin [87] dicussed how EPR/ENDOR was used to characterize the physical/electronic structure of the OEC manganese cluster. EPR was used as a tool to provide an insight into the physical/electronic structure of the manganese cluster and its interaction with tyrosine. Figure 1.18 shows the postulated structure of the manganese cluster, based upon ESE-ENDOR simulations.

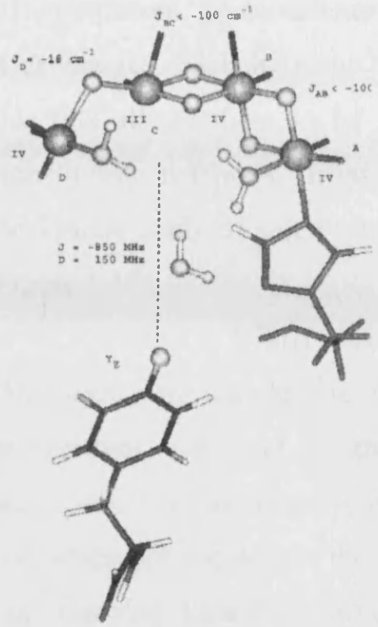

Figure 1.18: Postulated structure of the manganese cluster proposed by Britt and Peloquin, based upon ESE-ENDOR simulations [87]

1.7.3 *Nickel salen-type complexes*

A phenomenon of utmost importance for the functioning of biological systems and also for chemical synthesis is chiral recognition. The stereoselectivity resulting from chiral recognition involves reactions that may involve chiral and prochiral compounds. Such selectivity may arise from kinetic or thermodynamic sources. Kinetically controlled, stereoselectivity is a result of the energetically differentiated formation of diastereoisomeric intermediates and transition states, which leads to a significant difference in reaction rates. On the otherhand, thermodynamic stereoselectivity results from the nonstatistical distribution of diastereoisomeric products in equilibrium. Over recent years, there has been increased interest in the use of optically active metal complexes. Co-ordination complexes were used, mainly to obtain detailed information on the stereochemical steps of reaction mechanisms and to elucidate information on the structural applications. Examples include separation of enantiomers and development of systems for homogeneous catalysis. Transition metals are an important part of the chiral active site of proteins (redox-active) [88], where ligand substitution is one of the most important type of reactions of metal

complexes and is reported for many square-planar complexes with d^8 metal centers such as Pt(II), Pd(II) and also in Ni(II) complexes. In complexes like Ni(II), chirality has to be introduced through ligand exchange. Nickel(II) has biological relevance, eg., in ureases. It is this importance that allows them to be studied due to their chirality effects in different ligand substitution reactions. Elias *et al* studied this in depth, focussing their research on the kinetic study of salen type complexes (bis(N-alkylsalicylaldiminato)Ni(II)) [89] (Figure 1.19).

Elias *et al* [89] showed that in *trans*-N_2O_2 Schiff base complexes bis-(N-alkylsalicylaldiminato) nickel(II), [Ni(alkyl-sal)$_2$] tetradentate ligands of salen are found to have a second-order rate constant. *R*- and *S*- enantiomers of chiral alkylamines in metal complex formation leads to enantiomeric complexes "Ni(*R,R*)" and "Ni(*S,S*)", the chirality centers of which are located in the ligand sphere. This was the first example by Elias *et al,* showing ligand substitution in planar four-coordinate complexes. They found that the complexes react with the *R*- and *S*-enantiomers of chiral salen ligands stereospecifically in the sense that the second-order rate constant is greater for the diastereomeric complex pairs Ni(*RR*)/(*R*) and Ni(*SS*)/(*S*), than for Ni(*RR*)/(*S*) and Ni(*SS*)/(*R*).

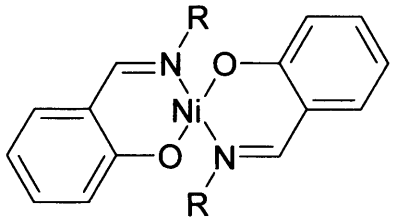

Figure 1.19: Ni(II) (bis(*N*-alkylsalicyaldiminato) - salen type complex, employed for kinetic studies[89].

Since the mid 1970's, when the discovery was made [90] that the hydrolytic enzyme urease contains nickel, the number of enzymes and proteins known to bind Ni has increased, including a group of redox active enzymes such as CO dehydrogenases, methyl coenzyme M reductase and hydrogenases. Figure 1.20, shows the redox active Ni(II) center, ligated by sulphur, which can participate in charge delocalization or in redox processes.

Hoffman and co-workers employed ENDOR and Electron Spin Echo Envelope Modulation (ESEEM), to understand the electronic structure of the oxidised nickel thiolate complexes [90]. EPR studies and molecular orbital calculations on the

monoanion, S = 1/2 state of $[Ni(mnt)_2]^-$ and $[Ni(tfd)_2]^-$ have tested whether the unpaired spin is located on the sulphur ligand or on the metal, as Ni(III). Their results supported the fact that the sulphur atoms are primarily involved in the oxidative chemistry associated with Ni sites in hydrogenases and other such Ni enzymes.

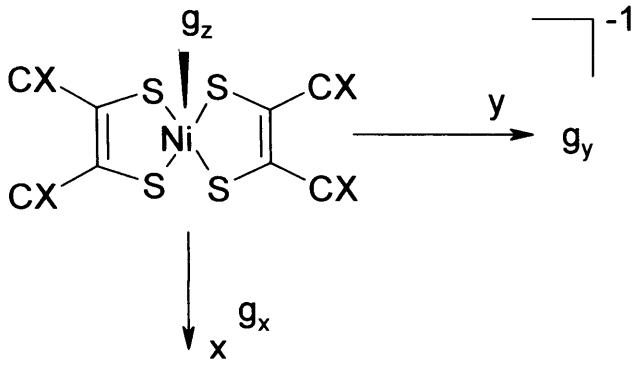

Figure 1.20: Nickel (II) thiolate complex showing the redox active centre, ligated by sulphur atoms. The ligand can participate in charge delocalisation or in a redox process [90].

The investigation of metal complexes with sulphur containing bases, have been studied widely, as they have anticancer activity [91]. Nickel(II) complexes with N_2O_2 Schiff base ligands derived from salicylaldehyde have long been used as homogeneous catalysts [92]. Understanding the role played by the electronic/structural effects to control the redox chemistry of these metal complexes is vital in the design of new catalysts. Figure 1.21 shows an example of a ligand design containing both a nitrogen and sulphur framework of atoms. The study of the oxidative chemistry of Ni(II) complexes with N_2O_2 Schiff base ligands (Figure 1.22) has been carried out by Freire *et al* [93], focusing on the oxidative chemistry in solvents with different coordinating strength and have found the oxidation products depend on the solvent system.

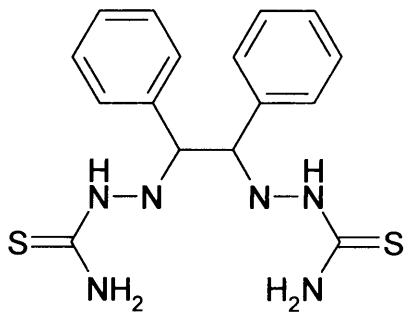

Figure 1.21: An example of a new ligand design, containing a nitrogen and sulphur framework of atoms [92].

The complexes studied by Freire were; *N,N'*-2-methylpropane-2,3-diyl-bis(salicylideneiminate)Ni(II) - [Ni(saldMe)], *N,N'*-1,2-cyclohexyl-1,2-diyl-bis(salicylideneiminate)Ni(II) – [Ni(salhd)] and *N,N'*-2,3-dimethylbutane-2,3-diyl-bis(salicylideneiminate)Ni(II) - [Ni(saltMe)] and exhibited a strong quasi-reversible diffusion-controlled one-electron transfer process in strongly coordinating solvents, such as DMF and $(CH_3)_2SO$. EPR spectra were recorded of the electrochemically generated species as a frozen solution and were found to be similar in both solvents. The oxidation of [Ni(saldMe)] and [Ni(salhd)] in DMF and $(CH_3)_2SO$ were shown to proceed through oxidation of the metal centre and axial coordination of solvent molecules which were observed for [Ni(salen)] and [Ni(saltMe)], producing Ni(III) complexes as $[Ni(L)(solv)_2]^+$. The bulky substituents in the imine bridge tended to produce the less stable Ni(III) in N_2O_2 Schiff base complexes. The sterically hindered solvent molecules coordinating axially, are shown in the sequence [Ni(salen)] < [Ni(salhd)] < [Ni(saldMe)] < [Ni(saltMe)], illustrating the hinderance on axial coordination. Freire also focused on the reductive electrochemical study of Ni(II) and their reactivity towards CO [94].

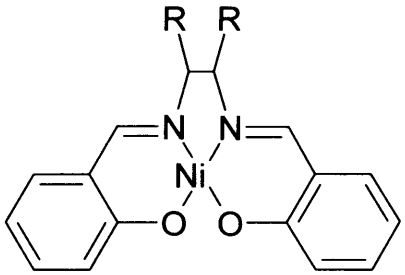

Figure 1.22: Ni(II) complex with N_2O_2 Schiff base ligand. R = bulky substituents [93].

The results showed that complexes with aliphatic diimine bridges are reduced to four coordinate Ni(I) species with a B_{1g} $(d_{xy})^1$ ground state, whereas those with aromatic diimine bridges are reduced to square-planar Ni(II) anion radical species, which quickly form dimers. In the presence of a strong π-acceptor ligand, such as CO, new Ni(I) species were formed and from EPR data, can be made as five-coordinate complexes with a B_{1g} $(d_{xy})^1$ ground state, $[NiL.CO]^-$, compared to binding pyridine, imidazole and triphenylphosphine.

Metal complexes of bis-1,2-dithiolenes have also been studied in addition to those studied by Friere, as a result of electronic and optical properties, which arises

from electronic delocalisation in such complexes. In order to find new types of extended, delocalised species, Robertson and Yellowlees prepared new thiolene complexes using redox active sandwich complexes [95].

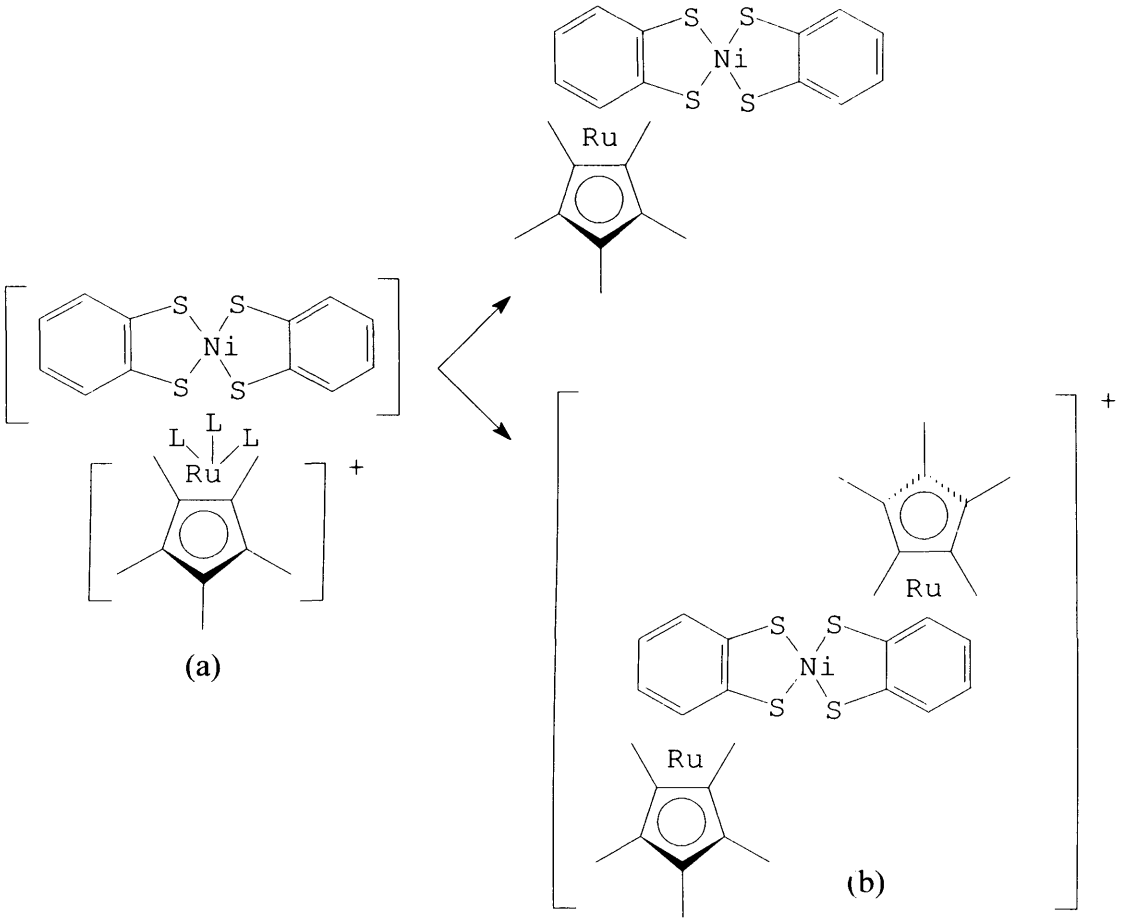

Figure 1.23: New thiolate complexes prepared using redox active sandwich complexes [95].

The complexes [Ni(bdt)(Cp*Rubdt)] and $[Ni(Cp^*Rubdt)_2][CF_3SO_3]$ (bdt = 1,2-benzenedithiolate) were prepared from reaction with $TBA[Ni(bdt)_2]$. It was found from EPR measurements that there is little difference between the new thiolate complexes and $[Ni(bdt)_2]^-$. However there is a deviation in parameters for complex shown in Figure 1.23(b) and was evidence for the fact that the electron is delocalised over the entire complex, involving both Ru centres in addition to the Ni centre.

Such studies with Nickel (II) complexes have led onto other investigations, namely using EPR spectroscopy to study paramagnetic species, obtained through radiation damage in transition metal cyanide complexes in alkali halide host lattices. A review by Vugman [96], studied the kinetics of oxidised and reduced Ni^{2+}

complexes produced by X-ray irradiation on NaCl single crystals, doped with $[Ni(CN)_4]^{2-}$. The generation of these two complexes is attributed to migration ofa charge compensating vacancy from the reduced to the oxidised complex in a reversible reaction.

The applications of EPR and ENDOR spectroscopy have also been widely used to study Ni(II) complexes at different frequencies. In a paper by Hoffman *et al*, EPR and ENDOR spectroscopy was used to investigate the Ni(I) form of Cofactor F_{430}[I] of Methanobacterium thermoautotrophicum (Figure 1.24a) and of Ni(I) Octaethylisobacteriochlorin (Figure 1.24b) [97]. They performed both pulsed and cw techniques at X- and Q- band frequencies on the nickel complexes. The EPR results at Q-band frequency, agree with those obtained from X-band. The spectra recorded at Q-band of $Ni(I)F_{430}$ is axial in aqueous solution with $g_{\|} = 2.244$, $g_{\perp} = 2.063$. In contrast to this result, the complex shown in Figure 1.24b showed slight rhombicity with $g_1 = 2.204$, $g_2 = 2.080$ and $g_3 = 2.063$.

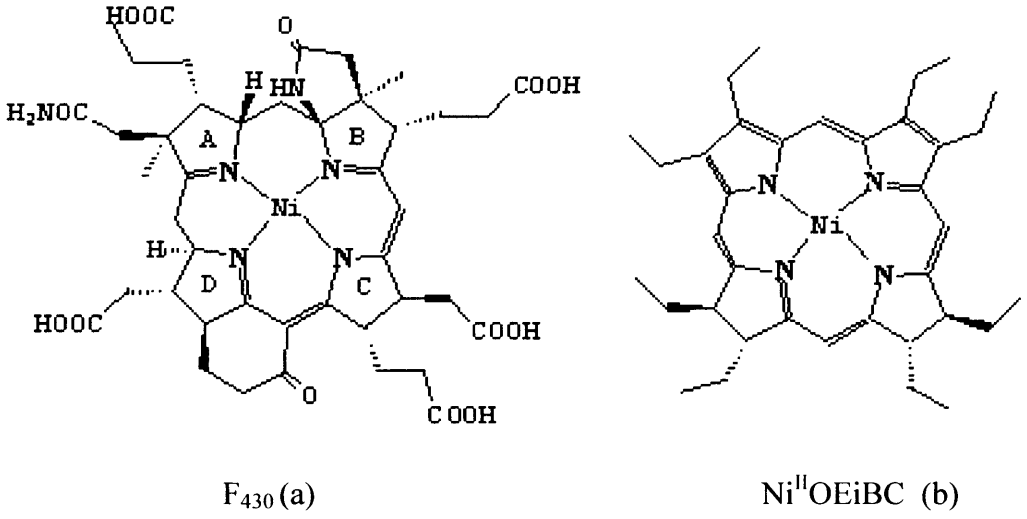

F_{430} (a) Ni^{II}OEiBC (b)

Figure 1.24: Nickel (I) complexes. (a) Ni(I) form of Co factor F_{4300} of methanobacterium thermoqutotrophicum; (b) Ni(I) octaethyl isobacteriochlorin [97].

The electronic structure of nickel(I) is extremely sensitive to ligand conformation and solvation effects. The ENDOR spectra for Figure 1.24b shows that the in-plane g tensor components are directed exactly between the bonds, resulting from ligand field effects at the metal. Such results have been seen in Cu(II) complexes and is now the case for Ni(I) complexes.

In previous years, nickel centres have been subjected to a number of physiochemical experiments, including X-ray crystallography to understand their structure-function relationship, especially in hydrogenases. The structure of the heterodimeric Ni-Fe hydrogenase from *desulfovibrio gigas* has been studied by Bharadwaj *et al* [98]. The EPR spectrum of the complex shown in Figure 1.25a shows a broad signal with g_{iso} = 2.03 at 295 K, that sharpens considerably on cooling to 77 K, without enhanced resolution of fine structure. In CH_3CN at 295 K, an isotropic signal is achieved with g_{iso} = 2.05. When the temperature is decreased to 77 K, there is a dramatic change in the EPR spectra, ie., a change to anisotropic profile with g_1 = 2.12, g_2 = 2.03 and g_3 = 2.01, which is typical of Ni(III) type complexes in S=1/2 ground state. The EPR spectrum does not change when a different solvent system is used, such as DMF or THF, consistent with a Ni(III) complex, where the unpaired electron is localised in the d_{xy} orbital.

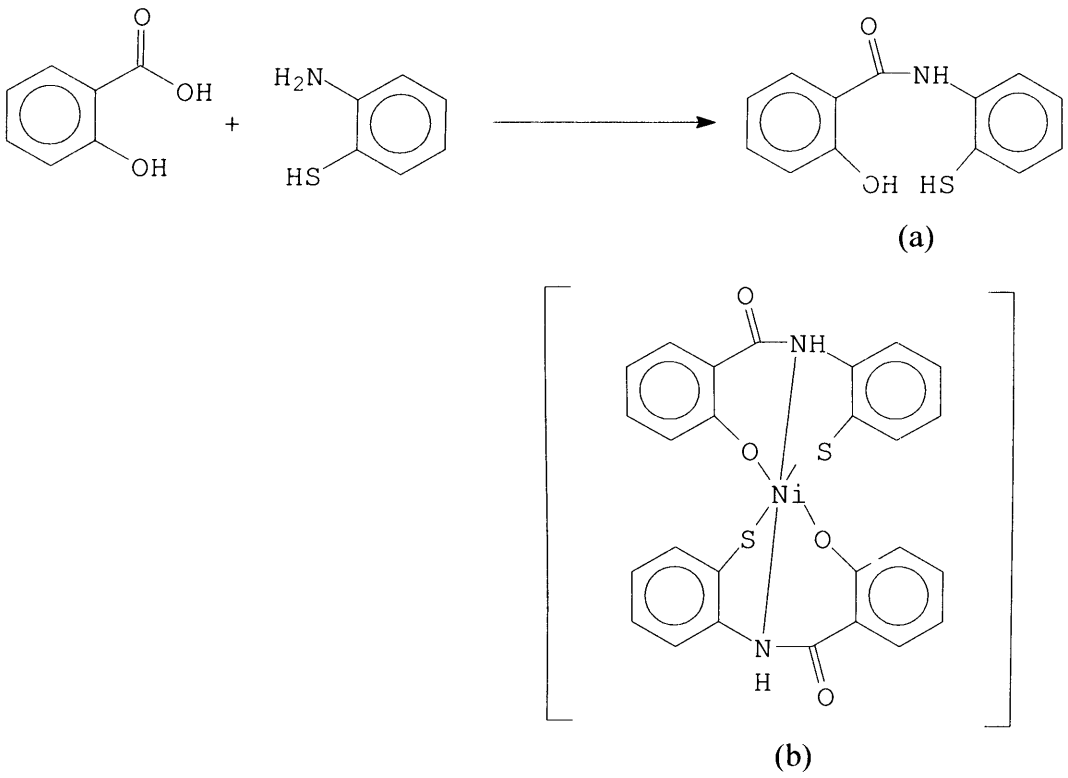

Figure 1.25: (a) Represents preparation of ligand before complexation; (b) nickel thiolate dimeric complex [98].

The high sensitivity associated with EPR and its selectivity to paramagnetic compounds, allowed Shmidt *et al* [99] to study the structure of intermediate cobalt

and nickel compounds in Ziegler-type metal complex catalysts, ie., the interaction between transition-metal complexes and organometallic compounds, ie., $Ni(acac)_2$-PBu_3-$AlEt_2Cl$. The Ni(I) complexes play an important part in the regeneration of catalytically active Ni(II) hydrides.

This use of incorporating different transition metals was also reported by Lu *et al* [100]. Lu studied a series of poly salen Ni(II) and Co(II) type complexes, where the catalysts performance in the dimerization of propylene, was studied in combination with aluminium co-catalysts and phosphine ligands. The results by Lu indicated that the productivity of the catalytic system was strongly dependent on the steric character of poly-salen ligand in Ni(II) and Co(II) complexes. It is well known that the catalytically active nickel species (nickel hydride), is required in nickel-catalyzed propylene dimerization. When large excesses of phosphine ligands are added, the strong bonding of Ni-R (R = N,O) might be weakened through coordinative bonding between phosphine and the ligand centre.

Recently, in view of the recent interest in the energetics of metal ligand binding in metal chelates involving N, O donor ligands, Garg and co-workers studied Schiff base complexes derived from *N,N'*-bridged tetradentate ligands involving N_2O_2 donor atoms [101]. They reported the synthesis, thermal and spectral studies of new Ni(II) complexes derived from *N,N'*-disalicylidene-1,2-phenylenediamine (H_2dsp), *N,N'*-disalicylidene-3,4-diaminotoluene (H_2dst), 4-nitro-*N,N'*-disalicylidene-1,2-phenylenediamine (H_2ndsp) and *N,N'*-disalicylidene ethylenediamine (H_2salen).

Metal salen type complexes and related chiral ligands are well recognised, due to their catalytic interest. However, one major drawback of applying metal-salen type complexes in homogeneous solution is the formation of μ-oxo-dimers and other polymeric species, as previously mentioned (Schiwei *et al* [100]). Maurya *et al* described the design of two series of coordination polymers, with polymeric coordinating salen ligands [102]. This widespread interest in redox polymers has been demonstrated by their applications in the area of chemically modified electrodes.

A new coordination polymer, prepared through the polycondensation reaction of α,ω-bis(chloromethyl)-polymethylphenylsilane with Ni(II)-bis(salicylidene) ethylenediamine was reported by Sacarescu *et al* [103]. The new polymer, prepared by *Sacarescu* contained redox active centers in the polysilane-conjugated backbone.

This type of polymer was fully characterised by electroactivity studies in the metal center, combined with a conjugative effect in the chain

Nickel salen (I) complexes, have also found applications in the formation of aldehydes and ketones, via a reduction of alkyl monohalides by nickel(I) salen (electrochemically generated) in dimethylformamide. Peters *et al* [104], discovered that, electrochemically generated salen is produced when a catalytically reducible alkyl monohalide (1-bromo-octane) is injected into oxygen free nickel (I). When the resulting mixture is exposed to light/air, an aldehyde (1-octanal) is prepared in high yields. Similar experiments with a secondary alkyl monohalide (2-bromohexane) gave rise to a ketone. The subject of polymers especially coordination polymers have recently attracted intense interest, because of their unique applications in heterogeneous catalysis, ion exchanges and molecular adsorption. Kondo and co-workers [105] studied and succeeded in the synthesis and structural characterization of a new hydrogen bonded polymer. The nickel (II) complex (*N,N'*-bis(2,5-dihydroxysalicylidene) ethylenediaminato was found to contain two hydroxyl groups at the terminal ends of the ligand. These hydroxyl groups form hydrogen bonds with a coordinating oxygen donor of an adjacent complex (Figure 1.26).

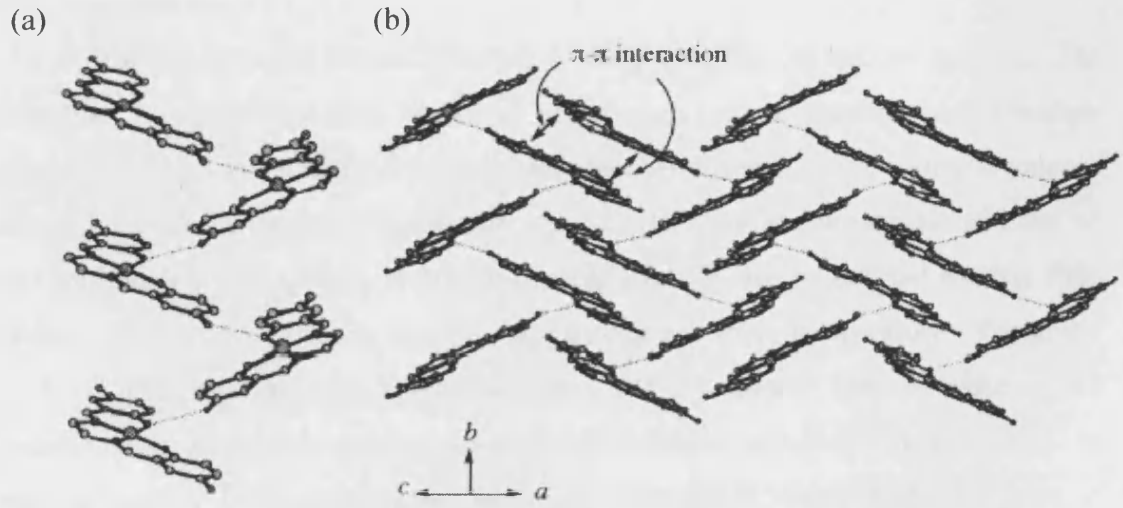

Figure 1.26: A new Nickel (II) hydrogen bonded polymer [105].

1.7.4 *Oxovanadium (IV) complexes*

1.7.4.1 *Spectral properties*

Studies of EPR spectra of paramagnetic transition metal chelates can lead to a detailed description of the electronic structure of these compounds. EPR is useful in qualitatively solving problems related to the binding of metals to organic ligands. This is true when the method is applied to metal chelates in complex biological systems. EPR spectroscopy can elucidate different kinds of information, namely (1) identification of the metal, its oxidation state and spin state; (2) identification of the binding site and symmetry; and (3) determination of the concentration of the paramagnetic metal ion. The methodology of EPR spectroscopy has been quite successfully applied to naturally occurring Cu^{2+} and Fe^{2+} chelate complexes. However, other transition metal complexes (paramagnetic) in biological systems have recieved very little attention. Vanadium is found to be a very important trace element in nature, ie., it is concentrated [106-114] by the marine animal *Phallusia Mamillata* and land plant, *Amanita Muscaria* (mushroom). Although vanadium containing fractions have been isolated from these systems, the exact binding of the vanadium atom is uncertain.

EPR spectroscopy is ideally suited to study vanadium in natural systems. The vanadium-51 nucleus (~100% abundant) has a large nuclear moment and a nuclear spin of 7/2. This gives rise to an eight line spectrum. Some of the common valence states of Vanadium are +2, +3, +4 and +5. The +5 state is diamagnetic and the +3 state, although paramagnetic, is not observable by EPR due to internal electric field effects. The +2 and +4 states can be easily detected at room temperature. Vanadium +2 is oxidatively unstable and yields the VO^{2+} cation. The +4 state exists predominantly as the oxovanadium(IV) ion and requires a non-cubic field for EPR. In order to employ EPR spectroscopy to obtain information about the binding site of vanadium in biological systems, suitable data on model compounds must exist. As a result of the wide interest in the electronic structure of VO^{2+} complexes, there is sufficient data in the literature for a variety of ligands (Table 1.2 and 1.3).

Table 1.2: EPR Parameters for oxovanadium (IV) Complexes in a range of solvents. [a] salen – bis(salicylaldehyde)-ethyl-enediimine, [b] TPP - α,β,γ,δ-tetraphenylporphyrin.

Complex	Ref	Host / Solvent	g_{iso}	$g_{\parallel}$	$g_{\perp}$	A_{iso} / G	$A_{\parallel}$ / G	$A_{\perp}$ / G
$VO(H_2O)_5^{2+}$	[106]	$Zn(NH_4)_2(SO_4)_2.6H_2O$	1.964	1.932	1.980	118.1	203	78
$VO(Cl)_5^{3-}$	[107]	$(NH_4)_2InCl_5.H_2O$	1.971	1.945	1.985	108.9	190	69
$VO(NCS)_5^{3-}$	[108]	$CHCl_3$	1.967	1.945	1.978	107.0	185	68
$VO(acac)_2$	[109]	Tetrahydrofuran	1.969	1.945	1.980	106.1	186	67
$VO(C_2O_4)_2$	[110]	$K_2TiO(C_2O_4)_2.2H_2O$	1.964	1.940	1.976	106.0	188	65
VO(salen)[a]	[111, 112]	Tetrahydrofuran	1.973	1.949	1.985	101.7	179	63
VO(TPP)[b]	[113]	$CHCl_3$	1.980	1.966	1.987	97.0	173	59
$VO(CN)_5^{3-}$	[108]	KBr	1.980	1.972	1.983	83.7	150	51
$VO(S_2CCN)_2^{2-}$	[114]	$CHCl_3$	1.992	1.975	2.000	69.9	132	43

1.7.4.2 *Electronic structure of oxovanadium (IV) complexes*

The fivefold coordination about the metal in $VO(acac)_2$ is square pyramidal. The axial oxygen atom is significantly closer to the vanadium than the other four beta-diketone oxygens. The overall molecular symmetry for $VO(acac)_2$ is C_{2V}. If only the donor atoms are considered, then the symmetry is raised to C_{4V}. Even for lower symmetry cases the effective symmetry appears to be C_{4V}. Oxovanadium complexes can also be six coordinate. The five coordinate complexes weakly add a sixth ligand to the vanadium atom in the axial coordination position. Since the vanadium to-ligand bond length is substantially longer in this case than the in-plane ligands, the interaction is justifiably considered only as a perturbation on the square pyramidal system. Ballhausen and Gray first formulated a ligand field picture of oxovanadium (IV) complexes [115].

The EPR spectra of VO^{2+} complexes are strongly dependent on the donor atoms bound to the central metal atom and are different for nitrogen and oxygen donors. Salen ligands are a good example as they consist of a *NNOO* ligand framework. As water molecules bind strongly to salen ligands, the result of this

strong bonding yields higher g values and lower hyperfine splitings. Table 1.3 represents some typical spin Hamiltonian values for an oxovanadium(IV) complex - β-ketamine in tetrahydrofuran (THF).

Table 1.3: Spin Hamiltonian parameters for oxovanadium (IV) complexes in THF.

Complex	g_{iso}	$g_{\perp}$	$g_{\parallel}$	A_{iso} / G	$A_{\parallel}$ / G	$A_{\perp}$ / G
VO(acen)	1.974	1.984	1.954	102.2	182	62
VO(acpn)	1.974	1.984	1.954	102.6	183	62
VO(bzen)	1.975	1.986	1.952	102.6	183	62
VO(bzpn)	1.975	1.984	1.957	103.4	182	64
VO(tfen)	1.974	1.983	1.955	104.6	183	63

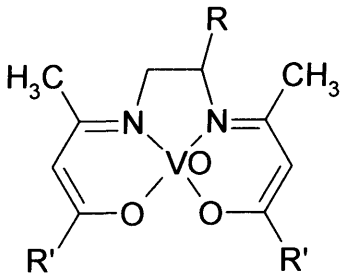

Compound	R	R'
VO(acen)	H	CH_3
VO(acpn)	CH_3	CH_3
VO(bzen)	H	C_6H_5
VO(bzpn)	CH_3	C_6H_5
VO(tfen)	H	CF_3

1.7.4.3 *Solvent effects*

It is well known that oxovanadium complexes form adducts with a wide variety of molecules. These adducts were studied by Kirste and Van Willigen [116], who reported the ENDOR spectra of bis(acetylacetonato) oxovanadium(IV) ($VO(acac)_2$) complex and its adducts with methanol and substituted pyridines. It had previously been assumed that the pyridine coordinates *via* a vacant axial position (*trans*). However, recent studies such as the X-ray study of 4-phenylpyridine have provided evidence in which the coordinated ligand is bound in a *cis* position (Figure 1.27) [117].

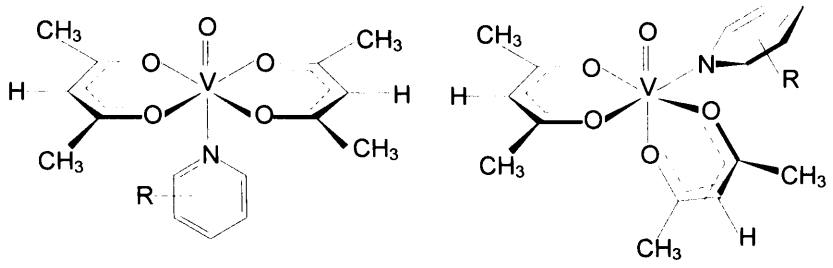

Figure 1.27: Two coordination modes of pyridine (py) with $VO(acac)_2$.

Experimental studies [116] provided information on the geometric and electronic structure of paramagnetic transition metal complexes, such as through measurements of ligand super hyperfine interactions, which are generally not resolved in the EPR spectrum of vanadyl complexes.

The ENDOR spectra of $VO(acac)_2$ in per-deuterated chloroform/toluene (mixture/glass) was reported by Van Willigen and showed one pair of lines and with the aid of $VO(acac\text{-}d_6)_2$ (80% deuterated methyl groups) it was established that the resonance peaks due to the CH protons are obscured probably by strong methyl peaks, but no definitive explanation was given for this observation, indicating that the position of this proton is not well defined [116].

Later studies by Attanasio [118] focused on the interpretation and extraction of structural parameters from the frozen solution of simple coordination compounds of VO(II), an ion that has been of use in the study of the metal binding sites of a variety of biological systems, as an EPR spin probe [119]. ENDOR studies of an extensive series of vanadyl Schiff base complexes taken at 100 K (Figure 1.28), showed that simple analysis of frozen solution ENDOR spectra of a series of structurally related complexes yield full hyperfine interactions of several protons, even in complicated systems.

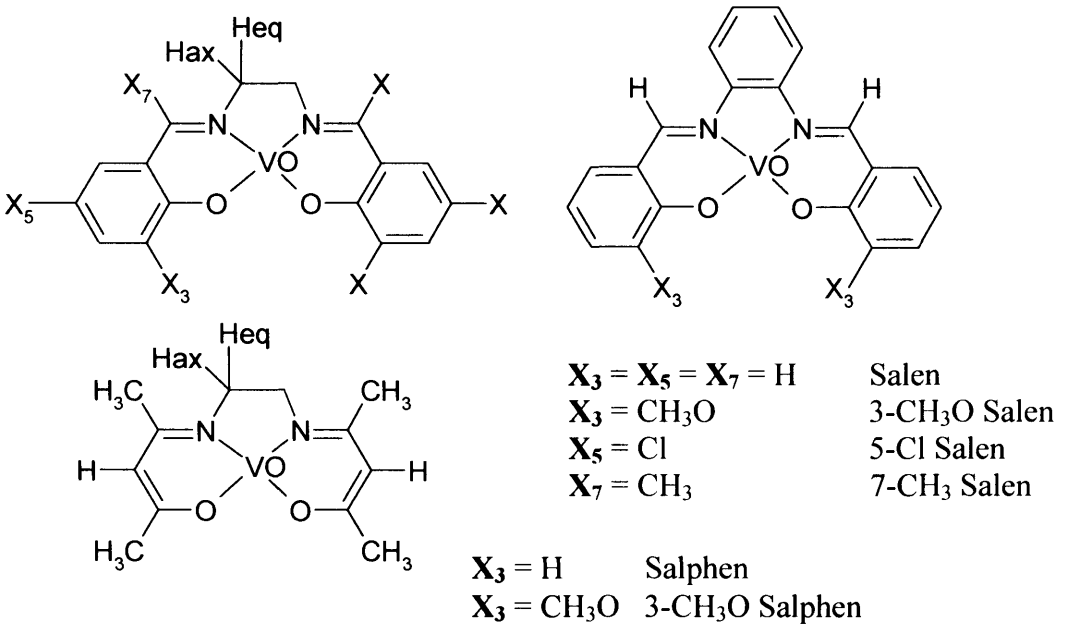

Figure 1.28: Molecular structure of Schiff base vanadyl complexes [118].

One of the main problems associated with this is that the experimental values are measured in the g-axes reference frame and as a result, the data obtained were not principle values of the magnetic interactions. Figure 1.29 illustrates that with axial symmetry only a single rotation angle (θ) is required, which relates the two sets of principal axes.

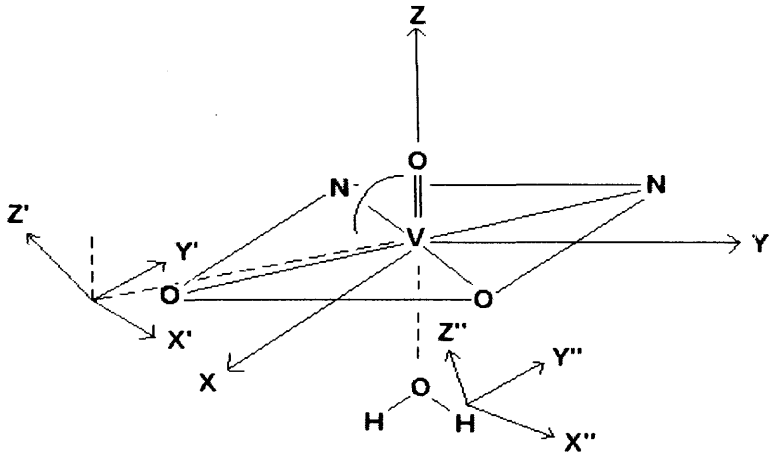

Figure 1.29: Orientation of the principal axis system for g and H^1 hyperfine tensors.

This rotation is defined about the X' axes, that lies in the *xy* plane of the g frame. Frozen solution ENDOR spectra in fully deuterated solvents completely

eliminate the presence of strong matrix ENDOR lines close to the free proton resonances due to surrounding magnetic nuclei.

Proton ENDOR studies of $VO(acac)_2$ dissolved in toluene-d_8/$CDCl_3$, as well as in toluene-d_8/$CHCl_3$ were reported in 1993 by Yordanov [120]. The formation of outer sphere complexes between the molecules of chloroform and $VO(acac)_2$ were observed, suggesting that the complex is formed through hydrogen bonding between the oxygen of the chelate ligand and the hydrogen of $CHCl_3$. The proposed model for this is shown in Figure 1.30.

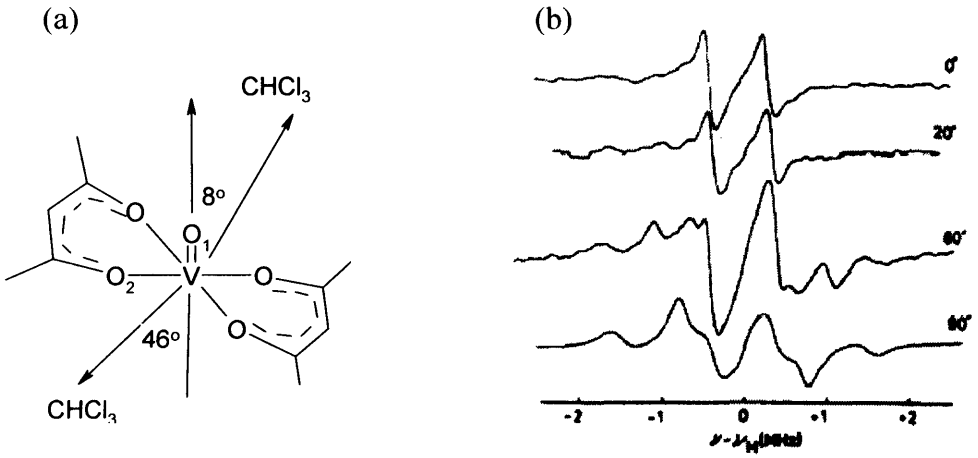

Figure 1.30: (a) Proposed model of outersphere complex and (b) associated proton ENDOR spectra of $VO(acac)_2$ dissolved in toluene-d_8/$CDCl_3$. The ENDOR spectra were recorded at various angles (0-90°) [120].

1.7.4.4 *Structure and mobility aspects*

ENDOR spectroscopy was also found to be a useful tool for the eludication of the structure of VO^{2+} in aqueous solutions adsorbed onto porous systems. Such a statement was suggested in a study by Martini [121], whose studies involved the structure and mobility of VO^{2+} ions in water adsorbed onto silica gels, through X and S band EPR and ENDOR spectroscopy.

The interactions of the vanadyl ion (VO^{2+}) with the adenine nucleotides AMP, ADP, ATP and the α,β-methylene analogue of ADP (AMP-CP) have also been investigated by EPR and ENDOR spectroscopy. It is important to understand the detailed molecular structure and geometry of nucleotide-metal complexes. The VO^{2+} ion has proved to be an effective paramagnetic substitute for many divalent metal ions in metalloproteins and metalloenzymes. On this basis Makinen *et al* [122]

determined the coordination geometry of ATP and ADP complexes of VO^{2+}, by employing ENDOR spectroscopy. Their results showed that VO^{2+} is coordinated to ATP and ADP by the phosphate groups and no detection of coordination to atoms of the nucleic acid base. The stereodiagram of $[VO(AMP\text{-}CP)_{2eq}(H_2O)_{ax}]$ was determined *via* EPR and ENDOR spectroscopy and molecular modelling calculations. In general Makinen established the metal binding sites, stoichiometry of metal-ligand binding and molecular geometry of the metal nucleotides in solution.

Sandwich complexes of the formula $M(C_nH_n)_2$ (M = transition metal) are well known and their crystal as well as electronic structures are established. An exception in this series is the paramagnetic complex $V(cot)_2$ (cot = η^8-C_8H_8). The synthesis of this complex was described briefly in 1966, but little information was available on its geometry. However, Gourier and Samuel [123] in 1992 reported crystal structures, showing that the vanadium is bound to one ring in an η^8 and to the other via η^4, supported by EPR and ENDOR studies. Variable-temperature ENDOR spectroscopy revealed molecular fluxionality in the solid state at low temperatures 30 K and also rapid molecular tumbling of the complex in polycrystalline solution was reported at temperatures below freezing. Lower temperatures slowed tumbling down and the complex orientated along the magnetic field in the solvent cages.

Application of ENDOR studies were also applied to an oxo-vanadyl enzyme, to gain information of the metal-binding site of imidazole glycerol phosphate dehydratase (IGPD). It has been known that the catalytic activity of IGPD is stimulated by the addition of Mn^{2+} ions, however in a communication by Petersen [124], divalent oxo-vanadium (VO^{2+}) was used, firstly for IGPD assembly and secondly as a paramagnetic spin centre which is suitable to probe the metal coordination enviroment by EPR and ENDOR spectroscopy. Vanadyl has been used successfully in the past in protein studies, which require the presence of divalent metals to substitute for other metals, resulting in an inactive metal-protein complex. Results showed that very detailed information about a paramagnetic metal center enviroment for both axial and equatorial positions can be obtained by ENDOR spectroscopy. Both EPR and ENDOR were employed to investigate the coordination enviroment of the IGPD metal center, assembled with VO^{2+}. Conclusions were made that methods such as EPR and ENDOR, indicated that some of the local metal centre ligand environments contain several nitrogens in the inner coordination sphere.

Figure 1.31 shows the proposed model for the two metal inner- sphere coordination environments of VO-IGPD in the α- and β- conformations [124].

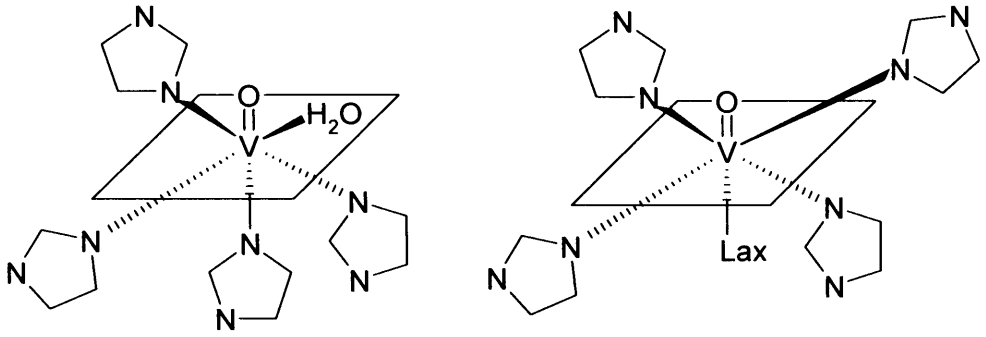

VO^{2+} - α - Configuration VO^{2+} - β - Configuration

Figure 1.31: Inner-sphere coordination environments of VO-IGPD, consistant with ENDOR and EPR data [124].

In order to obtain the structure and conformation of guanosine 5-monophosphate in certain hydrogen bonded assemblies, vanadyl (VO^{2+}) has been used as a paramagnetic spin probe for EPR and ENDOR spectroscopy. Guanosine and its derivatives are different to the other nucleic acid components of RNA and DNA, because they are capable of forming self-structured assemblies in solution, by means of hydrogen bonding. Proton ENDOR studies of the vanadyl – nucleotide complex indicated the presence of only an axially coordinated water ligand in the inner coordination sphere [125].

The use of computational / Density Functional Theory (DFT) has been widely used as a tool to compliment values extracted from EPR spectra. Kaupp and Munzarova reported the DFT study of EPR parameters for vanadyl complexes, containing Schiff base ligands [126]. Many computational studies have been undertaken to understand the effect of the ligand environment. Such studies by Larsen *et al* used computer methods to study the effect of the imidazole ring orientation on the EPR parameters for vanadyl-imidazole complexes [127]. The vanadium hyperfine coupling constant for vanadyl-imidazole complexes is found to depend on the orientation of the imidazole ring, with respect to the vanadyl bond. Larsen reported the DFT calculations of EPR hyperfine and quadrupole coupling constants.

1.7.5 *Copper salen-type complexes*

The immediate environment surrounding the metal center and its conformational flexibility are the main factors for a metalloprotein to carry out a specific physiological function, eg., dioxygen binding and oxygen utilization. To selectively mimic the biological activity of metalloproteins, especially their active sites and model metal complexes, Schiff base ligands have been made and reported for their dioxygen uptake [145]. Many of the earlier investigations were carried out with tetradentate Schiff base salen type ligands. However, tetrahydrosalen and *N,N'*-dimethylated tetrahydrosalen and their derivatives have rarely been studied with the exception of the hydrogenation product of non-substituted salen (H_2[H_4]salen).

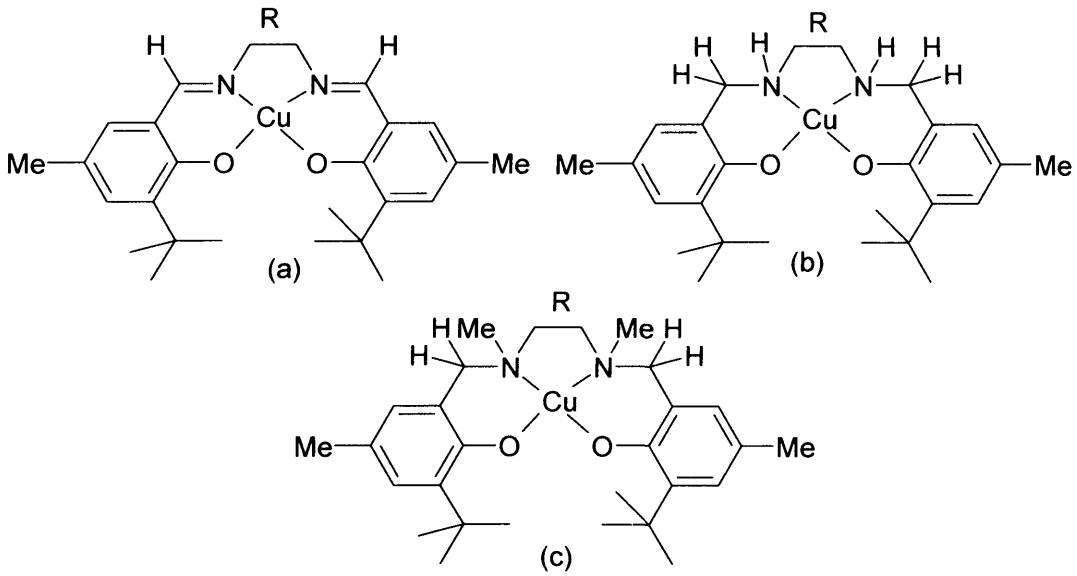

Ligand (L)	L^1= Salen	L^2= Saldimen	L^3= Saltmen	L^4= Salphen
Group A (Bridging)				

Figure 1.32: Copper (II) Schiff base complexes, which were used in a spectroscopic study [145]. (a) CuL, (b) Cu[H_4]L and (c) Cu[H_2Me_2]L.

On studying the ligand properties of salen and its hydrogenated analogue tetrahydrosalen, it is expected that there is increased *N*-basicity and greater flexibility as a consequence of C=N bond hydrogenation. This was reported in a recent publication, where Klement *et al* investigated the spectroscopic and electrochemical study of substituted salen, tetrahydrosalen, *N,N'*-dimethylated tetrahydrosalen and other copper (II) complexes [128] (Figure 1.32). They discussed the influence of the methylation of the ethylenediamine bridge and the effect of the phenylenediamine bridge on the structural / magnetic properties of the complexes.

The EPR spectra of CuL (Figure 1.32a) at 77 K and room temperature revealed that the well resolved lines may be attributed to the interaction of an unpaired electron spin with a copper spin, ^{14}N donor nuclei and to a distant interaction with two protons (equivalent): [$A^{Cu}_{(iso)}$ = 253 MHz, $A^{N}_{(iso)}$ = 43 MHz and $A^{N}_{(iso)}$ = 20 MHz. Table 1.4 shows the EPR spin Hamiltonian parameters for copper CuL, Cu[H_4]L and Cu[H_2Me_2]L complexes.

Copper (II) complexes with salen Schiff-base ligands derived from ethylenediamine or (*S,S*)-1,2-diphenylethylenediamine or 5-methoxy, 5-bromo and 5-nitrosalicyaldehyde have also been studied and been effectively employed as catalysts for the epoxidation of styrene with iodosylbenzene by Decinti *et al* [129]. Even though Schiff-base copper (II) complexes have been studied and known for approximately 100 years, no study about their catalytic performance in the epoxidation of olefins has been reported until recently. Decinti found that catalytic activity was dependent upon both the Lewis acidity of the metal complexes and the presence of phenyl substituents on the ethylene moiety.

Table 1.4: Spin Hamiltonian parameters for copper CuL, Cu[H_4]L and Cu[H_2Me_2]L complexes.

System	g_{iso}	$g_{\|}$	$g_{\perp}$	A^{Cu}_{iso} / G	$A^{Cu}_{\|}$ / G	$A^{Cu}_{\perp}$ / G	A^{N}_{iso} / G	$A^{N}_{\perp}$ / G	$A^{\|}_{iso}$ / G	$A^{\|}_{\perp}$ / G
CuL^1	2.094	2.194	2.041	253	621	87	43	42	20	20
CuL^2	2.094	2.194	2.041	253	621	94	43	43	20	22
CuL^3	2.094	2.191	2.040	270	627	80	46	41	23	17
CuL^4	2.096	2.198	2.041	260	625	87	42	42	18	19
$Cu\|H_4\|L^1$	2.106	2.225	2.044	249	576	95	27	32	...	...
$Cu\|H_4\|L^2$	2.103	2.216	2.042	253	592	101	27	33	...	...
$Cu\|H_4\|L^3$	2.100	2.213	2.042	253	590	32	25	32	...	...
$Cu\|H_4\|L^4$	2.121	2.267	2.044	215	524	...	...	...	...	...
$Cu\|H_2\|L^4$	2.098	2.210	2.041	247	590	86	42	41	21	22
$Cu\|H_2Me_2\|L^1$	2.106	2.220	2.044	249	572	96	26	32	...	...
$Cu\|H_2Me_2\|L^2$	2.105	2.213	2.041	253	592	98	29	37	...	...
$Cu\|H_2Me_2\|L^4$	2.124	2.246	2.0445	218	531	NR	24	NR	...	...

The conformational flexibility of the Schiff-base salen complexes and the variety of geometries they can adopt, ie., planar, umbrella and stepped conformations, in order to generate different oxidation reactions, make them the main factors for the biomimetic activity of these molecules, which is similar to that observed in metalloproteins. The encapsulation of these complexes [130, 131] in the supercages of Zeolites X and Y and mesoporous materials were reported by Ramasamy, Srinivas and Deshpande [132]. They studied this encapsulation process as, in addition to having the advantages of heterogeneous catalysts, ie., simplified catalyst separation, they also have advantages similar to that of homogeneous catalysts, such as their well-defined structure. They reported the synthesis and characterization of Zeolite-Y-encapsulated Cu(salen) and Cu(5-Cl-salen). The complexes, when not encapsulated, showed broad EPR spectra corresponding to near spin-spin interactions. However, the zeolite-encapsulated metal complexes showed well-resolved spectra with

hyperfine features, in dilute frozen solutions, which is indicative of monomeric salen complexes in zeolite complexes. Molecules which are absorbed onto the surface of the zeolite exhibit spectra similar to that of the non-encapsulated zeolite. The spin Hamiltonian parameters and molecular orbital coefficients for the Highest Occupied Molecular Orbital's (HOMO) revealed enhanced covalency as a result of structural changes through encapsulation.

The oxidation of *para*-xylene over zeolite-encapsulated copper and manganese complexes were also studied by Ratnasamy. The salen, saltin and salcyhexen complexes encapsulated in the cavities of zeolite NaX were investigated as catalysts for the aerobic oxidation of para-xylene [133].

1.8 References

[1] K.B. Sharpless, A.Y. Teranishi, J.E. Backväll, *J. Am. Chem. Soc.*, 1977, **99**, 3120.

[2] E.N. Jacobsen, *Asymmetric Catalytic Epoxidation of Unfunctionalised Olefins*. In: Ojima (ed) Catalytic Asymmetric Synthesis. VCH, New York, chap 4.2, 1993.

[3] E.N. Jacobsen, *Transition Metal-catalysed Oxidations: Asymmetric Epoxidation*. In: G. Wilkinson, F.G.A. Stone, E.W. Abel, L.S. Hegedus (eds) Comprehensive Organometallic Chemistry II. Pergamon, New York, chap 11.1, 1995.

[4] W. Zhang, J.L. Loebach, S.R. Wilson, E.N. Jacobsen, *J. Am. Chem. Soc.*, 1990, **112**, 2801.

[5] E.N. Jacobsen, W. Zhang, A.R. Muci, J.R. Ecker, L. Deng, *J. Am. Chem. Soc.*, 1991, **113**, 7063

[6] T.J. McMurry, J.T. Groves, In: Ortiz de Montellano PR (ed) Cytochrome P-450: Structure, Mechanism, and Biochemistry. Plenum, New York, chap 1, 1986.

[7] H.L. Holland, *Organic Synthesis with Oxidative Enzymes*. VCH, New York, 1992.

[8] E.J. Allain, L.P. Hager, L. Deng, E.N. Jacobsen, *J. Am. Chem. Soc.*, 1993, **115**, 4415.

[9] K.A. Jorgensen, *Chem. Rev.*, 1989, **89**, 431.

[10] R.A. Sheldon, J.K. Kochi, *Metal-Catalysed Oxidations of Organic Compounds*. Academic Press, New York, 1981.

[11] K.B. Sharpless, A.Y. Teranishi, J.E. Backväll, *J. Am. Chem. Soc.*, 1977, **99**, 3120.

[12] P.O. Norrby, C. Linde, B. Åkermark, *J. Am. Chem. Soc.*, 1995, **117**, 11035.

[13] T. Hamada, T. Fukuda, H. Imanishi, T. Katsuki, *Tetrahedron*, 1996, **52**, 515.

[14] T. Linker, *Angew. Chem. Int. Ed. Engl.*, 1997, **36**, 2060.

[15] D. Ostovic, T.C. Bruice, *J. Am. Chem. Soc.*, 1989, **111**, 6511.

[16] N.S. Finney, P.J. Pospisil, S. Chang, M. Palucki, R.G. Konsler, K.B. Hansen, E.N. Jacobsen., *Angew. Chem. Int. Ed. Engl.*, 1997, **36**, 1720.

[17] J.T. Groves, R.S. Myers, *J. Am. Chem. Soc.*, 1985, **105**, 5791.

[18] L. Deng, Y. Furukawa, L.E. Martínez, E.N. Jacobsen, *Tetrahedron*, 1994, **50**, 4323.

[19] J.A. Fruetel, J.R. Collins, D.L. Camper, G.H. Loew, P.R. Ortiz de Montellano, *J. Am. Chem. Soc.*, 1992, **114**, 6987.

[20] N.H. Lee, E.N. Jacobsen, *Tetrahedron Lett.*, 1991, **32**, 6533.

[21] R. Irie, K. Noda, Y. Ito, N. Matsumoto, T. Katsuki, *Tetrahedron Lett.*, 1990, **31**, 7345.

[22] E. Guilmet, B. Meunier, *Nouv. J. Chim.*, 1982, **6**, 511.

[23] C. Linde, M. Arnold, P.O. Norrby, B. Åkermark, Angew. *Chem. Int. Ed. Engl.*, 1997, **36**, 1723.

[24] H. Fu, G.C. Look, W. Zhang, E.N. Jacobsen, C.H. Wong, *J. Org. Chem.*, 1991, **56**, 6497.

[25] K. Srinivasan, P. Michaud, J.K. Kochi, *J. Am. Chem. Soc.*, 1986, **108**, 2309.

[26] I. Tabushi, N. Koga, *Tetrahedron Lett.*, 1979, **20**, 3681.

[27] E. Guilmet, B. Meunier, *Tetrahedron Lett.*, 1980, **21**, 4449.

[28] B. Meunier, *Chem. Rev.*, 1992, **92**, 1411.

[29] D. Mansuy, P. Battioni, J.P. Renaud, *J. Am. Chem. Soc.*, 1984, **106**, 1255.

[30] T.C. Bruice, *Aldrichimica Acta.*, 1988, **21**, 87.

[31] G.X. He, T.C. Bruice, *J. Am. Chem. Soc.*, 1991, **113**, 2747.

[32] L.C. Yuan, T.C. Bruice, *J. Am. Chem. Soc.*, 1986, **108**, 1643.

[33] M.W. Nee, T.C. Bruice, *J. Am. Chem. Soc.*, 1982, **104**, 6123.

[34] T. Higuchi, H. Ohtake, M. Hirobe, *Tetrahedron. Lett.*, 1989, **30**, 6545.

[35] L.C. Yuan, T.C. Bruice, *J. Chem. Soc. Chem. Commun.*, 1985, 868.

[36] S. Campestrini, A. Robert, B. Meunier, *J. Org. Chem.*, 1991, **56**, 3725.

[37] B. De Poorter, B. Meunier, *Nouv. J. Chim.*, 1985, **9**, 393.

[38] P. Pietikänen, *Tetrahedron Lett.*, 1994, **35**, 941.

[39] P. Battioni, J.P. Renaud, J.F. Bartoli, M. Reina-Artiles, M. Fort, D. Mansuy, *J. Am. Chem. Soc.*, 1988, **110**, 8462.

[40] P. Pietikänen, *Tetrahedron. Lett.*, 1995, **35**, 941.

[41] K.S. Suslick, F.V. Acholla, B.R. Cook, *J. Am. Chem. Soc.*, 1987, **109**, 2818.

[42] C. Querci, M. Ricci, *J. Chem. Soc. Chem. Commun.*, 1989, 889.

[43] J.T. Groves, R. Quinn, *J. Am. Chem. Soc.*, 1985, **107**, 5790.

[44] T. Nagata, K. Imagawa, T. Yamada, T. Mukaiyama, *Bull. Chem. Soc. Jpn.*, 1995, **68**, 1455.

[45] T. Nagata, K. Imagawa, T. Yamada, T. Mukaiyama, *Chem. Lett* , 1994, 1259.

[46] R.L. Haltermann, S.T. Jan, *J. Org. Chem.*, 1991, **56**, 5253.

[47] S. O'Malley, T. Kodadek, *J. Am. Chem. Soc.*, 1989, **111**, 9116.

[48] W. Zhang, E.N. Jacobsen, *J. Org. Chem.*, 1991, **56**, 2296.

[49] S. Banfi, F. Montanari, S. Quici, *J. Org. Chem.*, 1989, **54**, 1850.

[50] P.J. Pospisil, D.H. Carsten, E.N. Jacobsen, *Chem. Eur. J.*, 1996, **2**, 974.

[51] S. Chang, K.B. Hansen, A. Rippert, E.N. Jacobsen, 1999.

[52] J.F. Larrow, E.N. Jacobsen. In: *Topics in Organometalic Chemistry*; R.D. Larsen, ed; Springer-Verlag; Heidelberg, 2003.

[53] S.E. Schaus, B.D. Brandes, J.F. Larrow, M. Tokunaga, K.B. Hansen, A.E. Gould, M.E. Furrow, E.N. Jacobsen, *J. Am. Chem. Soc*, 2002, **124**, 1307.

[54] J.F. Larrow, K.E. Hemberger, S. Jasmin, H. Kabir, P. Movel, *Tetrahedron: Asymmetry*, 2003, **14**.

[55] D.E. White, E.N. Jacobsen, *Tetrahedron: Asymmetry*, 2003, **14**, 3633.

[56] G.J. Kim, H. Lee, S.J. Kim, *Tetrahedron. Lett.*, 2003, **44**, 5005.

[57] M. Tokunaga, J.F. Larrow, F. Katicicho, E.N. Jacobsen, *Science.*, 1997, **277**, 936.

[58] K. Faber, *Biotransformations in Organic Chemistry*, Springer-Verlag, New York, 1992, chapt 2; C.A.G.M. Weijers, *Tetrahedron. Asymmetry.*, 1997, **8**, 639.

[59] H. C. Kolb, M.S. VanNieuwenhze, K.B. Sharpless, *Chem. Rev.*, 1994, **94**, 2483.

[60] L.P.C. Nielsen, C.P. Stevenson, D.G. Blackmond, E.N. Jacobsen, *J. Am. Chem. Soc.*, 2004, **126**, 1360.

[61] E.N. Jacobsen, F. Kakiuchi, R.G. Konsler, J.F. Larrow, M. Tokunaga, Tetrahedron Lett., 1997, **38**, 773.

[62] J.M. Ready, E.N. Jacobsen, *J. Am. Chem. Soc.*, 2001, **123**, 2687.

[63] J.F. Larrow, E.N. Jacobsen, *Adv. Synth. Catal.*, 2001, **343**, 5.

[64] P-O. Norrby, O. Linde, B. Åkermark, *J. Am. Chem. Soc.*, 1995, **117**, 11035.

[65] T.D. Smith, J.R. Pilbrow. *Coord. Chem. Rev.*, 1981, **39**, 295.

[66] R.D. Jones, D.A. Summerville, F. Basolo, *Chem. Rev.*, 1979, **79**, 139.

[67] G.P. Däges, J. Hütterman, *J. Phys. Chem.*, 1992, **96**, 4787.

[68] F.A. Walker, *J. Magn. Reson.*, 1974, **15**, 201.

[69] J. Harmer, S. Van Doorslaer, I. Gromov, A. Schweiger, *Chem. Phys. Lett.*, 2002, **358**, 8.

[70] R.M. Kadam, M.K. Bhide, M.D. Sastry, J.V. Yakhmi, O. Kahn, *Chem. Phys. Lett.*, 2002, **357**, 457.

[71] J. Hanner, S. van Doorslaer, I. Gromov, A. Schweiger, *J. Phys. Chem. B*, 2002, **106**, 2801.

[72] R. Blaauw, J.L. Van de Bann, S. Balt, M.W.G. de Bolster, G.W. Klumpp, H. Kooijman, A.L. Speck, *Inorg. Chimica. Acta.*, 2002, **1**.

[73] S. van Doorslaer, R. Bachmann, A. Schweiger, *J. Phys. Chem.*, 1999, **103**, 5446.

[74] S. Van Doorslaer, A. Schweiger, *J. Phys. Chem*, 2000, **104**, 2919.

[75] J.J Chapman, C.S. Day, M.E. Welker, *Organometallics*, 2000, **19**, 1615.

[76] K. Kervinen, P. Lahtinen, T. Repo, M. Svahn, M. Leskelä, *Catal.. Today*, 2002, **75**, 183

[77] V.E. Marquez, J. R. Anacona, C.R. Barbarin, *Polyhedron*, 2001, **20**, 1885.

[78] M.R. Reddy, K.H. Reddy, K.M. Raju, *Polyhedron*, 1998, **17**, 1355.

[79] D.M. Goken, D.G. Peters, *Reactive Intermediates in Organic and Biological Electrochemistry*, 2001, **14**, 125.

[80] H. Isobe, B.P. Branchaud, *Tetrahedron Lett.*, 1999, **40**, 8747.

[81] M.C.R. Symons, T. Taiwo, A.M. Sargeson, M.M. Ali, A.S. Tabl, *Inorganica. Chimica. Acta.*, 1996, **241**, 5.

[82] K.P. Bryliakov, D.E. Babushkin, E.O. Talsi, *Mendeleev. Comm.*, 1999, **29**.

[83] P. Pietikäinen, *Tetrahedron*, 1998, **54**, 4319.

[84] N. Svenstrup, A. Bøgevig, R.G. Hazell, K.A. Jørgensen, *J. Chem. Soc. Perkin Trans.*, 1999, **1**, 1559.

[85] M.L. Merlau, W.J. Grande, S.T. Nguyen, J.T. Hupp, *J. Mol. Catal.*, 2000, **156**, 79.

[86] K-O. Schäfer, R. Bittl, W. Zweygart, F. Lendzian, G. Haselhorst, T. Weyhermüller, K. Wieghardt, W. Lubitz, *J. Am. Chem. Soc.*, 1998, **120**, 13104.

[87] J.M. Peloquin, R.D. Britt, *Biochimica. Biophysica. Acta.*, 2001, **1503**, 96.

[88] S. Padhye, G.B. Kauffman, *Coord. Chem. Rev.*, 1985, **63**, 127.

[89] R. Warmuth, H, Elias, *Inorg. Chem.*, 1991, **30**, 5027.

[90] J.E. Huyett, S.B. Choudhury, D.M. Eichhorn, P.A. Bryngelson, M.J. Maroney, B.M. Hoffman, *Inorg. Chem.*, 1998, **37**, 1361.

[91] D.L. Klayman, J.P. Scovill, J.F. Bartosevich, J. Bruce, *J. Med. Chem.*, 1983, **26**, 35; J.P. Scovill, D.L. Klayman, C. Lambos, G.E. Childs, J.D. Nortsch, *J. Med. Chem.*, 1984, **27**, 87.

[92] M. Cañadas, E.L. Torres, A.M. Arias, M.A. Mendiola, M.T. Sevilla, *Polyhedron*, 2000, **19**, 2059.

[93] I.C. Santos, M.V. Boas, M.F.M. Piedade, C. Freire, M.T. Duarte, B. de Castro, *Polyhedron*, 2000, **19**, 655.

[94] F. Azevedo, C. Freire, B. de Castro, *Polyhedron*, 2002, **21**, 1695.

[95] N. Robertson, X. Liu, L.J. Yellowlees, *Inorg. Chem. Comm.*, 2000, **3**, 424.

[96] M.B. de Araújo, N.M. Pinhal, N.V. Vugman, *Rad. Phys. Chem.*, 2002, **64**, 389.

[97] J. Telser, Y.C. Fann, M.W. Rener, J. Fajer, S. Wang, H. Zhang, R.A. Scott, B.M. Hoffman, *J. Am. Chem. Soc.*, 1997, **199**, 733.

[98] A. Tripathi, R.K. Syal, P.K. Bharadwaj, *Polyhedron*, 1999, **18**, 2229.

[99] V.V. Saraev, F.K. Shmidt, *J. Mol. Catal. A.*, 2000, **158**, 149.

[100] S. Wu, S. Lu, *J. Mol. Catal. A.*, 2003, **197**, 51.

[101] B.S. Garg, D.N. Kumar, *Spectrochimica. Acta. A*, 2003, **59**, 229.

[102] M.R. Maurya, I. Jain, S.J.J. Titinchi, *App. Catal. A*, 2003, **249**, 139.

[103] G. Sacarescu, R. Ardeleanu, L. Sacarescu, M. Simionescu, *J. Organometallic Chem.*, 2003, **685**, 202.

[104] P. Vanalabhpatana, D.G. Peters, *Tetrahedron Lett.*, 2003, **44**, 3245.

[105] M. Kondo, K. Nabari, T. Horiba, Y. Irie, M.K. Kabir, R.P. Sarker, E. Shimizu, Y. Shimizu, Y. Fuwa, *Inorg. Chem. Comm.*, 2003, **6**, 154.

[106] R.H. Borcherts, C. Kikuchi, *J. Chem. Phys.*, 1964, **40**, 2270.

[107] H. DeArmond, B.B. Garrett, H.S. Gutowsky, *J. Chem. Phys.*, 1965, **12**, 1019.

[108] H.A. Kuska, *Thesis, Michigan State University*, 1965.

[109] D. Kivelson, S.K. Lee, *J. Chem. Phys.*, 1964, **41**, 1896.

[110] R.M. Golding, *Mol. Phys.*, 1962, **65**, 153.

[111] L.J. Boucher, E.C. Tynan, T.F. Yen, *Inorg. Chem.*, 1968, **7**, 731.

[112] L.J. Boucher, E.C. Tynan, T.F. Yen, *Inorg. Chem.*, 1969, **8**.

[113] J.M. Assour, *J. Chem. Phys.*, 1965, **43**, 2477.

[114] N.M. Atherton, J. Locke, J.A. McCleverty, *Chem. Ind.*, 1965, 1300.

[115] C.J. Ballhausen, H.B. Gray, *Inorg. Chem.*, 1962, **1**, 111.

[116] B. Kirste, H. van Willigan, *J. Phys. Chem.*, 1982, **86**, 2743.

[117] J. Bernal, P.H. Rieger, *Inorg. Chem.*, 1963, **2**, 256.

[118] D. Attanasio, *J. Phys. Chem.*, 1986, **90**, 4952.

[119] N.D. Chasteen. *In Biological Magnetic Resonance*; L.J. Berliner, J. Reuben, Eds; Plenum: New York, 1981, **3**, 53.

[120] N.D. Yordanov, M. Zdravkova, *Polyhedron*, 1993, **12**, 635.

[121] S. Ristori, M.F. Ottaviani, G. Martini, *Langmuir*, 1991, **7**, 755.

[122] D. Mustafi, J. Telser, M.W. Makinen, *J. Am. Chem. Soc.*, 1992, **114**, 6219.

[123] D. Gourier, E. Samuel, B. Bachmann, F. Hahn, J. Heck, *Inorg. Chem.*, 1992, **31**, 86.

[124] J. Petersen, T.R. Hawkes, D.J. Lowe, *J. Bio. Inorg. Chem.*, 1997, **3**, 308.

[125] F.S. Jiang, M.W. Makinen, *Inorg. Chem.*, 1995, **34**, 1736.

[126] M.L. Munzarová, M. Kaupp, *J. Phys. Chem. B*, 2001, **105**, 12644.

[127] A.C. Saladino, S.C. Larsen, *J. Phys. Chem. A*, 2002, **106**, 10444.

[128] R. Klement, F. Stock, H. Elias, H. Paulus, P. Pelikán, M. Valko, M. Mazúr, *Polyhedron*, 1999, **18**, 3617.

[129] S. Zolezzi, E. Spodine, A. Decinti, *Polyhedron*, 2003, **22**, 1653.

[130] C.R. Jacob, S.P. Varkey, P. Ratnasamy, *Appl. Catal. A*, 1998, **168**, 353.

[131] C.R. Jacob, S.P. Varkey, P. Ratnasamy, *Microporous Mesoporous Mat*, 1998, **22**, 465.

[132] S. Deshpande, D. Srinivas, P. Ratnasamy, *J. Catal.*, 1999, **188**, 261.

[133] C.R. Jacob, S.P. Varkey, P. Ratnasamy, *Appl. Catal. A*, 1999, **182**, 91.

Chapter 2

Basic principles of *cw* EPR and ENDOR spectroscopy

Basic principles of *cw* EPR and ENDOR spectroscopy

2.1 Introduction

Electron Paramagnetic Resonance (EPR) Spectroscopy is the most direct technique for the detection and structural elucidation of paramagnetic and radical species. The first reported EPR spectrum was obtained in 1945 by E. Zavoisky [1] and since then EPR has been applied with considerable success to many branches of chemistry including; the study of organic radicals, catalysis, dosimetry, photochemistry, metal complexes and biological systems [2, 3, 4]. The EPR technique, however, is hampered by low resolution of weak electron-nuclear interactions with the nuclei of remote ligand substituents. This drawback of low resolution by EPR results from line broadening and line splitting effects, due to the couplings of the electron spins with many surrounding nuclear spins. Such information cannot be easily obtained through the NMR technique mainly because of the greatly increased line widths caused by the presence of the unpaired electron. This problem can be eliminated by performing a double resonance experiment namely Electron Nuclear Double Resonance (ENDOR) by detecting the NMR resonances *via* the intensity change of a simultaneously irradiated EPR line.

Before the technique of ENDOR spectroscopy is described more fully it is necessary to consider the fundamental principles that govern the EPR experiment. The basic physics of EPR spectroscopy is, in many ways similar to that of NMR and has been extensively described in a variety of texts [2, 3, 4].

2.2 Basic principles of EPR spectroscopy

If we consider the situation of a free electron in the absence of an applied magnetic field, the two possible spin states for the electron are $M_S = +1/2$ (α) and $M_s = -1/2$ (β). In the absence of a magnetic field these spin states are found to be degenerate, but on the addition of a large external magnetic field, **B**, this degeneracy is lifted, with the β state becoming lower in energy than the α state. The energies of these spin states are given by;

$$E = g\mu_B M_S \mathbf{B} \qquad (2.1)$$

where g is the Lande g factor (g = 2.0023 for a free electron) and μ_β is the Bohr magneton (μ_B =9.274 x 10^{-24} JT^{-1}). The two energy levels are termed the Zeeman levels and the energy difference between them is termed the Zeeman splitting (figure 2.1).

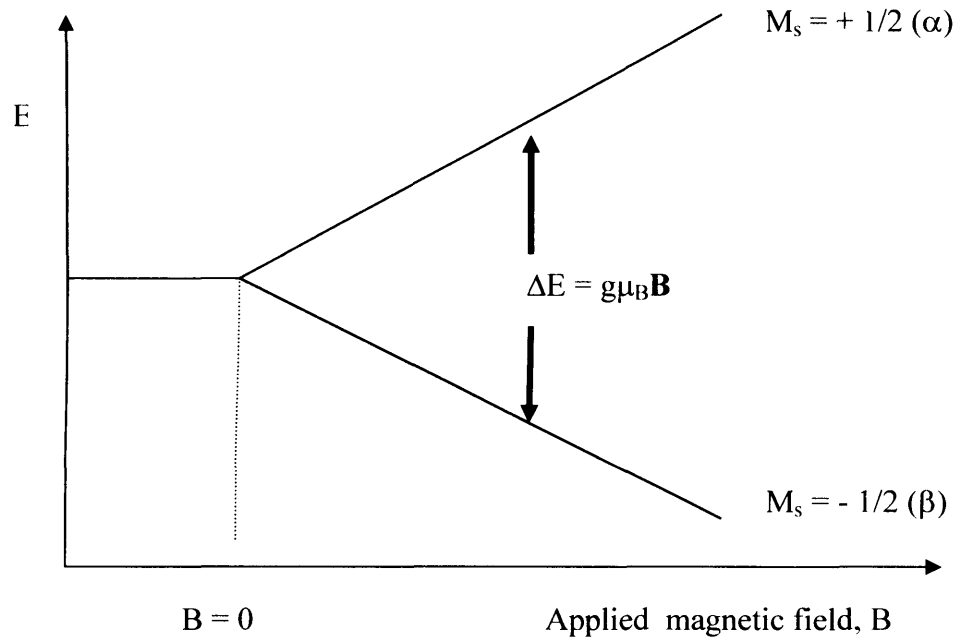

Figure 2.1: Energy level diagram for a system with 1 unpaired electron and no interacting nucleus

The energy difference between these two states is directly proportional to the magnitude of the applied magnetic field and the separation ΔE can be calculated from equation (2.2), where **B** is the magnetic flux density:

$$\Delta E = E_\alpha - E_\beta = g\mu_B \mathbf{B} \qquad (2.2)$$

Transitions beween the two Zeeman levels are induced when electromagnetic radiation of energy, $h\nu$, (where h is Planck's constant 6.626 x 10^{-34} Js and ν is the frequency of the incident radiation) becomes coincident with the separation energy ΔE (2.3):

$$\Delta E = h\nu \qquad (2.3)$$

The existence of electron Zeeman levels and the possibility of promoting transitions from the lower energy spin level (β) to the higher energy spin level (α) is the very basis of EPR spectroscopy. The EPR spectrometer detects these transitions from the β to α state as an absorption of energy from the incident microwave radiation. Clearly, the resonance experiment can be performed in two ways, either the magnetic field is kept constant and the applied frequency is varied, or, the applied frequency is kept constant and the magnetic field is varied. For technical reasons, it is easier to vary the magnetic field continuously rather than the frequency, so most EPR spectrometers operate at a fixed frequency, employing a variable magnetic field.

From equation (2.4), it is apparent that the EPR absorption position will vary with the magnitude of the applied magnetic field. It is therefore convenient to refer to an absorption in terms of its g value:

$$g = \Delta E/\mu_B \mathbf{B} = h\nu/\mu_B \mathbf{B} \qquad (2.4)$$

2.2.1 *Spin populations*

At thermal equilibrium and in the presence of an applied magnetic field, the ratio of the α and β spin state populations is given by the Maxwell-Boltzmann distribution law (2.5), where *k* is the Boltzmann constant (1.38×10^{-23} JK^{-1}) and T is the absolute temperature. At a temperature of 300 K and a magnetic field of 0.3 T, this relationship becomes simplified to (2.6) showing that the two Zeeman levels are nearly equally populated with a slight excess in the number of spins in the β state:

$$N\ (\text{upper})/N\ (\text{lower}) = \text{Exp}\ [-\Delta E/kT] = \text{Exp}\ [-g\mu_B \mathbf{B}/kT] \qquad (2.5)$$

$$N\ (\text{upper})/N\ (\text{lower}) = 1 - g\mu_B \mathbf{B}/kT = 0.9984 \qquad (2.6)$$

Resonance is therefore induced between the states with a net absorption of microwave radiation according to the selection rule $\Delta M_s = \pm 1$. If the microwave

intensity is too great, however, then the excess of spins in the β state will decrease, this in turn will reduce the net microwave absorption until there are no excess spins in the β state, preventing further microwave energy from being absorbed. If this process does happen, then the EPR signal is said to be saturated.

2.2.2 *Relaxation processes*

Relaxation processes are mechanisms by which electrons in the upper spin state can return to the lower spin state with a loss of their excess energy. If the relaxation process is fast enough, then the population difference between the two spin states can be maintained despite the net absorption of microwave energy. The time taken for a spin system to lose 1/e of its excess energy is called the relaxation time. The two processes known as spin-lattice and spin-spin relaxation are possible.

The spin-lattice relaxation process, comprises of radiation-less interactions between the spin system and the thermal motions of the surrounding lattice. A radical in solution will tumble freely due to its thermal energy. This is found to give rise to randomly fluctuating fields due to the motions of the electron and the nuclear spin in the solvent and solute molecules. If these motions are of an appropriate frequency, ω (Larmor frequency), then the interaction can occur enabling spins in the upper state to transfer energy to these lattice modes and return to the lower state.

The efficiency of the spin-lattice relaxation process is expressed in terms of a spin-lattice relaxation time T_1. The value of T_1 refers to the mean lifetime of a given spin state, ie., the time a spin remains in an excited state. If T_1 is long then the excited electrons cannot relax quick enough to maintain an excess population in the lower spin state and consequently, the EPR signal saturates.

The spin-spin relaxation process is caused by the interaction of the unpaired electron with other magnetic dipoles. The spin-spin relaxation time is represented by T_2 and it is a measure of the efficiency of spin-spin relaxation. The interaction of the unpaired electron with other magnetic dipoles produces varying local fields, so that for a given microwave frequency a range of fields will be found at which resonance will occur, leading to a broad EPR peak. This relaxation mode is particularly important when the concentrations of paramagnetic species are high, ie., when the paramagnetic spins are close together.

2.2.3 *Hyperfine structure*

By analogy to NMR spectroscopy, where local structural information can be obtained from the spin-spin coupling of nuclei in different molecular positions, in EPR spectroscopy the interaction of the unpaired electron with magnetic nuclei leads to splitting of the electronic Zeeman levels into hyperfine sublevels and therefore to additional EPR transitions. However, unlike NMR where spin-spin coupling is usually limited to nuclei in small fragments of the molecule, in EPR the possibility of delocalisation of the unpaired electron results in its coupling with all the magnetic nuclei.

The simplest case to consider is that in which the unpaired electron interacts with a hydrogen nucleus. The hydrogen nucleus consists of a single proton of nuclear spin I = 1/2, therefore the two possible spin states for the proton are $M_I = +1/2$ and $M_I = -1/2$. The interaction between the electron and the nucleus therefore results in a splitting of each of the electron Zeeman levels into two sublevels. The energies of the four sublevels produced are governed by equation (2.7):

$$E(M_S, M_I) = g\mu_B \mathbf{B} M_S - g_n \mu_N \mathbf{B} M_I + hA M_S M_I \qquad (2.7)$$

$g\mu_B \mathbf{B} M_S$ represents the contribution due to the interaction of the electron with the applied magnetic field. $g_n \mu_N \mathbf{B} M_I$ represents the interaction between the nucleus and the applied field (g_n is the nuclear g factor and μ_N is the nuclear magneton, 5.05×10^{-27} JT^{-1}) and $hAM_S M_I$ represents the energy of interaction between the electron and nuclear magnetic moments (where A is the hyperfine coupling constant).

Using equation (2.7), the energy values of the four sublevels can be calculated:

$$E_1 = +1/2 g\mu_B \mathbf{B} - 1/2 g_n \mu_N \mathbf{B} + 1/4 hA \qquad (\mathbf{M_S} + 1/2, \mathbf{M_I} + 1/2) \qquad (2.8a)$$

$$E_2 = +1/2 g\mu_B \mathbf{B} + 1/2 g_n \mu_N \mathbf{B} - 1/4 hA \qquad (\mathbf{M_S} + 1/2, \mathbf{M_I} - 1/2) \qquad (2.8b)$$

$$E_3 = -1/2 g\mu_B \mathbf{B} + 1/2 g_n \mu_N \mathbf{B} + 1/4 hA \qquad (\mathbf{M_S} - 1/2, \mathbf{M_I} - 1/2) \qquad (2.8c)$$

$$E_4 = -1/2 g\mu_B \mathbf{B} - 1/2 g_n \mu_N \mathbf{B} - 1/4 hA \qquad (\mathbf{M_S} - 1/2, \mathbf{M_I} + 1/2) \qquad (2.8d)$$

By application of the selection rules, $\Delta M_I = 0$ and $\Delta M_S \pm 1$, it will be found that two resonance transitions can occur ΔE_1 and ΔE_2:

$$\Delta E_1 = E_1 - E_4 = g\mu_B\mathbf{B} + 1/2hA \quad (2.9)$$

$$\Delta E_2 = E_2 - E_3 = g\mu_B\mathbf{B} - 1/2hA \quad (2.10)$$

These two possible transitions give rise to two absorption peaks that occur at different magnetic field positions, measured at constant frequency. These magnetic field positions B_1 and B_2 can be extracted directly from equation (2.3):

$$\Delta E_1 = h\nu = g\mu_B\mathbf{B} + 1/2hA \text{ rearranges to } B_1 = h\nu/g\mu_B - hA/2g\mu_B \quad (2.11)$$

A (MHz) is the hyperfine coupling constant and it can have positive or negative values. It is related to the isotropic hyperfine splitting constant, a_0, (magnetic field units, mT) by the expression, $a_0 = hA/g\mu_B$. Therefore equation (2.11) can be rewritten in terms of the isotropic hyperfine splitting constant:

$$B_1 = h\nu/g\mu_B - a_0/2 \text{ and for } B_2 = h\nu/g\mu_B + a_0/2 \quad (2.12)$$

The isotropic hyperfine splitting constant is therefore obtained from the differences beween the field positions at which these two transitions occur (2.13):

$$B_2 - B_1 = a_0 \quad (2.13)$$

Figure 2.2 includes the nuclear Zeeman splitting, however, from equation 2.12 in which the energies of the EPR transitions have been calculated, to a first order approximation, the nuclear Zeeman levels have no effect on the transitional energies. The presence of the nuclear Zeeman splittings are vital in ENDOR spectroscopy, whose theory will be discussed in section 2.3.

2.2.4 *Mechanism of hyperfine interaction*

The interaction of the unpaired electron with the magnetic nucleus results in the production of the EPR hyperfine structure. The hyperfine structure is by far the most important information that can be obtained from a radical based system and can arise by two distinct mechanisms:

(a) ***Dipole-dipole interactions***

This interaction is analogous to the classical interaction of a pair of magnetic dipoles. However, the dipole moment of the unpaired electron must be calculated quantum mechanically since the electron is distributed over space. Dipole-dipole interactions occur when the unpaired electron and the magnetic nuclei are sufficiently close to allow interactions between their magnetic moments.

The energy of this interaction is found to be inversely proportional to the cube of the distance between the electron and the nucleus, r and is given by:

$$E_{Dipolar} = (1 - 3\cos^2\theta)/r^3 \,.\, \mu_n \mu_e = \mathbf{B}_{Local}\, \mu_e \qquad (2.14)$$

Where μ_n and μ_e are the components of the nuclear and electron dipole moments respectively along the applied magnetic field, **B**. The dipoles are separated by the distance r and θ is the angle between the magnetic field direction and the vector joining the two dipoles. The dipole-dipole interaction is therefore anisotropic and depends critically on the relative orientations of the two spins.

This type of coupling is very important in solid state EPR. In liquids, however, the rapid tumbling motion of the radical through all possible orientations relative to the applied field, averages this interaction to zero. Furthermore, in a hydrogen atom where the electron is distributed in a spherical symmetric 1s orbital, $\cos^2\theta = 1/3$ and the dipole-dipole interaction is similarly found to average to zero.

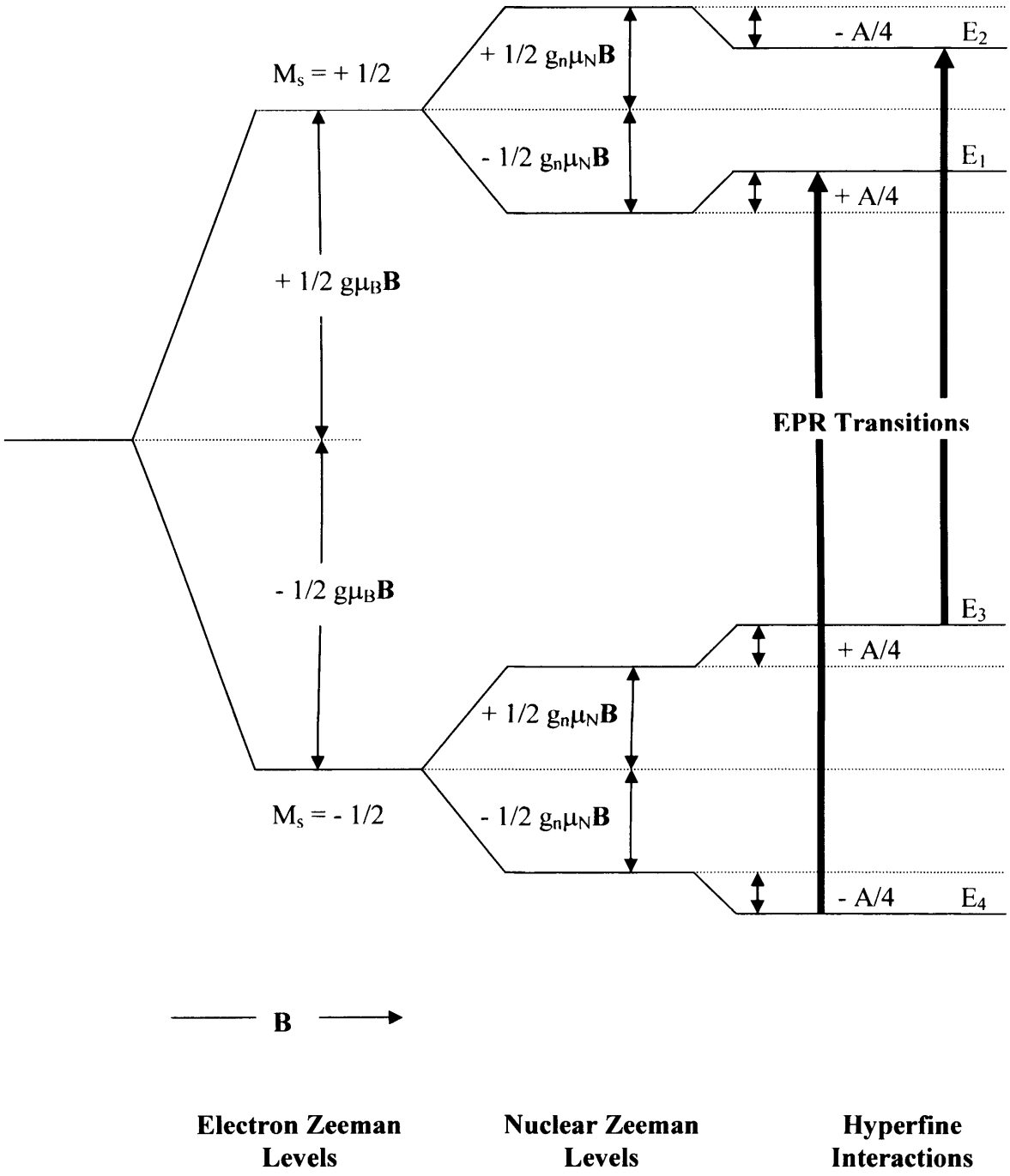

Figure 2.2: Energy level diagram summarising the interactions occurring between an unpaired electron ($S = 1/2$) and a single nucleus ($I = 1/2$), when ν_n (nuclear Zeeman splitting) > A/2 and A is positive.

(b) ***Isotropic or Fermi Contact Interaction***

This is a mechanism by which hyperfine couplings occur in solution. It is isotropic and independent of the orientation of the magnetic moment. The interaction arises because there is a non zero probability of finding the unpaired electron at the nucleus. Hence this interaction is only found for electrons in an s orbital or for electrons with partial s character, such as an sp^n hybrid orbital, since all other orbitals (p, d and f) have a nodal plane which give a zero probability for the wavefunction of the nucleus. The isotropic hyperfine coupling constant, A_0, is found to depend upon both the magnitude of the nuclear magnetic moment and the amount of unpaired spin density at the nucleus. The magnitude of the Fermi contact interaction is given by:

$$A_0 = (-8\pi/3)\,\mu_e\mu_n\,|\psi_{(0)}|^2 \qquad (2.15)$$

Where $\psi(0)$ represents the electron wavefunction at the nucleus, μ_e and μ_n the electron and nuclear dipole moments along the applied magnetic field and A_0, the isotropic coupling constant or Fermi contact interaction. The exact solution of the Hamiltonian predicts that A_0 for a hydrogen atom will have a value of 50.8 mT, which is in close agreement to the experimentally observed coupling constant for a gaseous hydrogen atom of 50.685 mT.

The Fermi contact interaction is not the only effect which contributes to the isotropic hyperfine coupling. Since the isotropic coupling is associated with unpaired electron spin density at the nucleus, then transition metals with unpaired electrons in d orbitals would not be expected to exhibit isotropic coupling. However, an appreciable isotropic coupling is always observed, eg., vanadyl VO^{2+} complexes have a_{iso} (^{51}V) values of up to nearly 12 mT.

Another example is constituted by organic radicals. In this case, the unpaired electron is located in a π molecular orbital that is constructed from a linear combination of $2p_z$ carbon atomic orbitals. Since each $2p_z$ atomic orbital possess a node in the plane of the molecule and this plane contains the bonding protons, then there should effectively be no unpaired spin density at the protons and no observed hyperfine splittings. Isotropic hyperfine couplings are, however, observed for π radicals and consequently there must be another mechanism to generate partial s

character in the wavefunction of the unpaired electron, to allow proton 1s orbitals to acquire a degree of unpaired electron spin density. This type of mechanism is termed *spin polarisation.*

Spin polarisation is best explained by considering an isolated >C-H fragment of an aromatic system which possesses one unpaired electron, residing in a $2p_z$ carbon orbital, that lies perpendicular to the plane of three trigonal bonds. A C-H sigma bonding orbital is formed by the overlap of the carbon sp^2 hybrid orbital with the proton 1s orbital. This orbital is occupied by two electrons and there are two possible assignments of the electron spins that form the C-H bond (Figure 2.3).

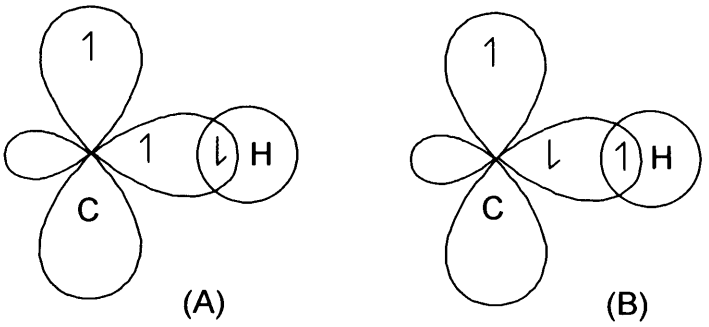

Figure 2.3: Diagram showing the two possible arrangements of the electron spin in the σ bond of a > C-H fragment.

If there was no unpaired electron in the 2pz orbital then the two possible configurations (A) and (B) would be equal. However, when an unpaired electron occupies the $2p_z$ orbital then the two arrangements are no longer equally probable. Hund's rule of multiplicity dictates that configuration (A) (in which the two electrons on the carbon atom have parallel spins) will be more stable and therefore more probable than configuration (B) (for which the two electron spins on the carbon atom are anti-parallel). The spin of the carbon sp^2 electron is thus slightly polarised in the same direction as the unpaired electron, resulting in a small net positive spin density at the carbon atom. As a result of this, a small net negative spin density will be generated on the proton, giving rise to a negative proton hyperfine splitting constant. This results in a mechanism by which small unpaired spin densities develop on the carbon sp2 and hydrogen 1s orbitals. It is the latter which gives rise to the isotropic hyperfine structure characteristics of π radicals.

In general, the s-character induced by the spin polarisation effect is small (cf., a 50 mT coupling for an unpaired electron on a hydrogen atom with 100% s character,

to the 2.3 mT coupling for the protons of a methyl radical). Therefore the unpaired electron density on a carbon atom is much less than unity and McConnell [5] has suggested the relationship:

$$a_0 = Q\rho \tag{2.16}$$

where a_0 is the hyperfine splitting constant due to the proton on the carbon atom, ρ the unpaired electron spin density and Q the McConnell constant with a value between -2 and -3 mT. This relationship is very useful for comparing experimentally calculated electron densities with those derived from MO calculations.

2.2.5 *Hyperconjugation*

Isotropic hyperfine couplings can also result from the direct orbital overlap between the proton and the π electron cloud. In unsaturated radicals, it is often found that the hyperfine coupling arising from the β carbon is greater than that from the α carbon. This phenomenon can be explained in terms of overlap between the hydrogen nucleus and the π orbital. The extent of hyperconjugation depends vitally on the dihedral angle, θ, between the π cloud and the β proton and is governed by the relationship:

$$a_0 = B_0 + B_1 \cos^2\theta \tag{2.17}$$

where B_0 is a measure of the spin polarisation, B_1 a measure of the hyperconjugation effect, a_0 the hyperfine splitting constant and θ the angle between the π cloud and the hydrogen nucleus. Clearly when θ is zero the overlap is greatest and the coupling constant is at a maximum and when θ is 90° the overlap will be least (as the orbitals will be perpendicular to each other) and the coupling will be at a minimum (Figure 2.3).

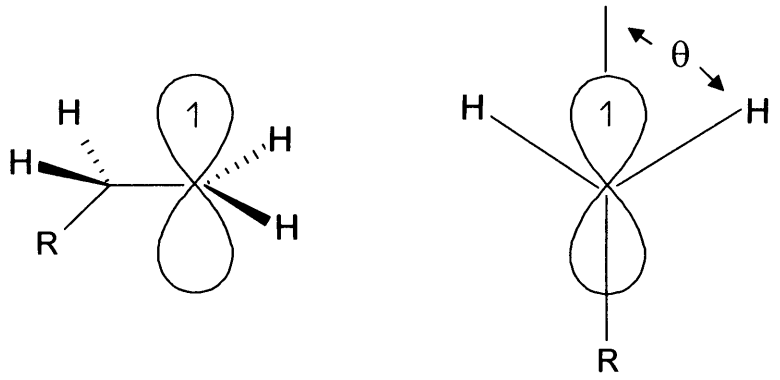

Figure 2.4: Diagram showing the dihedral angle between the p orbital and the β proton in hyperconjugation.

2.2.6 *The powder spectra of polycrystalline materials: Lineshape considerations*

The majority of EPR spectra recorded in the solid state come from polycrystalline materials or powders, whose spectra are usually called "powder" spectra. As many chemical systems of interest are polycrystalline or cannot be easily prepared as single crystals, the practical interest in powder EPR spectra is very high. Powder spectra are recorded for various real chemical systems such as glasses, ceramics, catalysts, minerals, micro and nanoporous materials and frozen solutions of coordination compounds. In the latter case, the comparison of a solution spectrum with the corresponding spectrum of the frozen solution is usually very fruitful for the determination of the properties of the paramagnetic compound.

A polycrystalline material is constituted by a large number of microcrystals randomly oriented in space so that all possible orientations of one crystal in the external field are equally probable. Since the sample is solid (the paramagnetic centres have not the typical motion of a molecule in solution and in many cases can be considered immobile) the anisotropy of the various magnetic interactions influence the spectra and the values are not averaged as in the solution case. A simple case may be considered of an $S = 1/2$ paramagnetic centre with no hyperfine splitting. The EPR spectrum is spread over the entire resonant field range ($\Delta B = B_{min} - B_{max}$) determined by the values of the principal g components. The intensity of the powder spectrum however is not uniform over all the ΔB range as shown in Figure 2.4, in the case of an axial g tensor ($g_{xx} = g_{yy} \neq g_{zz}$, $g_{\parallel} > g_{\perp}$) and in that of a rhombic g tensor ($g_{xx} \neq g_{yy} \neq g_{zz}$).

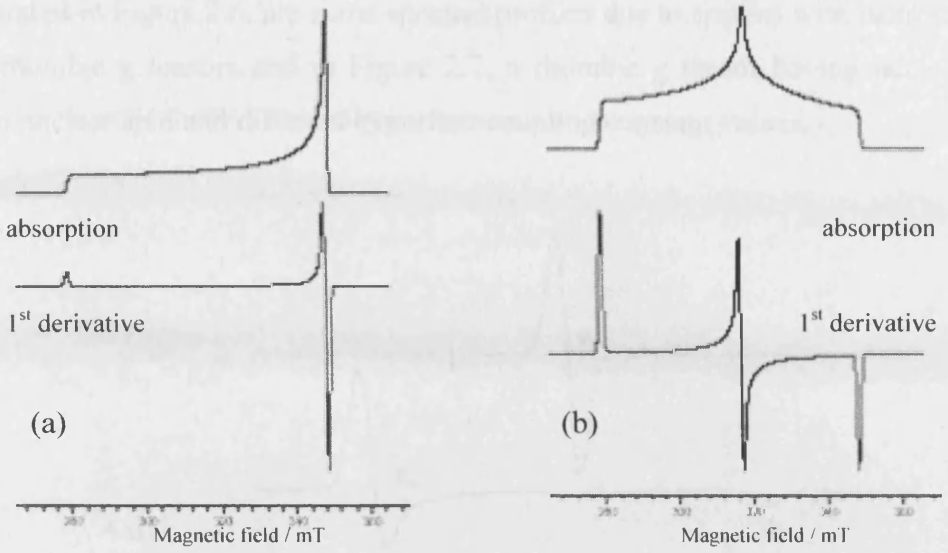

Figure 2.5: Calculated profiles (absorption and first derivative of absorption) of the powder spectra in the case of an (a) axial and (b) rhombic g tensor, in the absence of hyperfine interactions.

The non-uniformity of the intensity can be understood in practical terms, taking into account (for instance in the axial case) that, as $g_{xx} = g_{yy} = g_{\perp}$, the probability of having a microcrystal oriented in one of the two equivalent x and y directions, is twice the probability of an orientation along z. The simple powder spectra lines reported in Figure 2.5, can become rather complex in the presence of hyperfine interactions. The whole shape of the hyperfine powder spectrum depends on various factors:

- The nuclear spin of the magnetic nucleus (or nuclei) interacting with the unpaired electron.
- The isotropic abundance of the magnetic nucleus.
- The symmetry of the hyperfine tensor (axial, rhombic, etc.) and the values of the various elements of the tensor itself.

Illustrated in Figure 2.6, are some spectral profiles due to species with isotropic, axial and rhombic g tensors and in Figure 2.7, a rhombic g tensor having nuclei with a given nuclear spin and different hyperfine coupling constant values.

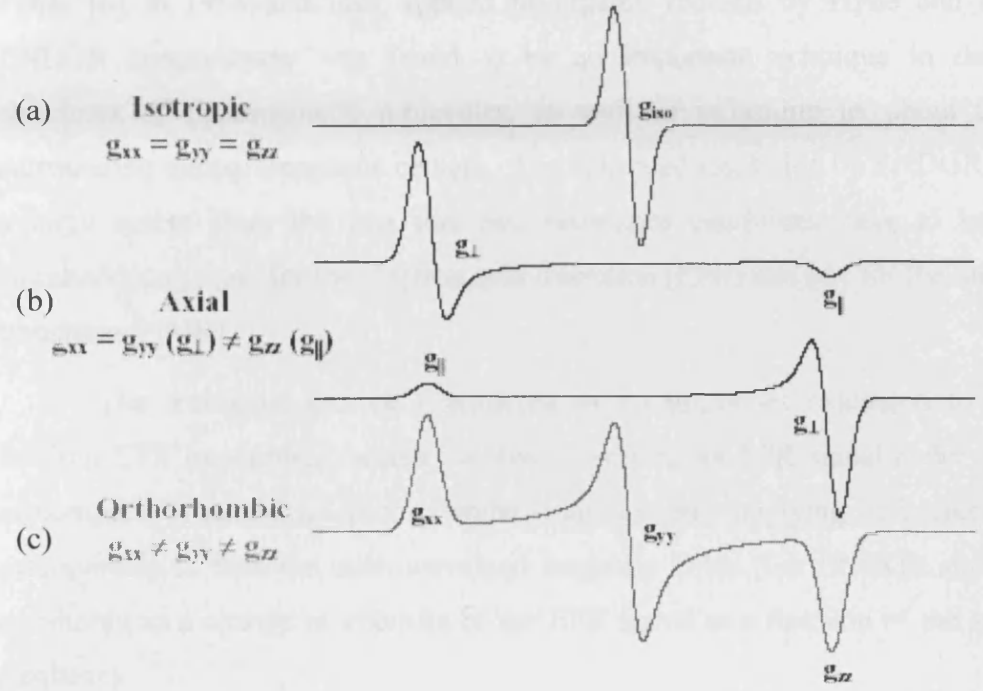

Figure 2.6: Calculated profiles (first derivative of absorption) of the powder spectra in the case of an (a) isotropic and (b) axial and (c) rhombic g tensor, in the absence of hyperfine interactions.

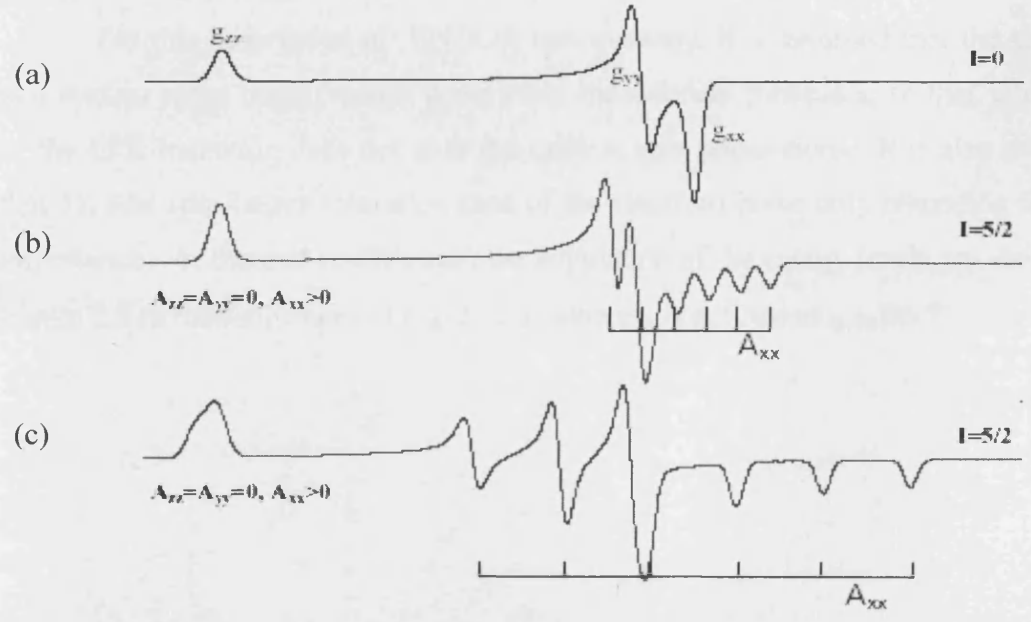

Figure 2.7: Calculated profiles of powder spectra of a species with rhombic g tensor. (a) no hyperfine interaction, (b) and (c) two cases with hyperfine structure due to one I=5/2 nucleus. Only the x component shows appreciable hyperfine coupling.

2.3 Basic principles of ENDOR spectroscopy

ENDOR is an electromagnetic resonance technique that can be described as EPR detected NMR. The technique of ENDOR spectroscopy was first applied by Feher [6] in 1956 and later applied to organic radicals by Hyde and Maki [7]. ENDOR spectroscopy was found to be an important technique in determining structures of paramagnetic molecules, as well as informing us about the atoms surrounding the paramagnetic centers. The enhanced resolution by ENDOR results to a large extent from the fact that two resonance conditions have to be fulfilled simultaneously, one for the electron spin transition (EPR) and one for the nuclear spin transition (NMR).

The technique can be considered as an important extension to the more familiar EPR experiment, which involves observing an EPR signal under conditions of complete or partial saturation, whilst simultaneously applying radiofrequency (*rf*) orthogonally to both the microwave and magnetic fields. The ENDOR signal is then monitored as a change in intensity of the EPR signal as a function of the applied RF frequency.

2.3.1 *Level populations of a simple description of the ENDOR effect*

For this description of ENDOR spectroscopy, it is assumed that the electron and nuclear spins relax through completely independent processes, so that saturation of the EPR transition does not alter the nuclear spin populations. It is also assumed that T_{1e} (the spin-lattice relaxation time of the electron) is the only relaxation time of importance. At thermal equilibrium, the population of the energy levels are shown by Figure 2.8 (a rearrangement of Figure 2.2) where ε is defined as $g\mu_B\mathbf{B}/kT$.

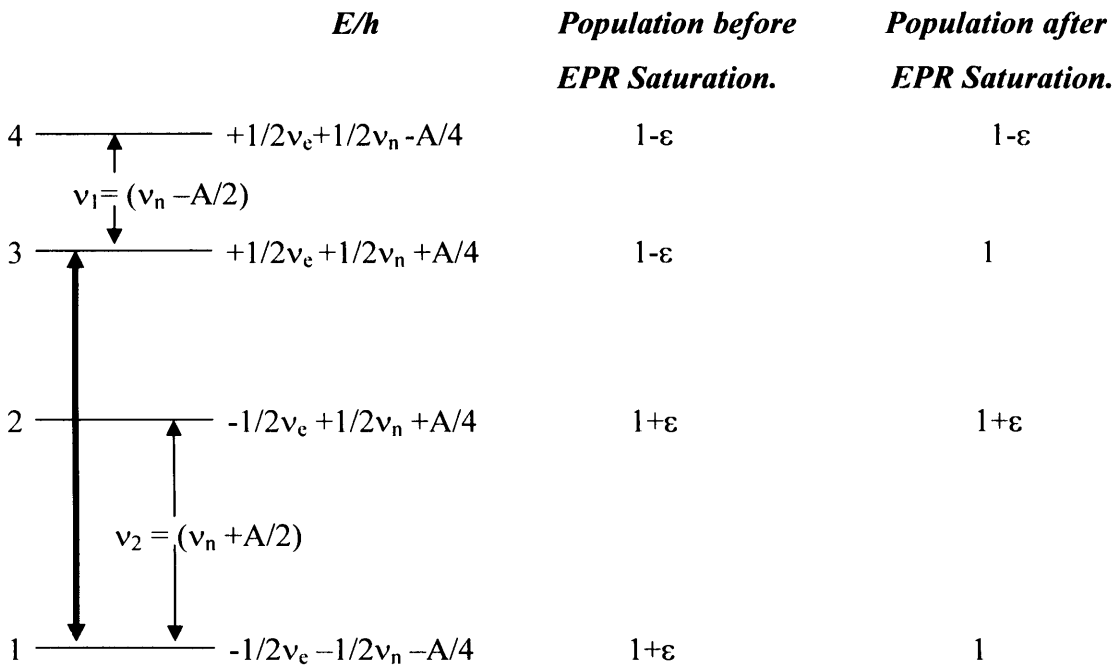

Figure 2.8: The ENDOR experiment for the case where $\nu_n > A/2$ and A is positive. The usual EPR transition 1→ 3corresponding to the selection rule $\Delta M_S = \pm 1$, $\Delta M_I = 0$ is shown with a wide arrow to indicate application of higher than usual microwave power. The solid lines represent nuclear transitions, $\Delta M_S = 0$, $\Delta M_I = \pm 1$ which give rise to the ENDOR spectrum.

If the EPR transition 1→3 is irradiated with microwave radiation so that it is saturated or partially saturated, then the spin populations of the two levels will equalise. If then, while continuously maintaining the partial saturated EPR transition 1→3, the system is irradiated with an intense RF field, when the radiofrequency matches the energy separation between the nuclear levels 3 and 4, nuclear transitions 3→4 will be induced (obeying the NMR selection rules $\Delta M_I = \pm 1$, $\Delta M_S = 0$) and RF energy will be absorbed. The absorption of energy occurs when:

$$\nu_I = \nu_n - A/2 \qquad (2.18)$$

The effect of removing spins from level 3 to 4 causes the population difference between levels 1 and 3 to be restored, thus removing the saturation of the EPR transition (1→3). This desaturation of the EPR transition gives rise to an increase in the EPR absorption that is recorded as an ENDOR signal (low frequency line). If the RF field is swept upwards until it matches the energy separation between the nuclear levels 1 and 2 (ie., when $\nu_I = \nu_n + A/2$) then the NMR transition 2→1

occurs via induced emission. This causes spins from level 2 to return back to level 1 so that the population difference between 1 and 3 is again restored. This causes a desaturation of the EPR transition 1→3 giving rise to a second ENDOR signal (high frequency line). The ENDOR spectrum therefore consists of two lines occuring at the RF frequencies corresponding to:

$$\nu_{ENDOR} = \nu_n \pm A/2 \tag{2.19}$$

symmetrically distributed around the Larmor frequency of the nucleus and separated by the hyperfine coupling constant A (MHz). If the coupling constant is positive, ν_n - A/2 (the low frequency line) refers to the $M_S = +1/2$ manifold and if the coupling is negative to the $M_S = -1/2$ manifold.

In the case where $\nu_n < A/2$, the order of the energy levels 3 and 4 are reversed so that the two ENDOR lines will appear when:

$$\nu_1 = A/2 - \nu_n \text{ and } \nu_2 = A/2 + \nu_n \tag{2.20}$$

Therefore, $$\nu_{ENDOR} = A/2 \pm \nu_n \tag{2.21}$$

The ENDOR spectra will consequently show two lines of equal height separated by $2\nu_n$ and symmetrically distributed around A/2.

Figure 2.9 shows an energy-level diagram of a hyperfine coupled spin system in a high magnetic field, consisting of one unpaired electron ($S = 1/2$) and four equivalent ($I = 1/2$) nuclei. Owing to the transition frequency degeneracies, five EPR transitions are obtained with binomial intensity distribution (1 : 4 : 6 : 4 : 1). The ENDOR spectrum, on the other hand, exhibits only two signals, since all NMR transitions in the same M_S state are degenerate.

To generalise, each group of equivalent nuclei, no matter how many nuclei belong to this group and what their spin quantum number is, contributes only two ENDOR lines to the spectrum. Addition of non-equivalent nuclei to the system causes a multiplicative increase of the number of signals in the EPR spectrum, but only an additive increase in the ENDOR spectrum. This enhancement in spectral

resolution can be expressed quantitatively by comparison of equations (2.22) and (2.23):

$$\text{Spectral density}_{\text{EPR}} = \frac{\prod_{i=1}^{k}(2N_iI_i+1)}{\sum_{i=1}^{k}2\,|a_i|\,N_iI_i} \qquad (2.22)$$

$$\text{Spectral density}_{\text{ENDOR}} = \frac{2k}{|a_{\max}|} \qquad (2.23)$$

There are k groups of i of equivalent nuclei with nuclear spin I_i and a number of nuclei N_i in each group; a_{max} denotes the largest hyperfine coupling constant, which in a homonuclear ENDOR experiment is equal to the spectral width. Therefore, resolution enhancement is offered by the ENDOR experiment only when non-equivalent nuclei are present.

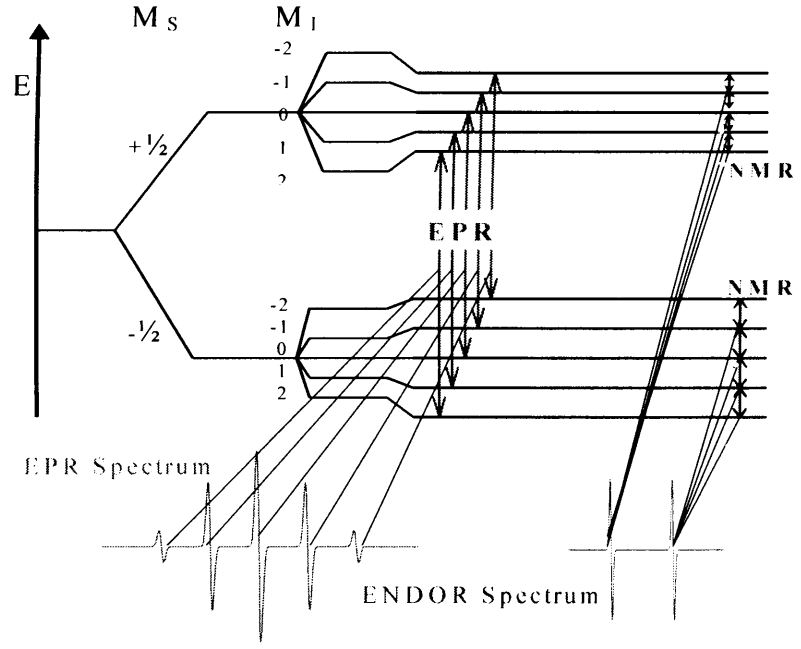

Figure 2.9: Energy level diagram for a system with 1 unpaired electron (S=1/2 and 4 equivalent nuclei (I=1/2)).

2.3.2 *Relaxation mechanisms in ENDOR spectroscopy*

The ENDOR description so far has assumed that the electron spin relaxation rate W_e (where $W_e = 1/T_{1e}$), is the only process operating. If this were the case then the experiment would only produce a transient ENDOR response, with the system reaching complete saturation and a loss of the ENDOR signal. Solution ENDOR has

alternative relaxation pathways which are available that lead to a re-establishment of the spin population differences and therefore produce steady state ENDOR signals. For a system with $S = 1/2$ and $I = 1/2$, all the possible relaxation pathways are shown in Figure 2.10. The solid arrows in Figure 2.10 represent the radiation-induced electron and nuclear spin transitions, whereas the thin arrows characterise the radiationless electron spin-lattice (W_e), nuclear spin-lattice (W_n) and cross-relaxation processes (W_{x1} "flip-flop" transition and W_{x2} "flop-flop" transition), where $W_n = 1/T_{1n}$.

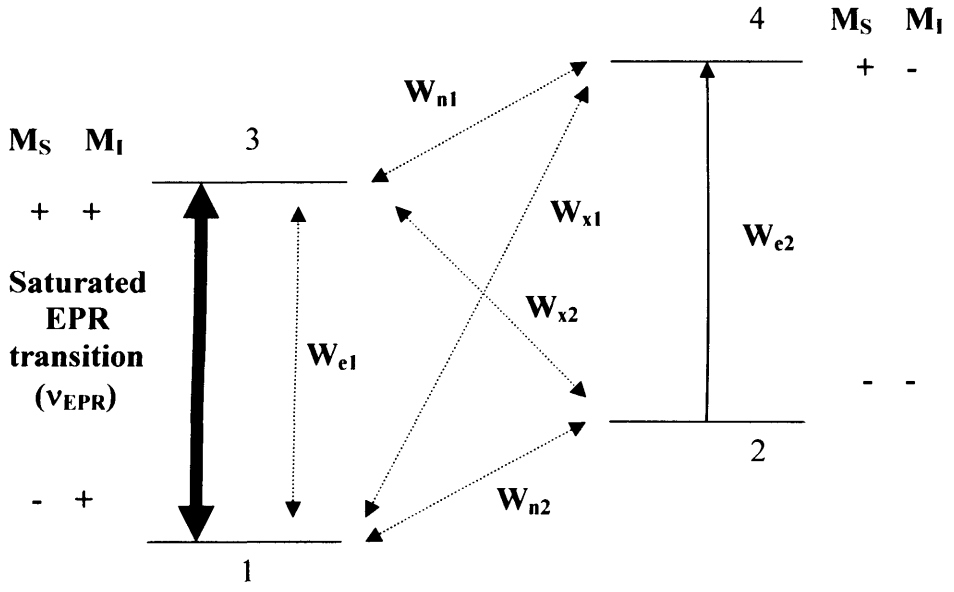

Figure 2.10: Relaxation pathways and rates in ENDOR, for a system with $S = 1/2$ and $I = 1/2$.

In EPR the most effective relaxation path for an electron in level 3 to return to level 1 is by a direct route *via* the electron spin-lattice rate W. The second possible route 3→4→2→1 is usually not as effective since it is controlled by the nuclear spin-lattice relaxation rates W_{n1} and W_{n2} that are generally much less than W_{e1}. Therefore for spins to relax efficiently by this alternative route, W_{n1} and W_{n2} must be sufficiently large as to prevent spins from congregating in levels 3 and 2. The "bottle neck" caused by W_{n1} may be removed by driving the nuclear transition 3→4, which effectively short circuits W_{n1}. The ENDOR experiment therefore creates a second effective relaxation path for the electron spins that is opened by driving the NMR transitions 3→4 or 2→1. This is known as the *steady state ENDOR effect.*

The cross relaxation rates W_{x1} and W_{x2} should also effectively enhance the spin relaxation process. For pure isotropic interactions, however, the W_{x2}

transition is forbidden, which leaves only one other possible relaxation pathway *via* $3 \rightarrow 4 \rightarrow 1$. In general it is found $W_e > W_{x1} > W_n$ and so the magnitude of the ENDOR effect depends crucially upon the relative magnitudes of these rates. Neglecting W_x processes, optimum ENDOR signals are obtained when W_e and W_n are comparable in magnitude, as under these conditions, no relaxation "bottle neck" appears along the bypass route for the electron spin.

The rates W_e and W_n are found to depend differently upon τ_R, where τ_R is the time constant for Brownian tumbling motion of the molecules in solution. W_e is inversely proportional to τ_R, whereas W_n is directly proportional to τ_R.

An adjustment of the relaxation rates can be achieved through temperature variation. This can be understood in terms of the Debye-Einstein equation (2.24). The equation relates τR to the effective molecular volume, ($V_{eff} = 4/3\ \pi r^3$, where r is the radius of the molecule, considered as a sphere), the viscosity η of the solvent and the temperature.

$$\tau_R = V_{eff}(\eta / k_B T) \qquad (2.24)$$

When there is a decrease in temperature and an increase in viscosity, W_e becomes smaller and W_n larger. The desired ratio $W_n/W_e = 1$, may be achieved through temperature-viscosity optimization of the solution. For protons, it is generally found that $W_n << W_e$, therefore experiments performed in solvents of low viscosity such as THF or toluene are expected to give maximum ENDOR signals at temperatures approaching the respective freezing point of the solvent.

In summary, the following conditions have to be fulfilled in order for a successful ENDOR experiment to be carried out:

- An EPR transition and an NMR transition have to be saturated. Higher microwave and radio frequency powers are required with increasing relaxation times.
- The relaxation rates W_e and W_n have to be of comparable magnitude.

Since the ENDOR signal intensity is essentially determined by the relaxation properties of the nuclei under investigation, unlike EPR, it is generally found that the magnitude of the ENDOR signal is not proportional to the multiplicity of the

hyperfine coupling. For small hyperfine couplings, it is commonly found that there is a systematic decrease in the ENDOR intensity as the coupling gets smaller [8]. Likewise, the high frequency component of an ENDOR line pair is often more intense than the low frequency one of the same power. This so called "hyperfine enhancement" effect [9], becomes further pronounced as the frequency difference between the two components increases, making assignment of individual ENDOR signals to particular molecular positions more difficult.

2.3.3 *The electric circuit analogy of the ENDOR effect*

The ENDOR effect can be advantageously be described in terms of an electric circuit diagram in which the various relaxation rates are regarded as conductances [10]. In conjunction with Kirchhoff's laws this is a simple approach to predicting the magnitude of the ENDOR effect. The electric circuit analogy was introduced by Bloch [11] and allows an estimate of the expected effects for various relaxation networks.

In Figure 2.11 the electric circuit is compared with the four-level system (S = 1/2, I = 1/2), already pictured in Figure 2.10, emphasizing the analogy of these two descriptions. The EPR signal is found to be proportional to the current I in this circuit and the EPR or NMR saturation is described by R_e and R_n, which are the internal shunt resistances. The voltage U in the EPR circuit represents the Boltzman population difference between the electron spin energy levels. No such battery is necessary in the NMR circuit, since the population difference between the nuclear spin levels is much smaller.

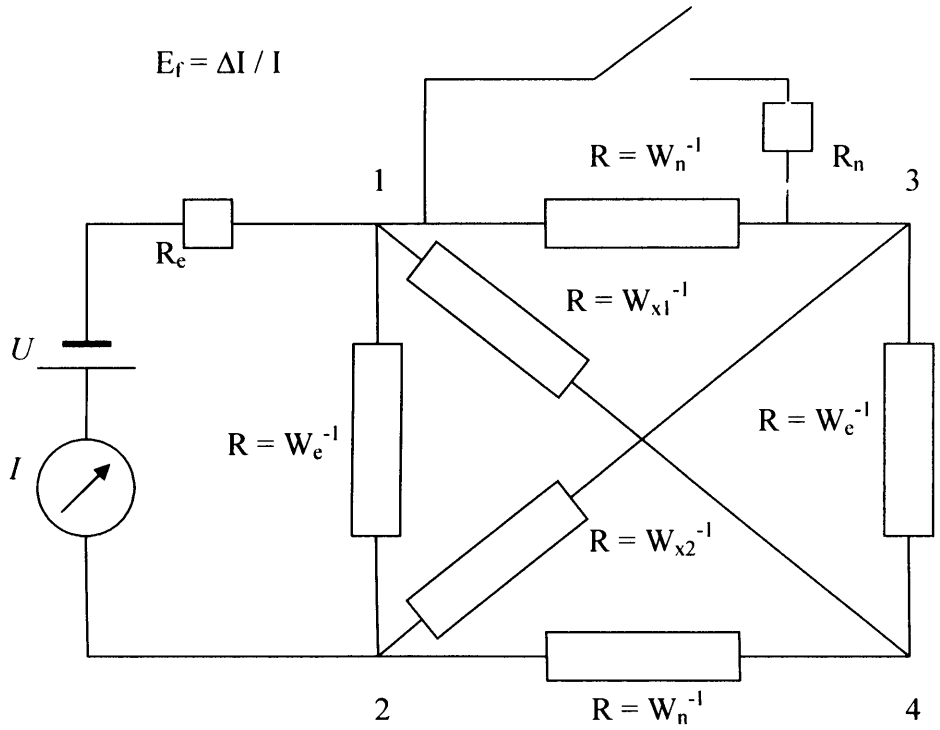

Figure 2.11: Electric circuit analogy of the ENDOR effect.

In the electric circuit analogy, the fractional ENDOR enhancement, E_f, can be obtained directly by measuring the relative change of the input conductance across the circuit branch belonging to the EPR transition (Figure 2.11, 1→2) after closing the switch in the NMR shunt (1→3).

The fractional ENDOR enhancement E_f is defined as the relative change of the EPR signal [12, 13], Where ΔT_{1e} is the change of relaxation time:

$$E_f = = -3/4 \, . \, \Delta T_{1e}/T_{1e} \qquad (2.25)$$

The situation of closing the switch in the NMR shunt, corresponds to exact on-resonance conditions and is usually the limit of high EPR and NMR saturation (R_e = R_n = 0) is chosen (NMR short circuited and internal EPR resistance neglected). Through applying Kirchhoff's rules for adding conductances in series or parallel, the relative numbers for the ENDOR enhancement may be obtained.

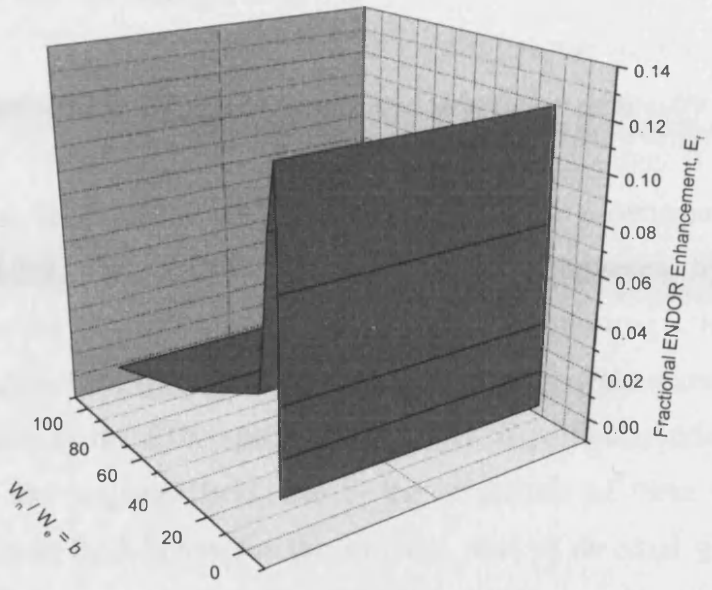

Figure 2.12: Dependence of the fractional ENDOR enhancement, E_f on $b = W_n / W_e$.

Figure 2.12 shows the dependence of the fractional ENDOR enhancement, E_f on b, where b is W_n/W_e. It can be seen that a bell-shaped curve is obtained with a maximum of $E_f = 0.125$ at $W_e = W_n$ ($b = 1$), ie., the maximum ENDOR enhancement amounts to 12.5% of the EPR signal. The curve shows a fall off for $W_e < W_n$ or $W_e > W_n$. Assuming $W_e = 10$, W_n ($b = 0.1$), an ENDOR enhancement of only 0.04 (4%), is obtained, since the second conductance (W_{nII}) is small and acts like a "bottle-neck" for the relaxation pathway. For $W_e = 0.1$ W_n ($b = 10$) the same value of 0.04 is obtained for the ENDOR enhancement, but now W_{eII} is the "bottle-neck". The enhancement is independent of the NMR transition being saturated and as a result the *two ENDOR signals will have equal intensity*. However, if $W_{x1} \neq W_{x2}$, which is the most frequent case, the relaxation network becomes asymmetrical and will consequently produce *asymmetric ENDOR signals*. The larger ENDOR effect will be observed for that NMR transition which forms a closed loop with the larger one of the two W_x rates.

Summarising, it can be stated that the electric circuit analogy gives a useful description of the various spin-relaxation rates, illustrating how different ENDOR signals are produced, be it asymmetric ENDOR signals or signals of equal intensity. The electric circuit analogy may also be furthermore extended to much more complex systems, such as the Triple resonance effect, where this approach has been used to

solve some theoretical problems of ENDOR spectroscopy [14], however, a description of this technique will not be given here.

2.3.4 *Angle selective ENDOR spectroscopy and simulation of spectra*

Structural information may be obtained from paramagnetic species in disordered systems, in particular transition metal complexes by carrying out measurements of the ENDOR spectra at various but specific magnetic field positions in the corresponding EPR spectrum. As the g and hyperfine values are anisotropic, the features that arise in the EPR spectra correspond to particular orientations of the paramagnets in the magnetic field, due to the magnitude of these tensors. This is illustrated in Figure 2.13 below for the simplest case of an axial g tensor with no hyperfine coupling to the central metal nucleus. Alternatively, one may use the paramagnet as a frame of reference and consider the magnetic field as a vector making an angle theta with the parallel direction of the g tensor.

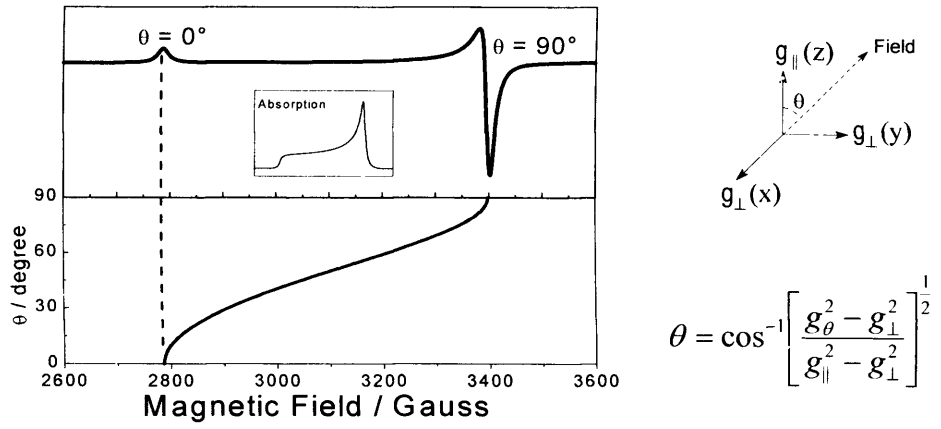

Figure 2.13: EPR spectrum and associated angular dependence of a paramagnetic system with axial symmetry (I=0).

By setting the magnetic field to the appropriate point in the EPR spectrum (Figure 2.13), any angle of theta between 0° and 90° may be selected. Because of the selectivity of the ENDOR experiment, only those paramagnets that are resonant at the selected magnetic field participate in the ENDOR experiment. This phenomenon, termed magnetic angle selection, enables the *direction* of a magnetic ligand nucleus to be determined relative to the central metal atom.

To determine ligand coordinates knowledge of distances as well as directions or angles between the metal centre and the distant nucleus is required. This may be obtained by assuming that the only magnetic interaction between the magnetic nucleus and the unpaired electron at the metal centre is a through-space, dipolar interaction. The distance (R) may then be calculated from equation 2.26 using the dipolar hyperfine coupling (A_{DIP}) term obtained from the ENDOR spectrum.

$$A^{\varphi}_{Dip.} = \left(\frac{\mu_0}{4\pi h}\right) \bullet \frac{2 g_{\varphi} \mu_{\beta} g_N \mu_N}{R^3} \left(3\cos^2 \varphi - 1\right) \qquad (2.26)$$

Where A^{α}_{DIP} is the dipolar hyperfine coupling (Hz) and μ_0 is the Permeability of a vacuum ($4\pi \times 10^{-7}$ $T^2J^{-1}m^3$). It is found that the dipolar hyperfine coupling constant is inversely proportional to the distance cubed, the angle φ above is the angle between the two dipoles and may be obtained from the angle θ selected by the magnetic field. Although the above equation is an approximation, the results produced are often comparable to those obtained from X-ray diffraction.

The ENDOR spectrum of a disordered systems consists of a summation of the ENDOR spectrum of each possible orientation of the paramagnets with the sample at the static magnetic field, selected from the EPR spectrum. To determine which orientations are resonant at the magnetic field, resonant fields for given values of theta are calculated using 2nd order pertubation theory (increases speed of calculation). As the vanadyl system may have axial symmetry, all values of phi are equivalent. It is necessary to use 2nd order due to the large hyperfine coupling constant of transition metals in such systems. The next step involves comparing field values to the static magnetic field, *ie.*, only corresponding values then have their ENDOR spectra determined.

The EPR linewidth is taken into consideration at this point; the broader the EPR linewidth, the more orientations will contribute to a given magnetic field value (a weighting factor is applied to the ENDOR spectrum to allow for the intensity or lineshape, which is *Gaussian*).

After determination of contributions for a given value of the static magnetic field, the ENDOR spectrum for each nucleus is in turn calculated and added to the total

spectrum, provided that this is not zero. However, before the ENDOR spectrum can be calculated all the tensors (matrices) have to be in the same reference frame.

Matricies are used, such as the g matrix and hyperfine matrix in their diagonal frame, that is the reason g_{xx}, g_{yy} and g_{zz} are used; this also applies to the hyperfine interactions (2.27):

$$\begin{bmatrix} g_{xx} & 0 & 0 \\ 0 & g_{yy} & 0 \\ 0 & 0 & g_{zz} \end{bmatrix} \qquad (2.27)$$

In EPR, this is not such a problem, because in high symmetry cases, such as for the vanadyl, the $A_{V=O}$ and g matrices are diagonal in the same axis system. For protons however, the axis system in which its diagonal is mainly that which follows the dipolar component of the hyperfine interaction, ie, the proton – metal direction.

As a result of this it is necessary to rotate the proton hyperfine matrix onto the same axis as the g or $A_{V=O}$ matrix. Due to the axial symmetry of the EPR spectrum, this is a simple rotation through an angle θ. As a result of this, the proton hyperfine matrix is no longer diagonal and the symmetry for the system has been lowered.

The lowering of the symmetry of the system means that, as only one angle (theta) is needed for the EPR spectrum, a second set of orientations is needed within the x-y plane (phi) when the ENDOR spectrum is calculated. This can explain why, in certain magnetic fields and proton angles, more than two pairs of lines may result in the ENDOR spectrum.

$$\nu_{II} = \left[\sum_{i=1}^{3} \left[\frac{m_s}{g_{(\theta,\phi)}} \left(\sum_{j=1}^{3} g_j h_j A_{ji} \right) - h_i \nu_0 \right]^2 \right]^{1/2} \qquad (2.28)$$

After the hyperfine matrix is rotated into the g frame, the ENDOR spectrum is calculated for each pair of theta and phi orientations, using $\nu_H = \pm |A/2|$. A formula given by *Hurst et al* [15] (2.28), allows for the fact that the magnetic moment of an electron in anisotropic systems does not lie along the direction of the applied

magnetic field. The program finally allows a statistical range of dipolar hyperfine terms which correspond to a range of distances to be determined.

2.3.5 *Powder ENDOR simulation procedure*

The main ENDOR simulation software comprises of two programs, either *rhdat* and *rhend* or *axend* and *axdat*. The software is used for both axial and rhombic programs. This dual approach allows one to facilitate both interactive simulations and allow batch processing when necessary. *axdat* is a terminal based data entry program which has been designed to be user friendly and intuitive. All limitations on the number of nuclei, ie., sweep range, frequency etc, are incorporated into the simulation program [115].

The second program, either *axend* or *rhend*, is the "Simulation engine". It has no restrictions placed on it, regarding the size of the calculation and is therefore limited by the physical resources of the computer and the time frame available. The program initially reads all the data from the input file.*inp* into the memory. The calculations run in the memory until the calculation has ended and creates two additional files, an out file, containing a summary of the parameters in English. These parameters are useful for printing. The second file, a.*dat* file, contains two columns of data for plotting., ie, RF frequency versus Intensity.

The program can incorporate any type of nucleus of any nuclear spin, however nuclear quadrupolar effects can not be calculated. Also, the program can only handle one species at a time, as multiple species require separate simulation and addition of the *.dat* files into a statistical graphing program. eg, *Origin*. It can also only simulate ENDOR spectra with an EPR symmetry down to rhombic, as the hyperfine and g tensor axis systems must be coincident. This is the strategy for an efficient ENDOR simulation;

- In the first instance, the EPR linewidth should be kept low, ideally 0.1 Gauss. This limitation restricts the number of orientations contributing to the ENDOR spectrum. This feature is particularly important as when broadened, there may be a shift in the ENDOR spectrum, as the EPR linewidth increases.

- The simulation of individual nuclei is important. As ENDOR spectra are additive and not multiplicative like EPR, the individual nuclei will give rise to a number of characteristic features in the ENDOR spectra. This allows us to identify which features in the spectrum arise from which protons.

- ENDOR spectra are not quantitative and therefore it is not necessary to reproduce numbers of equivalent protons appearing in the proton system. In most solid-state systems, as the symmetry decreases, chemically equivalent protons become non-magnetically equivalent.

Table 2.1, shows a list of programs that were used, in order to carry out the successful simulation of powder ENDOR simulations of transition metal complexes. The main programs listed will be explained further in Chapter 3, where the initial setup and use of the programs will be presented.

Table 2.1: Programs used for the ENDOR simulation of transition metal complexes. The programs were installed and ran on Redhat Linux systems.

axend	Simulation engine for axial EPR systems
axdat	Data preparation program for the axend program
rhend	Simulation engine for axial EPR systems
rhdat	Data preparation program for the rhend program
axdist2	Nuclear position calculating program for axend data input files
rhdist2	Nuclear position calculating program for rhend data input files
mspin	Hyperfine matrix calculator for delocalised electro spin
axangle	Angular variation (EPR) program for 1st order axial systems
axangle2	Angular variation (EPR) program for 2nd order axial systems
rhangle	Angular variation (EPR) program for 1st order rhombic systems
rhangle2	Angular variation (EPR) program for 2nd order rhombic systems
entangle	Angular variation (ENDOR) program for 1st order axial systems
enangle2	Angular variation (ENDOR) program for 2nd order axial systems
gnuplot	Graphical plotting program
rasmol	Molecular visualisation and measurement program
brukcon	ASCII data conversion program

2.4 References

[1] E. Zavoisky, *J. Phys. U. S. S. R.*, 1945, **9**, 211, 245.

[2] J.E. Wertz, J.R. Bolton," *Electron Spin Resonance – "Elementary Theory and Applications*", Pub. John Wiley and sons, 1986.

[3] H.M. Swartz, J.R. Bolton, D.C. Borg, *Biological Application of Electron Spin Resonance*, Pub, John Wiley and sons, 1972.

[4] W.J. Bruce, *J. Chem. Educ.*, 1987, **64**, 907.

[5] H.M. McConnell, *J. Chem. Phys.*, 1956, **24**, 764.

[6] G. Feher, *Phys. Rev.*, 1956, **103**, 834.

[7] J.S. Hyde, A.H. Maki, *J. Phys. Chem.*, 1964, **40**, 3117.

[8] N.M. Atherton, "Electron *Spin Resonance – Theory and Applications*", Pub. Ellis Horwood Ltd, Chichester, 1973.

[9] S. Geschwind, A.J. Freeman, R.B. Frankel, "*Hyperfine Interactions*", Academic press, New York., 1967, 225.

[10] K. Möbius, M. Plato, W. Lubitz, *Phys. Rep.*, 1982, **87**, 171.

[11] F. Bloch, *Phys. Rev.*, 1956, **102**, 104.

[12] H. Shikata, *Bull. Chem. Soc. Jpn.*, 1977, **50**, 3084.

[13] H. Shikata, K. Ishizu, *Bull. Chem. Soc. Jpn.*, 1977, **50**, 3090.

[14] N.M. Atherton, P.A. Kennedy, *Chem. Phys. Lett.*, 1976, **43**, 186.

[15] Hurst *et al. J. Am. Chem. Soc.*, 1985, **107**, 7294.

Chapter 3

Experimental

3.0 Experimental

3.1 Synthesis of Inorganic complexes

(R,R)-diammonium mono-tartrate salt – **(1)**

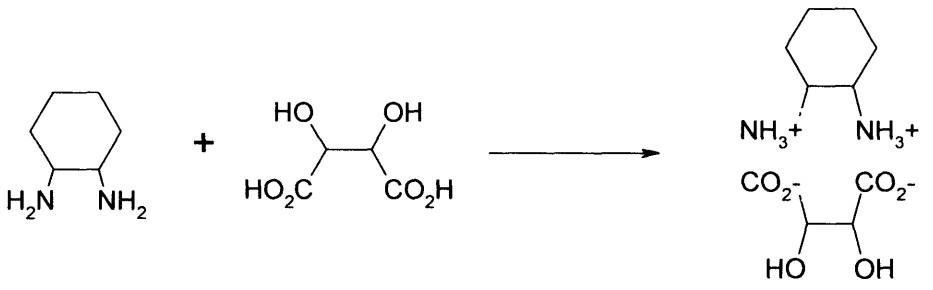

L-(+) tartaric acid (3.75g, 25mmol) was added in one portion to a beaker assembled with a stirrer and a thermometer charged with 25ml of distilled water. Solution stirred as racemic *trans* –1,2- diaminocyclohexane (5.74g, 50mmol) was added carefully in one portion. A slurry initially formed but complete dissolution was observed once addition was complete. Glacial acetic acid (2.5ml) was added and precipitate allowed to cool from 90°C to 5°C, with stirring over 3-4 hours. The temperature was maintained at 5°C for an additional hour, where the product was isolated by filtration. The resulting filter cake was washed with water (5°C, 10ml) and methanol (4x5ml). The product was dried under reduced pressure, with heating to yield (*R,R*)-1,2-diammoniumcyclohexane mono-(+)-tartrate salt as a white powder. Yield: 2.98g (90%) [1].

3,5-di-tert-butylsalicylaldehyde – **(2)**

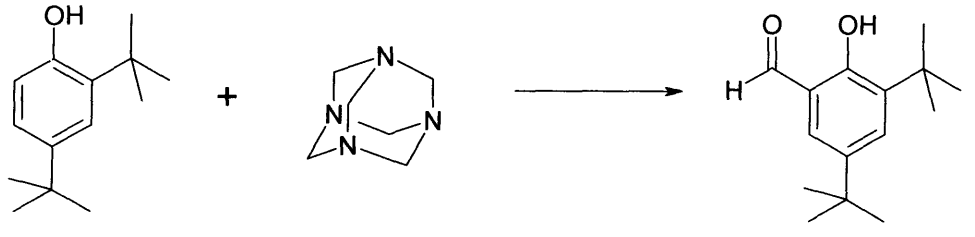

A three necked, round bottom flask with stirrer, reflux condenser and thermometer was charged with 2,4-di-*tert*-butylphenol (6.25g, 30mmol), hexamethylenetetramine

(8.5g, 40mmol) and glacial acetic acid (15ml). Mixture was heated to 130°C (3 hours) with stirring, after which was cooled to 80°C and H_2SO_4 [15ml of 33% (w/w)] added. After the resulting mixture was heated to reflux (105-110°C) for 30-60 min, the reaction mixture was cooled to 80°C and transferred to a separating funnel. The phases were allowed to separate while the temperature was maintained at 75°C on a hot plate. The lower aqueous phase was drawn off (pH 4-5) and the organic layer transferred to an erlenmeyer flask and cooled to 50°C, at which point MeOH was added with stirring. The mixture was cooled to room temperature and the temperature was taken down to 5°C in an ice bath (1 hour) with stirring. Product was collected by vacuum filtration and solid washed with MeOH(5°C, 3ml). The crude product was suspended in MeOH (1:1) w/v and mixture heated to 50-55°C with stirring. Solution was maintained at 5°C for 2 hours. The yellow product was then collected by vacuum filtration, washed with MeOH (5°C, 10ml) and allowed to air dry. Yield: 3.89g (67%) [1].

N,N'-bis(salicylidine)-1,2-ethylenediamine **– (3)**

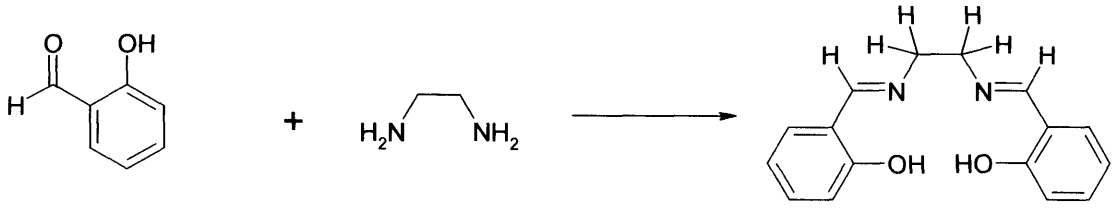

To a solution of salicylaldehyde (4.91g, 21mmol) in ethanol (100ml) was added 1,2-diaminoethane (0.60g, 10mmol) slowly over 10 minutes and the mixture brought to reflux. After 24 hours heating was discontinued and the solution cooled to 0°C and maintained for 1 hour. The yellow precipitate was filtered and washed with cold ethanol (20ml). The material required no further purification. Yield 2.5g (93%). ^{1}H NMR (400MHz, $CDCl_3$): δ 13.15 [s, 2H, O*H*], 8.25 [s, 2H, NC*H*C], 7.20 [m, 2H of Ar], 7.15 [dd, *J*=1.6 Hz, 7.7 Hz, 2H of Ar], 6.90 [d, *J*=8.2 Hz, 2H of Ar], 6.80 [m, 2H of Ar] and 3.90 [s, 4H, CH_2]. ^{13}C NMR (100MHz, $CDCl_3$): δ 165 [*C* of Imine], 160 [*C* of Ar], 131 [*C* of Ar], 130 [*C* of Ar], 118 [*C* of Ar], 116 [*C* of Ar] and 58 [CH_2]. Mass spectrum: molecular ion peak at *m/z* = 269.4 (calc. 268.3). IR (KBr disc, cm^{-1}): 3056, 2895, 1636, 1576, 1497, 1458, 1419, 1283, 1149, 1042, 1021, 857 and 749.

N,N'-bis(salicylidine)-1,2-d_4-ethylenediamine **– (4)**

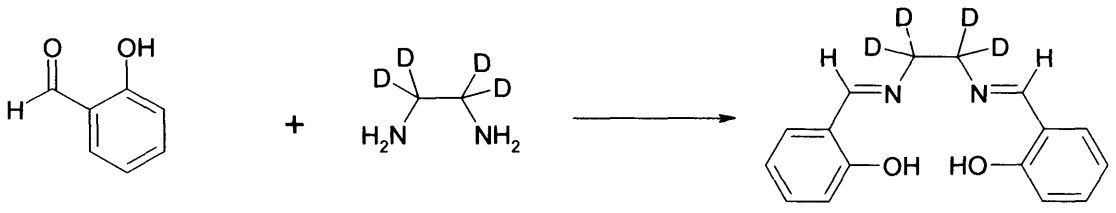

This material was prepared in a similar manner to that of *N,N'*-bis(salicylidine)-1,2-ethylenediamine – (**3**) using ethylene-d_4-diamine (1.0g, 16mmol) and salicylaldehyde (4.0g, 33mmol) to yield the product as a yellow solid. Yield 3.95g (90%). ^{1}H NMR (400MHz, $CDCl_3$): δ 13.15 [s, 2H, O*H*], 8.25 [s, 2H, NC*H*C], 7.20 [m, 2H of Ar], 7.15 [d, *J*=1.6 Hz, 7.7 Hz, 2H of Ar], 6.90 [d, *J*=8.2 Hz, 2H of Ar] and 6.80 [m, 2H of Ar]. ^{13}C NMR (100MHz, $CDCl_3$): δ 166 [*C* of Imine], 160 [*C* of Ar], 133 [*C* of Ar], 131 [*C* of Ar], 118 [*C* of Ar], 115 [*C* of Ar] and 56 [CH_2]. Mass spectrum: molecular ion peak at *m/z* = 273.3 (calc. 272.3). IR (KBr disc, cm^{-1}): 3050, 2896, 1632, 1568, 1498, 1454, 1419, 1282, 1152, 1042, 1021, 852 and 740.

N,N'-bis(salicylidine)-1,2-cyclohexanediamine – **(5)**

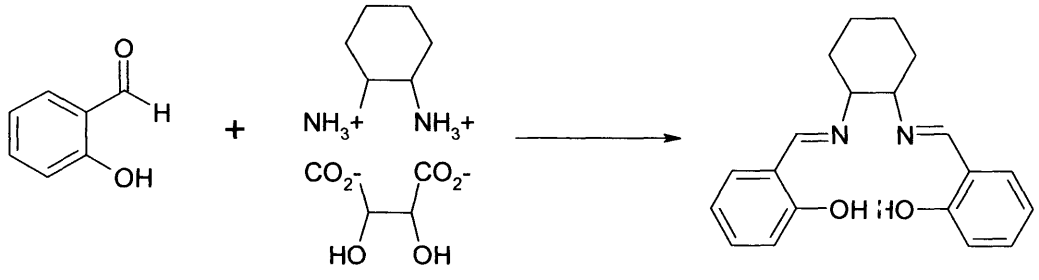

Trans-1,2-diammoniumcyclohexane mono-(+)-tartrate salt (10.0g, 87mmol) and K_2CO_3 (24.21g, 17mmol) were dissolved in deionised water (30ml). The mixture was stirred and EtOH added (40cm^3), the reaction was left to reflux for approximately 1 hr. Salicyaldehyde (21.39g, 17mmol) in ethanol (30cm^3) was added with stirring over 30mins. The reaction mixture was left again to reflux for a further 1hr. After

which time, was left in the fridge (5°C) for 24 hrs. The solid was collected, washed with cold ethanol (3x10 cm^3) and dissolved in dichloromethane (30cm^3). The mixture was finally washed with water (3x10cm^3) and evaporation afforded an oily solid. Yield: 27.50g. ^{1}H NMR (400MHz, $CDCl_3$): δ 13.25 [s, 2H, O*H*], 8.18 [s, 2H, NC*H*C], 7.18 [m, 2H of Ar], 7.08 [d, *J*=1.6 Hz, 7.7 Hz, 2H of Ar], 6.80 [m, 2H of Ar], 6.70 [d, *J*=8.2 Hz, 2H of Ar], 3.25 [m, 2H, CH_2CH], 1.86 [m, 2H, CHC(*H*)H], 1.82 [m, 2H, CHCH(*H*)], 1.65 [m, 2H, CH_2CH(*H*)] and 1.40 [m, 2H, CH_2C(*H*)H]. ^{13}C NMR (100MHz, $CDCl_3$): δ 165 [*C* of Imine], 161 [*C* of Ar], 133 [*C* of Ar], 132 [*C* of Ar], 119 [*C* of Ar], 117 [*C* of Ar], 73 [CHN], 34 [*C* of Ar], and 25 [*C* of Ar]. Mass spectrum: molecular ion peak at *m/z* = 323.5 (calc. 322.4). IR (KBr disc, cm^{-1}): 3467, 2935, 2855, 1629, 1493, 1458, 1418, 1272, 1147, 1091, 840 and 755 [2].

N,N'-bis(3,5-di-tert-butylsalicylidine)-1,2-ethylenediamine – **(6)**

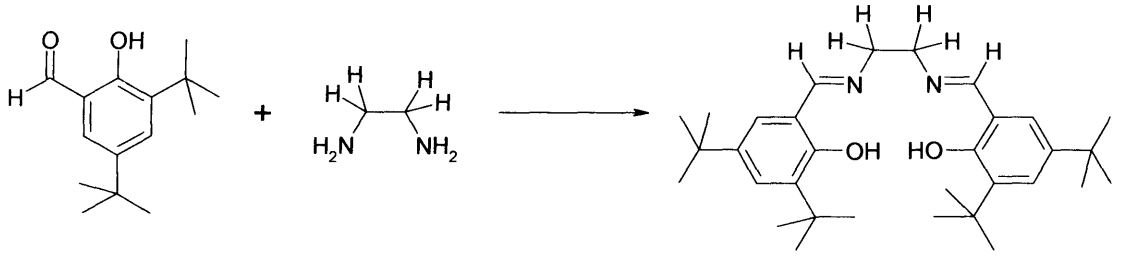

To a solution of 3,5-di-*tert*-butylsalicylaldehyde (5.00g, 21mmol) in EtOH (100ml) was added 1,2-diaminoethane (0.60g, 10mmol) slowly over 10 minutes and the mixture refluxed overnight. Heating was discontinued and the solution cooled to 0°C and maintained for 1 hour. The yellow precipitate was filtered and washed with cold ethanol (20ml). The material required no further purification. Yield 4.4g (90%). ^{1}H NMR (400MHz, $CDCl_3$): δ 13.60 [s, 2H, O*H*], 8.40 [s, 2H, NC*H*C], 7.40 [s, 2H of Ar], 7.10 [s, 2H of Ar], 3.90 [s, 4H, CH_2], 1.45 [s, 18H, CCH_3] and 1.30 [s, 18H, CCH_3]. ^{13}C NMR (100MHz, $CDCl_3$): δ 168 [*C* of Imine], 158 [*C* of Ar], 137 [*C* of Ar], 128 [*C* of Ar], 127 [*C* of Ar], 118 [*C* of Ar], 60 [CH_2N], 34 [CCH_3], 33 [CCH_3], 32 [CH_3] and 30 [CH_3]. Mass spectrum: molecular ion peak at *m/z* = 493.6 (calc. 492.7). IR (KBr disc, cm^{-1}): 3437, 2963, 2869, 1628, 1466, 1438, 1270, 1041, 879 and 830.

N,N'-bis(3,5-di-tert-butylsalicylidine)-1,2-d_4-ethylenediamine – (7)

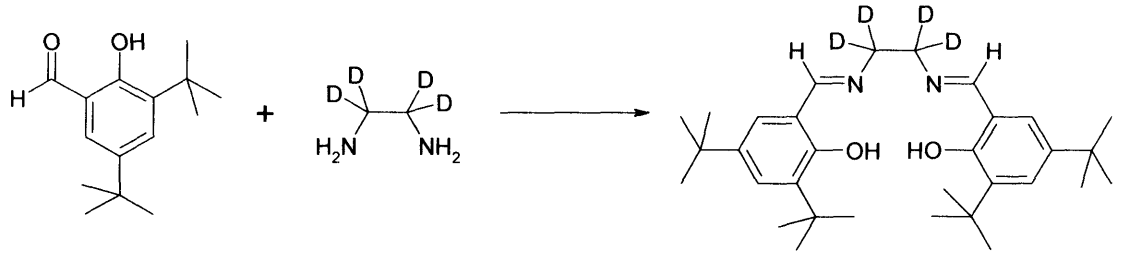

This material was prepared in a similar manner to that of *N,N'*-bis(3,5-di-*tert*-butylsalicylidine)-1,2-ethylenediamine – (**6**) using ethylene-d_4-diamine (1.0g, 16mmol) and 3,5-di-*tert*-butylsalicylaldehyde (7.80g, 33mmol) to yield the product as a yellow solid. Yield 7.91g (83%). ^{1}H NMR (400MHz, $CDCl_3$): δ 13.60 [s, 2H, O*H*], 8.38 [s, 2H, NC*H*C], 7.40 [s, 2H of Ar], 7.15 [s, 2H of Ar], 1.40 [s, 18H, CCH_3] and 1.30 [s, 18H, CCH_3]. ^{13}C NMR (100MHz, $CDCl_3$): δ 170 [*C* of Imine], 158 [*C* of Ar], 137 [*C* of Ar], 128 [*C* of Ar], 126 [*C* of Ar], 119 [*C* of Ar], 59 [*C*d_2N], 34 [*C*CH_3], 33 [*C*CH_3], 32 [*C*H_3] and 31 [*C*H_3]. Mass spectrum: molecular ion peak at *m/z* = 496.8 (calc. 496.5). IR (KBr disc, cm^{-1}): 3432, 2961, 2865, 1628, 1466, 1439, 1273, 1045, 877 and 830.

***(R,R)-N,N'-bis(3,5-di-tert-butylsalicylidine)-1,2-cyclohexanediamine* – (8)**

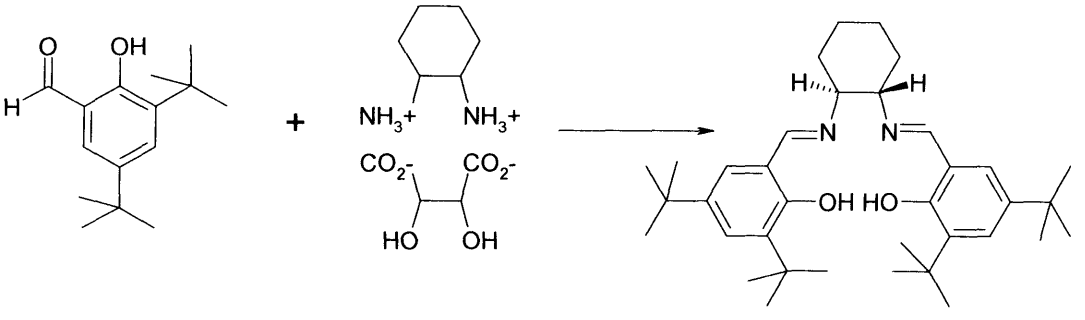

A 2-litre three necked, round bottomed flask equipped with a stirrer, reflux condenser and addition funnel is charged with (*R,R*)-1,2-diammoniumcyclohexane mono(+) tartrate salt (29.7g, 112mmol), K_2CO_3 (31.2g, 225mmol, 2eq) and water (150ml). The mixture was stirred until dissolution was achieved and EtOH (600ml) was added. The cloudy mixture was heated to reflux with a heating mantle and a

solution of of 3,5-di-*tert*-butylsalicyaldehyde (53.7g, 225mmol, 2eq) in EtOH (250ml) is then added in a slow stream over 30mins. The addition funnel was then rinsed with EtOH (50ml) and the mixture stirred at reflux for 2hrs, before heating is discontinued. Deionised water (150ml), was added and the stirred mixture cooled to 5°C over 2hrs and maintained at that temperature for another 1hr. The yellow solid is collected by vacuum filtration and washed with EtOH (100ml). After the solid was air dried, it was dissolved in methylene chloride (500ml). The organic solution was washed with water (2x300ml), followed by saturated aq NaCl (300ml). The organic layer was dried over Na_2SO_4 and filtered. The solvent was removed by rotary evaporation to yield the product as a yellow solid (mp=200°C). Yield 54g (88%). ^{1}H NMR (400MHz, $CDCl_3$): δ 13.60 [s, 2H, O*H*], 8.22 [s, 2H, NC*H*C], 7.22 [s, 2H of Ar], 6.90 [s, 2H of Ar], 3.25 [m, 2H, CH_2CH], 1.85 [m, 2H, CHC(*H*)H], 1.80 [m, 2H, CHCH(*H*)], 1.65 [m, 2H, CH_2CH(*H*)], 1.40 [m, 2H, CH_2C(*H*)H], 1.35 [s, 18H, CCH_3] and 1.15 [s, 18H, CCH_3]. ^{13}C NMR (100MHz, $CDCl_3$): δ 158, [*C* of Imine], 140 [*C* of Ar], 137 [*C* of Ar], 127 [*C* of Ar], 126 [*C* of Ar], 118 [*C* of Ar], 73 [*C*HN], 36 [*C* of Ar], 34 [*C*CH_3], 33 [*C*CH_3], 31 [*C*H_3], 30 [*C*H_3] and 25 [*C* of Ar]. Mass spectrum: molecular ion peak at *m/z* = 547.6 (calc. 546.8). IR (KBr disc, cm^{-1}): 3457, 2955, 2865, 1629, 1468, 1438, 1267, 1172, 1036, 876 and 825 [1, 2, 3].

N,N'-bis(salicylidine)-1,2-H$_4$ethylenediamine vanadium(IV) oxide – **(9)**

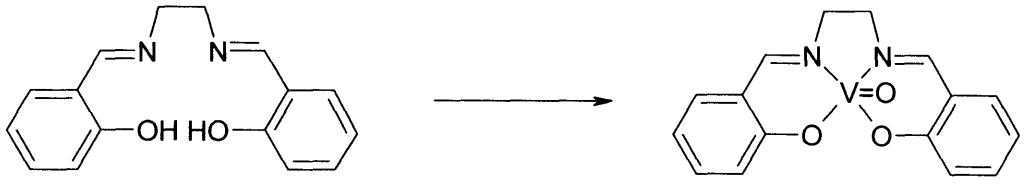

To a warm (70°C) solution of 1,2-diaminoethane (3.0 g, 50mmol) in ethanol (150 ml) was added salicylaldehyde (12.2 g, 100mmol) in one portion. The resulting yellow solution was stirred for 30 minutes at 70°C and allowed to cool. The resulting yellow precipitate (*N,N'*–ethylenebis-salicylideneamine) was filtered, air dried and re-dissolved in dichloromethane (100 ml). Excess $VOSO_4.H_2O$ (20 g) in water (150 ml) was added in one portion and the resulting two phase mixture was stirred vigorously

for 1 hour. The green dichloromethane layer was separated and dried ($MgSO_4$) and the solvent was removed to yield [$V^{IV}O$(salen)]. This material was recrystallised by evaporation of dichloromethane/ethanol solution to afford the desired product as deep green needles. Mass spectrum (APCI): molecular ion peak at *m/z* = 334 (calc. 333.0). IR (KBr disc, cm^{-1}): 3433, 2960, 2843, 1643, 1616, 1559, 1533, 1391,1261, 1169, 1086, 1024, 982 and 799. UV/Vis (MeCN, nm ($\varepsilon/dm^3mol^{-1}cm^{-1}$)): 626.0 and 333.6 (581.0).

N,N'-bis(salicylidine)-1,2-Cyclohexanediamine vanadium(IV) oxide – **(10)**

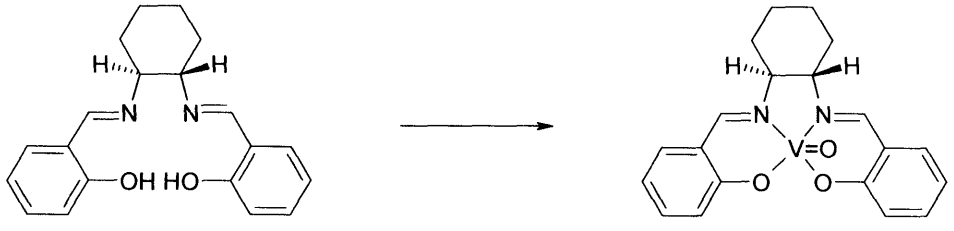

A warm solution (80 °C) of 1,2-cyclohexanediamine (3.00g, 11mmol) in ethanol (100ml) was added in one portion to a solution of salicylaldehyde (2.80g, 23mmol). The yellow solution was stirred for 1 hour at 80 °C and allowed to cool at room temperature over a further 2 hours. The resulting precipate was filtered, air dried and re-dissolved in dichloromethane (75ml). An excess of $VOSO_4.H_2O$ (20g) in water (150 ml) was added in one portion and the resulting homogeneous solution was stirred vigorously for 1 hour. The dark green dichloromethane layer was separated off, dried ($MgSO_4$) and solvent removed under vacuum. The solid was recrystallised in a warm mixture of dichloromethane and ethanol, affording the product as deep green needles. Yield =3.2g (87%). Mass spectrum: molecular ion peak at *m/z* = 388.4 (calc. 387.1). IR (KBr disc, cm^{-1}): 3410, 2935, 2853, 1615, 1492, 1458, 1421, 1312, 1272, 1147, 1091, 979, 840 and 755.

(R,R)-N,N'-bis(3,5-di-tert-butylsalicylidine)-1,2-cyclohexanediamino vanadium(IV) oxide – **(11)**

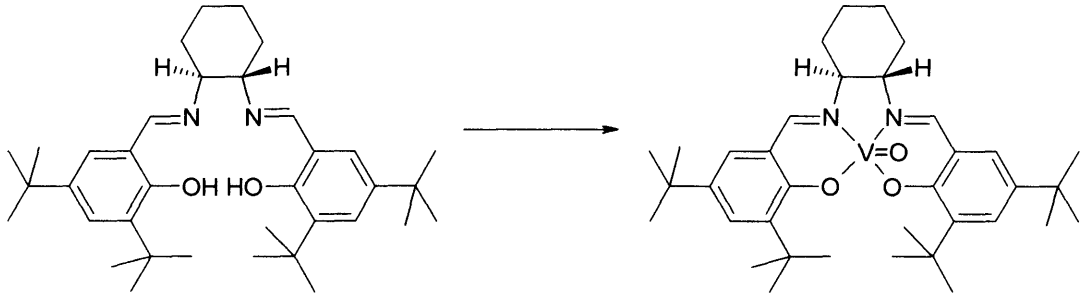

To a solution of (*R,R*)-*N,N'*-bis(3,5-di-*tert*-butylsalicylidine)-1,2-cyclohexanediamine (2.00g, 3.6mmol) in chloroform (50ml) and ethanol (20ml) was added an aqueous (10ml) solution of $VOSO_4.H_2O$ (0.65g, 4mmol) to produce a homogeneous solution. The mixture was stirred overnight. The solution was transferred to a separating funnel and chloroform (50ml) was added, the organic solution was washed with distilled water (2x20ml). The organic solution was dried ($MgSO_4$), filtered and the solvent removed by rotary evaporation to yield a green solid. The material was re-crystallised from a minimum amount of warm chloroform and ethanol. Yield 2.05g (92%). Mass spectrum: molecular ion peak at *m/z* = 612.5(calc. 611.7). IR (KBr disc, cm^{-1}): 3407, 2945, 2855, 1609, 1533, 1458, 1433, 1388, 1342, 1312, 1247, 1197, 1172, 1031, 981, 830 and 745. UV/Vis (MeCN, nm ($\varepsilon/dm^3mol^{-1}cm^{-1}$)): 625.0 and 376.1 (532.2).

(S, S)- N, N'-bis(3,5-di-tert-butylsalicylidene)-1,2-cyclohexane-diamino-vanadium (IV) oxide – **(12)**

This complex was prepared using the procedure described for (*R, R*)-[VO(**11**)] and had identical spectroscopic properties. *Anal. Calcd* for $C_{36}H_{52}N_2O_3V$ (M_r = 611.76): C, 70.7; H, 8.6: N, 4.6. Found: C, 70.4; H, 8.2; N, 4.2.

***N,N'-bis(3,5-di-tert-butylsalicylidene)-1,2-ethylenediamine vanadium (IV) oxide* – (13)**

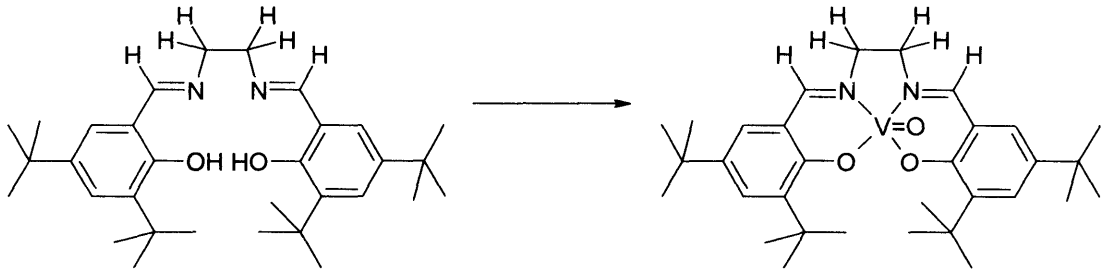

H_2**6** was converted to [VO(**13**)] using the procedure described for (*R, R*)-[VO(**11**)]. Mass spectrum: molecular ion peak at *m/z* = 558.4 (calc. 557.3). IR (KBr disc, cm^{-1}): 3427, 2959, 2856, 1628, 1476, 1434, 1270, 1150, 1041, 971, 840, and 775. UV/Vis (MeCN, nm ($\varepsilon/dm^3mol^{-1}cm^{-1}$)): 626.0 and 380.2 (525.0)

***N,N'-bis(3,5-di-tert-butylsalicylidine)-1,2-d_4-ethylenediamine vanadium (IV) oxide* – (14)**

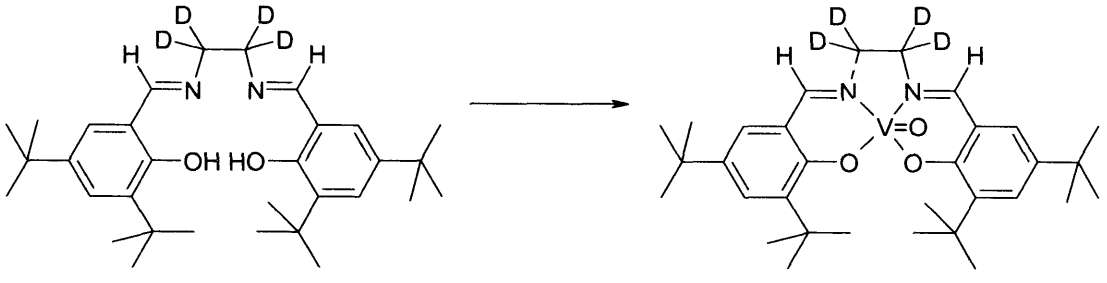

H_2**7** was converted to [VO(**14**)] using the procedure described for (*R, R*)-[VO(**11**)]. Mass spectrum: molecular ion peak at *m/z* = 558.4 (calc. 557.3). IR (KBr disc, cm^{-1}): 3281, 2960, 2868, 2843, 1652, 1616, 1559, 1533, 1464, 1436, 1412, 1391, 1361, 1321, 1269, 1249, 1227, 1199, 1133, 1086, 1024, 971, 930, 916, 893 and 736. UV/Vis (MeCN, nm ($\varepsilon/dm^3mol^{-1}cm^{-1}$)): 626.0 and 380.2 (525.0)

N,N'-bis(salicylidine)-1,2-d_4-ethylenediamine vanadium(IV) oxide – **(15)**

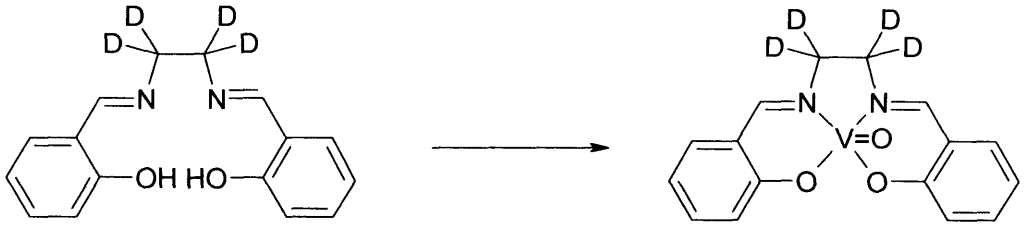

H_2**4** was converted to [VO(**15**)] using the procedure described for (*R*, *R*)-[VO(**11**)]. Mass spectrum: molecular ion peak at *m/z* = 334 (calc. 333.0). IR (KBr disc, cm^{-1}): 3433, 2960, 2843, 1643, 1616, 1559, 1533, 1391,1261, 1169, 1086, 1024, 982 and 799. UV/Vis (MeCN, nm (ε/$dm^3mol^{-1}cm^{-1}$)): 626.0 and 333.6 (581.0)

bis(acetylacetonato) – vanadium(IV) oxide - [V^{IV}=O(acac)$_2$] – **(16)**

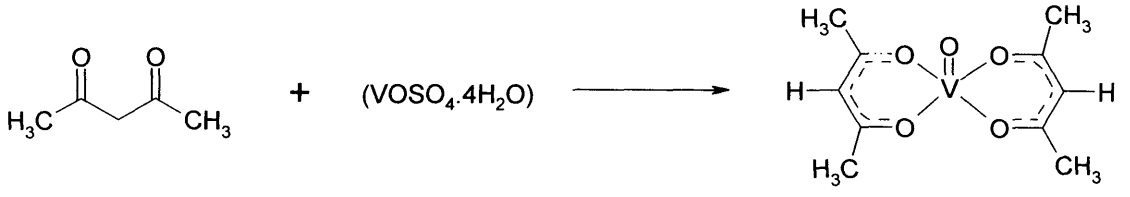

An excess of freshly distilled acetylacetone (pentane-2,5-dione, 5.01 g, 50 mmol) was added to a solution of $VOSO_4.4H_2O$ (4.70 g, 20 mmol) in deionised water (50 ml). The reaction was basified by the addition of small portions of sodium bicarbonate until CO_2 evolution ceased. The resulting green/blue precipitate was filtered and washed with portions of water (2 x 20 ml) and cold acetone (2 x 10 ml). The product was twice recrystallised from a minimum volume of boiling acetone to afford the required material as small lustrous green/blue prisms. Yield 3.55 g (67 %).

***bis(acetylacetonato)-vanadium(IV) oxide - [V^{IV}=O(acac)$_2$-d_2]* – (17)**

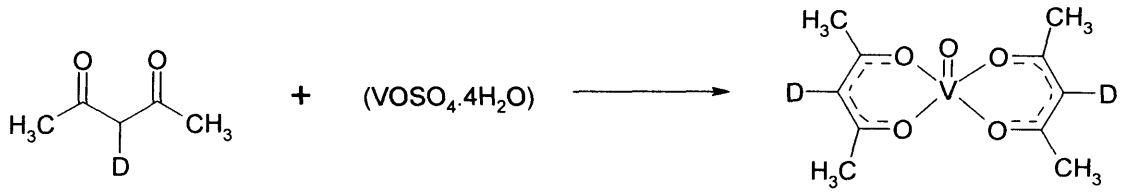

The partially deuterated material [V^{IV}=O (3-^{2}H-acac)$_2$] was prepared from 3,3-$^2H_2$-2,5-pentanedione prepared *in situ* by the addition of a catalytic quantity of triethylamine (0.1 ml) to acetylacetone (5 g) in D_2O (50 ml). The homogenous solution was stirred for 5 minutes before the addition of vanadyl acetate and sodium carbonate as described above. The work up was identical to that of [V^{IV}=O(acac)$_2$] Yield 3.05 g (58 %).

***(R,R)-N,N'-bis(3,5-di-tert-butylsalicylidine)-1,2-cyclohexanediamine copper(II)* – (18)**

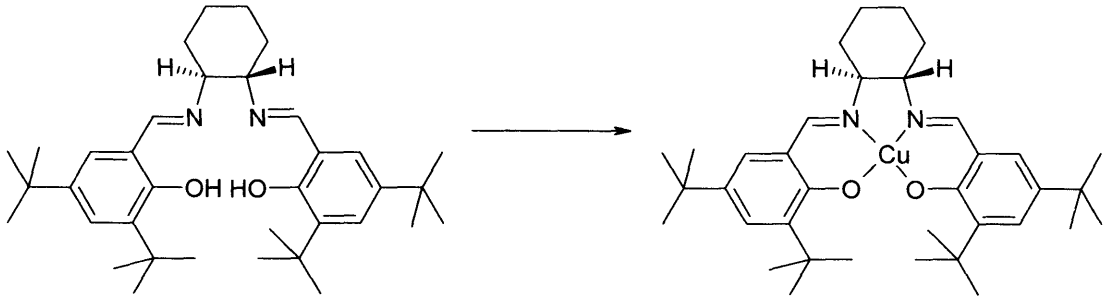

To a solution of (*R,R*)-*N,N'*-bis(3,5-di-*tert*-butylsalicylidine)-1,2-cyclohexanediamine (0.10g, 0.5 mmol) in toluene (20ml) heated at 110°C under an inert nitrogen flow, was added dropwise $Cu(OAc)_2.4H_2O$ (0.25g, 1 mmol) in ethanol (20ml). The yellow solution changed to a blue/grey precipitate over a 2 hour period. The mixture was stirred for a further 4 hours, after which the solvent was evaporated under reduced pressure. The solid was re-crystallised from warm ethanol and chloroform (20ml), affording the Cu(II) complex as a dark blue solid. Yield 1.00g (95%). Mass spectrum: molecular ion peak at m/z = 611.7 (calc. 610.3) . IR (KBr disc, cm^{-1}): 3337, 2956, 2367, 2360, 2355, 2358, 1622, 1525, 1480, 1346, 1253, 1201,

1182, 1167, 1073, 1024, 994, 973, 894, 878 and 788. UV/Vis (MeCN, nm(ε/dm^{3}mol^{-1})): 570 and 375 (447).

(R,R)-N,N'- bis(3,5-di-nitro-salicyaldehyde)-1,2-cyclohexanediamine – **(19)**

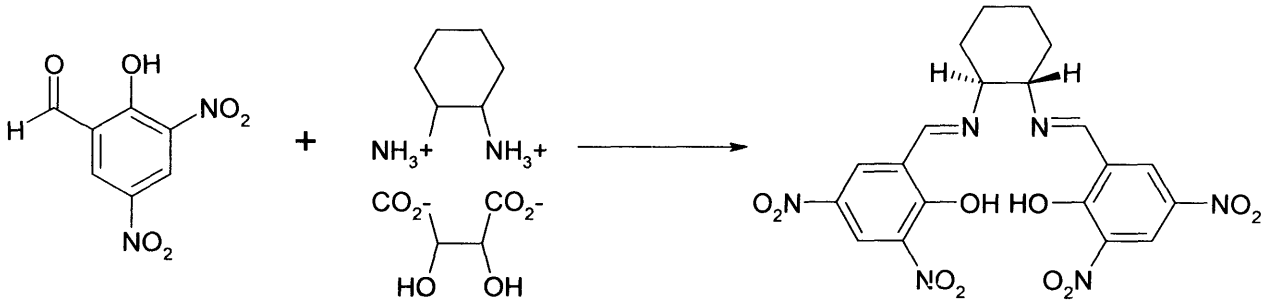

In a 50ml schlenk flask, (*R,R*)-1,2-diammonium cyclohexane (1.315g, 10mmol) was dissolved in ethanol (10ml). The solution was heated under reflux and a solution of 3,5-dinitro salicyaldehyde (2.12g, 20mmol) in ethanol (10ml) was added over a 30min period. After the reaction mixture was left to cool to room temperature. The crystalline product was collected and washed with ethanol (5ml) and diethyl ether (5ml), affording the product as an orange crystalline powder (mp=245^{0}C). Yield 1.25g (95%). ^{1}H NMR (400MHz, DMSO-d$_6$): δ 13.55 [s,2H,O*H*], 8.90 [s, 2H, NC*H*C], 8.75 [d, *J*=3.4 Hz, 2H of Ar], 8.70 [d, *J*=3.4 Hz, 2H of Ar], 4.25 [m, 2H, NC*H*C*H*N], 2.1-1.0 [m, 8H of cyclohexane]. ^{13}C NMR (100MHz, DMSO-d$_6$): δ 170 [C of Imine], 168 [C of Imine], 140 [C of Ar], 138 [C of Ar], 130 [C of Ar], 127 [C of Ar], 117 [C of Ar], 63 [*C*HN], 30 [C of Ar], 23 [C of Ar]. Mass spectrum: molecular ion peak at m/z = 503.5 (calc. 502.1) [4].

(R,R)-N,N'- bis(3,5-di-nitro-salicyaldehyde)-1,2-cyclohexanediamine copper(II) – **(20)**

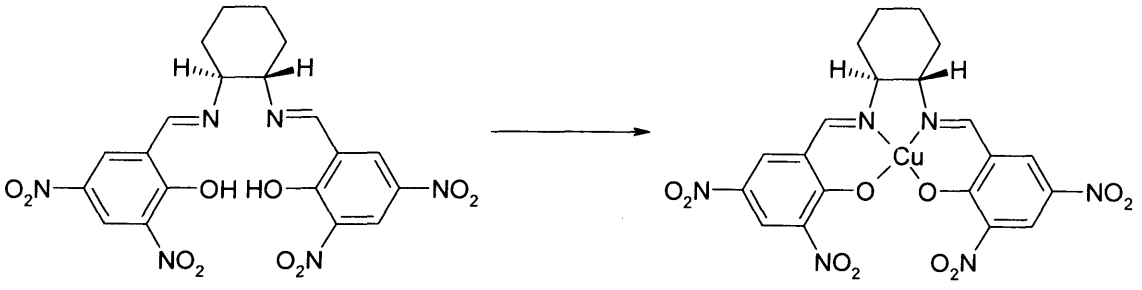

H_2**19** was converted to [Cu(**20**)] using the procedure described for (*R, R*)-[Cu(**18**)]. Yield 1.25g (95%). Mass spectrum: molecular ion peak at m/z = 567.5 (calc. 566.1). IR (KBr disc, cm^{-1}): 3111, 2956, 2889, 1703, 1615, 1571, 1483, 1340, 1296, 1230, 1119, 920, 765 and 677. UV/Vis (MeCN, nm (ε/$dm^3mol^{-1}cm^{-1}$)): 570 and 350 (540).

***(R,R)-N,N'-bis(5-nitro-salicylidene)-1,2-cyclohexanediamine* – (21)**

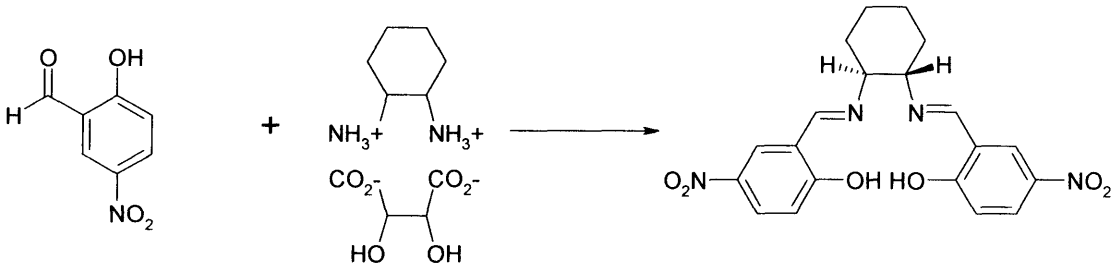

(*R,R*)-1,2-diammoniumcyclohexane (0.114g, 1mmol) was dissolved in ethanol (20ml). The solution was then heated to reflux (110°C) and a solution of 5-nitrosalicyaldehyde (0.366, 2mmol) in toluene was added dropwise over 30mins. The reaction was stirred for a further 2 hours at reflux. Following this, the solution precipitated out as a yellow solid and the mixture was allowed to cool to room temperature. The crystalline product was washed with ethanol (10 ml) and diethylether (5 ml), affording the product as a yellow crystalline solid. (mp=220°C). Yield 2.00g (95%). ^{1}H NMR (400MHz, $CDCl_3$): δ 14.3 [s,2H,O*H*], 8.36 [s, 2H, NC*H*C], 8.15-8.12 [m, 4H of Ar], 6.90 [d, 2H of Ar], 3.52-3.45 [m, 2H, NC*H*C*H*N], 2.1-1.5 [m, 8H of cyclohexane]. ^{13}C NMR (100MHz, $CDCl_3$): δ 167 [C of Imine], 163 [C of Imine], 139 [C of Ar], 130 [C of Ar], 127 [C of Ar], 118 [C of Ar], 71 [CHN], 33 [C of Ar], 24 [C of Ar] [4].

***(R,R)-N,N'-bis(5-nitro-salicylidene)-1,2-cyclohexanediamine copper(II)* – (22)**

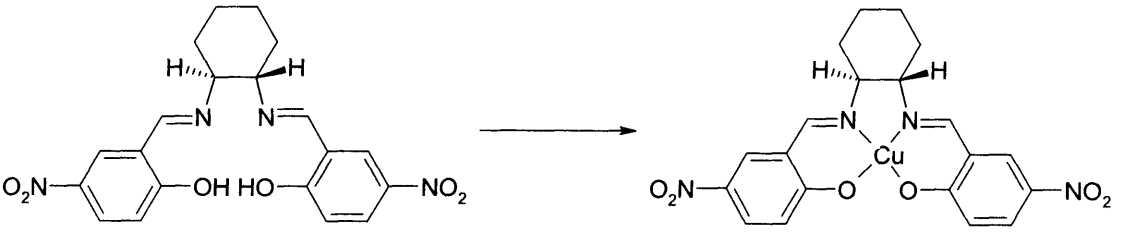

H_2**21** was converted to [Cu(**22**)] using the procedure described for (*R, R*)-[Cu(**18**)]. Yield 1.50g (97%). Mass spectrum: molecular ion peak at m/z = (calc.). IR (KBr disc, cm-1): 344, 2943, 1634, 1541, 1463, 1408, 1338, 1241, 1185, 1133, 1102, 1049, 937, 909, 837 and 778. UV/Vis (MeCN, nm (ε/$dm^3mol^{-1}cm^{-1}$)): 565 and 355 (540).

Propylene oxide – **(23)** was resolved by the method of Jacobsen [6] and the optical purity was determined to be greater than 98% as determined by chiral GC-MS analysis (Supelco, Beta Dex 120 capillary column, 30m x 0.25mm x 0.25 μm film thickness) of the thiophenol adducts, the preparation of which are detailed below.
(*R*)-2-hydroxypropane-1-phenylsulphide

To a stirred solution of thiophenol (0.20g, 2mmol) in ethanol (25ml) was added (*S*)-epoxypropane (0.10g, 1mmol) over 1 minute. A catalytic amount of triethylamine was added and the solution stirred overnight. All volatiles and solvent were removed under reduced pressure to yield the product as a white solid. Yield 0.14g (85%). ^{1}H NMR (400MHz, $CDCl_3$): δ 7.20 [m, 5H of Ar], 3.75 [m, 1H, C(OH)(*H*)], 3.05 [m, 1H, SC(H)(*H*)], 2.75 [m, 1H, SC(*H*)(H)], 2.35 [br s, 1H, O*H*] and 1.20 [d, 3H, CH_3]. ^{13}C NMR (100MHz, $CDCl_3$): δ 130 [*C* of Ar], 129 [*C* of Ar], 128 [*C* of Ar], 127 [*C* of Ar], 126 [*C* of Ar], 65 [COH], 43 [CH_2S] and 22 [CH_3]. Mass spectrum: molecular ion peak at *m/z* = 151.0 (calc. 151.2 for M-OH). IR (KBr disc, cm^{-1}): 3407, 3056, 2955, 1634, 1573, 1473, 1433, 1383, 1071, 1061, 735 and 685 [6].

(S)-2-hydroxypropane-1-phenylsulphide

This material was prepared in a similar manner to that of (*R*)-2-hydroxypropane-1-phenylsulphide using thiophenol (0.20g, 2mmol) and (*R*)-epoxypropane (0.10g, 1mmol). Yield 0.13g (79%). Spectroscopic data for this material was exactly the same as that of (*R*)-2-hydroxypropane-1-phenylsulphide [6].

In all synthetic procedures, both R,R and S,S enantiomers gave exactly the same spectroscopic data. This held true for racemic mixtures of the complexes.

3.2 Manipulation of air-sensitive compounds

Due to the structural sensitivity of the ligands and complexes to an oxygen atmosphere, it was necessary for the synthesis and manipulation to be carried out under a atmosphere of inert gas (argon or nitrogen), with the exclusion of oxygen and moisture from the sample. One such method employed, was the use of a standard Schlenk line technique and was needed in the handling of the majority of the compounds prepared here.

3.2.1 *Inert atmosphere techniques*

The exclusion of oxygen/air using an inert gas such as nitrogen or argon is one of the most common methods for the manipulation of air sensitive compounds. The method utilised in this work is the Schlenk line technique, providing a suitable means for performing inert atmosphere reactions on the bench, through the use of specially designed equipment, ie., Erlenmeyer attachments, etc. The Schlenk line used throughout the manipulation, provided an inert atmosphere under which solids and liquids could be reacted and transferred, whilst still in an inert gas atmosphere. The Schlenk line used was a Pyrex glass cylindrical tube, featuring a number of two-way stopcocks, providing a "junction" by which the inert gas could be changed to a vacuum and vise-versa. To maintain the vacuum, all joints were sealed with grease "Dow Corning High Vacuum grease" which was applied sparingly. The experimental apparatus was attached to the line via, thick walled rubber tubing, so that a number of manipulations could be carried out at once.

A mechanical rotary pump was used to create the vacuum, in conjunction with a liquid nitrogen cooled trap to collect volatiles and prevent contamination of the pump. The inert gas (commonly nitrogen) was introduced into the apparatus from a cylinder and then through a molecular sieve column to remove moisture. The amount of nitrogen used was monitored by use of a mercury bubbler and also to prevent excessive pressure. Inert atmosphere technique was achieved using the "Pump and Fill" method, which involves the evacuation of the glassware, immediately followed by purging with inert gas. This evacuation and purging is repeated several times, to maximise an oxygen free atmosphere. Solutions were transferred between Schlenk line apparatus by the use of syringes and cannulae, through rubber septas.

3.3 Experimental conditions

All reactions were carried out under an inert argon atmosphere, employing standard Shlenk line techniques. Solvents were purified by standard methods, ie., dichloromethane was distilled from CaH_2. All commercially available reagents were used as received from Aldrich/Fluka. UV/Vis spectra were measured using a Lambda 800/900 Perkin-Elmer spectrometer and a Jasco V-570 UV/Vis/NIR spectrometer. GC analysis were performed on a Perkin-Elmer 8700 series instrument (column: Supleco- BETA DEX^{TM} 120 fused silica capillary, 30m x 0.25mm x 0.25μm film thickness, chiral- permethylated β-cyclodextrin column). Infra-red measurements were performed on a Jasco FT/IR-660 and nuclear magnetic resonance spectra were recorded on a Bruker DPX-400 (400 MHz) spectrometer, with automated sampler. APCI/EI Mass spectra were recorded with a Fisons Platform II mass spectrometer.

3.3.1 *EPR and Electron Nuclear Double Resonance (ENDOR) experimental*

The X- and Q-band EPR and ENDOR spectra were recorded on a cw *Bruker ESP 300E* series spectrometer equipped with an ESP360 DICE ENDOR unit, operating at 12.5 kHz field modulation. The X-band EPR/ENDOR measurements were performed in a Bruker EN801 ENDOR cavity, while the Q-band EPR/ENDOR measurements were performed in a Bruker ER5106QT resonator. The ENDOR spectra were obtained at 10K using 8 dB RF power from an ENI A-300 RF amplifier, with 50 kHz RF modulation depth and 200μW power at X-band, and using 12 dB RF power from a *3200L* RF amplifier, 250 kHz RF modulation depth and 150μW power at Q-band. Accurate g values were obtained using a Bruker ER 035 M NMR Gaussmeter calibrated using the perylene radical cation in conc. H_2SO_4, g = 2.002569. Accurate frequencies at Q-band were determined using a Agilent 53152A frequency counter.

Figure 3.1 shows a digital photograph taken of the EPR/ENDOR spectrometer and low temperature Q-band resonator (35 GHz)- ER 5016 Qt-E (Figure 3.2).

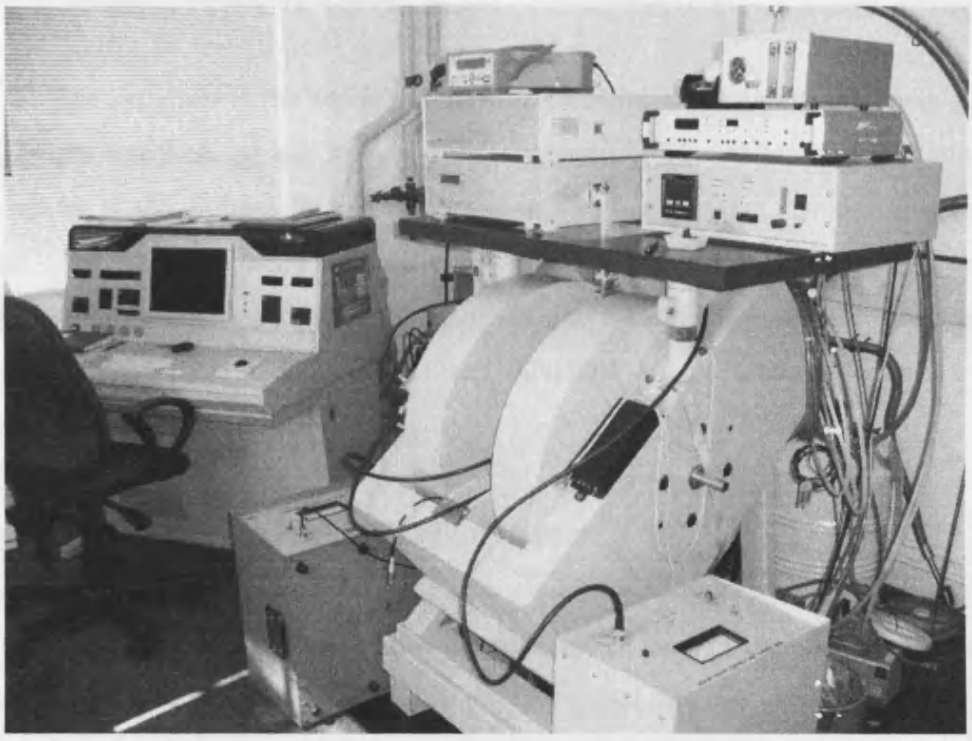

Figure 3.1: EPR/ENDOR spectrometer (Bruker ESP 300E).

Figure 3.2: Q-band resonator (ER 5106 QT-E).

3.3.2 *Initial ENDOR simulation setup*

The program is run using a *X*-terminal emulation program, which is standard and is pre-installed on all Redhat Linux systems. The *rhdat* or *axdat* program, depending if the system is axial or rhombic, may be started using the command, *rhdat*. A data or menu option can be selected by simply pressing the key corresponding to the required highlighted option. The program is split into a number of sub-shells, where EPR, spectral and ENDOR values may be edited and are explained as follows:

Electron Paramagnetic Resonance (EPR) menu

This menu contains the electronic parameters, such as the g values ($g_{\|}$ and $g_{\perp}$) and hyperfine coupling constant values. The nuclei entered into this menu should only be those that have resolved hyperfine splitting in the EPR spectrum. If a nuclei contributes to the powder ENDOR spectrum, it needs to be entered again in the ENDOR menu.

Electron Nuclear Double Resonance (ENDOR) menu

The parameters contained in this menu, are for nuclei that contribute to the ENDOR spectrum. In the absence of quadrupolar (spin > ½) effects, the ENDORspectrum is not dependent upon the value of the nuclear spin; hence this parameter does not appear in the ENDOR menu. Nuclear g values, ie., ^{1}H = 5.5856910, were obtained from the Bruker Almanac.

Euler angles: These angles define the orientation of the local hyperfine tensor for the nucleus with respect to the g frame (as this is a Rhombic EPR program, the EPR hyperfine axes must be coincident with the g axes).

The angle Alpha is equivalent to the angle phi in a polar coordinate system (phi = 0, along the x-axis). However, because of the transformation used, the value entered for the alpha must be (phi + 90°), ie., Phi is usually measured from g1 and an angle of 90° for beta transforms g_z into g_y , hence the 90° to bring g_y onto g_x.The

second angle, Theta , is exactly equivalent to the angle theta in the polar coordinate g frame, ie., the angle between the z direction and the x, y plane. Finally, the third angle, Gamma, is a "twist" angle and rotates the local nuclear hyperfine tensor around the local z direction, ie., around the metal-nuclear direction. This parameter only has meaning if the nucleus has a rhombic hyperfine tensor. In the majority of cases, the nucleus has an axial tensor and this value may be set to zero.

Hyperfine standard distribution: This parameter is to allow for the fact that a nucleus may have a range of positions from the central metal atom. This in turn allows a normal distribution in the dipolar component of the hyperfine coupling (based on the assumption that the isotropic coupling remains constant). Such an effect, will broaden the outermost features of the ENDOR spectrum more than the inner features and this is observed for water ligands. This parameter should be used qualitatively, it is not based on real physics such as energy minimisation.

Spectral parameters menu

Theta Integration Menu: This sub menu is primarily composed of three parameters. Theta refers to the polar coordinate, theta value is used for the integration and is the angle between the z direction and the x, y plane. The *range* parameter in the menu, sets the range that the program integrates over to produce the spectrum. This depends mainly on the symmetry of the problem. The *increment* that needs to be set is dependent upon the size of the hyperfine couplings of the EPR and ENDOR linewidths; the smaller the increment, the longer the calculation will take to run. A value of 0.015 degrees is chosen for ENDOR simulation, however, in the initial stages of simulation, larger increment values are chosen to speed computational calculations. If the value is too large, then artefactual extra features will appear in the spectrum, so this value must be reduced periodically to check that the simulated spectrum remains unchanged.

The programs mentioned here can be used to simulate the ENDOR spectrum of a powder (polycrystalline) sample, ie., transion metal complexes, such as vanadyl VO^{2+} and Copper Cu^{2+} systems. It is imperative that a systematic approach is undertaken when carrying out these simulations as a good fit, does not necessarily

mean a correct fit. Therefore, other companion programs are employed to aid simulation. Such programs like *Rhdist2(Rhdist)* and *Axdist2(Axdist)*, using the point dipole approximation, calculate the distances to a single "electron" for the ENDOR nuclei. Another companion program, *Mspin*, enables the calculation of a hyperfine matrix for a nucleus coupled to an unpaired electron (which is delocalised across one or more nuclei) and calculates the distances to that nucleus. These programs in turn help facilitate a successful powder ENDOR simulation, allowing accurate hyperfine matrix values to be extracted from the experimental ENDOR spectrum.

3.4 Gas chromatography

Gas chromatography, specifically gas-liquid chromatography, involves a sample being vapourised and injected onto the head of the chromatographic column. The sample is transported through the column by the flow of an inert, gaseous mobile phase. The column itself contains a liquid stationary phase which is adsorbed onto the surface of an inert solid.

3.4.1 *Instrumental components*

3.4.1.1 *Carrier gas*

The carrier gas must be chemically inert. Commonly used gases include nitrogen, helium, argon, and carbon dioxide. The choice of carrier gas is often dependant upon the type of detector which is used. The carrier gas system also contains a molecular sieve to remove water and other impurities, ie., molecular zeolites.

3.4.1.2 *Sample injection port*

For optimum column efficiency, the sample should not be too large, and should be introduced onto the column as a "plug" of vapour - slow injection of large samples causes band broadening and loss of resolution. The most common injection method is where a microsyringe is used to inject sample through a rubber septum into a flash vapouriser port at the head of the column. In this study, due to the volatile nature of the compounds (epoxides – (**24**)), a start temperature of 30-34oC was used and then

the temperature was ramped up. For packed columns, sample size ranges from tenths of a microlitre up to 20 microlitres. With respect to capillary columns, these need much less sample, typically around 10^{-3}ml. For capillary gas chromatography, split/splitless injection is used.

The injector can be used in one of two modes; split or splitless. The injector contains a heated chamber containing a glass liner into which the sample is injected through the septum. The carrier gas enters the chamber and can leave by three routes (when the injector is in split mode). The sample vapourises to form a mixture of carrier gas, vapourised solvent and vapourised solutes. A proportion of this mixture passes onto the column, but most exits through the split outlet. The septum purge outlet prevents septum bleed components from entering the column. The advantages associated with the split on include enhanced peak resolution

3.4.1.3 *Detectors*

There are many detectors which can be used in gas chromatography. Different detectors will give different types of selectivity. A non-selective detector responds to all compounds except the carrier gas, a selective detector responds to a range of compounds with a common physical or chemical property and a specific detector responds to a single chemical compound

3.5 References

[1] (*R,R*)-N,N'-Bis(3,5-di-tert-butylsalicylidene)-1,2-cyclohexanediamino manganese (III) chloride. A Highly Enantioselective Epoxidation Catalyst, *Organic Synthesis.*, **75**, 1.

[2] G. Pozzi, M. Cavazzini, F. Cinato, F. Montanari, S. Quici, *Eur. J. Org. Chem.*, 1999, 1947.

[3] M. Cavazzini, A. Manfredi, F. Montanari, S. Quici, G. Pozzi, *Eur. J. Org. Chem.*, 2001, 4639.

[4] X. Yao, M. Qiu, W. Lü, H. Chen, Z. Zheng, *Tetrahedron: Asymmetry*, 2001, **12**, 197.

[5] M. Cavazzini, S. Quici, G. Pozzi, *Tetrahedron*, 2002, **42**.

[6] M. Tokunaga, J.F. Larrow, F. Kakiuchi, E.N. Jacobsen, *Science*, 1997, **277**, 936.

Chapter 4

Conformational changes of a bis(acetylacetonato) oxovanadium(IV) complex-[V^{IV}=O(acac)$_2$] in coordinating and non-coordinating solvents

Conformational changes of a bis(acetylacetonato)oxovanadium(IV) complex - $VO(acac)_2$ in coordinating and non-coordinating solvents

4.1 Introduction

The vanadyl ion (VO^{2+}) has been widely used as a molecular probe to investigate the interactions between metal complexes and target molecules of chemical and biological interest [1,2,3,4]. Numerous examples exist where the ion has successfully been employed as an effective paramagnetic substitute for divalent metal ions in metalloproteins and metalloenzymes [5,6]. By comparison, there are fewer cases where the ion has been used as a probe to study the interactions occurring in paramagnetic coordination compounds and between homogeneous catalysts and their substrates [7]. In the latter case, the specific conformations and structure adopted by the ligands in solution, are crucial to the transfer of stereochemical information from the active metal complex to a reaction substrate. To understand how these processes occur in solution, it is necessary to elucidate the detailed molecular structure and geometry of the metal ligand complexes themselves.

By replacing the metal binding site of a homogeneous catalyst with the vanadyl ion, the structure of the complex in frozen solution can be explored using Electron Magnetic Resonance techniques. Electron Paramagnetic Resonance (EPR) offers limited insight into the nature of the ligands binding *trans* to the V=O group or the geometry of the ligands themselves, because the ligand superhyperfine splittings are unresolved [8]. However, electron-nuclear double resonance (ENDOR) can provide far greater detail on the weak couplings between the electron spin of the transition metal ion and the ligand nuclei [9]. In this way, information on the spatial arrangement of the ligand nuclei in the catalyst and the substrates can, in principle, be determined.

In order to interpret and extract the valuable information from the powder ENDOR spectra, and subsequently translate this into a meaningful geometric description of the metal complex-ligand interactions in solution, an ENDOR simulation program has been developed based on the resonance expression of Hurst *et al.* [10]. The effects of EPR linewidth on the ENDOR spectrum and hyperfine enhancement [11] are incorporated into the program. A broadening mechanism is included for ligands such as water. The structural parameters obtained from the

ENDOR experiments can then be compared to the theoretical models obtained through DFT calculations [12]. In the current chapter, the complimentary information provided by the two techniques will be demonstrated, by examining the structure and conformation of the simple bis(acetylacetonato)oxovanadium(IV) complex-(**16**) in the presence of both coordinating and non coordinating solvents. The ENDOR analysis of this complex in frozen solution has been reported previously [13,14,15]. Nevertheless the precise determination of the complete coupling matrix for the C-H protons has never been conclusively achieved. More importantly, in the presence of strongly coordinating ligands such as pyridine, uncertainty remains about the absolute conformation adopted by the metal complex and ligand in frozen solution [13], and whether the incoming ligand occupies a position *cis*- or *trans*- to the oxo group [16,17]. The consensus in the literature, however, suggests that the incoming ligand coordinates *trans* to the oxo group in the case of neutral oxygen donors [17]. Although pyridine can occupy an axial (*trans* isomer, Scheme 1) or equatorial position (*cis* isomer, Scheme 1), it was reported that the EPR and ENDOR data indicated the presence of only a single species with pyridine as added base [16].

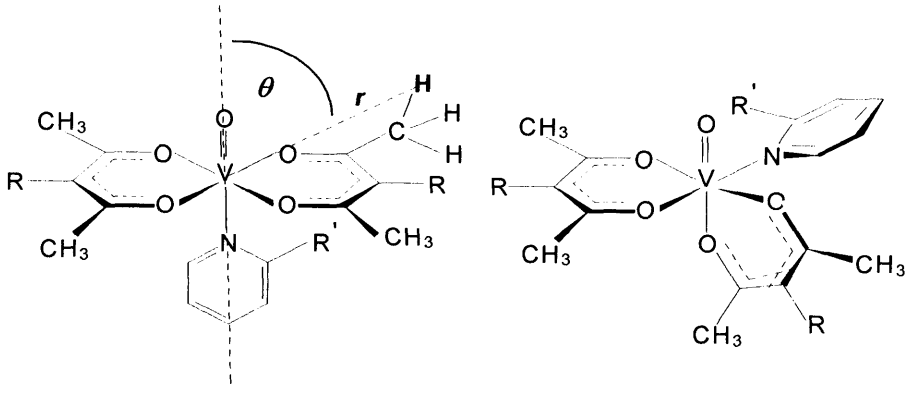

Scheme 1

If an equilibrium existed between the two isomers with a low energy barrier, then both species should be present in solution. In this Chapter ENDOR will be used to discriminate between the two possible isomers, and thereby determine the actual distribution ratios between the *cis* and *trans* isomers in a coordinating solvent.

4.2 Experimental

4.2.1 *Measurement and analysis of EPR / ENDOR spectra*

For EPR/ENDOR measurements a small quantity (*ca.* 10 mg) of the appropriate complex [VO-(**16,** R=H) or VO-(**17,** R=D)] was dissolved in the non-coordinating (dichloromethane) or coordinating solvents (pyridine or 2-picoline). A small amount of deuterated toluene was added to improve the quality of the glass in the frozen solution. All deuterated solvents, including dichloromethane, (CD_2Cl_2), pyridine (C_5D_5N, hereafter abbreviated to Py-d_5), 2-picoline (C_6D_8N, hereafter abbreviated to Pc-d_8) and toluene (C_7D_8), were obtained from *Fluorochem* in sealed ampoules. The solvents were used without further purification. However, they were found to contain small traces of water, which was detected in the ENDOR spectrum.

The EPR/ENDOR spectra were recorded on a CW X-band *Bruker ESP 300E* series spectrometer equipped with an ESP360 DICE ENDOR unit, operating at 12.5 kHz field modulation in a Bruker EN 801 cavity. All spectra (EPR and ENDOR) were recorded at 10 K; the ENDOR spectra were obtained using 8 dB RF power from a ENI A-300 RF amplifier and 50 kHz RF modulation depth. Accurate g values were obtained using a Bruker ER 035 M NMR Gaussmeter calibrated using the perylene radical cation in conc. H_2SO_4, g = 2.002569.

Accurate spin Hamiltonian parameters for the EPR spectra were obtained by computer simulation (*Simfonia*) and the results are presented in Table 4.1. The ENDOR spectra were simulated using an in house programme based on the resonance expressions of Hurst *et al* [10]. Analysis of the A tensors enabled dipolar hyperfine coupling constants to be extracted and using the point dipole approximation, the distance between the unpaired electron and the interacting nuclei was calculated.

4.2.2 *DFT calculations*

The complexes were optimised using gradient corrected density functional theory (DFT) with the exchange and correlation functionals due to Becke [18] and Lee, Yang and Parr (BLYP) [19] respectively, in the program ADF [20]. ADF employs Slater type orbitals as basis functions and for all the calculations presented here a basis set of triple zeta quality with polarisation functions for each atom except

vanadium (ADF level IV basis set), was used. The core orbitals for each atom are frozen during the calculations, with the V core being composed of all orbitals up to and including 2p and second row atoms have the 1s shell frozen. Vanadium is formally in the +4 oxidation state (d^1) and so the electronic structure was modelled assuming a doublet ground state and a charge neutral complex.

4.3 Results and Discussion

4.3.1 *EPR analysis of $VO(acac)_2$ in coordinating and non-coordinating solvents*

The EPR spectra of the frozen solution [$VO^{IV}(acac)_2$-(**16**)] in CD_2Cl_2, Py-d_5 or Pc-d_8 produced similar spectra typical of the d^1 VO^{2+} system (Figure 4.1). The accurate spin Hamiltonian parameters for each spectra were determined by computer simulation. The simulated spectrum and angular dependencies of $VO(acac)_2$-(**16**) in CD_2Cl_2 is shown in Figure 4.2 and the results are presented in Table 4.1. After analysis of the angular dependencies of the hyperfine lines, the ^1H ENDOR spectra were measured at a static magnetic field corresponding to the -7/2 parallel and -3/2 perpendicular EPR absorption features (ie., a position where the x and y features are equivalent at this magnetic field: see angular dependency plot in Figure 4.2). In the frozen solution the VO^{2+} ion has a pseudo-axially symmetric g matrix and exhibits eight parallel and eight perpendicular absorption lines. In this case the EPR spectra of the vanadyl complex (**16**) was measured in non-coordinating (CD_2Cl_2) and coordinating (Py-d_5, Pc-d_8) solvents. All three EPR spectra when simulated gave identical g_{iso} values and subtle changes between the A_{iso} values of the non-coordinating (CD_2Cl_2) and coordinating solvents.

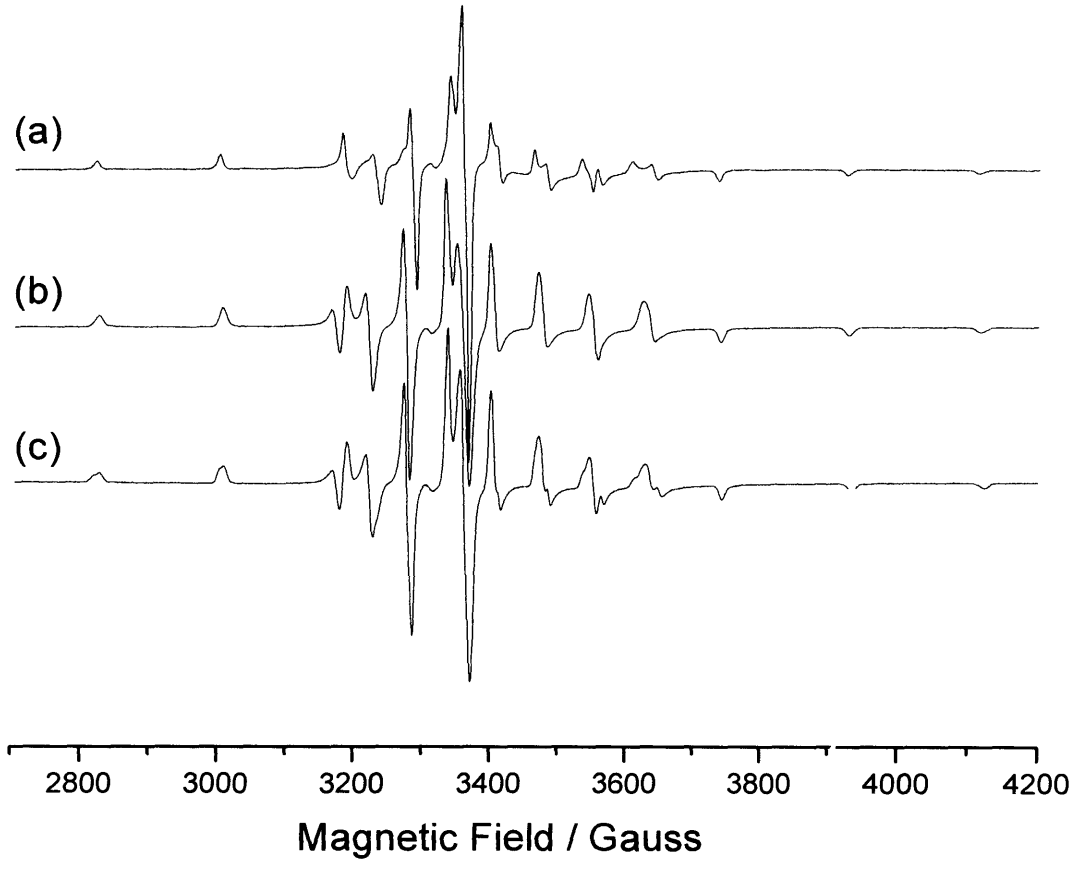

Figure 4.1: X-band EPR spectrum of [VO(acac)$_2$-(**16**)] in (a) CD_2Cl_2, (b) Pyridine–d_5 and (c) 2-Picoline–d_8. EPR spectra recorded with a microwave power of 2.02 mW at 10 K.

In this way, because of the almost pure axial nature of the system, the molecular z-axis coincident with the V=O bond is oriented parallel or perpendicular, respectively, to the static magnetic field. The corresponding ENDOR spectra will hereafter be labelled "Parallel" or "Perpendicular".

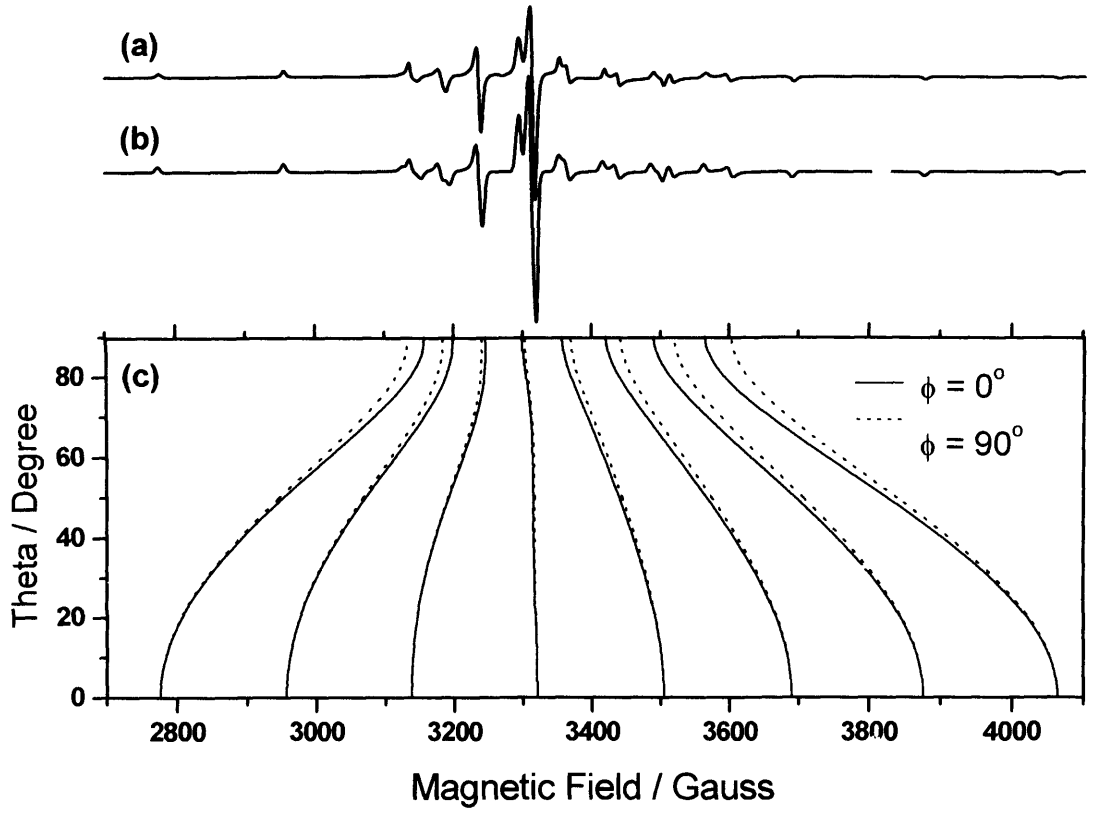

Figure 4.2: X-band EPR spectrum of [VO(acac)$_2$-(**16**)] in CD_2Cl_2 / toluene-d_8 recorded with a microwave power of 2.02 mW at 10 K. (a) Experimental spectrum; (b) simulated spectrum and (c) angular dependencies

Table 4.1: Spin Hamiltonian parameters for the bis(acetylacetonato)oxovanadium (IV) complex – (**16**) in frozen solutions of deuterated dichloromethane (CD_2Cl_2), pyridine (C_5D_5N) and 2-picoline (C_6D_8N). A small amount of deuterated toluene (C_7D_8) was added in each case to improve the quality of the glass.

Solvent	g_1	g_2	g_3	g_{iso}	A_1 / MHz	A_2 / MHz	A_3 / MHz	A_{iso} / MHz
CD_2Cl_2	1.978	1.974	1.948	1.967	163.6	182.8	501.7	282.7
Pyridine -d^5	1.979	1.978	1.944	1.967	178.2	186.1	503.1	289.1
2-Picoline - d^8	1.979	1.978	1.944	1.967	178.2	186.1	503.1	289.1

4.3.2 *ENDOR and DFT analysis of [VO(acac)$_2$-(16)] in non-coordinating solvent (CD_2Cl_2)*

Simulation of the ENDOR spectra was facilitated by deuterating the C-H protons in both of the acac ligands (Scheme 1, R = D [VO(**17**)]) thus providing ENDOR spectra comprising solely of the methyl protons. A careful subtraction of these spectra from the appropriate spectra of the protic [VO(acac)$_2$-(**16**)] resulted in the ENDOR spectra of the acac CH groups alone; the CH spectra and the methyl spectra could thus be simulated separately. The parameters from the separate simulations were then combined to provide a simulation of the complete protic system. Vanadium - proton distances were calculated from the hyperfine matrices using the point dipole approximation [9].

It should be clearly stated that the hyperfine couplings to the protons were found to be almost purely dipolar in nature and the Fermi contact term was negligible in each case. It should also be noted that the point dipole approximation used in the work is a valid assumption as the electron in the d^1 VO system is localised almost completely on the vanadium ion. The V=O direction is used to define the angle θ between the z axis of the system and the direction of the interacting proton (see scheme 1). Due to the high symmetry of the EPR system, the ENDOR experiment only sees angles of θ in the range 0-90°, hence an actual angle of 100° would correspond to an observed angle of 80° in ENDOR.

Tables 4.3 - 4.7 present the results from DFT and ENDOR on the distance between the unpaired electron and the interacting proton (VO...H distance). The simulations were performed using the minimum number of methyl protons for an acceptable fit as the methyl groups might be expected to adopt a variety of conformations or be freely rotating. In the [V^{IV}=O(acac)$_2$ – (**16**)]... CD_2Cl_2 situation, the resolution of the ENDOR was sufficiently good to distinguish six distinct sets of couplings from the four methyl groups. In the case of [V^{IV}=O(acac)$_2$(C_5D_5N)] the resolution was less good. As a result only the average couplings from the four methyls are observed in the ENDOR spectra because of the lower resolution, while DFT reveals all the individual VO...H distances.

For comparison with the ENDOR results, a series of theoretical calculations on the basic [VO(acac)$_2$–(**16**)] complex in its alternative isomers with and without

adduct molecules present were also conducted. In the optimised structure of the simple complex, the expected C_{2v} symmetry of the system is almost perfectly maintained although no symmetry constraints were used in any of the calculations. Table 4.2 shows the calculated energies for each complex with different added ligands.

In the case of dichloromethane (CD_2Cl_2), the *trans* structure has a slightly higher energy (6.9 $KJmol^{-1}$) compared to the *cis* structure, and a dihedral twist angle of 23.7^0 is observed (ie., the twist angle of one of the *acac* moieties). In other words the classic square based pyramidal structure for [$VO(acac)_2$-(**16**)] is found, as indeed observed through simulation of the ENDOR spectra, as the experimental spectrum was fitted using the proton coordinates of the non-coordinating CD_2Cl_2 solvent. A small difference in energy occurs in the Pyridine (Py) adduct which favours the equilibrium position of the donor. In other words a 50:50 mixture of the two isomers is predicted by DFT, again in excellent agreement to ENDOR studies. Furthermore a similar case occurs with 2-Picoline (Pc).

Table 4.2: DFT comparison between the relative energies of added ligands, adopting different conformations.

Added Ligand	confomer	Energy ($kJmol^{-1}$)	Rel. Energy ($kJmol^{-1}$)	X...V (Å)
None	*Axial*	-17195.82	0	
	Equatorial	-17188.93	6.9	
Pyridine	*Axial*	-23715.19	0	2.61
	Equatorial	-23717.75	-2.6	2.25
2-Picoline	*Axial*	-25238.28	0	2.85
	Equatorial	-25232.45	5.8	2.34

The ^1H ENDOR spectrum of [$VO(acac)_2$-(**16**)] in CD_2Cl_2 is shown in Figure 4.3, along with the associated computer simulations. Using deuterated solvent, only the protons present on the acetylacetonato ligand will contribute to the ENDOR spectrum (ie., the added complexities of the couplings arising from the solvent are therefore avoided). The spectra are particularly well resolved, so that subtle differences in the in-equivalencies of the different sets of protons are revealed. The ^1H ENDOR spectra were satisfactorily simulated based on the presence of two principle

sets of couplings, arising from the C-H protons and the methyl protons of the ligand. By analysis of the ^{1}H superhyperfine coupling tensors, the distances between the unpaired electron and the protons were calculated using the point dipole approximation and the results are presented in Table 4.3. Traces of coordinated water (present as a contaminant in the system) could also be observed (labelled by *) and is responsible for the large coupling in the parallel spectrum (Figure 4.3a) with additional features in the perpendicular spectrum; this assignment was made by comparison with data obtained from a sample of $VOSO_4$ in aqueous solution.

In the DFT calculations, it was assumed that solvent affects and the influence of the H_2O contaminant could be ignored in determining the structure of the vanadyl ion, therefore optimisation of the DFT parameters for the simple isolated complex was undertaken. The resulting complex is shown in Figure 4.4 and although symmetry restrictions were not imposed, the structure conforms to the C_{2v} point group. In addition to the expected square pyramidal geometry, a DFT calculation was carried out with the vacant site initially *cis* to the vanadyl oxygen atom. Upon optimisation this structure changed considerably, moving toward the square pyramidal geometry. At the end of the optimisation the torsion angle defined using the four co-ordinating oxygen atoms had changed from 90° to just 24° indicating that the *cis* arrangement, with no additional ligand present, is energetically unfavourable. The final distorted square pyrimidal structure had a calculated energy 7 $kJmol^{-1}$ higher than the symmetric planar configuration.

The full set of VO...H distances and angles from the low energy square pyramidal structure are shown in Table 4.3, and a good correlation can be found between the calculated (DFT) and experimental (ENDOR) distances. In particular, the VO...C-H distances were determined as ~4.49Å and ~4.41 - 4.40Å respectively by DFT and by ENDOR. The methyl protons show similar agreement with the range of values for VO...CH_3 being 4.60 – 5.18Å from DFT and 4.32 – 5.09Å from ENDOR measurements. These results suggest a small, systematic, overestimation of interatomic distances. The symmetry of the DFT optimised structure also appears higher than that from the ENDOR spectra. For example, the four methyl groups give identical VO...CH_3 distances from the calculations but six distances are distinguished experimentally. These small differences are likely to arise from the weak interactions which occur between the water contaminant detected by ENDOR and from weak dichloromethane...[$VO(acac)_2$-(**16**)] interactions which were not considered in the

DFT analysis. The pyramidal structure of the complex results in most of the VO...H angles measured from the DFT model being greater that 90°. However the ENDOR simulation can only distinguish the angle made between the VO...H vector and the line of the V-O axis, so will always give the smaller angle below 90°. For comparison a second column for the DFT results, quoting the angle expected in the ENDOR simulation, have been inserted into Table 4.3.

Previous ENDOR studies [13] have reported that the square pyramidal structure of $[V^{IV}=O(acac)_2$-(**16**)] is retained in $CHCl_3$ solution, but one $CHCl_3$ molecule was found to hydrogen bond to an oxygen atom of the acetylacetonato ligand while a second molecule was weakly coordinated along the symmetry axis (V=O) *via* a hydrogen bond with the V=O oxygen atom. These weak outer sphere solvent interactions are likely to occur with CD_2Cl_2 and may be responsible for the subtle perturbation of the complex as evidenced by the smaller VO...CH distances of ~4.42Å determined by ENDOR and the larger number of distinct VO...CH_3 distances resolved experimentally. Despite these small discrepancies, it is clear that ENDOR and DFT are in excellent agreement and that in CD_2Cl_2 solvent, the proposed structure of the $[V^{IV}=O(acac)_2$-(**16**)] complex is as shown in Figure 4.4.

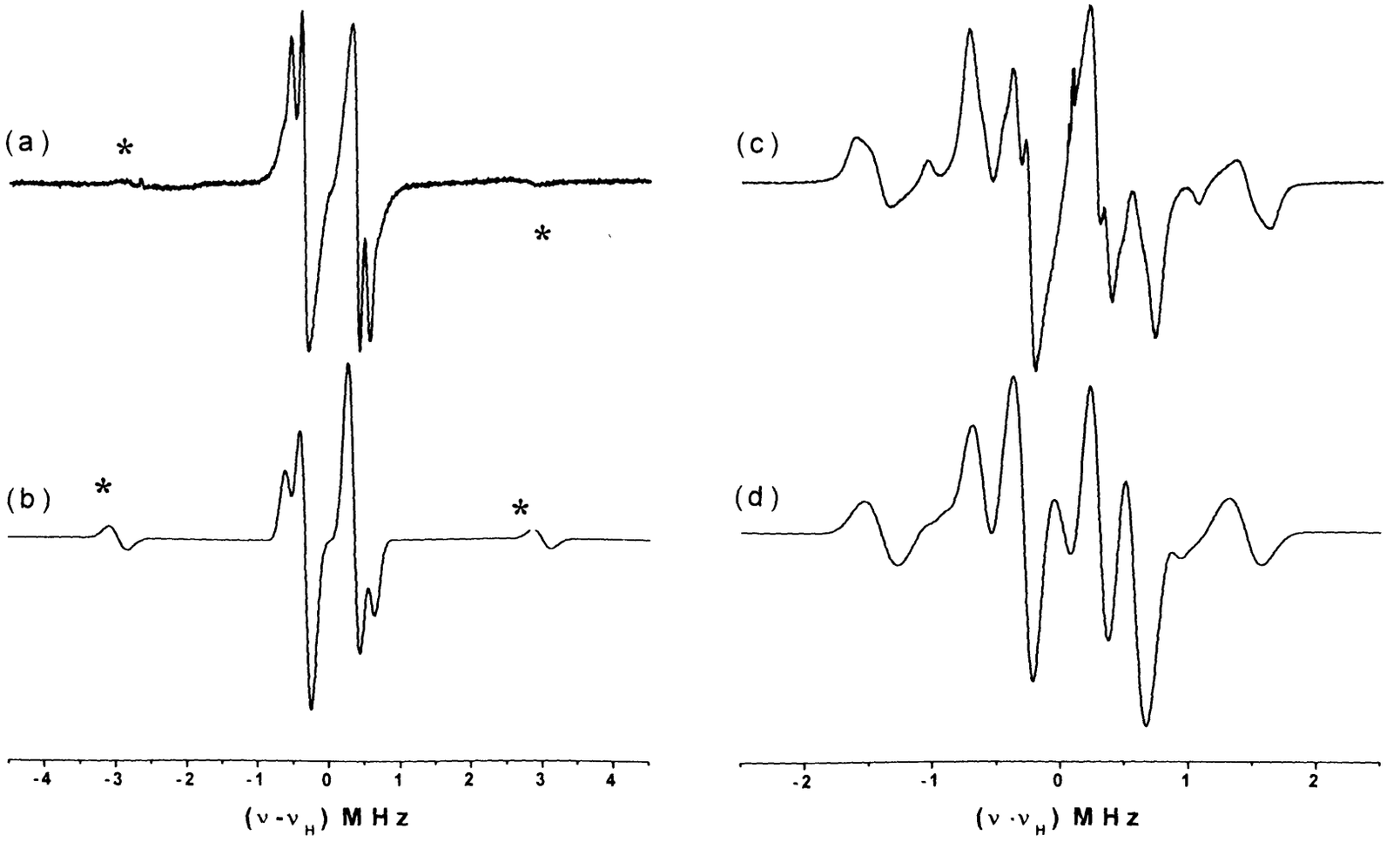

Figure 4.3: X-band ^{1}H ENDOR spectra of $VO(acac)_2$ in CD_2Cl_2 / toluene-d_8 (1:1) recorded with a microwave power of 1.6 mW at 10 K. (a) Experimental spectrum parallel position (2826.5 Gauss); (b) simulated spectrum; (c) experimental spectrum perpendicular position (3289.0 Gauss) and (d) simulated spectrum. Resonances due to traces of water are marked with a *

Table 4.3: Comparison of DFT and ENDOR VO...H distances/angles for bis(acetylacetonato)oxovanadium(IV) in CD_2Cl_2 / toluene-d_8.

Substituent	DFT Distance (R) /Å	DFT Angle (90>θ) / °	|| dipolar coupling / MHz	A_{iso} / MHz	Hyperfine Tensor / MHz		ENDOR Distance (R) / Å	ENDOR Angle (θ) / °
					$A_\perp$	$A_\parallel$		
[a]CH_3	4.600 (×4)	86.2(×4)	1.933	0.157	-0.810	2.090	4.321	78.0
[a]CH_3	4.610 (×4)	65.0(×4)	1.628	-0.040	-0.850	1.580	4.584	86.0
[a]CH_3	....	....	1.527	0.013	-0.750	1.540	4.675	82.0
[a]CH_3	....	....	1.457	-0.097	-0.825	1.360	4.748	77.0
[a]CH_3	....	....	1.440	0.030	-0.690	1.470	4.767	79.0
[a]CH_3	5.180 (×4)	71.6(×4)	1.183	-0.223	-0.815	0.960	5.087	68.0
[b]CH	....	....	1.780	-0.200	-1.909	1.580	4.440	70.0
[b]CH	4.490 (×2)	70.6	1.820	-0.400	-1.310	1.420	4.407	71.0
H_2O	....	....	6.067	-0.067	-3.100	6.000	2.928	10.0
H_2O $_{Dist}$	....	....	1.187	-0.007	-0.600	1.187	5.061	0.0

a = Coupling to protons of the methyl (CH_3) groups.
b = Coupling to protons of the CH groups.
(x...) indicates the equivalent number of adducts.

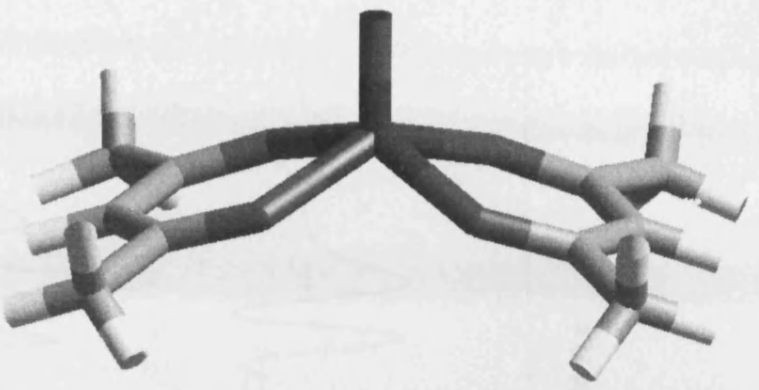

Figure 4.4: DFT model of $VO(acac)_2$ with non-coordinating dichloromethane (CH_2Cl_2).

4.3.3 *ENDOR and DFT analysis of [VO(acac)$_2$-(16)] in coordinating solvents (C_5D_5N and 2(CD_3)-C_5D_4N)*

The frozen solution ^1H ENDOR spectra of [$VO(acac)_2$-(**16**)] in deuterated pyridine (C_5D_5N) and the slightly bulkier substituted pyridine, 2-picoline (2(CD_3)-C_5D_4N), are shown in Figure 4.5 and 4.6 respectively, along with the associated computer simulations. The spectra are now significantly different compared to those previously observed in dichloromethane (Figure 4.3), indicating a dramatically altered ligand conformation in the frozen pyridine or 2-picoline solution. The anomalous peak intensities in the simulations appear in features arising from the water protons (*e.g.* Figures 4.5(c) and (d)) due to the limitations of the broadening model applied to them; this does not compromise the data obtained from the other protons. The analysis of the ^1H superhyperfine tensors was again performed and the resulting vanadyl - proton distances, estimated according to the point dipole approximation, are listed in Tables 4.4 and 4.5. These tables represent the results for the ligand coordinates arising from a simulated *cis* conformation (Table 4.4) and/or a simulated *trans* (Table 4.5) conformation of the pyridine – [$VO(acac)_2$-(**16**)] adduct; the presence of the two isomers will be discussed below. The analogous table of results for the *cis* : *trans* ligand coordinates for the 2-picoline [$VO(acac)_2$-(**16**)] adduct are shown in Tables 4.6 and 4.7 respectively.

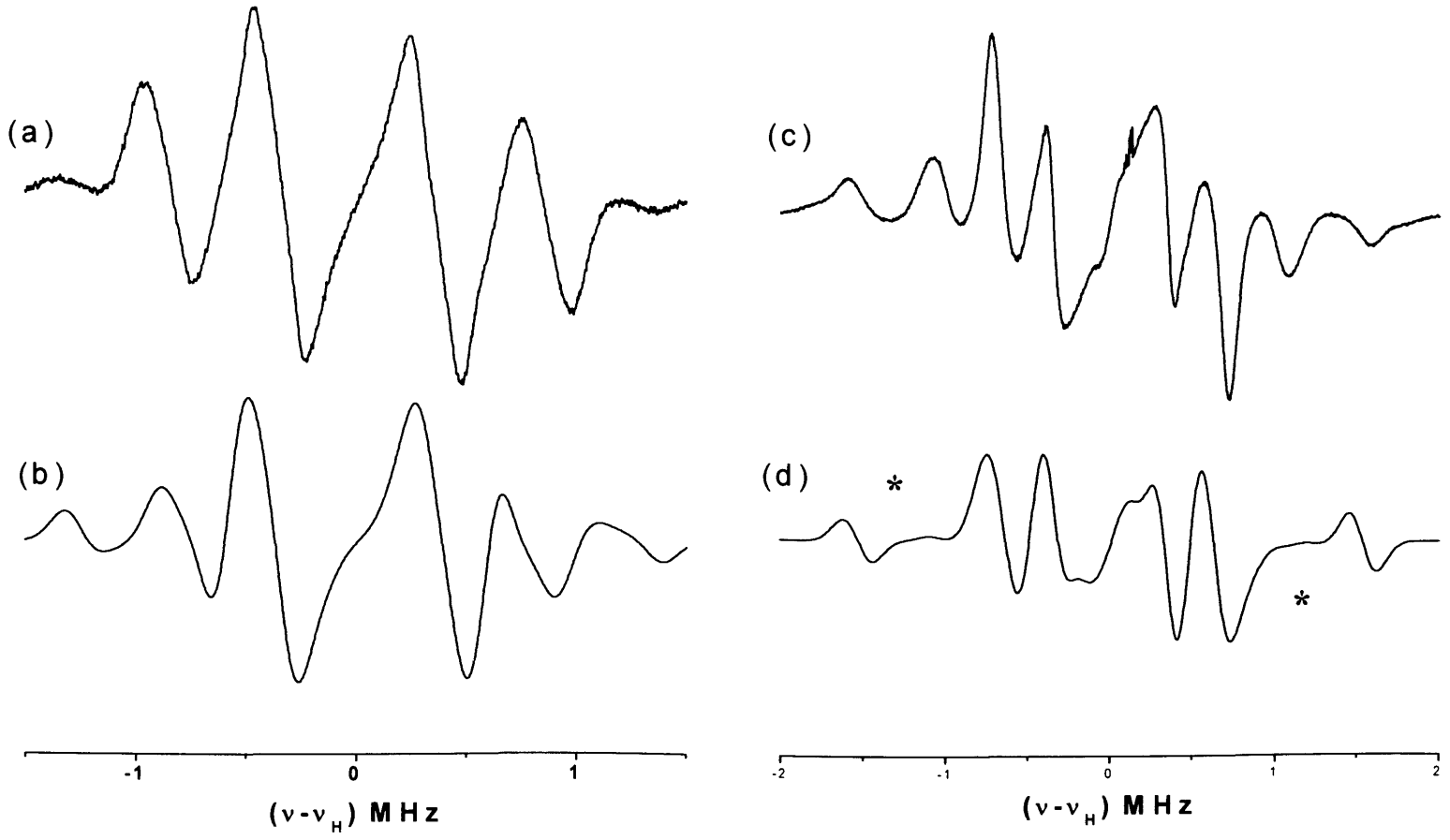

Figure 4.5: X-band ^{1}H ENDOR spectra of $VO(acac)_2$ in pyridine–d_5 / toluene–d_8 (1:1) recorded with a microwave power of 2.5 mW at 10 K. (a) Experimental spectrum parallel position (2829.0 Gauss); (b) simulated spectrum; (c) experimental spectrum perpendicular (3277.7 Gauss) and (d) simulated spectrum. Contribution to intensity of peak marked * is due to water.

Table 4.4; Comparison of DFT and ENDOR V...H distances/angles for bis(acetylacetonato)oxovanadium(IV) in pyridine-d_5 : toluene-d_8 ~ *Cis* isomer. The DFT results have the protons from each methyl group placed consecutively.

Substituent	DFT Distance (R) /Å	DFT Angle (90>θ) / °	|| dipolar coupling / MHz	A_{iso} / MHz	Hyperfine Tensor / MHz		ENDOR Distance (R) / Å	ENDOR Angle (θ) / °
					$A_\perp$	$A_\parallel$		
[a]CH_3	4.594	83.0	1.753	0.127	-0.750	1.880	4.443	16.0
[a]CH_3	4.650	74.9	1.413	0.027	-0.680	1.440	4.800	88.0
[a]CH_3	5.166	86.4	1.187	-0.013	-0.680	1.100	5.061	19.0
[a]CH_3	4.538	79.6	....	....	....	....	....	....
[a]CH_3	4.696	78.4	....	....	....	....	....	....
[a]CH_3	5.162	89.7	....	....	....	....	....	....
[a]CH_3	4.573	87.5	....	....	....	....	....	....
[a]CH_3	4.662	83.3	....	....	....	....	....	....
[a]CH_3	5.233	69.3	....	....	....	....	....	....
[a]CH_3	4.816	15.4	....	....	....	....	....	....
[a]CH_3	4.862	5.8	....	....	....	....	....	....
[a]CH_3	5.373	18.1	....	....	....		....	....
[b]CH	4.606	42.8	1.513	-0.013	-0.770	1.500	4.676	42.0
[b]CH	4.438	89.6	1.900	-0.450	-1.400	1.450	4.349	86.0
H_2O	....	....	4.333	-1.033	-3.200	3.300	3.287	22.0
H_2O	....	....	2.300	-0.100	-1.250	2.200	4.078	71.0

a = Coupling to protons of the methyl (CH_3) groups.
b = Coupling to protons of the CH groups.

Table 4.5; Comparison of DFT and ENDOR V...H distances/angles for bis(acetylacetonato)oxovanadium(IV) in pyridine-d_5 / toluene-d_8 ~ *Trans* isomer. The DFT results have the protons from each methyl group placed consecutively.

Substituent	DFT Distance (R) /Å	DFT Angle (90>θ) / °	|| dipolar coupling / MHz	A_{iso} / MHz	Hyperfine Tensor / MHz		ENDOR Distance (R) / Å	ENDOR Angle (θ) / °
					$A_\perp$	$A_\parallel$		
[a]CH_3	4.629	67.0	1.887	-0.317	-1.260	1.570	4.355	66.0
[a]CH_3	4.659	88.7	1.853	-0.343	-0.343	1.510	4.381	67.0
[a]CH_3	5.190	76.1	1.660	0.030	-0.800	1.690	4.547	75.0
[a]CH_3	4.618	72.4	....	....	....	....	....	....
[a]CH_3	4.638	86.7	....	....	....	....	....	....
[a]CH_3	5.189	78.1	....	....	....	....	....	....
[a]CH_3	4.640	87.9	....	....	....	....	....	....
[a]CH_3	4.647	71.0	....	....	....	....	....	....
[a]CH_3	5.193	77.5	....	....	....	....	....	....
[a]CH_3	4.581	66.9	....	....	....	....	....	....
[a]CH_3	4.685	87.9	....	....	....	....	....	....
[a]CH_3	5.186	72.9	....	....	....	....	....	....
[b]CH	4.474	74.8	1.987	-0.407	-1.400	1.580	4.280	65.0
[b]CH	4.471	76.9	2.027	-0.537	-1.550	1.490	4.256	86.0

a = Coupling to protons of the methyl (CH_3) groups.
b = Coupling to protons of the CH groups.

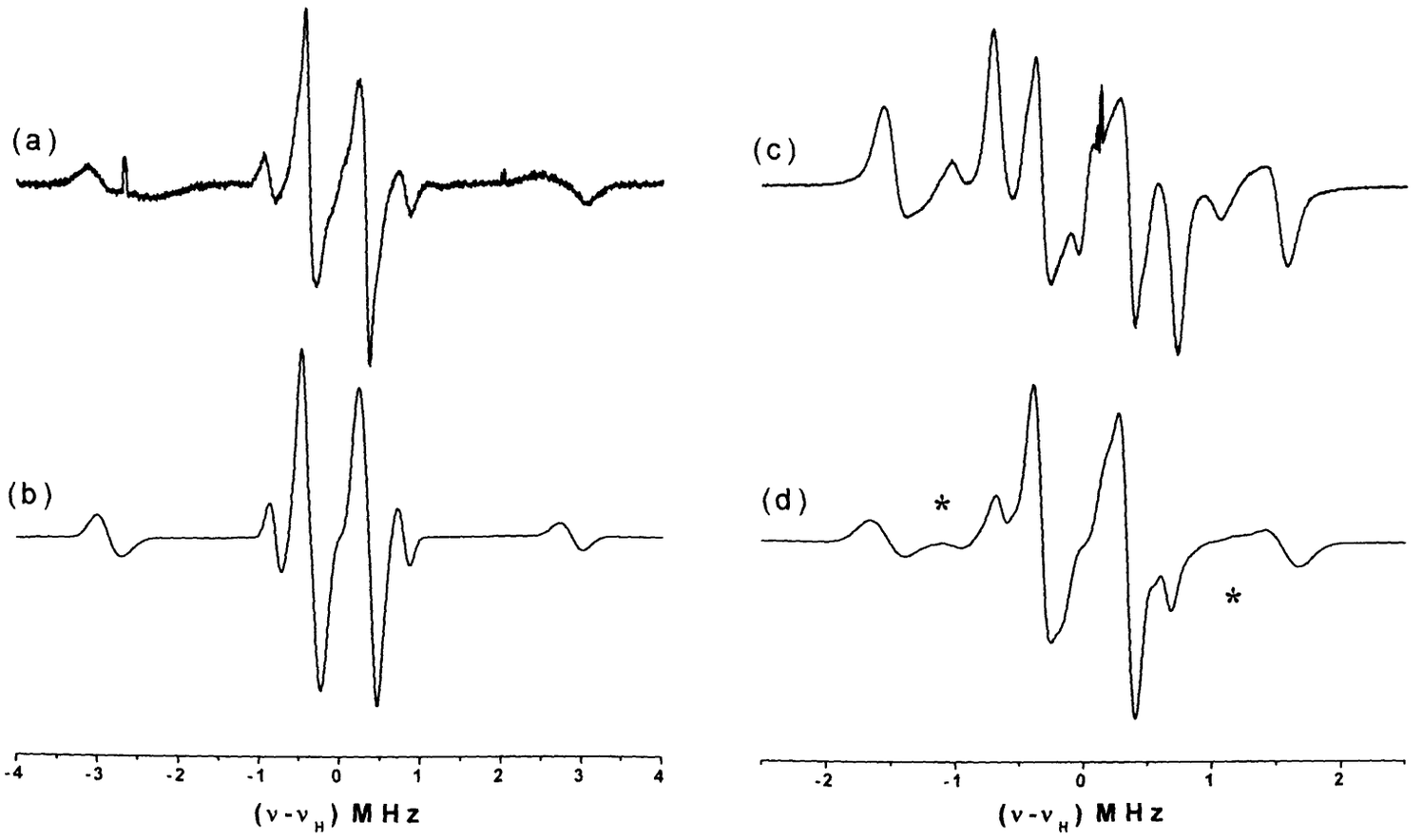

Figure 4.6: X-band ^{1}H ENDOR spectra of $VO(acac)_2$ in 2-picoline-d_7 / toluene-d_8 (1:1) recorded with a microwave power of 2.5 mW at 10 K. (a) Experimental spectrum parallel position (2828.5 Gauss); (b) simulated spectrum; (c) experimental spectrum perpendicular position (3277.7 Gauss) and (d) simulated spectrum. Resonances due to traces of water are marked with a *.

Table 4.6; Comparison of DFT and ENDOR V...H distances/angles for bis(acetylacetonato)oxovanadium(IV) in 2-picoline-d_7 / toluene-d_8 ~ *Cis* isomer. The DFT results have the protons from each methyl group placed consecutively.

Substituent	DFT Distance (R) /Å	DFT Angle (90>θ) / °	|| dipolar coupling / MHz	A_{iso} / MHz	Hyperfine Tensor / MHz		ENDOR Distance (R) / Å	ENDOR Angle (θ) / °
					$A_\perp$	$A_\parallel$		
[a]CH_3	4.553	84.0	1.933	0.157	-0.810	2.090	4.323	78.0
[a]CH_3	4.667	74.0	....	....	....	....	....	....
[a]CH_3	5.183	85.0	....	....	....	....	....	....
[a]CH_3	4.624	89.0	....	....	....	....	....	....
[a]CH_3	4.640	69.0	....	....	....	....	....	....
[a]CH_3	5.184	79.0	....	....	....	....	....	....
[a]CH_3	4.616	88.0	....	....	....	....	....	....
[a]CH_3	4.682	86.0	....	....	....	....	....	....
[a]CH_3	5.261	73.0	....	....	....	....	....	....
[a]CH_3	4.793	20.0	....	....	....	....	....	....
[a]CH_3	4.850	6.0	....	....	....	....	....	....
[a]CH_3	5.366	23.0	1.120	-0.120	-0.680	1.000	5.159	19.0
[b]CH	4.622	47.0	1.513	-0.013	-0.770	1.500	4.676	42.0
[b]CH	4.479	81.0	1.620	-0.040	-0.850	1.580	4.586	86.0

a = Coupling to protons of the methyl (CH_3) groups, b = Coupling to protons of the CH groups.

Table 4.7; Comparison of DFT and ENDOR V...H distances/angles for bis(acetylacetonato)oxovanadium(IV) in 2-picoline-d- / toluene-d_8 ~ *Trans* isomer. The DFT results have the protons from each methyl group placed consecutively.

Substituent	DFT Distance (R) /Å	DFT Angle (90>θ) / °	|| dipolar coupling / MHz	A_{iso} / MHz	Hyperfine Tensor / MHz		ENDOR Distance (R) / Å	ENDOR Angle (θ) / °
					$A_\perp$	$A_\parallel$		
[a]CH_3	4.592	65.4	....	....	....	....	....	....
[a]CH_3	4.685	86.8	1.527	0.013	-0.750	1.540	4.678	82.0
[a]CH_3	5.191	72.9	1.277	-0.177	-0.815	1.100	4.961	68.0
[a]CH_3	4.619	86.9	....	....	....	....	....	....
[a]CH_3	4.656	72.0	1.457	-0.097	-0.825	1.360	4.750	77.0
[a]CH_3	5.193	78.2	....	....	....	....	....	....
[a]CH_3	4.660	89.0	....	....	....	....	....	....
[a]CH_3	4.616	78.0	1.440	0.030	-0.690	1.470	4.769	79.0
[a]CH_3	5.194	76.0	....	....	....	....	....	....
[a]CH_3	4.631	89.0	....	....	....	....	....	....
[a]CH_3	4.648	67.4	....	....	....	....	....	....
[a]CH_3	5.192	76.0	....	....	....	....	....	....
[b]CH	4.481	75.0	1.727	-0.227	-1.090	1.500	4.487	70.0
[b]CH	4.483	75.0	1.800	-3.800	-1.280	1.420	4.425	71.0
H_2O	....	....	6.133	-0.133	-3.200	6.000	2.926	10.0
H_2O Dist	....	....	1.453	0.147	-0.580	1.600	4.727	0.0

a = Coupling to protons of the methyl (CH_3) groups, b = Coupling to protons of the CH groups.

To model the interaction of pyridine and picoline with [$VO(acac)_2$-(**16**)], the complex was again optimised using DFT. In each case, two possible conformations of the acetylacetonato ligands were found; i.e., a *cis* and *trans* isomer (Scheme 1). The two isomers, as modelled for the case of pyridine, are shown in Figure 4.7a and 4.7b and, despite the changes in conformation, the calculated VO...H distances remain quite similar (see Tables 4.4 and 4.5). The difference in energy between the two isomers was found to be only *ca.* 3 $kJmol^{-1}$ with the *cis* isomer lower in energy than the *trans*, so that it is reasonable to assume that both conformations can exist in frozen solution, and may therefore be observed simultaneously by ENDOR.

Previous EPR and ENDOR studies of [V^{IV}=$O(acac)_2$-(**16**)] in protic pyridine solutions have concluded that the *cis* conformation of the ligand is favoured in the presence of pyridine [15,16]; i.e., the pyridine binds *cis* to the oxo group and one of the acetylacetonato ligands is displaced, allowing one oxygen from the acac ligand to bind from the *trans* position while the other binds *cis* to the oxo bond (Scheme 1). However, other studies have found that most pyridine and substituted pyridine adducts of bis-(2,4-diketonato)oxovandium(IV) complexes can only be present as *cis* or a mixture of *cis* and *trans* isomers in solution [15,16,21,22].

Since the DFT calculations have already indicated that only a small energy difference (3 $kJmol^{-1}$) separates the *cis* and *trans* isomers, we may expect both structures (Figure 4.7) to co-exist in solution. This situation, in which two isomers are present simultaneously in solution, would likely create a more complex ENDOR spectrum (Figure, 4.5 and 4.6). Therefore in the simulation of the spectra, it was considered that the experimental spectrum was actually a composite profile arising from the two individual isomers. In other words, the parameters used to simulate the proton coordinates of the *trans*-[V^{IV}=$O(acac)_2(C_5D_5N)$] adduct (i.e., a pseudo-octahedral structure analogous to the [V^{IV}=$O(acac)_2$-(**16**)]... CD_2Cl_2 situation in Figure 4.3) were combined with the expected proton coordinates of the *cis*-[V^{IV}=$O(acac)_2(C_5D_5N)$] adduct, based on the theoretical model presented in Figure 4.7b. When this combined simulation was carried out, a good fit between the experimental and simulated spectrum was obtained by adopting a 60:40 ratio of *cis* to *trans* isomer. An unsatisfactory fit was obtained in the case where only the *cis* or *trans* structure was individually simulated, or if the mixing ratio used in the simulation was not 60:40 *cis* : *trans* isomer.

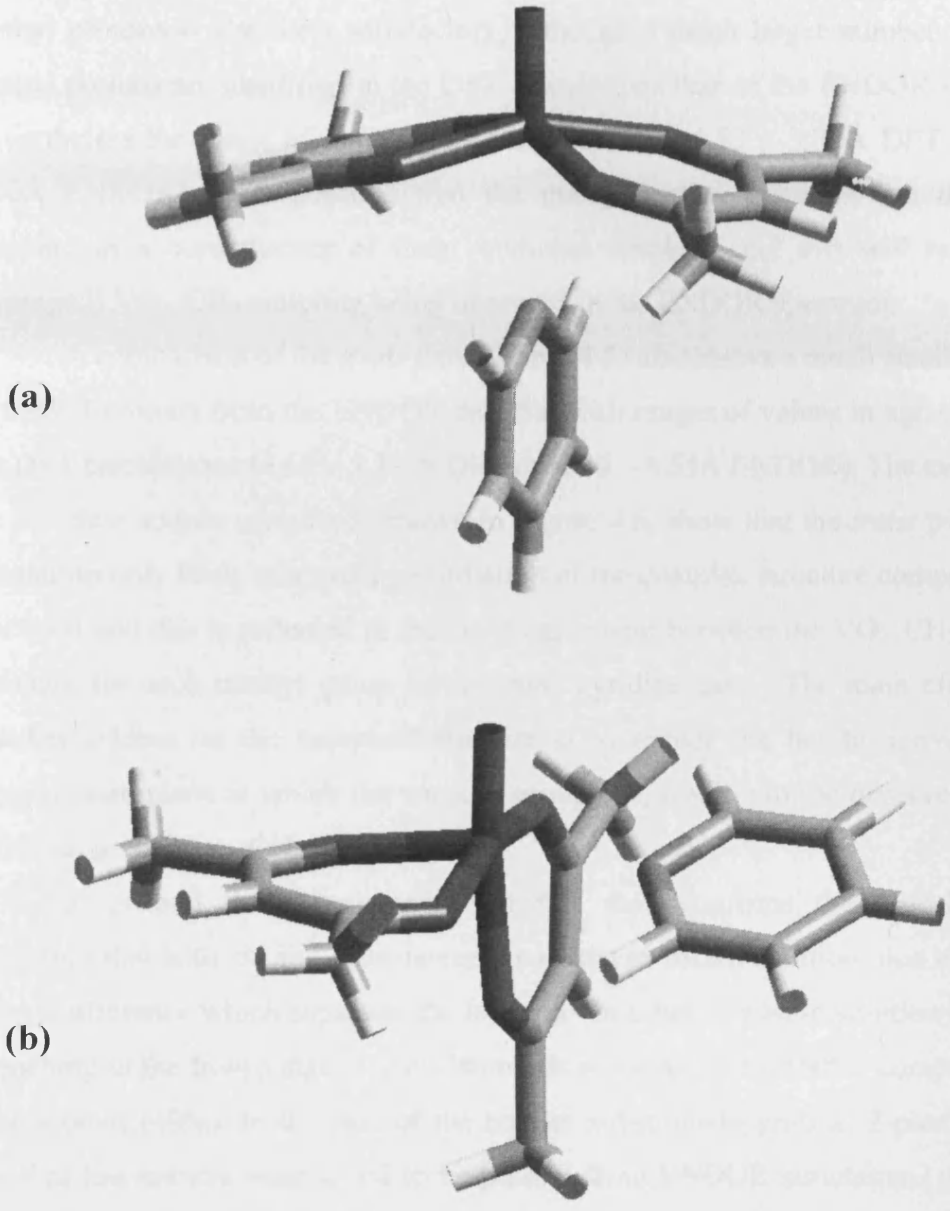

Figure 4.7: DFT models of the $[V^{IV}{=}O(acac)_2(C_5D_5N)]$ adduct; (a)*Trans* - (b) *Cis - isomer.*

The results extracted from the ENDOR simulation for pyridine are presented in Table 4.4 (*cis* isomer) and 4.5 (*trans* isomer). The simulated spectra shown in Figure 4.5 represent the combination of the data in Table, 4.4 and 4.5. These tabulated experimental results compare favourably with the calculated VO - proton distances based on the DFT calculations. In the *cis* isomer VO...CH distances of 4.35 and 4.68Å agree well with the theoretical DFT models with predicted VO...CH distances of 4.44 and 4.61Å and the corresponding VO...H angles also show good agreement. The third VO...CH coupling from the *cis* complex (Table 4.4) is likely obscured due

to the other overlapping peaks. The agreement between the positions of the remaining methyl protons is also very satisfactory, although a much larger number of distinct methyl protons are identified in the DFT calculations than in the ENDOR simulation. Nevertheless the range of values obtained is similar (4.53 – 5.37Å DFT *cf.* 4.44 – 5.06Å ENDOR). It is possible that the methyl proton positions are difficult to compare as a consequence of their rotational freedom, and this will result in an 'averaged' VO...CH_3 coupling being observed in the ENDOR spectrum.

A comparison of the *trans* data (Table 4.5) also shows a much smaller number of methyl protons from the ENDOR data but with ranges of values in agreement with the DFT calculations (4.62 – 5.19 Å DFT *cf.* 4.36 – 4.55Å ENDOR). The structures of the pyridine adduct complexes shown in Figure 4.6, show that the *trans* pyridine co-ordination only leads to a small perturbation of the complex structure compared to the free case and this is reflected in the close agreement between the VO...CH_3 distances obtained for each methyl group in the *trans* pyridine case. The main effect of the pyridine adduct on the complex structure is to reduce the height above the acac oxygen atom plane at which the vanadyl group sits, leading to the observed decrease in the range of VO...CH_3 distances.

In general the experimental ENDOR data confirms the modelling data, indicating that both *cis* and *trans* isomers co-exist in frozen solution, due to the small energy difference which separates the isomers. In other words, in solution just before quenching to the frozen state, the *cis* isomer is in slight excess (60%) compared to the *trans* isomer (40%). In the case of the bulkier substituted pyridine, 2-picoline, equal ratios of the isomers were found to be present from ENDOR simulation. In order to achieve a good fit a 50:50 mixing of the relative ratios was performed, using a data manipulation program (*Origin*). Other isomer ratio attempts failed to produce a satisfactory fit. As 2-picoline is slightly bulkier than pyridine, the energy difference separating the isomers can be considered negligible.

4.4 Conclusions

The structure and conformations of the [V^{IV}=O(acac)$_2$-(**16**)] complex in a series of coordinating and non-coordinating solvents have been studied using a combination of angular selective ENDOR spectroscopy and DFT calculations. By simulation of the ^{1}H ENDOR spectra, information on the ligand coordinates in frozen

solution have been obtained and compared to coordinates determined from the optimised structure in the DFT calculations. In the non-coordinating solvent (dichloromethane) the complex adopts the expected square pyramidal structure. The vanadyl- proton coordinates obtained by DFT and ENDOR simulations were in good agreement with each other and with this expected structure. Small variations in the VO...CH distances were ascribed to weak H-bonding interactions between CD_2Cl_2 and $VO(acac)_2$, which were not accounted for in the DFT calculations. Pyridine and substituted pyridines coordinate strongly to the $[V^{IV}{=}O(acac)_2]$ complex and two different isomers of the resulting $[V^{IV}{=}O(acac)_2(C_5D_5N)]$ adduct have been identified. Owing to the small energy difference between the two isomers, both appear to co-exist in solution before freezing, with only a slight predominance of the *cis* structure over the *trans* structure in the frozen state. In the case of the 2-picoline adduct, $[V^{IV}{=}O(acac)_2(C_6D_8N)]$, an equal ratio of *cis* and *trans* isomers was found The present results demonstrate the power of combined ENDOR and DFT studies to discriminate subtle structural differences between coordination compounds, even when present as a mixture of isomers in frozen solution.

In reflection to the obtained results, the full structural analysis of the vanadyl system $[V^{IV}{=}O(acac)_2]$ was carried out with great success, allowing not only detailed coordinates of the ligand proton positions, but also showed how computational DFT results complimented the ^1H ENDOR data. For the spectra to be simulated successfully, it was necessary to fully understand the electronic structure of the metal-ligand system and as a result allowed precise hyperfine tensor coordinates to be extracted. Due to the relatively large mathematical content of the simulation program, these simulations would run for days at a time, therefore it was important to fully understand the chemistry of the complex in frozen solution. From undertaking this investigation, it has not only illustrated how sensitive the ENDOR technique is at identifying minor perturbations in the ligand structure, in frozen solution, but also how reliable the extracted data is, when complimented with theoretical models.

The next chapter will demonstrate how effective ENDOR is at elucidating detailed structural parameters in a similar metal-ligand complex $[V^{IV}{=}O(Salen)]$, demonstrating how DFT and ENDOR can be used in compliment, to resolve structural changes in solution.

4.5 References

[1] S.S. Eaton, G.R. Eaton, *Vanadium in Biological Systems*, Kluwer Academic Publishers, Boston, 1990, 199.

[2] C.V. Grant, W. Cope, J.A. Ball, G.G. Maresch, B.J. Gaffney, W. Fink, R.D. Britt, *J. Phys. Chem. B.*, 1999, **103**, 10627.

[3] E. Garribba, E. Lodyga-Chruscinska, D. Sanna, G.Micera, *Inorganica. Chimica. Acta.*, 2001, **322**, 87.

[4] Makinen, W. Marvin, Brady, J. Matthew, *J. Bio. Chem.*, 2002, **14**, 277.

[5] D. Mustafi, J. Telser, M.W. Makinen, *J. Am. Chem. Soc.*, 1992, **114**, 6219.

[6] J. Petersen, T. R. Hawkes, D. J. Lowe, *J. Inorg. Chem.*, 2000, **80**, 161.

[7] A. Togni, G. Rist, G. Rihs, A. Schweiger, *J. Am. Chem. Soc.*, 1993, **115**, 1908.

[8] C.R. Cornman, K.M. Geiser-Bush, S.P. Rowley, P.D. Boyle, *Inorg. Chem.*, 1997, **36**, 6401.

[9] D. Attanasio, *J. Phys. Chem.*, 1986, **90**, 4952.

[10] G. C. Hurst, T. A. Henderson, R. W. Kreilick, *J. Am. Chem. Soc.*, 1985, **107**, 7294; T. A. Henderson, G. C. Hurst, R. W. Kreilick, *J. Am. Chem. Soc.*, 1985, **107**, 7299.

[11] A. Schweiger, Hs. H. Guenthard, *Chem. Phys.*, 1982, **70**, 1.

[12] S. C. Larsen, *J. Phys. Chem. A.*, 2001, **105**, 8333.

[13] B. Kirste, H. van Willigen, *J. Phys. Chem.*, 1982, **86**, 2743.

[14] B. Kirste, H. van Willigen, *Chem. Phys. Lett.*, 1982, **87**, 589.

[15] N.D. Yordanov, M. Zdravkova, *Polyhedron*, 1993, **12**, 635.

[16] G.R. Hanson, Y. Sun, C. Orvig, *Inorg. Chem.*, 1996, **35**, 6507.

[17] S.S. Amin, K. Cryer, B. Zhang, S.K. Dutta, S.S. Eaton, O.P. Anderson, S.M. Miller, B.A. Reul, S.M. Brichard, D.C. Crans, *Inorg. Chem.*, 2000, **39**, 406.

[18] A.D.Becke, *Phys. Rev. A.*, 1988, **38**, 3098.

[19] C.Lee, W.Yang and R.G.Parr, *Phys. Rev..B*, 1988, **37**, 785.

[20] ADF 2.3.0, Theoretical Chemistry, Vrije Universiteit, Amsterdam, E.J.Baerends *et al. Chem.Phys.*, 1973, **2**, 41; G. te Velde, E.J.Baerends, *J.Comp.Phys.*, 1992, **99**, 84; C. Fonseca Guerra *et al. METECC.*, **95**, 305, (1995).

[21] N.M. Atherton, P.J. Gibbon, M.C.B. Shohoji, *J. Chem. Soc., Dalton Trans.*, 1982, 2289.

[22] M.R. Caira, J.M. Haigh, L.R. Nasimbeni, *J. Inorg. Nucl. Chem.*, 1972, **34**, 3171.

Chapter 5

Solvatochromic effects of a *N,N'*-ethylene-bis(salicylideneamine)oxovanadium(IV) complex-[V^{IV}=O(Salen)]

Solvatochromic effects of a *N,N'*-ethylene-bis(salicylideneamine)oxovanadium (IV) complex – VO(Salen)

5.1 Introduction

Based on the success of the ENDOR/DFT approach to study weak conformational changes, the approach was then applied to investigate weak solvatochromic effects in frozen solution.

In order to investigate the importance of solvation effects in solution, it is also necessary to elucidate the detailed metal ligand geometry and thoroughly describe the nature of the complex-solvent interaction. The phenomenon of solvatochromism is classically defined as:

"*the (pronounced) change in position and sometimes intensity of an electronic absorption or emission band, accompanying a change in the polarity of the medium*" [1].

In this Chapter the definition will be somewhat extended to cover shifts in the positions of transitions in any spectroscopic measurement; in the current case those observed in the ENDOR spectra. Typical solvatochromic effects are usually analysed in terms of such parameters as solvent dipole moments and polarisability and do not go as far (nor is it always appropriate) as to define what particular structures in solution are responsible for a given spectrum. In this account solvation (*i.e.* solvatochromatic) effects in solution were observed by ENDOR spectroscopy and, through a combination of spectral simulations and density functional theory allowed generation of detailed models of the metal complexes in question.

Here the ENDOR analysis of the solvatochromic effects of a well characterized vanadyl complex, *N,N'*–ethylenebis (salicylideneamine) oxovanadium(IV) (hereafter abbreviated as [V^{IV}=O(salen)]-(**9**)) will be described in the presence of both coordinating (dimethylformamide; Scheme 5.1a) and non-coordinating (dichloromethane; Scheme 5.1b) solvents. DFT calculations have also been carried out in order to enhance the interpretation of the ENDOR data. ENDOR investigations of [V^{IV}=O(salen)-(**9**)] type complexes have been studied in the past [2] together with related biologically significant complexes [3-4]. However a comprehensive analysis of the complex in solution combining both ENDOR and DFT methods is unpublished. While vanadyl complexes are well known to adopt a 5-

coordinate square pyramidal structure or in some cases 6-coordinate disordered octahedral [5] structure, the minor pertubation of the square pyramidal structure in the presence of a ligating solvent (coordinating axially, *trans* to the V^{IV}=O bond) is difficult to study, particularly with respect to the positions of the axial and equatorial protons of the 1,2-ethylenediamine back bone (see Scheme 5.1). This chapter presents how ENDOR spectroscopy and DFT calculations, can be employed to detect subtle structural changes in the ligand geometry of a metal complex in frozen solution, and probe the spatial arrangement of the interacting solvent molecules around the complex.

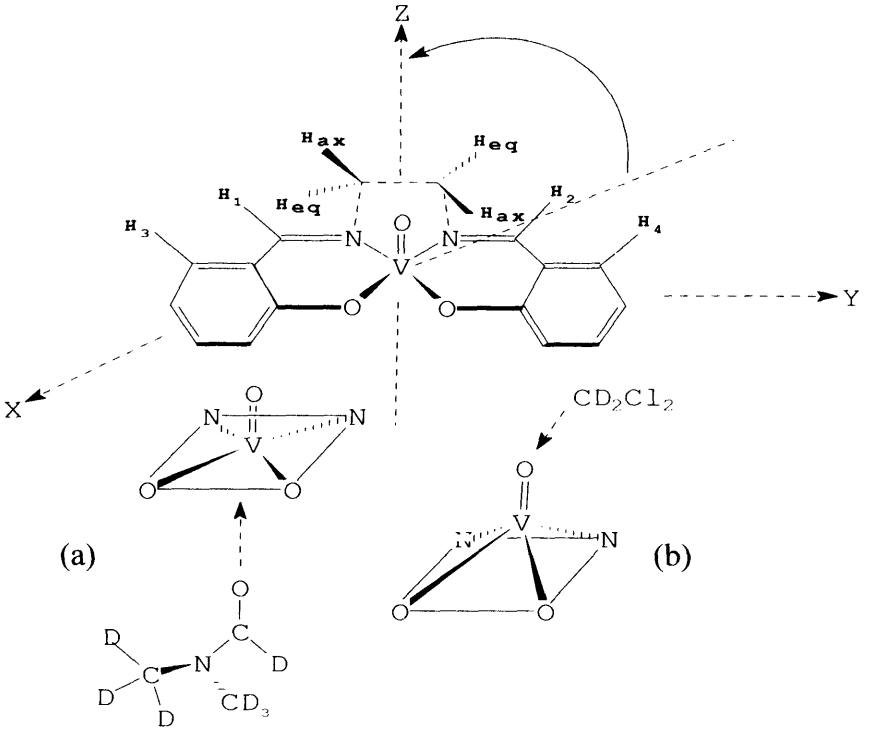

Scheme 5.1

5.2 Experimental

5.2.1 *Measurement and analysis of EPR/ENDOR spectra*

A small amount (ca. 10 mg) of the appropriate complex [V^{IV}O(salen)-(**9**)] was dissolved in the *non-coordinating* (dichloromethane) or *coordinating* solvents (DMF). A small amount of deuterated toluene (a non coordinating solvent) was added to improve the quality of the glass in the frozen solution.

5.3 Results and Discussion

5.3.1 *EPR analysis of VO(salen) in coordinating and non-coordinating solvents*

The frozen solution EPR spectra of [V^{IV}=O(salen)-(**9**)] in dichloromethane-d_2 and dimethylformamide-d_7 produced spectra typical of the VO^{2+} ion, as described elsewhere [6] (Figure 5.1). The experimental and simulated spectrum of VO(salen)-(**9**) in CD_2Cl_2 is shown in Figure 5.2 and the spin Hamiltonian parameters are presented in Table 5.1. Accurate spin Hamiltonian parameters for each EPR spectrum were obtained by computer simulation (using the Bruker programme: *Simfonia*). After analysis of the EPR spectra, ^{1}H ENDOR spectra were recorded at a static magnetic field corresponding to the –7/2 parallel (field position = 2826 G) and –3/2 perpendicular (field position = 3289 G) EPR absorption features.

Table 5.1: Spin Hamiltonian parameters obtained by computer simulation of the EPR spectra for [VO(salen)-(**9**)] in frozen solutions of deuterated dichloromethane (CD_2Cl_2) and deuterated dimethylformamide (C_3D_7NO). A small amount of deuterated toluene (C_7D_8) was added in each case to improve the quality of the frozen solution "glass".

Solvent	g_1	g_2	g_3	g_{iso}	A_1 / MHz	A_2 / MHz	A_3 / MHz	A_{iso} / MHz
CD_2Cl_2	1.984	1.978	1.956	1.972	162.7	172.0	485.0	273.2
DMF-d_7	1.981	1.976	1.956	1.971	147.0	167.0	474.0	262.7

V^{4+} usually exhibits octahedral or tetrahedral symmetry in co-ordination compounds which splits the five-fold degenerate state of the free ion into two states, t_{2g} and e_g, which are respectively triply and doubly degenerate. The degeneracy of these two states is further lifted by other effects leading to structural distortions. The two most common cases experienced in EPR are tetragonal distortion by compression of tetrahedral and octahedral structures. Where for tetrahedral $g_{\|} > g_{\perp}$, while in the octahedral case the g values take the form $g_{\perp} > g_{\|}$.

The V^{4+} ions have a d^1 electronic structure, and based on the g values reported above, it can be assumed that the cation has a tetragonally distorted crystal field environment. In this case, the high abundance of ^{51}V dominates the V^{4+} spectrum, with two overlapping 8-line hyperfine patterns (I=7/2, number of lines is therefore $2nI+1 = 8$) (Figure 5.1).

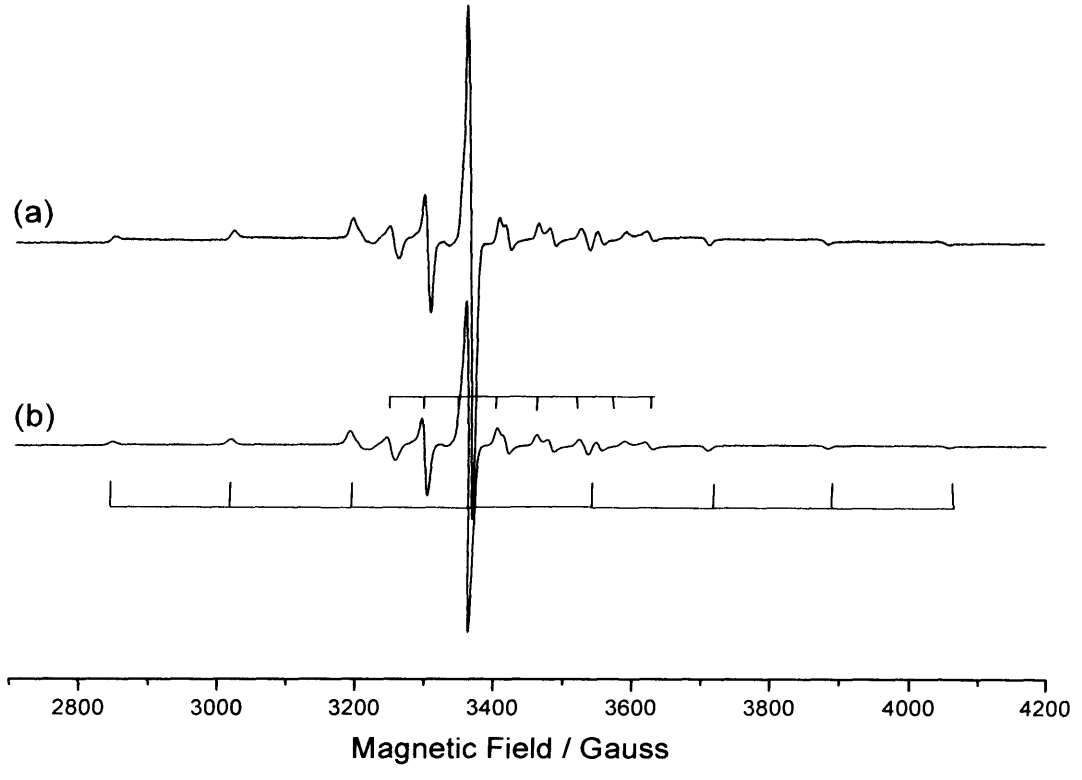

Figure 5.1: X-band EPR spectrum of [VO(salen)-(**9**)] in (a) CD_2Cl_2 and (b) C_3D_7NO. EPR spectra recorded with a microwave power of 2.02 mW at 10 K

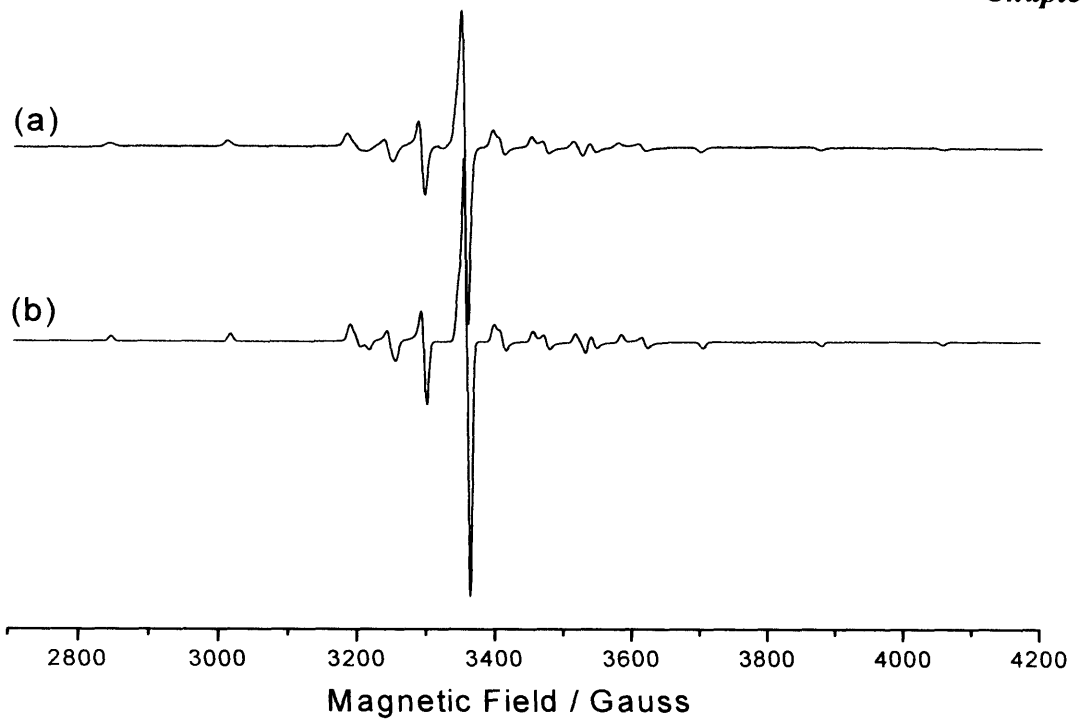

Figure 5.2: X-band EPR spectrum of [VO(salen-(**9**)] in CD_2Cl_2 / toluene-d_8 recorded with a microwave power of 2.02 mW at 10 K. (a) Experimental spectrum and (b) simulated spectrum.

5.3.2 *ENDOR analysis*

5.3.2.1 *Structure of [V^{IV}=O(salen)-(9)] in non-coordinating solvent (CD_2Cl_2)*

The ^1H ENDOR spectra of [V^{IV}=O(salen)-(**9**)] in the non coordinating solvent, (deuterated dichloromethane, CD_2Cl_2), are shown in Figure 5.3. Using the fully deuterated solvent only the protons arising from the salen ligand contribute to the ENDOR spectrum in Figure 5.3 (since ν_n for ^1H = 14.902 MHz and ν_n for ^2H = 2.287 MHz at a field of 3500 G). The ENDOR measurements were obtained at low temperature (10K) providing well resolved spectra revealing the subtle differences in the in-equivalency of the remote ligand protons (ie., the protons labeled H_1 - H_4 in Scheme 5.1). ENDOR measurements were also performed on a selectively deuterated [V^{IV}=O(salen-d_4)-(**15**)] complex, in which the axial and equatorial protons of the 1,2-ethylenediamine bridge (labeled H_{ax} and H_{eq} in Scheme 5.1) were deuterated. This simplifies considerably the analysis and simulation of the polycrystalline spectra and allowed unambiguously identification of the resonances associated with the remote H_1-H_4 protons compared to the 1,2-ethylenediamine protons (for clarity the peaks associated with the latter protons are indicated with an + in Figure 5.3).

The simulated ENDOR spectra are also shown in Figure 5.3. Analysis of the accurate ^{1}H hyperfine coupling tensors from the simulated spectra enabled distances to be calculated between the unpaired electron on the vanadyl ion (VO^{2+}) and the protons of the *N,N'*-bis (salicylidene)-1,2-ethylenediamine ligand using the point dipole approximation [10]. The complete set of tensors and VO...H distances are given in Table 5.2. The VO...H_1-H_4 distances were calculated as 4.234Å(H_1), 3.885Å(H_2), 5.273Å(H_3) and 5.388Å(H_4) while a significant degree of inequivalency was found for the axial and equatorial 1,2-ethylenediamine protons; 3.172Å(H_{ax}), 3.558Å(H_{ax}) and 3.902Å(H_{eq}). In the latter case, the two equatorial protons were found to be equivalent and therefore cannot be differientiated in the ENDOR spectrum. The pronounced in-equivalency between the axial and equatorial protons however arises as a consequence of the symmetry of the complex, since the V=O group is positioned above the *NNOO* ligand plane. Therefore one of the axial protons will be closer to the V=O group while the second will appear more remote and produce a smaller coupling.

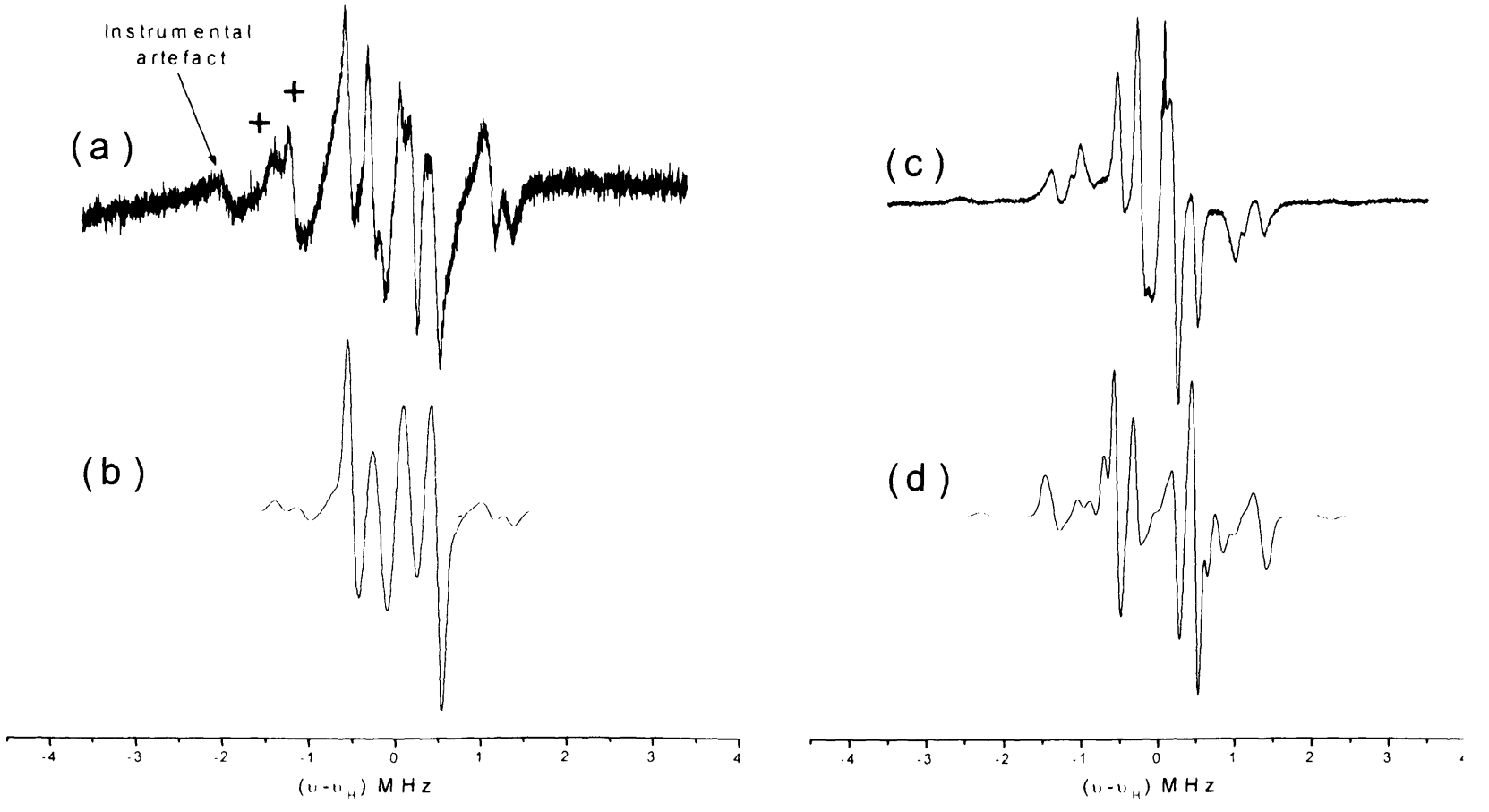

Figure 5.3: X-band ^{1}H ENDOR spectra of $[V^{IV}{=}O(salen)]$ in (CD_2Cl_2)/toluene-d_8 (1:1 ratio) recorded with a microwave power of 2 mW at 10 K. (a) Experimental spectrum measured at the parallel position (2826.0 G); (b) simulated spectrum; (c) experimental spectrum measured at the perpendicular position (3289.0 G), and (d) simulated spectrum.

Table 5.2: Comparison of DFT and ENDOR V...H distances/angles for the ligand protons of the [V^{IV} O(salen)] complex in CD_2Cl_2.

Substituent	DFT Distance (R) /Å	DFT Angle (90>θ) / °	|| dipolar coupling / MHz	g / theta	A_{iso} / MHz	Hyperfine Tensor / MHz		ENDOR Distance (R) / Å	ENDOR Angle (θ) / °
						$A_\perp$	$A_\parallel$		
H_1	4.078	75.2	2.060	1.9803	-0.010	-1.040	2.050	4.234	79.0
H_2	4.060	75.3	2.667	1.9803	0.033	-1.300	2.700	3.885	79.0
H_3	5.464	79.2	1.067	1.9799	-0.017	-0.550	1.050	5.273	77.0
H_4	5.508	73.3	1.000	1.9805	0.100	-0.400	1.100	5.388	80.0
H_{ax}	3.195	75.4	4.900	1.9797	-0.300	-2.750	4.600	3.172	76.0
H_{ax}	3.644	56.5	3.467	1.9805	0.083	-1.650	3.550	3.560	60.0
H_{eq}[a]	3.981 3.928	79.9 82.2	2.633	1.9813	0.267	-1.050	2.900	3.902	87.0

The hyperfine coupling tensor, dipolar coupling constant and θ angle used in the ENDOR simulations are also included. Note a) For the DFT calculated equatorial hydrogen atoms the two values from the calculated structure are quoted.

Figure 5.4 shows the DFT calculated structure of the isolated [V^{IV}=O(salen)-(**9**)] complex which would be expected to be a good model of the structure in the non-coordinating solvent. As expected the V=O group has a square pyramidal structure with the V atom sitting above the plane of the co-ordinating N and O atoms. In addition it can be seen that the ligand itself is not planar since the angles made by each of the phenyl rings with the V=O bond are greater than 90°.

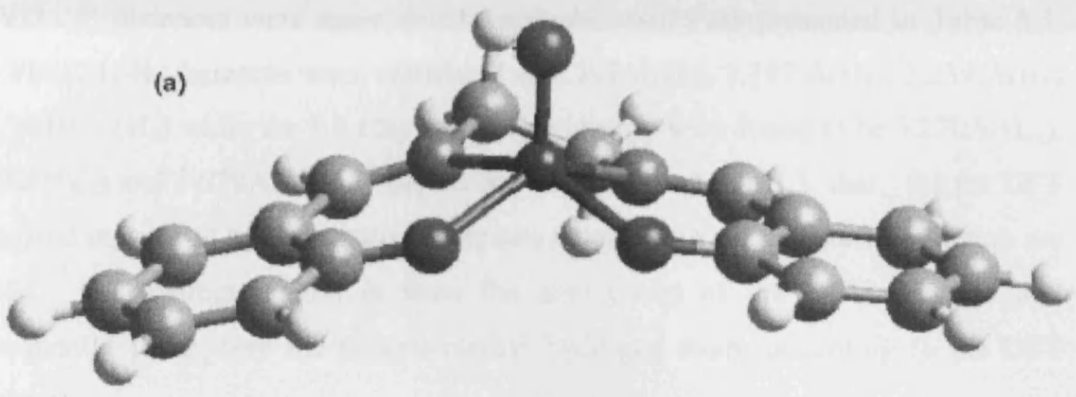

Figure 5.4: DFT model of (a) [V^{IV}=O(salen)-(**9**)] with non-coordinating dichloromethane (CD_2Cl_2).

The VO…H distances and VO…H angles calculated from the DFT simulation are also included in Table 5.2 for comparison with the data derived from the ENDOR analysis based on the point dipole model. In general the DFT calculated distances and those derived from the spectra agree to within 0.2Å of each other and the angles generally show differences within 4°. The largest discrepancies are found for the hydrogens from regions of the ligand with significant π-bonding character (H_1 to H_4) and this may be due to anisotropic shielding effects that are not currently accounted for in the dipolar model. The ethylene bridge region (H_{ax} and H_{eq}) shows much closer agreement between the DFT and ENDOR derived data with differences in calculated VO…H distances below 0.1 Å. The difference between the V…H_{ax} distances in both data sets is consistent with the square pyramidal arrangement around the vanadium centre. The VO…H angles for H_1 to H_4 also suggest that the disposition of the phenyl groups shown in Figure 5.4, which gives a slightly folded structure for the salen ligand, is consistent with the ENDOR data.

5.3.3 *Structure of [V^{IV}=O(salen)-(9)] in coordinating solvent (C_3D_7NO)*

The experimental and simulated ENDOR spectra for [V^{IV}=O(salen)-(**9**)] in the coordinating solvent (deuterated dimethylformamide, C_3D_7NO) are shown in Figure 5.5. The profile of the spectra, particularly in the parallel region, are slightly different compared to that previously observed for [V^{IV}=O(salen)-(**9**)] - CD_2Cl_2 (Figure 5.3). Analysis of the simulated spectra provided a complete set of hyperfine tensors so that the VO...H distances were again determined; the results are presented in Table 5.3. The VO...H_1-H_4 distances were calculated as 3.797 Å(H_1), 3.797 Å(H_2), 5.239 Å(H_3) and 5.410 Å (H_4) while the 1,2-ethylenedimine protons were found to be 3.270Å(H_{ax}), 3.605Å(H_{ax}) and 3.978Å(H_{eq}), It should be noted that in Table 5.3, that; for the DFT calculated equatorial hydrogen atoms, the two values from the calculated structure are quoted, the hydrogen atom is from the acyl group of the DFT structure and subsequently these were the nearest methyl hydrogen atoms according to the DFT structure.

These distances can be understood with respect to the manner in which the DMF interacts with the metal complex. As the strongly interacting dimethylformamide solvent coordinates trans to the V=O group, the vanadyl ion is effectively pulled further down into the NNOO equatorial xy ligand plane. As a result, the distance between the unpaired electron and the H_1-H_4 protons is now reduced (eg., within the range 3.797 – 5.410 Å) compared to the previous case from the non-coordinating solvent (eg., within the range 3.885 - 5.388 Å). The VO...H distances for the 1,2-ethylenediamine protons of the [V^{IV}=O(salen)-(**9**)] complex in the DMF solvent (Table 5.3) are similar to those already observed in the CD_2Cl_2 case (Table 5.2). While these differences appear small, they are significant and illustrate the resolution of ENDOR to discriminate subtle changes to the positions of the protons in the frozen solution.

Using the isolated model of the [V^{IV}=O(salen)-(**9**)] complex (Figure 5.4) as a starting point, DFT calculations of the complex with a coordinated DMF solvent molecule were carried out with all degrees of freedom of the system relaxed. Several starting orientations were used in these calculations, but on optimization the extremely weakly coordinating DMF molecule was usually found to dissociate from the complex. The structure shown in Figure 5.6 is the only optimization that ended with a stable structure in which the DMF molecule is coordinated. In this case the

interaction between the complex and the solvent molecule appears to be stabilized by a secondary NOC-H...O interaction (2.416 Å). Despite the generally weak interaction, the structure of the complex is altered by the presence of the DMF molecule.

Comparing Figure 5.6 with Figure 5.4, one can see that the V=O group has moved toward the plane of the coordinating atoms of the salen ligand on addition of the DMF molecule, in agreement with the conclusions drawn from the spectral data. The effect on protons H_1-H_4 results from a movement of the phenyl rings away from the coordinating DMF molecule so that they are now almost perpendicular to the V=O direction. This is also indicated in the spectral data, by the increase of the corresponding calculated VO...H angles.

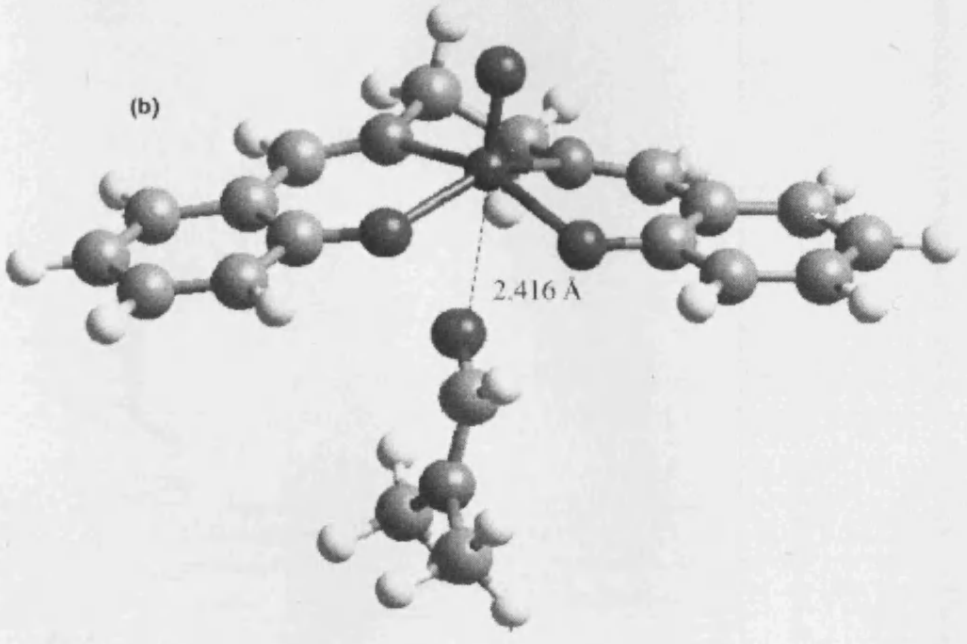

Figure 5.6: DFT model of [V^{IV}=O(salen)-(**9**)] with coordinating dimethylformamide (C_3D_7NO).

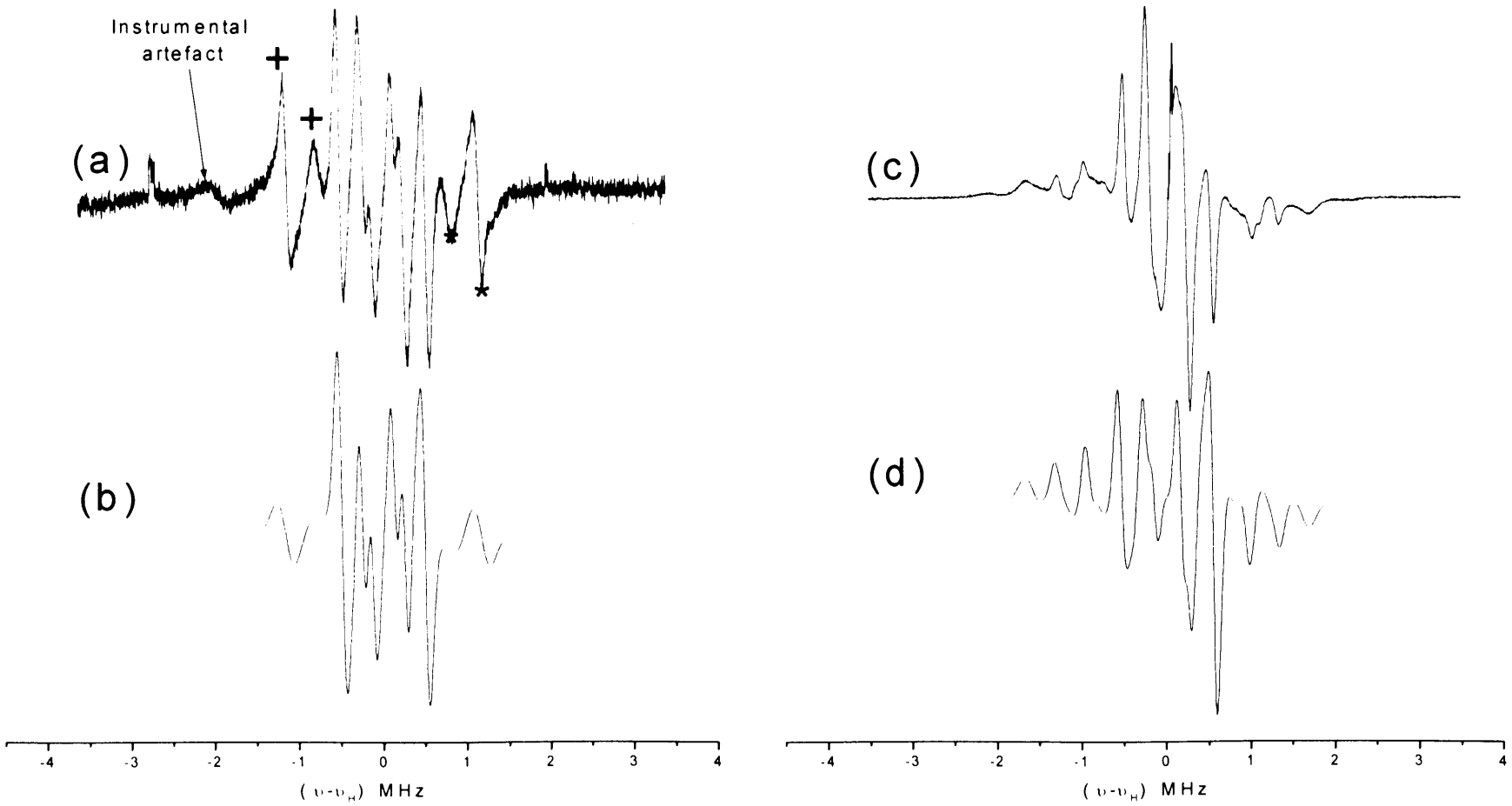

Figure 5.5: X-band ^{1}H ENDOR spectra of [V^{IV}=O(salen)] in dimethylformamide (C_3D_7NO)/toluene-d_8 (1:1 ratio) recorded with a microwave power of 2 mW at 10 K. (a) Experimental spectrum measured at the parallel position (2826.0 G); (b) simulated spectrum; (c) experimental spectrum measured at the perpendicular position (3289.0 G), and (d) simulated spectrum.

Table 5.3: Comparison of DFT and ENDOR VO...H distances/angles for the ligand protons of the [V^{IV} O(salen)-(**9**)] complex in DMF-d_7. The hyperfine coupling tensor, dipolar coupling constant and angle used in the ENDOR simulations are also included. The VO...H distances/angles to the coordinated (protic) DMF molecule are included.

Substituent	DFT Distance (R) /Å	DFT Angle (90>θ) / °	|| dipolar coupling / MHz	g / theta	A_{iso} / MHz	Hyperfine Tensor / MHz		ENDOR Distance (R) / Å	ENDOR Angle (θ) / °
						$A_\perp$	$A_\parallel$		
H_1	4.040	76.6	2.853	1.97842	0.370	-1.100	3.310	3.797	86.69
H_2	4.028	80.4	2.853	1.97839	0.447	-0.980	3.300	3.797	86.00
H_3	5.446	74.2	1.647	1.97849	0.013	-0.530	1.100	5.239	89.00
H_4	5.389	86.9	1.487	1.97816	0.113	-0.380	1.100	5.410	83.00
H_{ax}	3.484	73.1	3.333	1.97781	0.017	-1.650	3.350	3.605	80.00
H_{ax}	3.193	56.8	4.467	1.97844	-0.167	-2.400	4.300	3.270	87.00
H_{eq}[a]	3.945, 3.930	81.9, 82.6	2.481	1.97844	0.169	-1.100	2.650	3.978	87.00
(DMF)[b]	3.222	32.4	2.853	1.96002	0.377	-1.050	3.230	3.786	26.00
(DMF)[c]	5.349	36.0	2.233	1.96316	0.050	-0.500	1.150	5.204	35.00
(DMF)[c]	5.150	11.5	1.240	1.96509	-0.130	-0.750	1.110	5.002	40.00

5.3.4 *Solvent coordination in [V^{IV}=O(salen)-(9)] - C_3H_7NO*

In order to directly confirm the interaction of dimethylformamide with the vanadyl complex, and to determine the spatial arrangement of coordinated DMF with the complex, further ENDOR and DFT calculations were performed. In the first case, the ENDOR spectra of the [V^{IV}=O(salen)] complex were recorded using protic DMF (C_3H_7NO) so that the VO...H distances (or couplings) between the VO group and the coordinated DMF solvent could be observed in the spectrum. To facilitate the simulation of the spectra, the ENDOR measurements were obtained on a deuterated [V^{IV}=O (salen-d_4)-(**15**)] complex (ie., the protons of the 1,2-ethylenediamine bridge were deuterated). In this case, only the H_1-H_4 protons of the salen ligand and the protons of the DMF can be observed in the spectrum. The resulting experimental and simulated ENDOR spectra are shown in Figure 5.5. In the parallel spectrum, the observed resonances originate primarily from the H_1-H_4 salen-ligand protons. However, in the perpendicular spectrum, the appearance of new peaks associated with the DMF can be clearly seen. Simulation of the spectra and subsequent analysis of the hyperfine coupling tensors enabled one to calculate the V...H distances between the d^1 electron and the protons on the coordinated DMF molecule as 3.786 Å, 5.204 Å and 5.002 Å (see Table 5.3).

These distances are consistent with the DFT calculated values for the aldehyde (3.222 Å) and methyl protons (5.150 Å) indicating that the DMF molecule is co-ordinated and orientated to avoid steric interactions between the salen ligand and DMF methyl groups.

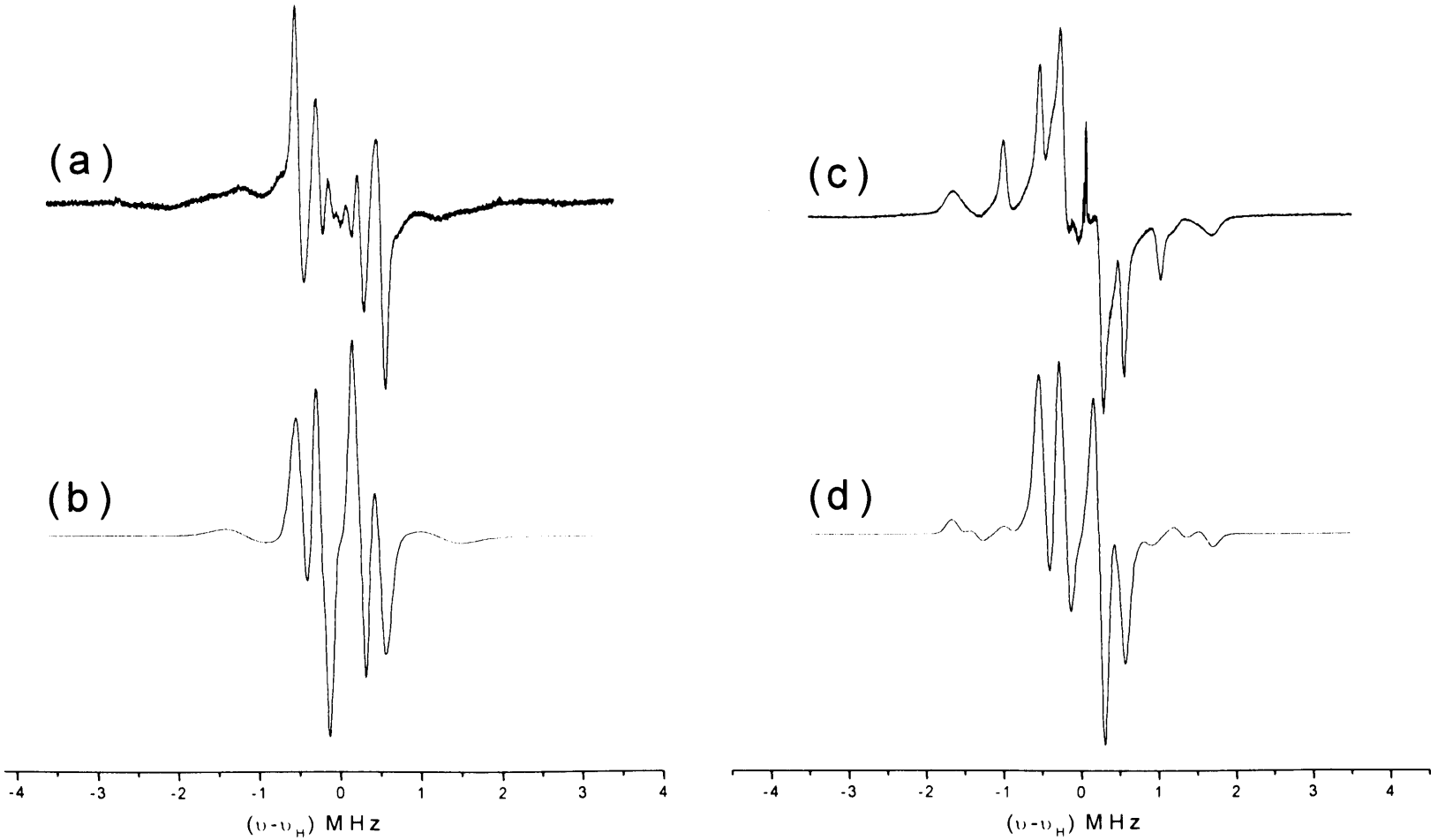

Figure 5.7: X-band ^{1}H ENDOR spectra of $[V^{IV}=O(salen\text{-}d_4)]$ in protic dimethylformamide (C_3H_7NO)/toluene-d_8 (1:1 ratio) recorded with a microwave power of 2 mW at 10 K. (a) Experimental spectrum measured at the parallel position (2826.0 G); (b) simulated spectrum; (c) experimental spectrum measured at the perpendicular position (3289.0 G), and (d) simulated spectrum.

5.4 Conclusions

An angular selective ENDOR study in combination with DFT calculations was carried out on the *N,N'*-bis(salicyledene) 1,2-ethylenediamine oxovanadium complex [V^{IV}=O(salen)] in both coordinating (DMF) and non-coordinating (CD_2Cl_2) solvents. Analysis of the ^1H ENDOR spectra by computer simulation, enabled the structural elucidation of the ligand coordinates in frozen solution to be obtained and compared to calculations taken from the optimised DFT model. In the presence of a non-coordinating solvent (dichloromethane), the expected square pyramidal symmetry of the V=O ion is confirmed both by ENDOR and DFT. However, in the coordinating solvent (dimethylformamide), changes to the observed V...H distances in the ENDOR spectra evidenced the lowering of the V=O group into the equatorial ligand plane through coordination with DMF. The axial coordination of the solvent, *trans* to the vanadyl oxo-ligand, was also confirmed by ENDOR and DFT. The V...H coordinates obtained by ENDOR spectroscopy were in excellent agreement with models based on DFT calculations. The above results clearly demonstrate that "solvatochromic" effects can be detected not only as previously referenced in the literature by monitoring shifts to the electronic spectra of the transition metal ions, but also by exploring the weak structural changes to the ligand through combined ENDOR and DFT studies.

From carrying out this study, it has been confirmed that ENDOR spectroscopy is a valuable tool in determining precise distances and angles of ligand protons (and solvent protons) to a central transition metal centre. As this chapter focused on the solvatochromic effects of an oxo-vanadium complex, rather than conformational changes of the ligand structure (as in Chapter 4), it is clearly evident that the stronger coordinating dimethylformamide solvent, pulls the V=O back into the *NNOO* ligand plane, as confirmed by DFT calculations.

To further illustrate the complimentary nature between DFT and ENDOR, the next chapter will describe the ability of ENDOR to detect and quantify exceedingly weak interactions in solution, with an epoxide substrate.

5.5 References

[1] P. Müller, *Pure Appl. Chem.*, 1994, **66**, 1077.

[2] D. Attanasio. *J. Phys. Chem.*, 1986, **90**, 4952.

[3] B. Kirste, H. Van Willigan. *Chem. Phys. Lett.*, 1982, **87**, 589.

[4] B. Kirste, H. Van Willigen. *J. Phys.Chem.*, 1982, **86**, 2743.

[5] S. Larsen, *J. Phys. Chem. A.*, 2001, **105**, 8333.

[6] D.M. Murphy, I.A. Fallis, R.D. Farley, R.J. Tucker, K.L. Avery, D.J. Willock, *Phys. Chem. Chem. Phys.*, 2002.

Chapter 6

Direct observation of diastereomeric interactions between chiral vanadyl salen-type complexes-[V^{IV}=O(Jacobsen)] and epoxide substrates in solution

Direct observation of diastereomeric interactions between chiral vanadyl salen complexes and epoxide substrates in solution.

6.1 Introduction

In recent years metal complexes of chiral *N, N'*-bis-salcylidene-ethylenediamine (salen) have been established as one of the most important classes of asymmetric catalysts. Jacobsen [1] and Katsuki [2] have developed chiral manganese salen complexes as highly efficient epoxidation catalysts for prochiral alkenes. Jacobsen has also demonstrated that analogous chromium and cobalt complexes are effective catalysts for the enantioselective ring opening of meso-epoxides [3] and the hydrolytic kinetic resolution (HKR) of racemic epoxides respectively [4]. In general enantio- or diastereoselective reactions can occur by one of two possible mechanisms, namely by the diastereomeric discrimination of one specific enantiomer of a substrate, or, in the case of achiral substrates, the induction of chirality via diastereomeric transition states. Additionally, for Jacobsen's chromium and cobalt catalysed reactions, a second order dependence on catalyst concentration has been observed [5]. This not only implies that these reactions require the activation of a nucleophile (e.g. water), but also the enantiomeric discrimination of the epoxide substrate by the catalyst. The presence of such diastereomeric adducts are often presumed as mechanistic intermediates, but are rarely directly observed. Katsuki has reported the x-ray structure of a Mn-salen complex bearing a co-ordinated *meso*-epoxide in which the Mn-$O_{epoxide}$ bond lengths are typically ~2.3 Å, indicative of a weakly co-ordinated O-donor ligands [6], whilst Chin has examined the structures of diamagnetic chiral Co^{III}-salen *bis*-aziridine complexes crystallographically and by ^{1}H-NMR [7]. Whilst these studies provide valuable insight into the nature of complex-substrate interactions, very few spectroscopic or structural techniques can provide accurate structural data (*e.g.* bond lengths and angles) for homogeneous catalysts *in solution.* In order to establish the mode of chiral epoxide discrimination in metal salen catalysed reactions, Electron Nuclear DOuble Resonance (ENDOR) spectroscopy has been used to study the weak diastereomeric complexes formed between model vanadyl complexes (*R,R*)-[VO(**11**)] and (*S,S*)-[VO(**12**)] and non-racemic epoxides ((*R*) and (*S*)-propylene oxide). The structures of the proposed complexes (Scheme

6.1) have been subsequently confirmed in a complimentary density functional theory (DFT) study.

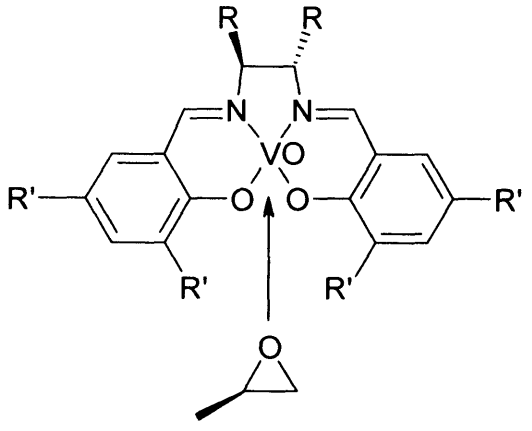

(11,12) R=1/2$(CH_2)_4$ R'=$C(CH_3)_3$

(13) R=H R'=$C(CH_3)_3$

(9) R=H R'=H

Scheme 6.1

6.2 Experimental

6.2.1 Measurement and analysis of EPR / ENDOR spectra

For EPR/ENDOR measurements a small quantity (*ca.* 10 mg) of the appropriate complex [VO-(**11**),VO-(**12**)] was dissolved in (*R*) and (*S*) epoxide (propylene oxide). A small amount of deuterated toluene was added to improve the quality of the glass in the frozen solution. Accurate spin Hamiltonian parameters for the EPR spectra were obtained by computer simulation (eg., *Simfonia*) and the results are presented in Table 6.1. The ENDOR spectra were simulated using an in house programme based on the resonance expressions of Hurst *et al* [8].

6.2.2 DFT calculations

Density Functional Theory (DFT) calculations were carried out using the ADF code, BLYP functionals and TZP STO level basis (ADF IV) for the inner part of the

vanadyl complex described in the following chapter. The outer part, including the tert-butyl groups were optimised in MOPAC PM3 with the central section held in the optimised DFT geometry. DFT calculations lead to the optimum structure shown in Figure 6.2 in which the closest epoxide H...V atom distances are 3.37 and 3.71Å and corresponding O=V..H angles of 142° and 146°, in good agreement with the value deduced from the ENDOR spectra.The angles are larger than those determined from the ENDOR simulations which would suggest that the epoxide is arranged so that the CCO plane in the figure is more vertical than shown. This may result from steric interactions of the epoxide and extended salen ligand structure. These calculations were carried out at the B3LYP level with a 631G(d) basis set using the Gaussian98 package. As commented on in this chapter the interaction between the vanadyl and epoxide is extremely weak. To gain an initial starting point a series of constrained optimisations at different O=V..$O_{epoxide}$ distances were undertaken and the relative energies plotted as shown in Figure 6.1. The minimum structure from this plot was then optimised without constraints applied.

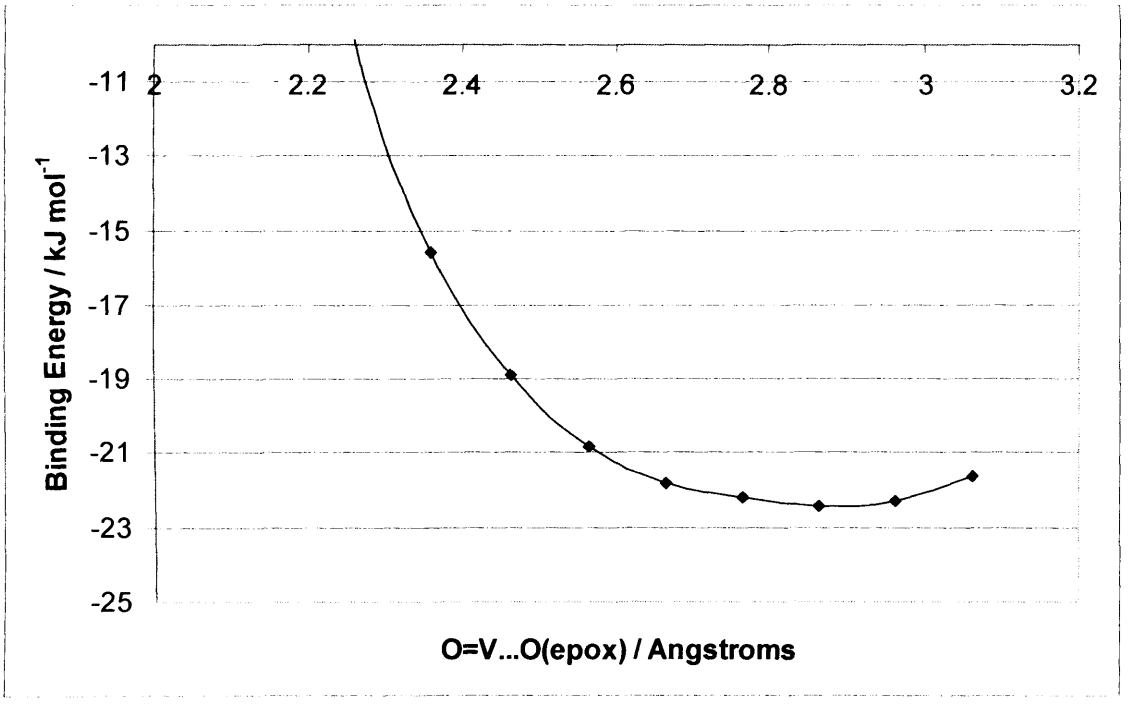

Figure 6.1: Binding energy of model vanadyl / epoxide dimer as a function of O=V...O_{epox} distance. Binding energy was defined as the difference of total energy calculated for the dimer and that for separate optimisations of the vanadyl complex and epoxide at the same level of theory.

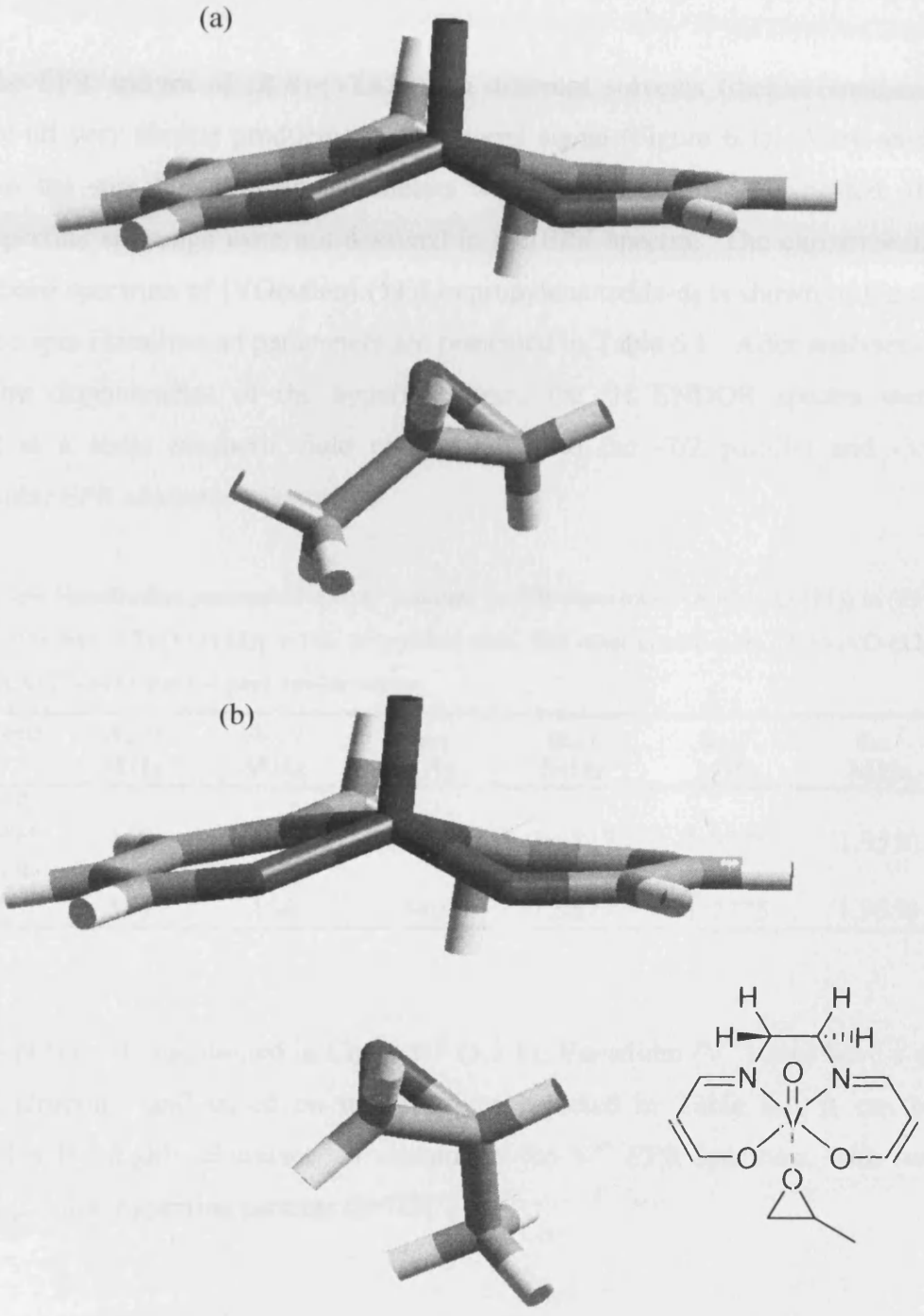

Figure 6.2: Calculated structure for the vanadyl(Salen) complex with a co-ordinated propylene oxide molecule. In these calculations, the [VO(1)] ligand was simplified to a Salen type structure in which the phenyl sections are represented by C=C double bonds (Inset). ; (a) (*R,R*) VO(Jacobsen) in (*R*)-Propylene Oxide and (b) (*S,S*) VO(Jacobsen) in (*S*)-Propylene Oxide.

6.3 Results and Discussion

6.3.1 *EPR analysis of [VO-(11,12)] in propylene oxide (epoxide)*

The EPR spectra of (*R,R*)-[VO(**11**)] in different solvents (dichloromethane, dmf) were all very similar producing a quasi-axial signal (Figure 6.3). Very small changes in the spin Hamiltonian parameters were observed and, as expected, the ligand hyperfine splittings were not resolved in the EPR spectra. The experimental and simulated spectrum of [VO(salen)-(**11**)] in propylene oxide-d_6 is shown in Figure 6.3 and the spin Hamiltonian parameters are presented in Table 6.1. After analysis of the angular dependencies of the hyperfine lines, the ^{1}H ENDOR spectra were measured at a static magnetic field corresponding to the -7/2 parallel and -3/2 perpendicular EPR absorption features.

Table 6.1: Spin Hamiltonian parameters used to simulate the EPR spectra of (*R,R*)-[VO-(**11**)] in (*R*) – propylene oxide and (*S,S*)-[VO-(**12**)] in (*R*)- propylene oxide. The other enantiomers, (*S,S*)-[VO-(**12**)] in (*S*) and (*R,R*)-[VO-(**11**)] in (*S*) gave similar values.

Experiment	A_{xx} / MHz	A_{yy} / MHz	A_{zz} / MHz	g_{xx} / MHz	g_{yy} / MHz	g_{zz} / MHz
RR-(11) in *(R) propylene oxide*	152	167	479	1.9827	1.9775	1.9550
SS-(12) in *R propylene oxide*	155	168	480	1.9827	1.9775	1.9550

As previously mentioned in Chapter 5 (5.3.1), Vanadium (V^{4+}) ions have a d^1 electronic structure, and based on the g values reported in Table 6.1, it can be assumed that the highly abundant ^{51}V dominates the V^{4+} EPR spectrum, with two overlapping 8-line hyperfine patterns (I=7/2).

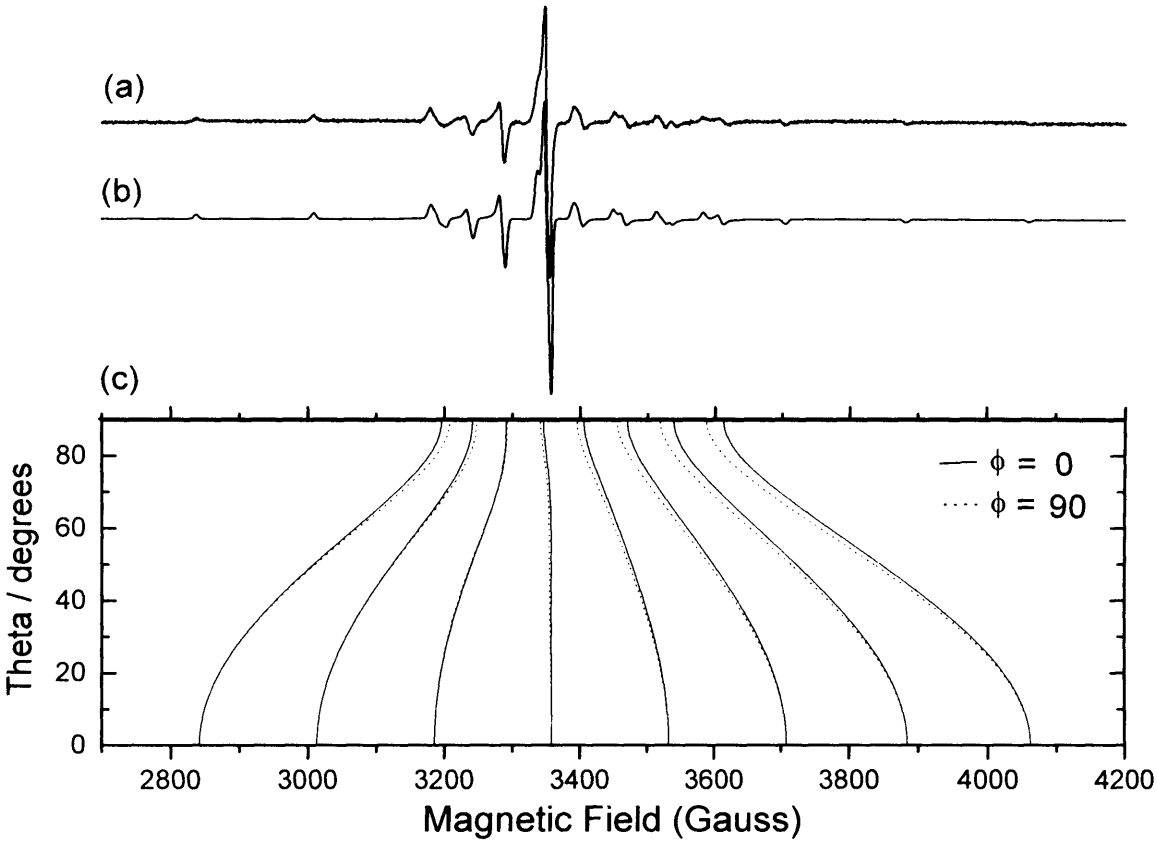

Figure 6.3: X-band EPR spectrum of (*R,R*)-[VO-(**11**)] in epoxide solution (*R*) (with a drop of toluene-d_8) recorded with a microwave power of 2.02 mW at 10 K. (a) Experimental spectrum; (b) simulated spectrum and (c) angular dependencies. The ENDOR spectra shown in Figure 6.4 were recorded at the field position of 3290 G corresponding to a pure perpendicular feature in the single crystal type ENDOR spectrum.

6.3.2 *ENDOR analysis*

6.3.2.1 *Solvent interactions*

The X-band ^{1}H ENDOR spectra of (*R,R*)-[VO(**11**)] in different solvents, CH_2Cl_2, DMF, (*R*) or (*S*)-2-(diethylamino)-propan-1-ol (chosen as a polar, chiral, but sterically demanding co-ligand) and *R*-propylene oxide are shown in Figure 6.4a-d respectively. A complete angular selective ENDOR analysis was carried out on each sample, but for brevity only the pure perpendicular ^{1}H ENDOR spectra (*i.e.*, field orientation perpendicular to the V=O bond axis) will be discussed in the following chapter. The ENDOR spectra were recorded at a field position of 3280 G, and are complicated at this perpendicular field setting due to the two-dimensional powder

form of the spectrum [9]. To assist in the interpretation of these spectra the simplified complexes [VO(**13**)] and [VO(**9**)] were also examined by ENDOR. This revealed that the largest hyperfine coupling in [VO(**11**)] is due to the two axial diamine methine protons (*ca.* H-V distances of 3.05 Å and 3.46 Å, based on the analysis of the ^{1}H superhyperfine tensors using a point dipole model) followed by the two imine protons (H-V distance of 4.03(2) Å).These distances are in close agreement with those determined by DFT calculations (3.04(2) Å and 3.48(2) Å for the diamine protons and 4.03Å for the imine proton). DFT calculations were carried out at the BLYP/TZP level using the ADF program, with a simplified complex in which the phenyl groups in [VO(**9**)] are replaced by carbon double bonds. To consider the extended ligand structure the DFT optimised model was used as the basis to construct ligand (**8**). This model was then optimised using semi-empirical methods (PM3) [10] with the atoms common to our simplified model held at their DFT optimised co-ordinates.

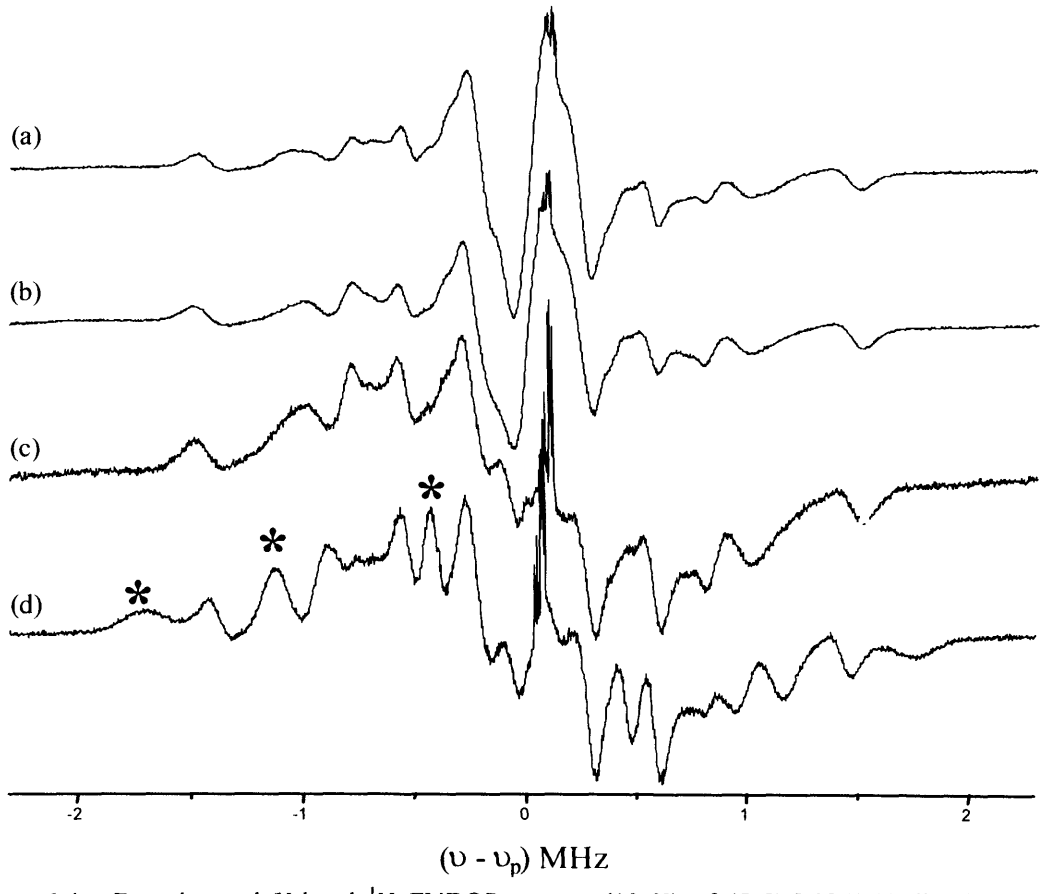

Figure 6.4: Experimental X-band ^{1}H ENDOR spectra (10 K) of (*R,R*)-[VO(**11**)] dissolved in (a) CH_2Cl_2, (b) DMF, (c) (*R*) or (*S*)-2-(diethylamino)-propan-1-ol and (d) *R*-propylene oxide. Recorded with a microwave power of 2 mW and measured at the perpendicular position 0.3290 T.

From this the H-V distances for the *tert*-butyl groups (at the 6 position) of [VO(**1**)] were found to be ~3.38 Å to ~4.05 Å, due to their rotational freedom (structures differing by rotations of the *tert*-butyl groups were estimated to be within ~2 kJ mol^{-1} of each other). Therefore, the ^{1}H ENDOR positions of these groups may not be well defined even in frozen solution. Nevertheless, comparison of the ENDOR spectra of [VO(**11**)], and [VO(**13**)], revealed an additional set of resonances in [VO(**11**)] with an estimated H-V distance of 3.74Å, which were assigned to the protons of the 6-*tert*-butyl groups. Thus, whilst the ENDOR spectra for [VO(**11**)] are complex, the largest couplings can be confidently assigned to (i) the diamine methine protons, (ii) the imine protons and (iii) the protons of the 6-*tert*-butyl groups.

6.3.2 Diastereomeric interactions

Regardless of solvent used the ENDOR spectra of [VO(**11** and **12**)] are very similar (Figure 6.4a-c). The chiral sterically hindered solvent 2-(diethylamino)-propan-1-ol was used in order to establish if the were any significant diastereomeric outer sphere interactions that might cause changes in the ENDOR spectra, but again no significant changes in the spectra were observed. However, the spectrum recorded for (*R,R*)-[VO(**11**)] in (*R*)-propylene oxide was noticeably different (Figure 6.4d), with the observation of new features (labelled *). ENDOR spectra were subsequently measured for (*R,R*)-[VO(**11**)] dissolved in (*R*)- and (*S*)- propylene oxide (see Figure 6.5). The spectra clearly reveal strong correlations between the positions and intensities of the new peaks (labelled *) in the spectrum of (*R,R*)-[VO(**11**)] dissolved in (*R*)-epoxide (Figure 6.5a) and the (*R,R*)-[VO(**11**)] in (*Racemic*)-epoxide (Figure 6.5d). When the experiment was repeated using (*R,R*)-[VO(**11**)] and (*S*)-epoxide, or (*S,S*)-[VO(**12**)] and (*R*)-epoxide a significantly different ENDOR spectrum was produced (Fig. 6.5b). The similarities in the spectra of epoxide-complex pairs (Figure 6.5a,c and 6.5b) are evidence of diastereomeric complexes formed between [VO(**11**)] and the associated epoxide. This result was further confirmed by dissolving the (*Racemic*)-[VO(**11**)] complex in the (*Racemic*) propylene oxide, producing the expected mixed ENDOR spectrum (Figure 6.5e). Figure 6.6 shows an expanded region of the spectra seen in Figure 6.5 (range 12-14 MHz). It is clearly evident that the position of the peaks attributed to the coordinated epoxide (labelled *) change

slightly when different enantiomers of propylene oxide are added to the vanadyl complex.

To extract precise structural information on the weakly coordinated epoxides, ENDOR simulations and DFT calculations were carried out. The new peaks clearly arise from the coordinated epoxide molecule (as they are absent in the spectra of other solvents; Figure 6.4a-c). This statement is supported *via* per-deuterated studies where the epoxide-d_6 (Aldrich) is fully deuterated (Figure 6.7). Performing ^{1}H ENDOR experiment with the per-deuterated epoxide, allowed unambiguious identification of the weakly coordinating epoxide. Several studies have identified ENDOR peaks associated with coordinated solvents, usually *trans* to the oxo group, in vanadyl complexes [11, 12, 13].

In [VO(**11**)], the epoxide is expected to coordinate trans to V=O in the same way. Simulation of the three peaks labelled * in Figure 6.4d are shown in Figure 6.8b and 6.8d, and analysis of the resulting hyperfine tensors yielded two H-V distances of 3.76 Å and 3.66 Å for (*R,R*)-[VO(**11**)] in (*R*)-epoxide and 3.72 Å and 3.57 Å for (*R,R*)-[VO(**11**)] in (*S*)-epoxide (θ = 134° and 150° in both cases, with respect to the V=O bond direction), for the pair of vicinal protons on the epoxide. This demonstrates the ability of ENDOR spectrosocpy to structurally characterise weak diastereomeric complexes in solution (Tables 6.2 and 6.3).

Table 6.2: Calculated DFT and ^{1}H ENDOR distances (H...V=O).

Substrate	**Distance, R (H...V=O), Å**	
	DFT	***ENDOR***
Diamine methane protons	3.04(2), 3.42(2)	3.05, 3.46
Imine protons	4.03(2)	4.03
6-tert butyl groups	....	3.74
Epoxide; R,R in R		3.76, 3.66
Epoxide; R,R in S	3.37, 3.71	3.72, 3.57
Metal Epoxide-Oxygen distance = 2.90 Å		

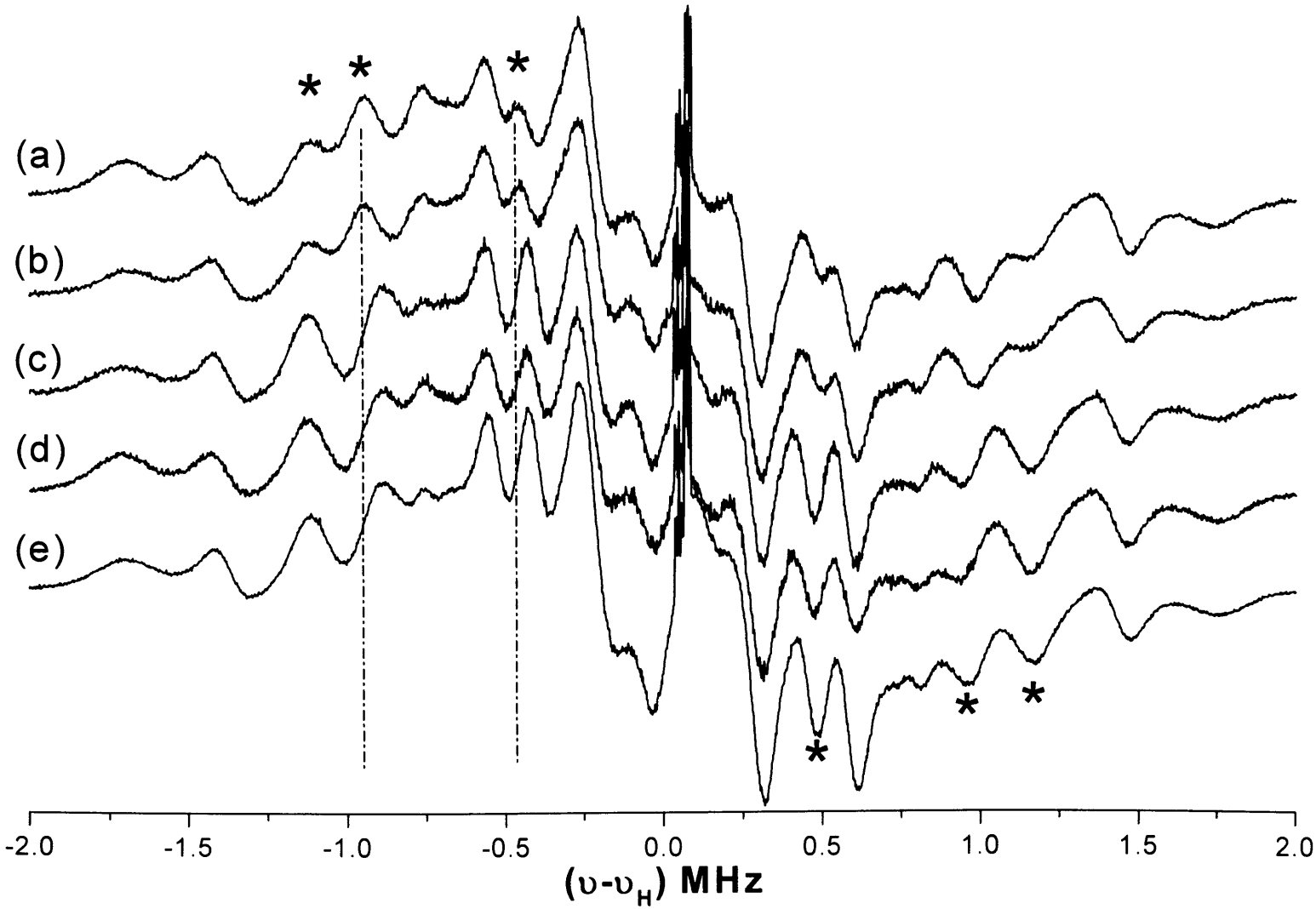

Figure 6.5: X-band ^{1}H ENDOR spectra (10 K) of the diastereomeric states formed between enantiomers of [VO(**11**)] dissolved in (R) or (S) propylene oxide. (a) (*R,R*)-[VO(**11**)] in (S*)* epoxide, (b) (*S,S*)-[VO(**11**)] in (*R*) epoxide, (c) (*R,R*)-[VO(**11**)] in (*R*) epoxide, (d) (*S,S*)-[VO(**11**)] in (*S*) epoxide and (e) (*racemic*)-[VO(**11**)] in (*Racemic*) epoxide. Peaks marked with a * are due to the coordinated epoxide.

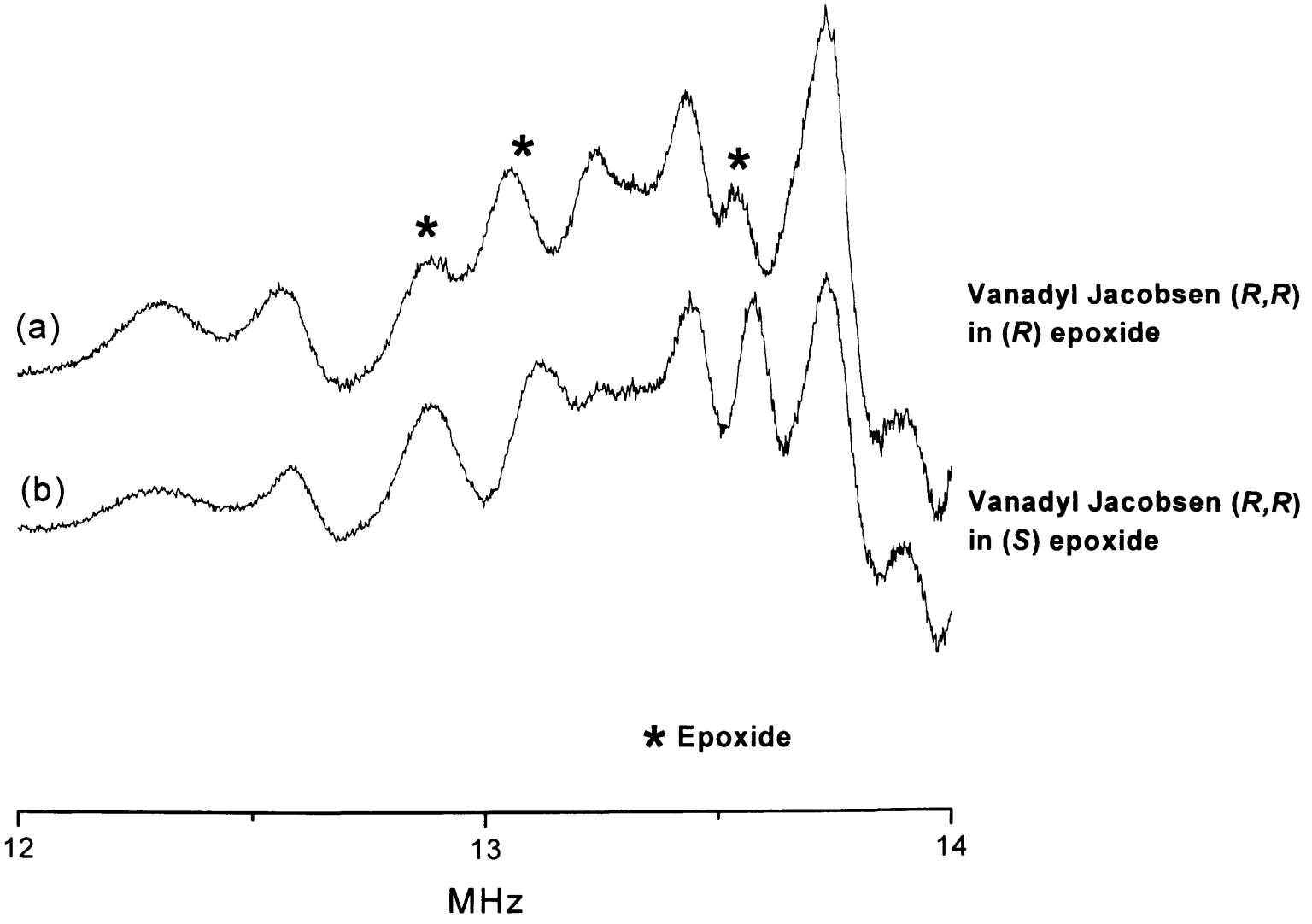

Figure 6.6: X band ^{1}H ENDOR spectra (10 K) of the diastereomeric states formed between enantiomers of [VO(**11**)] dissolved in (a) (R)-propylene oxide and (b) (S)-propylene oxide. * represents co-ordinated propylene oxide.

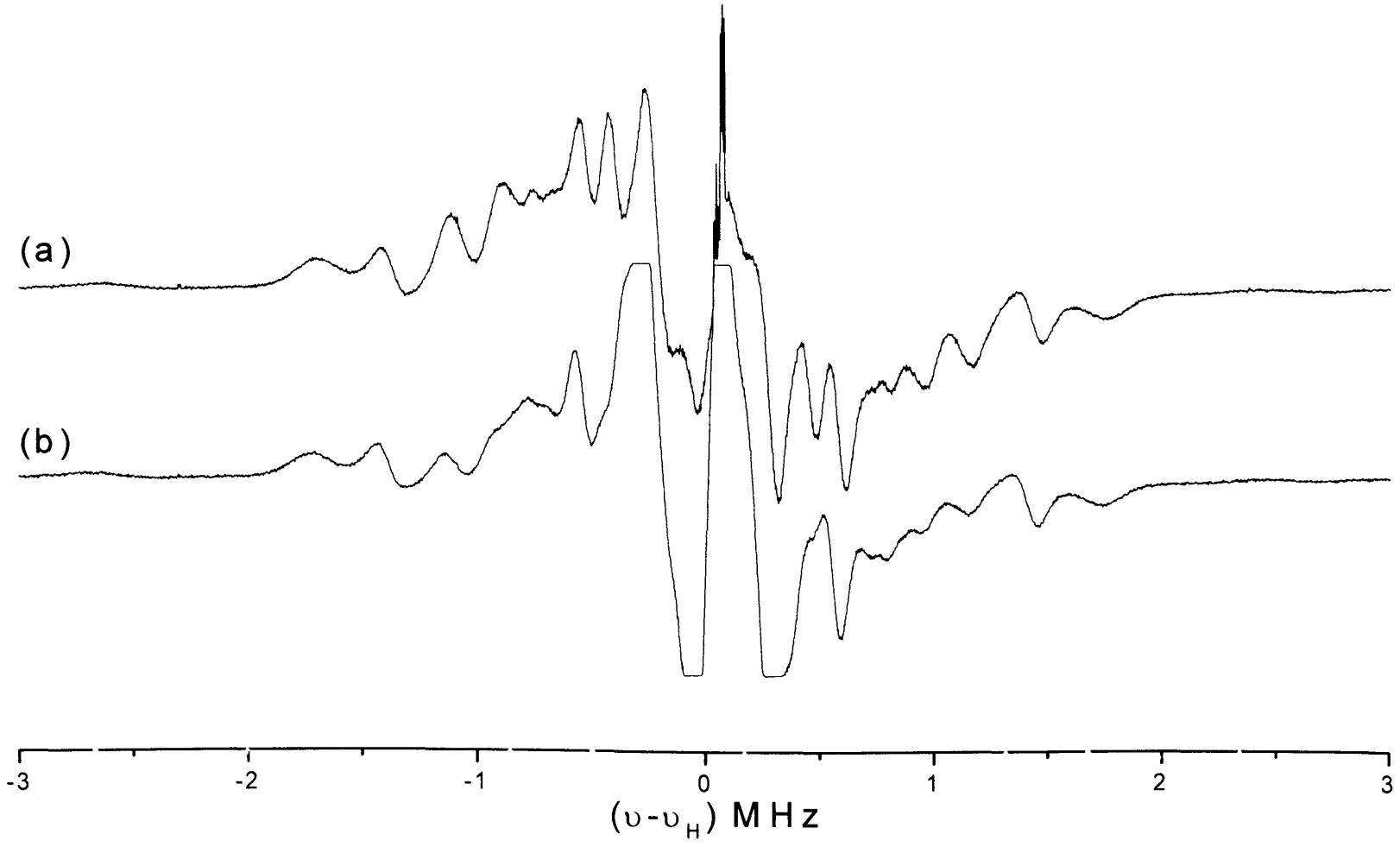

Figure 6.7: X band ^{1}H ENDOR spectra (10 K) of (*R,R*)- [VO(**11**)] dissolved in (a) (*R*)-propylene oxide and (b) (*R*)-propylene oxide-d_6.

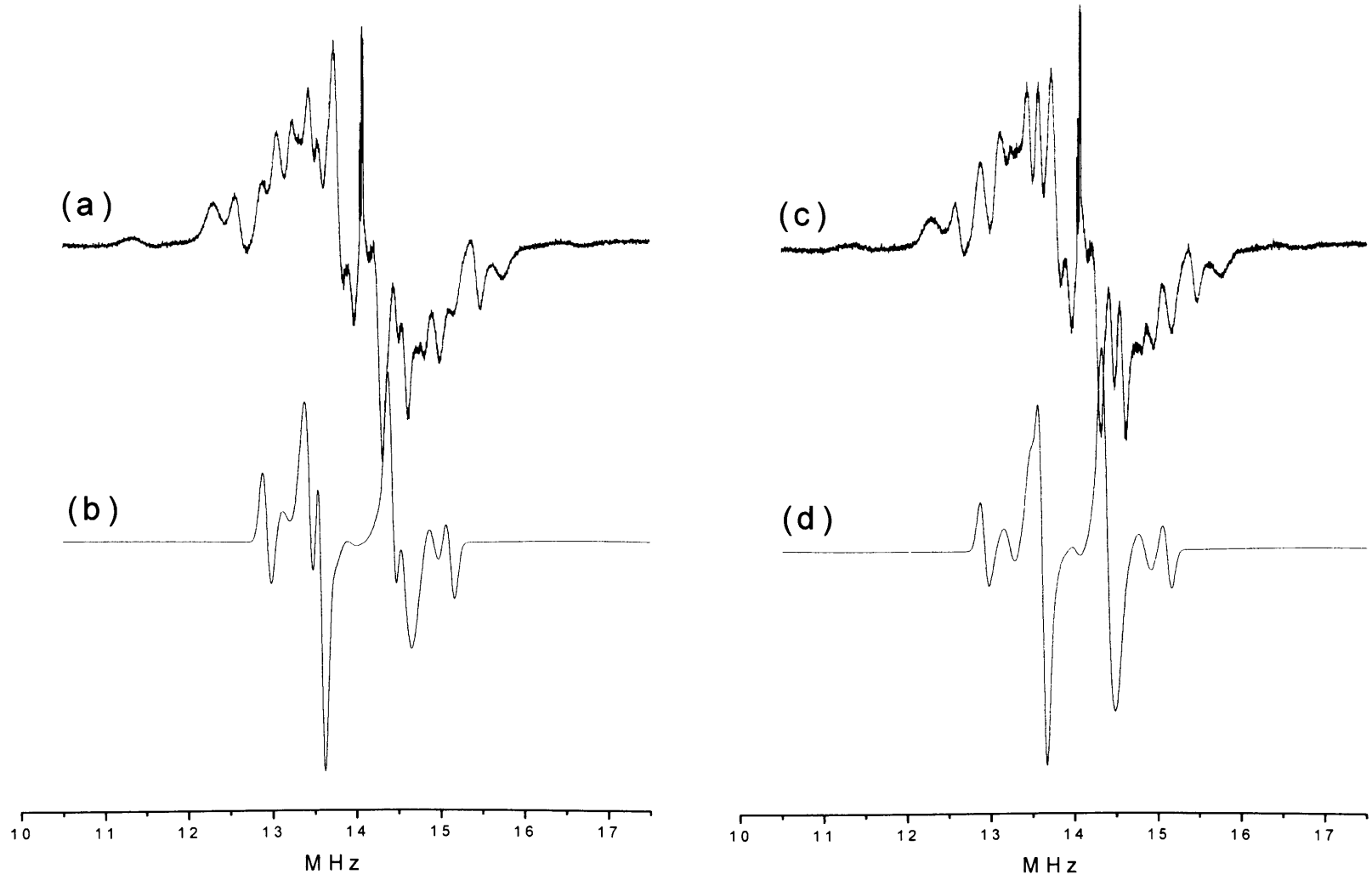

Figure 6.8: X-band ^{1}H ENDOR spectra (recorded at the perpendicular field position 3290G of (a) (*R,R*) - [VO-(**8**)] in (*S*)-**24**, Experimental, (b) (*R,R*) - [VO-(**8**)] in (*S*)-**24,** Simulation, (c) (*R,R*) - [VO-(**8**)] in (*R*)-**24**, Experimental and (d) (*R,R*) - [VO-(**8**)] in (*R*)-**24,** Simulation, illustrating the epoxide peaks only.

Table 6.3: Comparison of ENDOR angle for the ligand protons of the [VO(**11**)] complex in (*R*) and (*S*) propylene oxide.

Substrate	Hyperfine Tensors MHz	A_{iso} / MHz	|| dipolar coupling / MHz	ENDOR angle (θ) / °
(R,R) in (R) epoxide	-0.990, -0.990, 3.390	0.470	2.920	44.0
	-1.10, -1.10, 3.640	0.473	3.167	59.70
(R,R) in (S) epoxide	-1.089, -1.089, 3.430	0.417	3.013	44.0
	-1.450,-1.450, 3.680	0.260	3.420	59.0

6.3.3 *Steric influences*

The ^{1}H ENDOR spectra of a range of vanadyl-schiff base complexes are shown in Figures 6.10 (parallel) and 6.11 (perpendicular region). Figure 6.10a shows salen complexes with the deuterated 1,2-ethylenendiamine backbone. This has been previously analysed and through simulation, accurate hyperfine coupling values extracted (Chapter 5). When the salen is fully protic (Figure 6.10b), peaks arising from the 1, 2-ethylendiamine backbone are evident while a significant degree of inequivalency was found for the axial and equatorial 1,2-ethylenediamine protons (labelled H_{ax}, H_{eq}); 3.172Å(H_{ax}), 3.558Å(H_{ax}) and 3.902Å(H_{eq}). In the latter case, the two equatorial protons were found to be equivalent and therefore cannot be differentiated in the ENDOR spectrum. The difference between the axial and equatorial protons however arises as a result of the complex's symmetry, since the V=O group is positioned above the xy plane. Therefore one of the axial protons will be closer to the V=O group while the second will appear more remote and produce a smaller hyperfine coupling (point dipole approximation).

As the V^{IV}=O complexes increase in bulk (sterically), the ^{1}H ENDOR spectra also increase in complexity. Figures 6.10 and 6.11 are the ^{1}H ENDOR spectra of a series of vanadyl complexes, recorded at parallel and perpendicular EPR absorbtion features respectively. As can be seen from Figure 6.10c, the ENDOR spectra is much

more complicated, however through selective deuteration and changing functional groups, accurate assignements can be made relating to specific proton resonances.

To assist in the interpretation of the ^{1}H ENDOR spectra (and to subsequently differentiate the ligand derived peaks from the epoxide derived peaks), the ENDOR spectra of the following range of protic and deuterated Schiff base vanadyl complexes were measured (Figure 6.9).

In a separate study, solvatochromic interactions in some of these complexes (using protic solvents) have been studied [14]. Figure 6.10c, shows a [V^{IV}=O(salen)-Jac]-(**9**) Jacobsen type complex with bulky *tert-butyl* groups and a cyclohexane backbone. The axial and equatorial protons of the cyclohexane backbone, can be clearly assigned, by analysing a less bulky complex, ie., [V^{IV}=O(salen)-Jac-D_4]-(**14**) (Figure 6.10d).

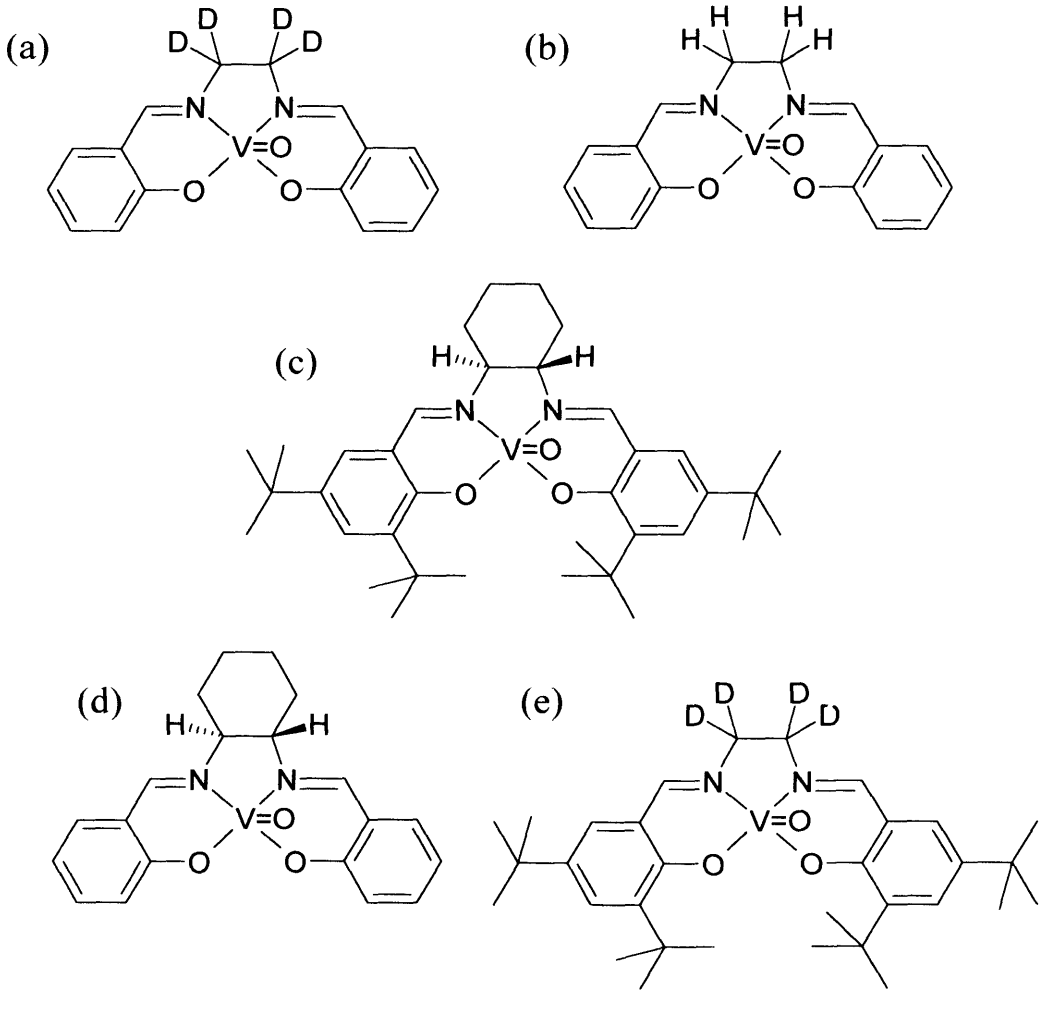

Figure 6.9: A range of vanadyl-Schiff base complexes, (a) [VO(d_4)-(**15**)], (b) [VO-(**9**)], (c) [VO-(**11**)], (d) [VO-(**10**)] and (e) [VO(d_4)-(**14**)].

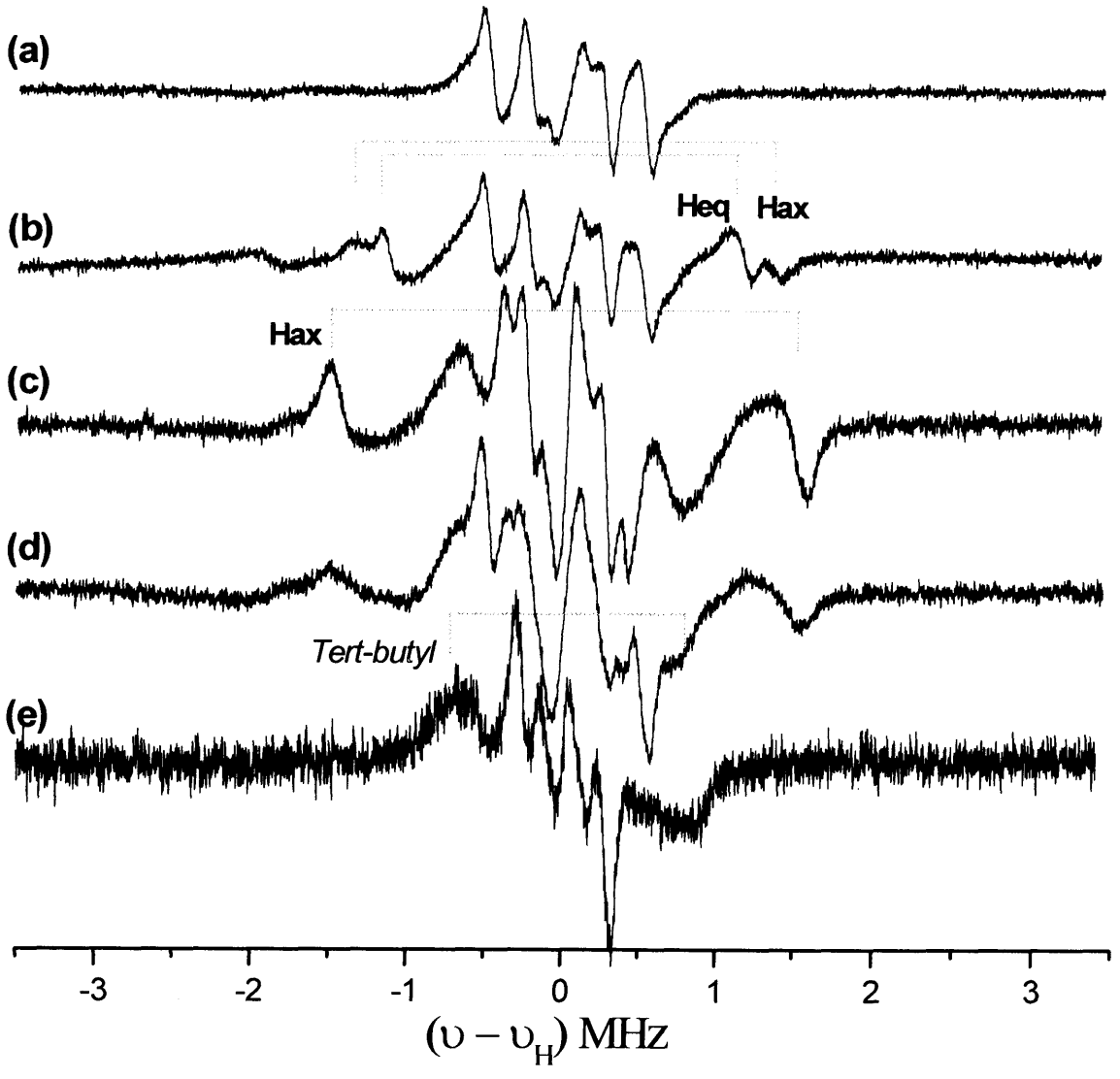

Figure 6.10: X-band ^{1}H ENDOR spectra (parallel position, 2826.0 G) of a range of vanadyl-schiff base complexes ,recorded with a microwave power of 2 mW at 10 K in (a) [V^{IV}O-d_4]-(**11**), (b) [V^{IV}=O-H4]-(**9**), (c) [V^{IV}=O-Jac]-(**9**), (d) [V^{IV}=O-Salophen]-(**10**) and (e) [V^{IV}=O-Jac-D_4]-(**14**). A small amount of toluene-d_8 was added (a-d) in each case, to aid "glass" formation, recorded with a microwave power of 2 mW at 10 K.

In this case the H_{ax} and H_{eq} proton resonances have completely disappeared, but are, however still present in Figure 6.10d. As can be seen from both Figures 6.10 and 6.11, as the "simple" salen complex becomes more sterically hindered, the ENDOR spectra becomes complicated. Although the ENDOR spectra are more complex, accurate coupling constants, bond angles and distances may be obtained, by systematically changing the ligand environment.

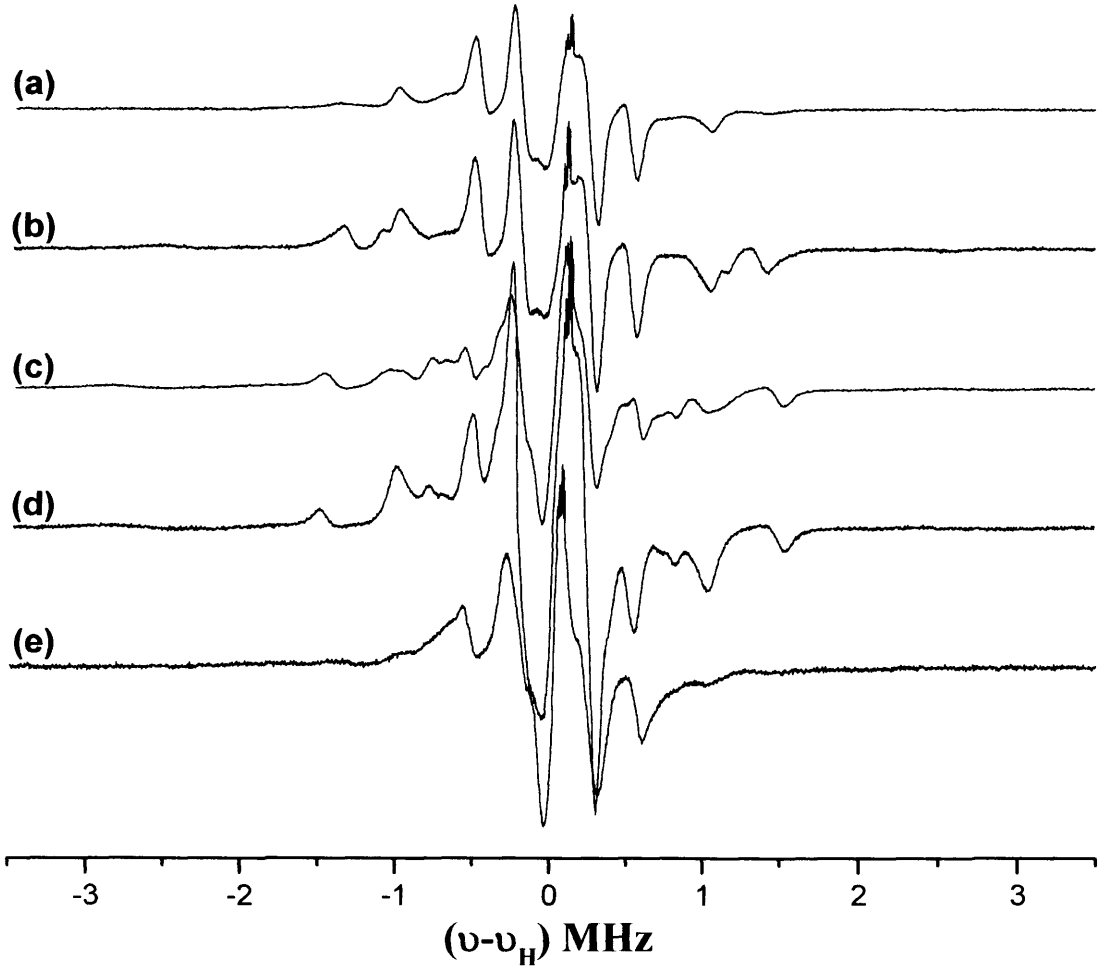

Figure 6.11: X-band ^{1}H ENDOR spectra (perpendicular position, 3289.0 G) of a range of vanadyl-schiff base complexes ,recorded with a microwave power of 2 mW at 10 K in (a) [V^{IV}=O-d_4]-(**11**), (b) [V^{IV}=O-H4]-(**9**), (c) [V^{IV}=O-Jac]-(**11**), (d) [V^{IV}=O-Salophen]-(**10**) and (e) [V^{IV}=O-Jac-D_4]-(**14**). A small amount of toluene-d_8 was added (a-d) in each case, to aid "glass" formation.

6.4 Conclusions

In the Hydrolytic Kinetic Resolution of epoxides (HKR) [15] and related [CrCl(**8**)] catalysts [16], the active species bear an anionic π-basic donor group *trans* to the bound epoxide, similar to the current [VO(**8**)] model. A recent mechanistic study [17] indicates that the key step in enantio-discrimination in the HKR of epoxides by [Co(**8**)(X)] species (X = anion) is the interaction of the activated nucleophile [Co(**8**)(H_2O)(OH)] and the activated epoxide complex [Co(**8**)(OH)(epoxide)] and *not* the enantioselective binding of epoxide substrates by [Co(**8**)(X)] species. The current ENDOR study supports this by showing that chiral Lewis acids, such as [VO(**8**)], bind the 'mismatched' epoxide more strongly, ie., (*R,R*) binds (*R*) epoxide more strongly . If this mismatched species were involved in the hydrolysis step, the opposite enantiomers would be observed as products. The implication of these results is that although, for example, the *R,R*-[Co(**8**)(OH)] and (*R*) epoxide complex is likely to have a higher formation constant than *R,R*-[Co(**8**)(OH)] and (*S*) epoxide, it is the more rapid reaction of the latter complex with [Co(**8**)(H_2O)(OH)] that determines the stereochemical outcome.

^{1}H ENDOR spectroscopy of the chiral complex [VO(**8**)] dissolved in a chiral epoxide solvent in conjunction with DFT calculations, has revealed the presence of additional features originating from the protons of the propylene epoxide, thus illustrating the ability of ENDOR to detect and quantify exceedingly weak interactions in solution. Both ENDOR and DFT were in good agreement with the geometrical structure of the coordinated epoxide. In addition, this chapter presents the identification of distinct diastereomeric transition state models for a coordinated epoxide and have for the first time demonstrated the use of a paramagnetic complex as a chiral ENDOR shift reagent and also the structural parameters on the weak diastereomeric states between the chiral complex and the chiral epoxide in solution have been identified for the first time.

6.5 References

[1] M. Palucki, N. S. Finney, P. J. Pospisil, M. L. Guler, T. Ishida and E. N. Jacobsen, *J. Am. Chem. Soc.*, 1998, **120**, 948.

[2] T. Katsuki, *Coord. Chem. Rev.*, 1995, **140**, 189.

[3] (a) L. E. Martinez, J. L. Leighton, D. H. Carsten and E. N. Jacobsen, *J. Am. Chem. Soc.*, 1995, **117**, 5897-5898. (b) K. B. Hansen, J. L. Leighton, E. N. Jacobsen, *J. Am. Chem. Soc.*, 1996, **118**, 10924.

[4] M Tokunaga, J. F. Larrow, F. Kakiuchi and E. N. Jacobsen, *Science*, 1997, **277**, 936.

[5] S. E. Schaus, B. D. Brandes, J. F. Larrow, M. Tokunaga, K. B. Hansen, A. E. Gould, M. E. Furrow and E. N. Jacobsen, *J. Am. Chem. Soc.*, 2002, **124**, 1307.

[6] T. Hashihayata, T. Punniyamurthy, R. Irie, T. Katsuki, M. Akita and Y. Moro-oka, *Tetrahedron*, 1999, **55**, 14599.

[7] R. Bobb, G. Alhakimi, L. Studnicki, A. Lough, J. J. Chin, *J. Am. Chem. Soc.*, 2002, **124**, 4544.

[8] D.M. Murphy, I.A. Fallis, R.D. Farley, R.J. Tucker, K.L. Avery, D.J. Willock, *Phys.Chem.Chem.Phys.*, 2002, **4**, 4937.

[9] D. Attanasio, *J.Phys.Chem.*, 1986, **90**, 4952.

[10] See chapter for details on computational work.

[11] G.H. Rirst, J.S. Hyde, *J.Phys.Chem.*, 1970, **52**, 4633.

[12] B.M. Hoffman, J. Martinsen, R.A. Venters, *J.Magn.Reson.*, 1984, **59**, 110.

[13] G.C. Hurst, T.A. Henderson, R.W. Kreilick, *J.Am.Chem.Soc.*, 1985, **107**, 7294.

[14] R.J. Tucker, I.A. Fallis, R.D. Farley, D.M. Murphy, D.J. Willock, *Chem. Phys. Letts.*, 2003, **380**, 757.

[15] M. Tokunaga, J.F. Larrow, F. Kakiuchi, E.N. Jacobsen., *Science*, 1997, **277**, 936.

[16] K.B. Hansen, J.L. Leighton, E.N. Jacobsen, *J. Am. Chem. Soc.*, 1996, **118**, 10924.

[17] L.P.C. Nielsen, C.P. Stevenson, D.G. Blackmond, E.N. Jacobsen, *J. Am. Chem. Soc.*, 2004, **126**, 1360.

Chapter 7

Observations of diastereomeric interactions in an amine-copper (II) Schiff-base complex

Observations of diastereomeric interactions in an amine-copper (II) Schiff-base complex

7.1 Introduction

Chiral metal salen type compounds, have been widely studied over the years and an in-depth investigation has been comprehensively carried out into their excellent catalytic properties, especially in homogeneous asymmetric catalysis [1-4]. They have also been studied in view of their significance as biomimetic catalysts [5-7] and in chemical oxidation. Huang *et al* [8] reported the use of copper (II) salen for the catalytic oxidation of alcohols to the associated carbonyl compounds, while Jiang and Xi [9], showed that the same complex, in the presence of a base, could be employed for use in the catalytic oxidation of cyclohexanol, via oxygen. Asymmetric catalysts are predominately based on transition metal complexes, as the coordination geometry of the transition metal, eg Cu(II), Ni(II) or Co(II), can in principle prevent movement of the relative positions of the reactants and the oxidation state may facilitate the catalytic reaction [10]. This unique ability to fix the mutual orientation of the chiral ligands and substrates in the coordination sphere of the complex, provides the necessary chiral template for chiral recognition in the reaction's transition state [11,12]. This is especially the case for achiral substrates, where chirality is introduced *via* these transition states. However, enantioselective or diastereomeric reactions may occur by the chiral discrimination of one enantiomer of the substrate [13]. In the latter case, the orientation and structural properties adopted by the ligands in solution, are of importance to transcribe the stereochemical information from the metal complex (Cu(II)) to the reaction substrate. To fully understand how these complexes convey this chemical information in solution, it is necessary to structurally elucidate the environment immediately surrounding the metal centre and study the molecular geometry of the metal complexes themselves.

Unlike the previous chapter where the metal binding site of the ligand was replaced by the vanadyl ion (V=O) [14,15] using a weakly interacting substrate (ie., an epoxide), in this chapter copper has been employed as the bound metal ion using a more strongly interacting substrate (ie., an amine) in different salen-type ligands (see scheme 1). As electron-nuclear double resonance (ENDOR) can supply greater

information on the neighbouring couplings between the electron spin of the transition metal and the nuclei of the ligand or substrate, one can determine the spatial arrangement of the ligand protons in a frozen solution state. In order to extract and interpret information from the *cw* proton ENDOR spectra, and hence transcribe this data into a meaningful spatial geometric description of the metal complex in frozen solution, an ENDOR simulation program based on the resonance expression of Hurst *et al* [16] was used to extract detailed information on proton coordinates in solution.

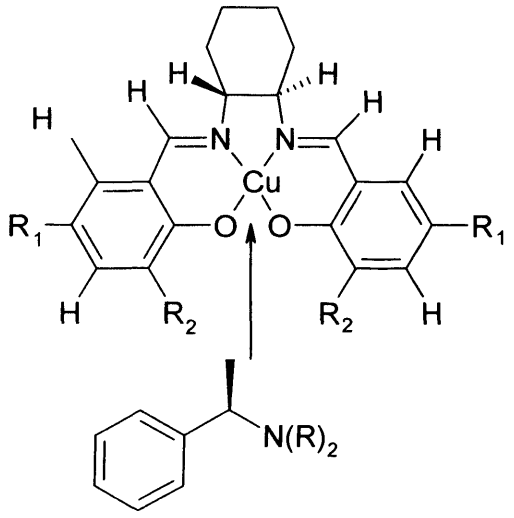

(**18**) - R_1 = *t*-bu R_2 = *t*-bu **R** = H or D
(**20**) - R_1 = NO_2 R_2 = NO_2
(**22**) - R_1 = NO_2 R_2 = H

Scheme 7.1

This chapter therefore describes a preliminary study on the investigation of chiral discrimination between a chiral amine (methyl benzyl amine; MBA) and a series of derivatives of the copper (II) salen-type complex (see Scheme 7.1). To further understand the degree of chiral discrimination of the axially coordinated amine, a wide range of structurally similar ligand systems were synthesised with subtle changes in electronic and steric configurations (Scheme 7.1). It is widely published that stereochemical communication between the environment surrounding the ligand and the substrate is essential in catalysis for obtaining high enantioselectivities [17]. Even though ligand steric properties contribute substantially to asymmetric chiral induction mechanisms, electronic effects have also been shown to be of much importance in the catalytic process [18, 19, 20, 21].

In the current chapter, it will be demonstrated how *cw* ENDOR can be used to discriminate between diastereomeric states of the substrate-complex adducts and illustrate how ENDOR spectroscopy can detect the subtle coordination effects in

frozen solution, through altering the electronic and steric bulkiness of the metal-ligand complex. The results presented in this chapter were obtained in the last period of the PhD thesis, and hence only a preliminary analysis of the spectra will be presented.

7.2 Experimental

7.2.1 *Measurement and analysis of EPR / ENDOR spectra*

EPR/ENDOR measurements were performed using a small quantity (*ca.* 5mg) of the copper (II) complex (**18**), (**20**) and (**22**) dissolved in 100μL of the chiral amine ((*R*- or *S*-) methylbenzyl amine, *Aldrich*, 98%). A small amount of deuterated toluene (10μL) was added to the sample to enhance the quality of the glass in the frozen solution. Partially deuterated methylbenzyl amine (hereafter abbreviated to MBA-d_2) was prepared by refluxing with D_2O for 1 hour and the MBA removed by distillation. ^1H NMR integration data (DPX-400 (400 MHz)) showed deuteration levels of >90% and the amine was used without further purification.

Accurate spin Hamiltonian parameters for the EPR spectra were obtained by computer simulation (*Simfonia*) and the results are presented in Table 7.1.

7.3 Results and Discussion

7.3.1 *EPR analysis of the copper (II) complexes*

The EPR spectra of the complexes (**18**), (**20**) and (**22**) were recorded in a variety of solvents including neat toluene, MBA and MBA-d_2. In the latter two cases, a small quantity of toluene was usually added. In most cases the solutions were prepared under relatively dilute conditions because at high concentrations, the complexes are known to aggregate upon freezing, as reported by Hyde *et al* [22]. Because ENDOR is inherently less sensitive than EPR, the solutions prepared for ENDOR analysis are stronger than those for EPR analysis. In that case, the EPR spectra occasionally possess traces of other minor components possibly due to this aggregation effect, as the sample is more concentrated.

In principle, it should be possible to determine how many MBA molecules are coordinated to the essentially square planar copper(II) complexes (**18**), (**20**) and (**22**), since the spin Hamiltonian parameters of Cu(II) species are very characteristic of the local symmetry. Therefore the EPR spectrum of racemic [Cu(**18**)] was first recorded in neat toluene, and the resulting spectrum is shown in Figure 7.1. The EPR spectra at 10K exhibit axial symmetry with well-resolved parallel (||) features and superhyperfine (shf) structures in the perpendicular region of the spectra [23,24]. It can also be observed that there is an additional "overshoot" feature in the perpendicular region resulting from the angular dependence of the copper hyperfine lines [25]. This EPR spectrum is typical of a square planar type copper species, as confirmed by computer simulations (shown later). After addition of one equivalent of MBA per copper centre, the spectrum changes to that shown in Figure 7.1b. The parallel values appear to have shifted to lower field, as expected for axial coordination of a donor substrate. However, the changes to the g and A values is only small. Subsequently, racemic [Cu(**18**)] was dissolved in neat MBA and the resulting spectra are shown in Figure 7.1c. This spectrum is very similar to that recorded for an MBA:Cu ratio of 1:1. This observation suggests that one MBA molecule coordinates axially to the copper complex. It is interesting to note that the spin Hamiltonian parameters (particularly $A_{||}$) measured for [Cu(**18**)] in neat MBA are only slightly smaller than those determined for [Cu(**18**)] in toluene, but by far larger than those expected for a copper species possessing well defined square pyramidal or pseudo octahedral symmetry. In other words, while the EPR spectra in Figure 7.1 confirm MBA coordination to the copper complex, they also indicate that the interaction is relatively weak (ie., not strong enough to produce an octahedral symmetry from an EPR viewpoint). While amines are expected to strongly coordinate to copper(II) centres (particularly square planar systems), the presence of the bulky *t*-butyl substituents on the ligand and the aromatic group of the MBA donor may serve to render a weak interaction.

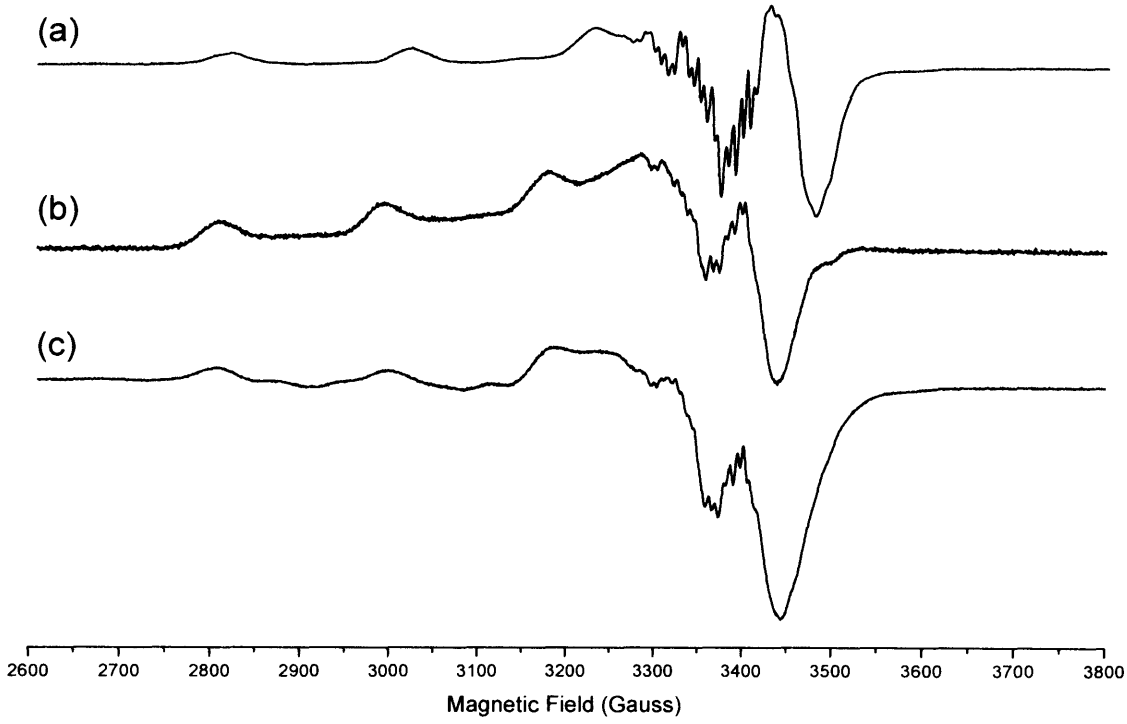

Figure 7.1: X-band (9 GHz) EPR spectra of racemic copper (II) salen-type complex [Cu(**18**)] in (a) neat toluene, (b) one equivalent of methylbenzyl amine (MBA) and (c) an excess of MBA. The spectra were measured at 10 K.

Table 7.1: Spin Hamiltonian parameters for the copper complexes in (*S*)-MBA and toluene.

Experiment	A_{xx} / **MHz**	A_{yy} / **MHz**	A_{zz} / **MHz**	g_{xx}	g_{yy}	g_{zz}
Racemic-[Cu(**18**)]	$^{Cu}90$	$^{Cu}90$	$^{Cu}610$	2.043	2.043	2.194
in toluene	$^{N}38.5$	$^{N}37.4$	$^{N}50.17$			
	$^{H}17.1$	$^{H}17.95$	$^{H}21.7$			
(*R,R*)-[Cu(**18**)]	$^{Cu}98$	$^{Cu}98$	$^{Cu}570$	2.053	2.053	2.229
in (*S*)-MBA						
(*R,R*)-[Cu(**20**)]	$^{Cu}98$	$^{Cu}98$	$^{Cu}510$	2.053	2.053	2.233
in (*S*)-MBA						

The EPR spectrum of [Cu(**18**)] in neat toluene was simulated using the SIMFONIA software. The resulting simulation is shown in Figure 7.2. While the superhyperfine couplings to the ligand nuclei are not so clearly resolved in the parallel features, they are well resolved in the perpendicular region. In particular the ligand nitrogen nuclei, and the large couplings to the imine protons complicate this region of the spectrum. Nevertheless these couplings were accurately determined in the ENDOR spectra (as discussed later). Therefore using the results from the ENDOR spectra for ^{N}A and ^{H}A, the spectrum was successfully simulated, and the spin Hamiltonian parameters are presented in Table 7.1. These values are typical for other copper Schiff base type complexes [26] and confirm the square planar arrangement of the copper.

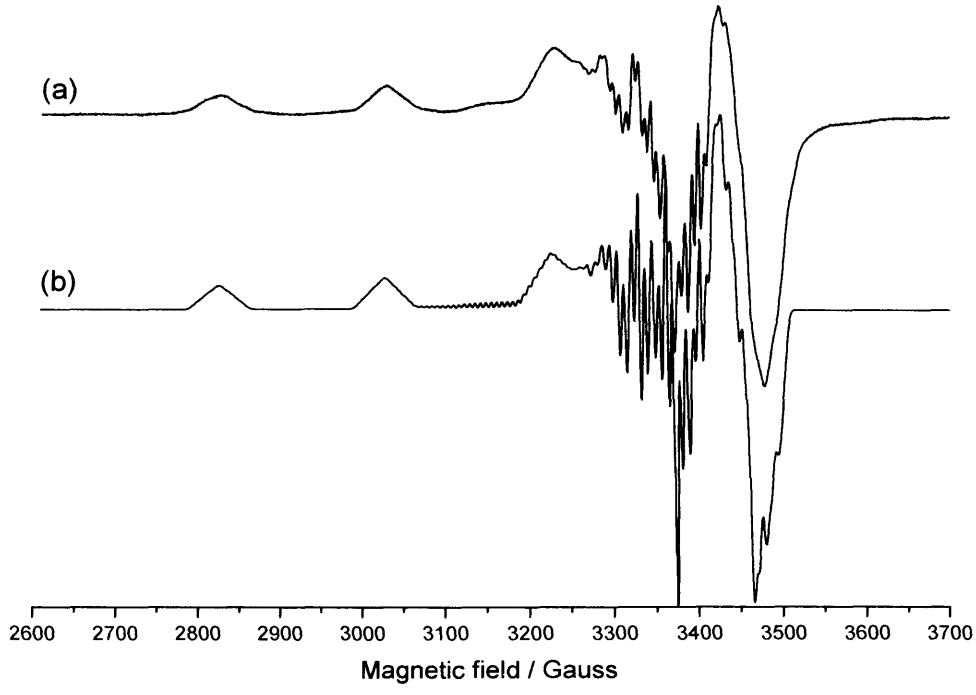

Figure 7.2: X-band (9 GHz) EPR spectra of Racemic-[Cu(**18**)] dissolved in toluene (a) experimental, and (b) simulation. The spectra was measured at 10K.

EPR simulations of the [Cu(**18**)] complex in MBA were also carried out. However, the ^{14}N superhyperfine region of the spectra were more complicated in this case. The ^{14}N ENDOR peaks were also broader and more difficult to resolve compared to the situation in neat toluene only. Accurate ^{14}A couplings were therefore difficult to extract, so the X-band simulation is shown. However, a reliable estimate of

the g and A parameters was possible by recording the Q-band EPR spectra, which was easily simulated (Figure 7.3). The resulting Cu spin Hamiltonian parameters are listed in Table 7.1, and once again confirm the slight shift in values due to weak coordination of MBA.

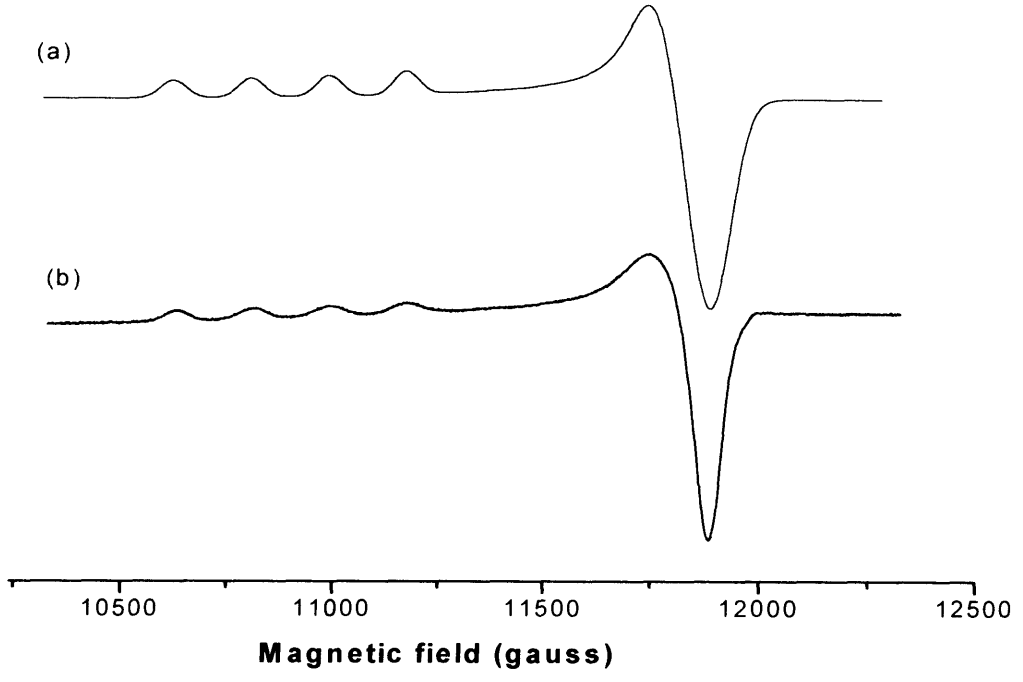

Figure 7.3: Q-band (34GHz) EPR spectra of (*R,R*)-(**18**)] dissolved in (*S*)-methylbenzyl amine (MBA) / toluene-d_8, (a) experimental and (b) simulation. The spectrum was measured at 10K.

The above EPR results confirm that MBA coordinates (weakly) to the racemic [Cu(**18**)] complex. Therefore, a series of experiments was carried out to investigate whether EPR (and later ENDOR) could evidence any diastereomeric pairs between individual enantiomers of the complex and enantiomers of the MBA. The resulting EPR spectra for (*R,R*)-[Cu(**18**)] in (*R*)-MBA, (*S,S*)-[Cu(**18**)] in (*S*)-MBA, (*R,R*)-[Cu(**18**)] in (*S*)-MBA, (*S,S*)-[Cu(**18**)] in (*R*)-MBA and finally racemic Cu(**18**)] in racemic MBA are shown in Figure 7.4. At first glance the spectra all appear very similar. However careful inspection of the superhyperfine splittings in the perpendicular region, reveal some slight differences between the spectra. Specifically it appears that the spectra of (*R,R*)-[Cu(**18**)] in (*R*)-MBA and (*S,S*)-[Cu(**18**)] in (*S*)-MBA are similar to each other while (*R,R*)-[Cu(**18**)] in (*S*)-MBA and (*S,S*)-[Cu(**18**)] in (*R*)-MBA are also similar to each other, but different from the first pair. Unlike the

case described in the last chapter for [VO(**11**)] in propylene oxide, no evidence of diastereomeric pairs could be seen in the EPR spectra alone (ENDOR was required to reveal the subtle differences in binding modes of the epoxide). In this case the MBA molecules probably bind more strongly compared to the epoxide, so the manner of binding is felt more strongly by the metal center (ie., it is visible in the EPR spectra). Further comfirmation of differences in enantiomer binding is provided in the ENDOR spectra (as discussed later).

It is well known that changes to the functional groups of the ligand can alter the electronic properties of the central metal ion itself. Therefore in an attempt to alter the Lewis acidity of the copper, and thereby influence the strength of the MBA interaction, the $-NO_2$ derivatives of [Cu(**20**)] and [Cu(**22**)] were prepared and their EPR spectra recorded in MBA. Unfortunately, the solubility of these ligand in MBA was quite poor, compared to [Cu(**18**)], so that it was difficult to obtain a good glass during the EPR measurements. The resolution of the spectra, particularly in the informative perpendicular region are not good. Based on the EPR results alone, it is not possible to distinguish any differences between the binding mode of enantiomers of [Cu(**20**)] (Figure 7.5) and [Cu(**22**)] (Figure 7.6) in *R*- or *S*- MBA. However, since the Lewis acidity of the copper ion has increased by the presence of the $-NO_2$ groups, the strength of the MBA binding would be expected to increase, effectively smearing out any subtle differences in diastereomers. This observation is confirmed in the ENDOR spectra, as discussed later.

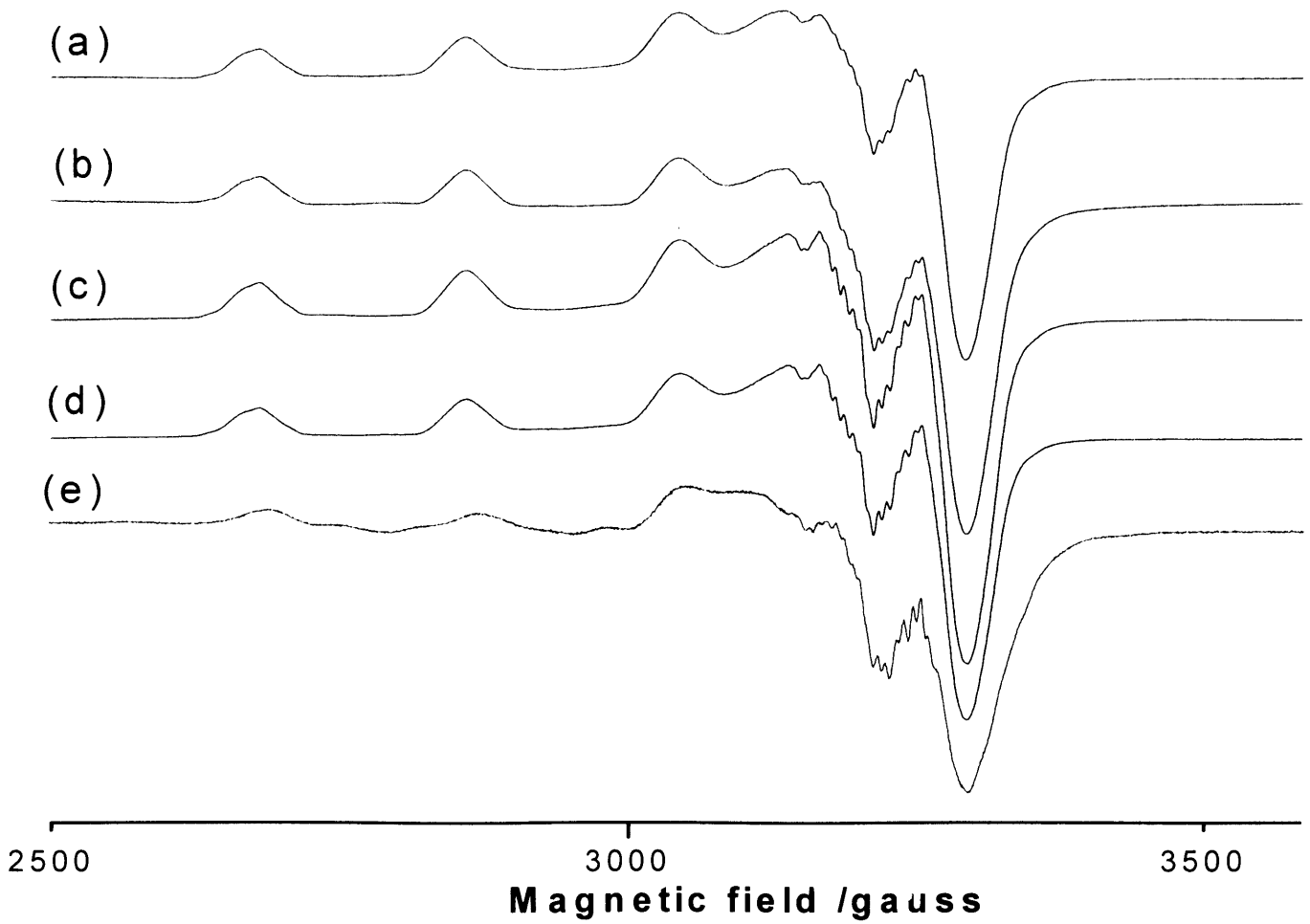

Figure 7.4: X-band (9 GHz) EPR spectra of [Cu(**18**)] dissolved in Methylbenzyl amine (MBA). (a) (*R,R*)-[Cu(**18**)] in (*R*), (b) (*S,S*)-[Cu(**18**)] in (*S*), (c) (*R,R*)-[Cu(**18**)] in (*S*), (d) (*S,S*)-[Cu(**18**)] in (*R*) and (e) racemic –[Cu(**18**)] in racemic-MBA. The spectra were measured at 10K.

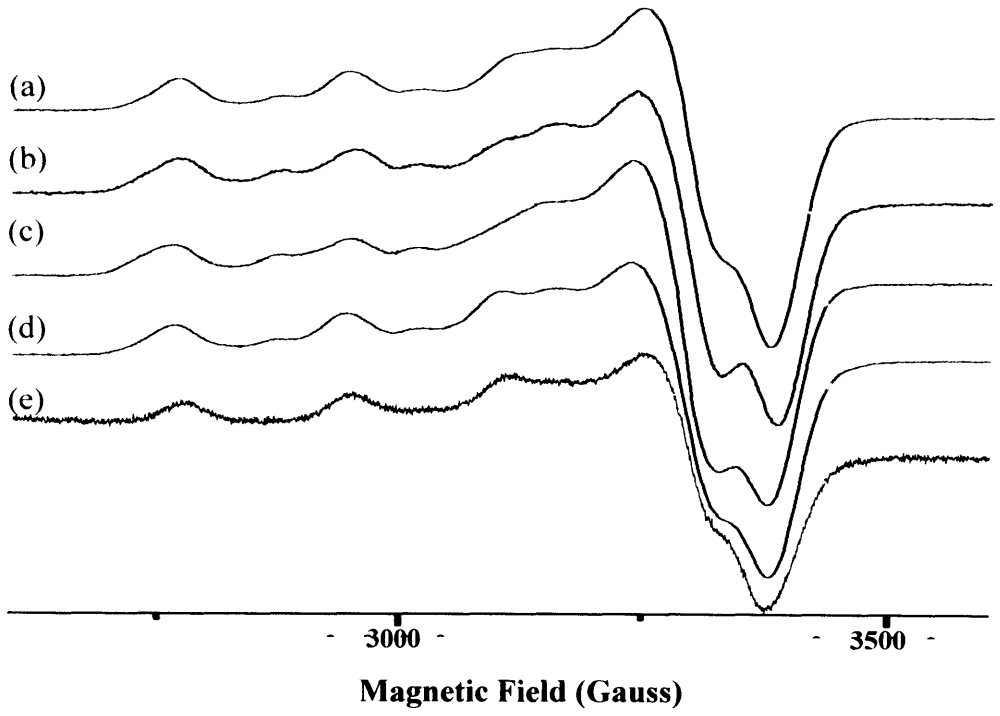

Figure 7.5: X-band (9 GHz) EPR spectra of [Cu(**20**)] dissolved in methylbenzyl amine (MBA), (a) (*R,R*)-[Cu(**20**)] in (*R*), (b) (*R,R*)-[Cu(**20**)] in (*S*), (c) (*S,S*)-[Cu(**20**)] in (*R*), (d) (*S,S*)-[Cu(**20**)] in (*S*) and (e) racemic –[Cu(**20**)] in racemic-MBA. The spectra were measured at 10K.

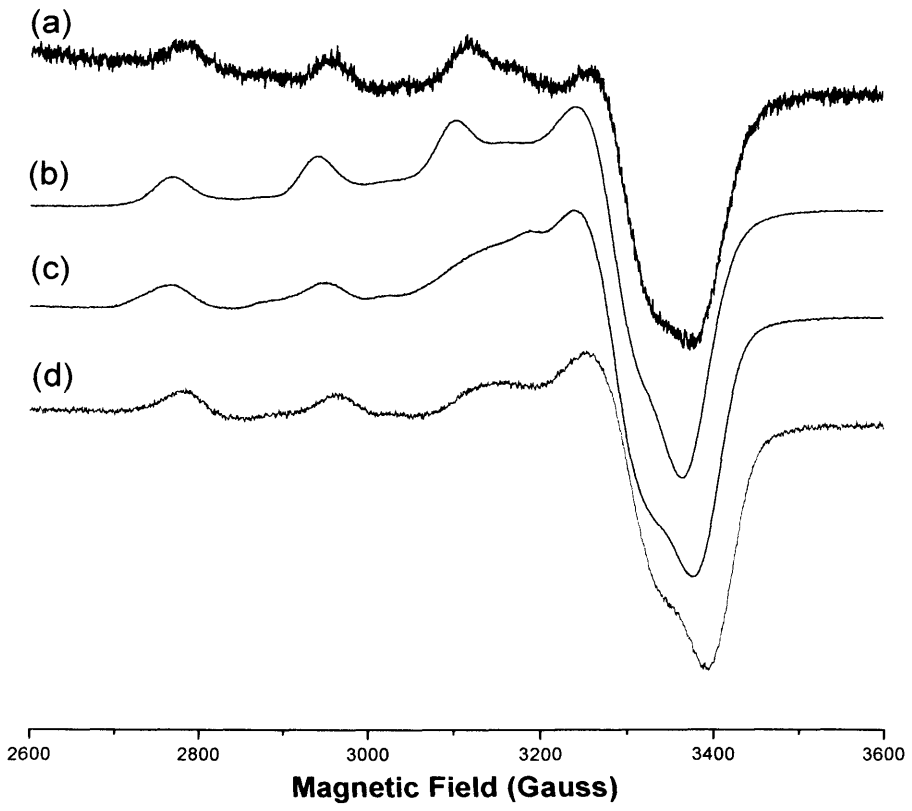

Figure 7.6: X-band (9 GHz) EPR spectra of [Cu(**22**)] dissolved in methylbenzyl amine (MBA), (a) (*R,R*)-[Cu(**22**)] in (*R*), (b) (*S,S*)-[Cu(**22**)] in (*S*), (c) (*S,S*)-[Cu(**22**)] in (*R*), and(d) (*R,R*)-[Cu(**22**)] in (*S*). The spectra were measured at 10K.

7.3.2 *ENDOR analysis of the copper complexes*

The ^{1}H ENDOR spectra of racemic [Cu (**18**)] in toluene, and in MBA are shown in Figure 7.6. In (**18**), the equatorial protons are not present due to the cyclohexyl ring, and therefore only the axial protons should produce observable splittings. This is indeed the case, and peaks at 5.2 MHz and 3.2 MHz can clearly be seen in the wings to the ENDOR spectrum (Figure 7.7a, labelled with a dashed line). The remaining peaks in this spectrum are due to the weak couplings from (a) the aromatic protons of the (**18**) ligand, and (b) either the $-CH_2$ groups of the cyclohexyl ring or the *t*-butyl groups themselves. These assignments must be confirmed by simulation, and by use of the "naked" derivative of (**18**) in which the *t*-butyl groups are absent.

The couplings to the ligand protons of [Cu (**18**)] dissolved in toluene are also visible when the same complex is dissolved in MBA (Figure 7.7b and c). A small shift in the couplings to the axial ethylenediamine protons has occurred (5.2 MHz and 3.05 MHz) following coordination of the MBA. However more importantly new peaks have appeared in the spectrum, which must be assigned to the amine protons. As seen later this assignment was confirmed by deuteration of the $-NH_2$ groups in MBA, which resulted in the lost of the peaks marked * in Figure 7.7. The associated proton ENDOR spectra recorded at the low field copper parallel peak is also shown for completeness in Figure 7.8. This data will be used to complete the ENDOR simulations of this system.

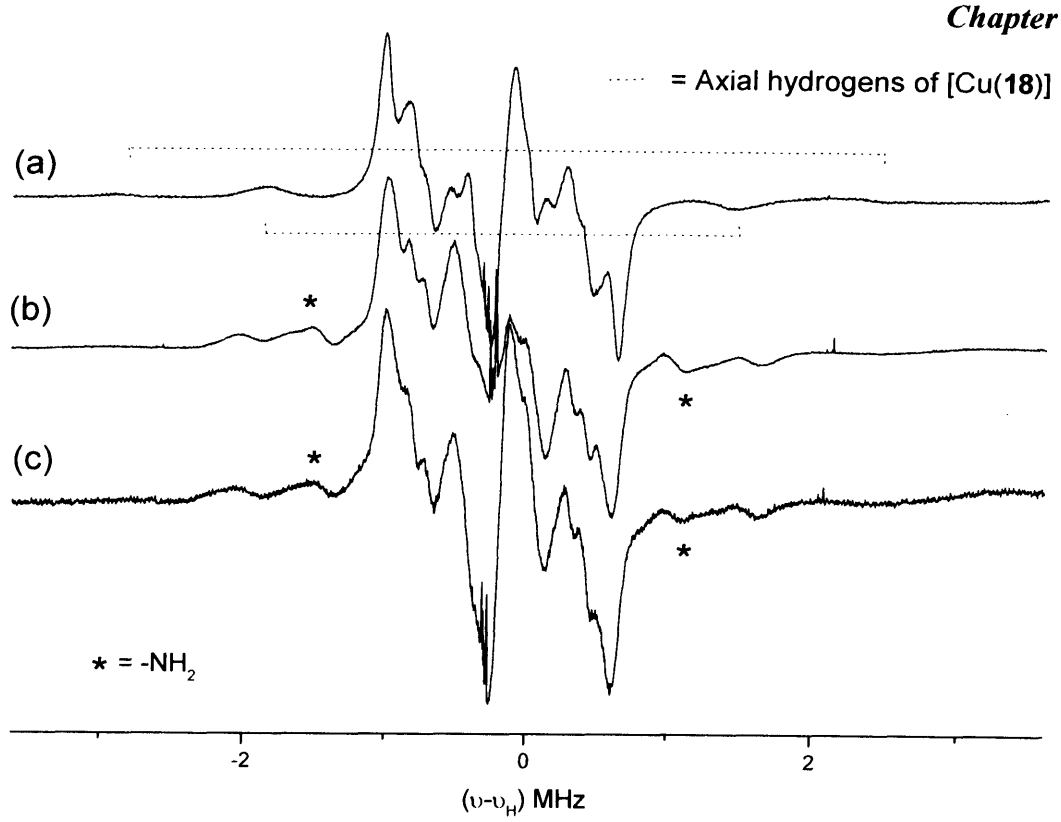

Figure 7.7: X-band (perpendicular) ^{1}H ENDOR spectra of *racemic*-[Cu(**18**)] (3312 Gauss) in (a) toluene, (b) *racemic*-MBA (one equivalent) and (c) an *excess* of MBA.

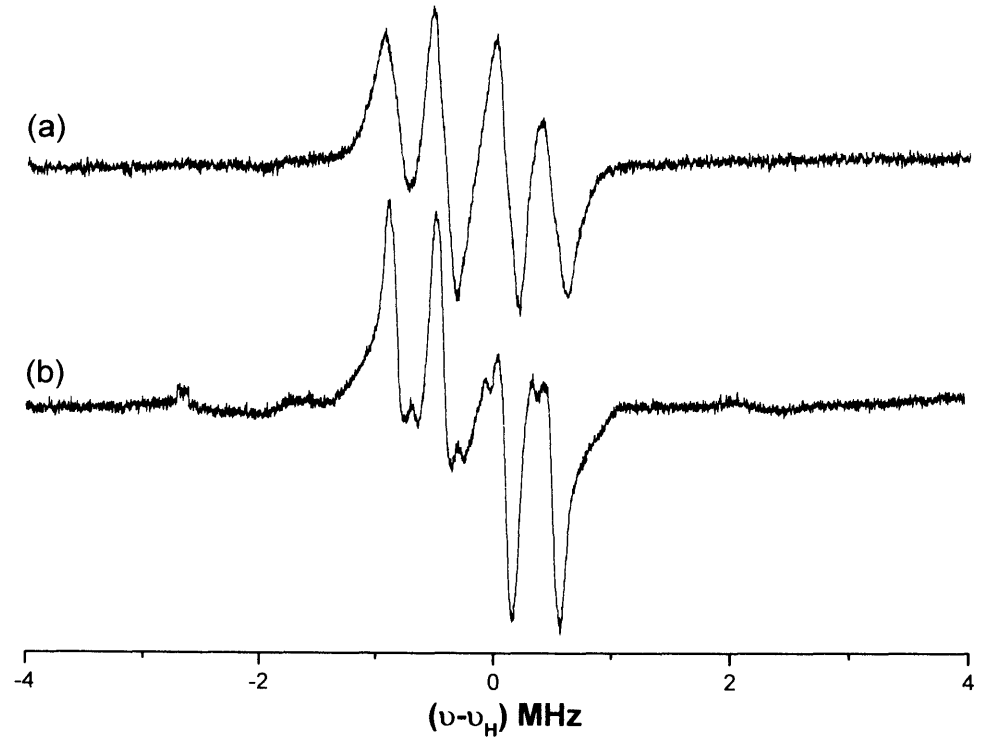

Figure 7.8: X-band (parallel) ^{1}H ENDOR spectra of *racemic*-[Cu(**18**)] (2773 Gauss) in (a) toluene and (b) *racemic*-MBA (one equivalent).

It is known from related work on copper Schiff base ligands, that the $d_{x^2-y^2}$ ground state of copper results in substantial isotropic spin densities on the ligand nitrogens and also large isotropic couplings to the imine protons (see Scheme 7.1). While this large imine coupling can be observed in the X-band ENDOR spectrum, it is far more easily resolved in the Q-band ENDOR spectrum. A representative example of this resolution is shown in Figure 7.9 for (*S,S*)-[Cu(**18**)] dissolved in *S*-MBA. The clearly resolved couplings of 21.5, 17.4 and 16.8 MHz are seen in the spectra. These couplings can be compared to 22.8, 19.4 and 18.4 for [Cu(**18**)] in toluene. The reduction in the isotropic coupling is due to the coordination of the MBA to the copper ion. Decreased hyperfine couplings from the chelate nitrogens and from the imine protons have been reported for pyridine coordination to copper salen complexes as the fifth ligand causes a significant reduction in the covalent bonding in the complex plane [27]. Further confirmation of this binding is found in the reduced ^{14}N couplings.

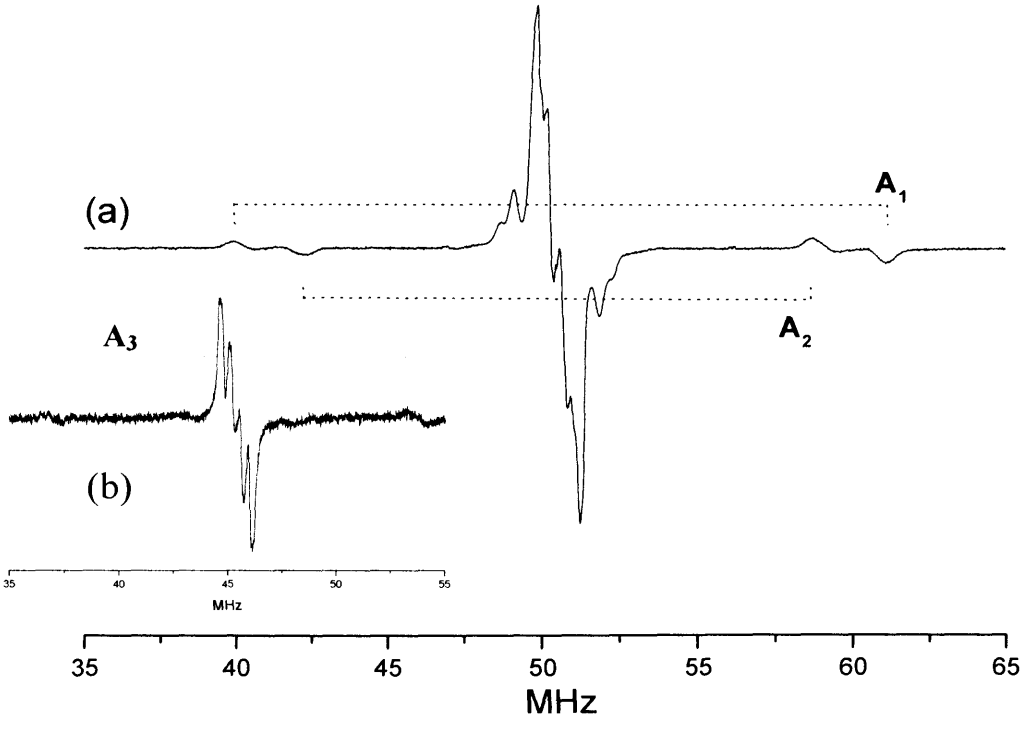

Figure 7.9: Q-band ^1H ENDOR spectra of (*S,S*)-[Cu (**18**)] dissolved in (*S*) – Methylbenzyl amine (MBA) / toluene-d_8 (1:1) recorded with a microwave power of 2.5 mW at 10K. (a) Experimental spectrum perpendicular position and (b) parallel position.

The wide sweep ENDOR spectrum of racemic [Cu (**18**)] in toluene and in MBA are shown in Figure 7.10. The nitrogen couplings are clearly resolved in all cases. Computer simulations of these couplings were not carried out, however a preliminary analysis of the spectra can reveal the magnitude of the hyperfine and quadrupolar couplings (Figure 7.11). Approximate couplings of ^{N}A= [50.8, 37.5, 38.5] MHz and ^{N}Q = [-1.15, 0.7, 0.45] MHz were determined for [Cu (**18**)] in toluene, while couplings of A(N)= [49.8, 36, 36.5] MHz and Q(N) = -1.20, 0.7, 0.5] MHz were determined for [Cu (**18**)] in MBA. Although small, these shifts confirm the proton results that a decrease in the covalent bonding in the complex due to MBA coordination, results in a decreased spin density on the ligand nitrogens.

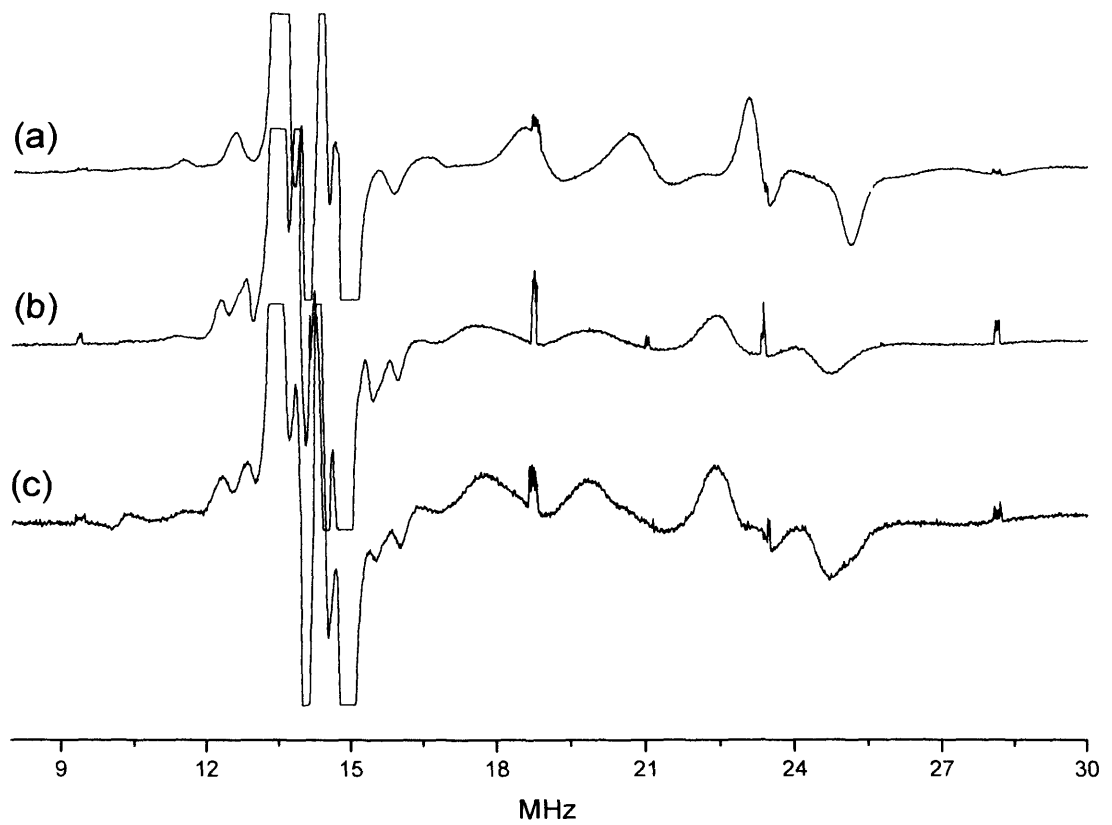

Figure 7.10: X-band (perpendicular-wide sweep) ^{1}H ENDOR spectra of *racemic*-[Cu(**18**)] in (a) toluene, (b) *racemic*-MBA (one equivalent) and (c) an *excess* of MBA. A small quantity of deuterated toluene was added in each case to aid homogeneous glass formation.

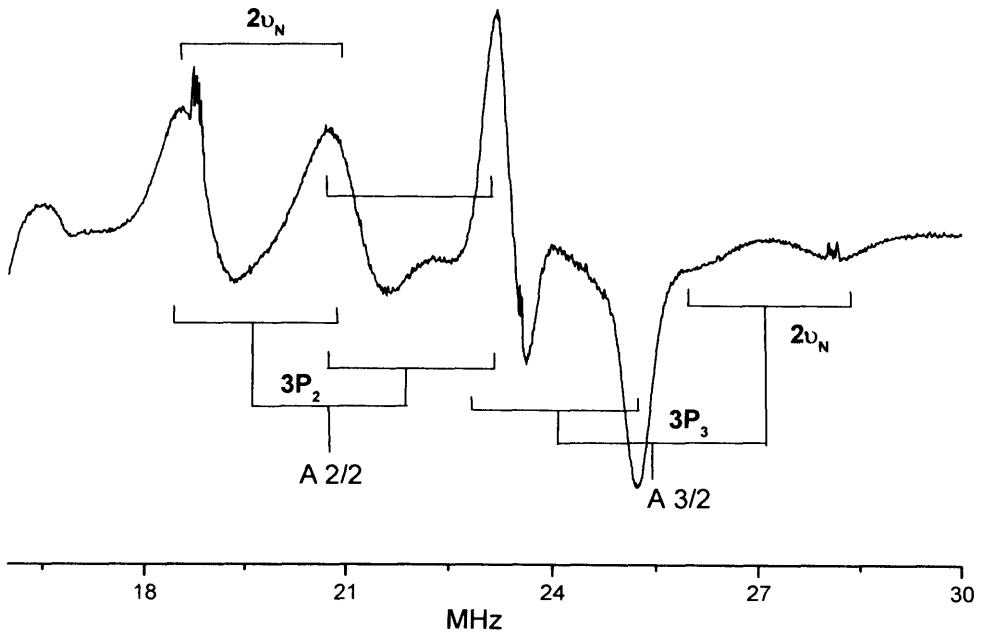

Figure 7.11: X-band (perpendicular) nitrogen ENDOR spectra of *racemic*-[Cu(**18**)] in toluene.

Earlier the EPR results were presented for the series of experiments in which individual enantiomers of the complex and enantiomers of the MBA were recorded (Figure 7.3). The corresponding proton ENDOR spectra from this set of EPR experiments (namely (*R,R*)-[Cu(**18**)] in (*R*)-MBA, (*S,S*)-[Cu(**18**)] in (*S*)-MBA, (*R,R*)-[Cu(**18**)] in (*S*)-MBA and (*S,S*)-[Cu(**18**)] in (*R*)-MBA are shown in Figure 7.12. It should be noted that simplification of the ^{1}H ENDOR spectra was facilitated by selective deuteration of the MBA protons (Scheme 1, R= H or *D*). This not only simplified the ENDOR spectra but also allowed unambiguous identification of the co-ordinated amine protons. A closer inspection of these spectra reveals that while the position of the ligand peaks remains unchanged, the peaks associated with the $-NH_2$ group of the bound amine have definitely changed. This difference is highlighted by the vertical lines drawn on the figure. This situation is analogous to that previous reported in the last chapter for the bound epoxide molecule, due to the presence of difference diastereomeric states. Clearly the two enantiomers of MBA (*R*- or *S*-) bind differerently to the two enantiomers of the copper complex (*R,R* or *S,S*) which results in slight differences in the spatial arrangement of the $-NH_2$ protons with respect to the copper centre. Further simulations are required to extract the structural information

from these experimental spectra (ie., differences in Cu...$^{1}H_{MBA}$ distances). Nevertheless, these preliminary results prove that the chiral interactions observed for [VO(**11**)] with proplyene oxide were not unique to that system, and they can also be observed for other related complexes with different substrates (ie., amines).

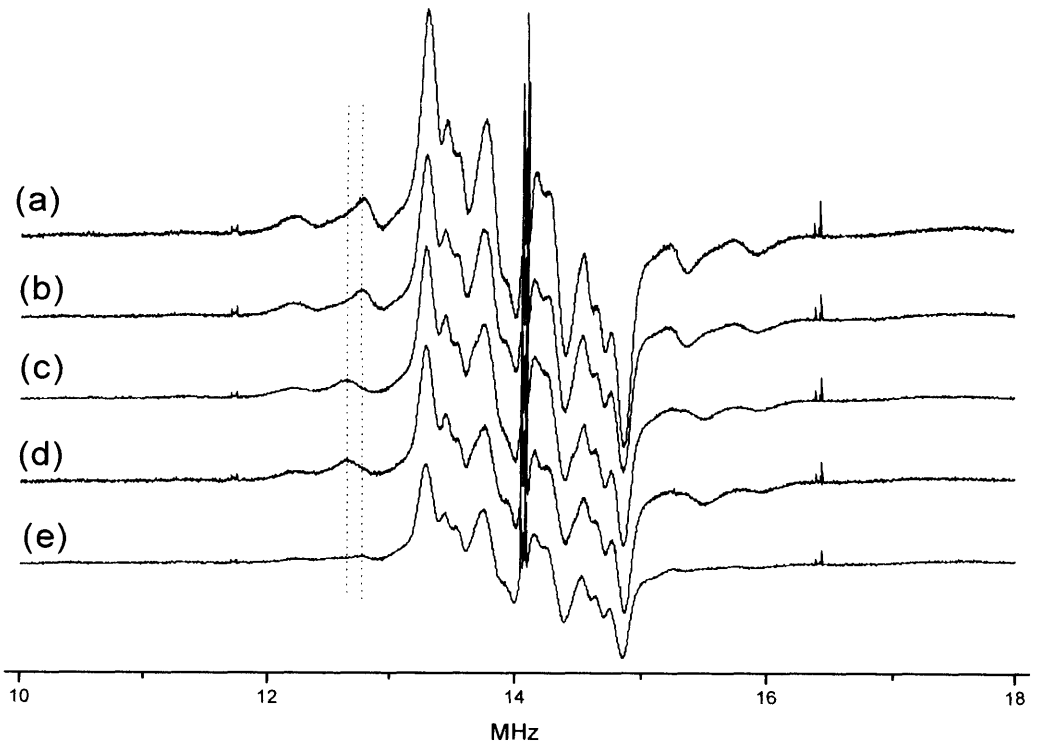

Figure 7.12: X-band ^{1}H ENDOR spectra of [Cu (**18**)] dissolved in Methylbenzyl amine (MBA), (a) (*R,R*)-(**18**)] in (*S*), (b) (*S,S*)-[Cu (**18**)] in (*R*), (c) (*S,S*)-[Cu (**18**)] in (*S*), (d) (*R,R*)-[Cu (**18**)] in (*R*) and (e) (*R,R*)-[Cu (**18**)] in (S)-MBA-d_2. The spectra were measured at 10K.

The experimental X-band ^{1}H ENDOR spectrum of [Cu(**20**)-NO_2] in MBA is shown in Figure 7.13. The spectral profile, especially the features around υ_H in the perpendicular region, is similar to that observed for the [Cu(**18**)] complex. However, a wide experimental scan shows that the couplings to the protons associated with the isotropic imine protons (N-H_{imine}) have disappeared. This suggests that the introduction of the electron withdrawing -NO_2 group, pulls electron density away from the copper metal centre towards the NO_2 groups, and thereby increases the Lewis acidity of the complex. This increased Lewis acidity in turn, influences the electronic nature of the ligand framework and causes the imine peak position to change significantly (ie., the large isotropic contribution of the imine protons

decreases). Furthermore, and perhaps more importantly, the shift in the positions of the $-NH_2$ protons is very much smaller in [Cu(**20**)-NO_2] (Figure 7.13) compared to [Cu(**18**)-NO_2] (Figure 7.12). This can possibly be explained on the grounds of the strength of the interaction, or ΔG of amine binding. As ΔG increases, due to the increased Lewis acidity of the copper site, then the smaller differences in energy between the diastereomers ($\Delta\Delta G$) becomes less significant and less apparent.

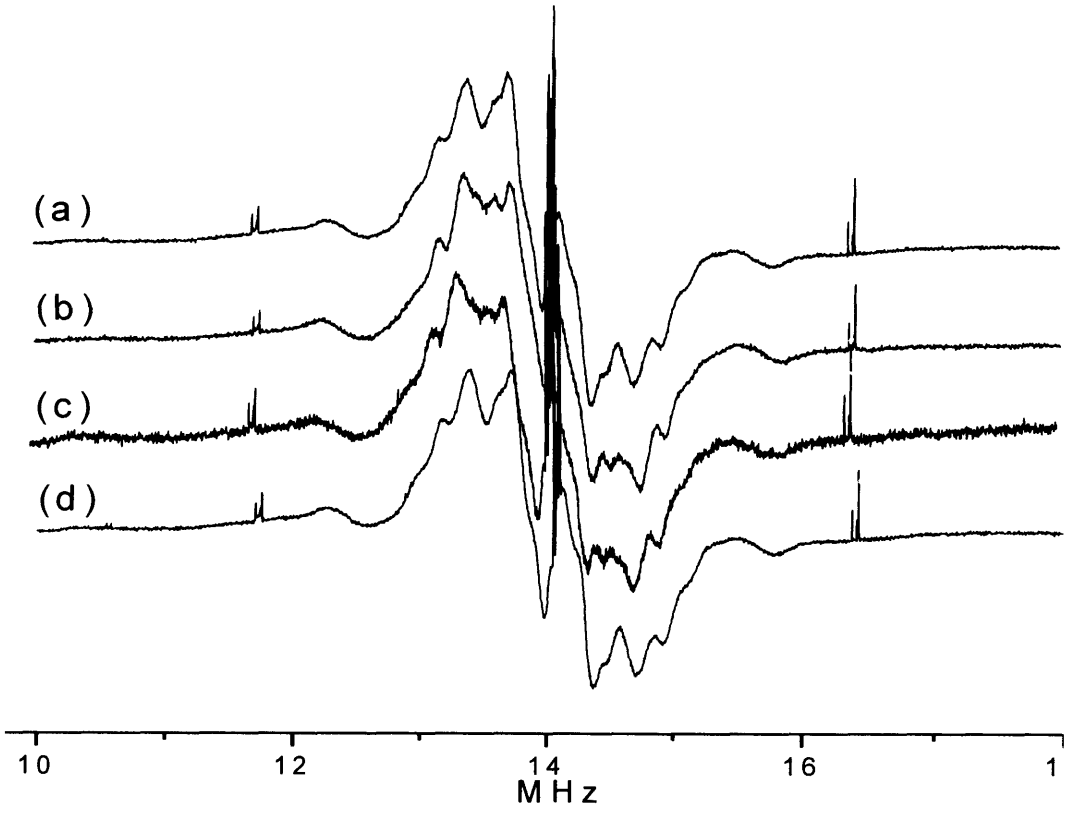

7.13: X-band ^{1}H ENDOR spectra of [Cu(**20**)-NO_2] dissolved in Methylbenzyl amine (MBA), (a) (*R,R*)-[Cu(**20**)-NO_2] in (*S*), (b) (*R,R*)-[Cu(**20**)-NO_2] in (*R*), (c) (*S,S*)-[Cu(**20**)-NO_2] in (*S*) and (d) (*S,S*)-[Cu(**20**)-NO_2] in (*R*). The spectra were measured at 10K.

Finally, in the case of the partially nitrated complex [Cu(**22**)-NO_2], analysis of the experimental perpendicular ^{1}H ENDOR spectra reveal only the protons from the ligand itself and no additional features arising from the imine proton or coordinated MBA protons could be detected. However, the quality of both the EPR and ENDOR spectra were very poor in this case, so a confident assignment of the spectra is not possible at this stage. Figure 7.14 shows the change in spectral features associated with the complexes [Cu(**20**)-NO_2], [Cu(**22**)-NO_2] and chiral MBA for comparison.

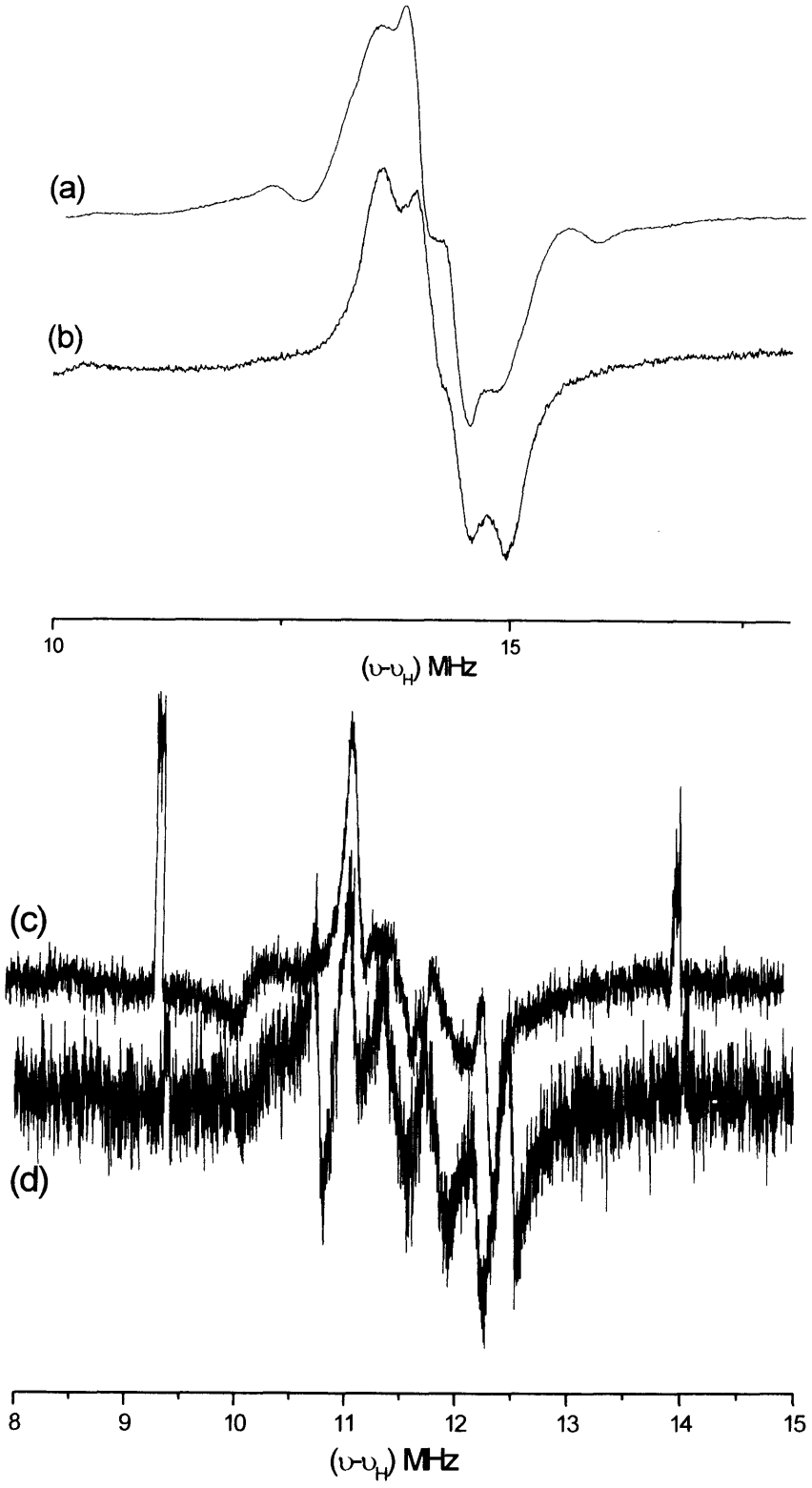

Figure 7.14: X-band ^{1}H ENDOR spectra of [Cu(**20**)-NO_2] and [Cu(**22**)-NO_2] dissolved in Methylbenzyl amine (MBA) / toluene-d_8 (1:1) recorded with a microwave power of 2.5 mW at 10K. (a) Experimental [Cu(**20**)-NO_2] spectrum perpendicular position, (b) Experimental [Cu(**22**)-NO_2] spectrum perpendicular position, (c) Experimental [Cu(**20**)-NO_2] spectrum parallel position and (d) Experimental [Cu(**22**)-NO_2] spectrum parallel position.

7.4 Conclusions

A full EPR and ^{1}H ENDOR study was carried out on the copper salen type complexs (**18**), (**20**) and (**22**) both in toluene (for [Cu(**18**)]) and in the chiral amine (Methylbenzyl amine-MBA). A preliminary analysis of the ^{1}H ENDOR spectra, in toluene and MBA enabled assignments to be made on the ligand derived peraks and those originating from the MBA itself. In the case of [Cu(**18**)] in MBA, diastereomeric interactions were observed between enantiomers of the complex and enantiomers of the chiral amine. The axial coordination of the chiral amine was also confirmed by EPR spectroscopy, from the changes to the Cu(II) spin Hamiltonian parameters. The preliminary work presented in this chapter has clearly demonstrated that, similar to the previous chapter on vanadyl systems, diastereomeric interactions can be observed by ENDOR for other transition metal systems (copper). This study also involved analysing a range of different ligand frameworks, to monitor the effects of altering the Lewis acidity of the complex. Such structural changes, dramatically altered the ENDOR spectra.

In conclusion, ENDOR spectroscopy has been used once again to monitor weak structural, electronic and steric changes of a metal complex coordinated to an amine.

7.5 References

[1] T.Tanaka, B.Saito, T.Katsuki, *Tetrahedron Lett*, 2002, **43**, 3259.

[2] M.S.Sigman, E.N.Jacobsen, *J.Am.Chem.Soc*, 1998, **120**, 5315.

[3] W.Zhang, L.J.Loebach, S.R.Wilson, E.N.Jacobsen, *J.Am.Chem.Soc*, 1990, **112**, 2801.

[4] H.Sakaki, R.Irie, T.Katsuki, *Synlett*, 1993, 300.

[5] R.Irie, K.Noda, Y.Ito, T.Matsumoto, T.Katsuki, *Tetrahedron Lett*, 1990, **31**, 7345.

[6] W.Zhang, E.N.Jacobsen, *J.Org.Chem*, 1991, **56**, 2296.

[7] E.N.Jacobsen, W.Zhang, A.Muci, J.R.Ecker, L.Deng, *J.Am.Chem.Soc*, 1991, **113**, 7063.

[8] J.Huang, Z.Xi, *Cuihua Xuebao*, 1989, **10**, 326.

[9] Z.Jiang, Z.Xi, *Cuihua Xuebao*, 1991, **12**, 286.

[10] E.M.Vogl, H.Groger, M.Shibasaki, *Angew.Chem.Int.Ed*, 1999, **38**, 1570.

[11] H.B.Kagan, *Bull.Soc.Chem.Fr*, 1988, **5**, 846.

[12] I.W.Davies, P.J.Reider, *Chemistry and Industry*, 1996, **6**, 412.

[13] I.A.Fallis, D.M.Murphy, R.J.Tucker, D.J.Willock, R.Strevens, K.Avery, *J.Am.Chem.Soc*, 2004.

[14] R.J.Tucker, I.A.Fallis, R.D.Farley, D.M.Murphy, D.J.Willock, *Chem.Phys.Lett*, 2003, **380**, 758.

[15] D.M.Murphy, I.A.Fallis, R.D.Farley, R.J.Tucker, K.L.Avery, D.J.Willock, *Phys.Chem.Chem.Phys*, 2002, **4**, 4937.

[16] G.C.Hurst, T.A.Henderson, R.W.Kreilick, *J.Am.Chem.Soc.*, 1985, **107**, 7294; T. A.Henderson, G.C.Hurst, R.W.Kreilick, *J.Am.Chem.Soc.*, 1985, **107**, 7299.

[17] C.Walsh, *Enzymatic Reaction Mechanisms*; W.H.Freeman, New York, 1979.

[18] E.N.Jacobsen, W.Zhang, M.L.Guler, *J.Am.Chem.Soc*, 1991, **113**, 6703.

[19] E.N.Jacobsen, *J.Am.Chem.Soc*, 1998, **120**, 984.

[20] A.S.Cieplak, B.D.Tait, C.R.Johnson, *J.Am.Chem.Soc*, 1989, **111**, 8447.

[21] R.L.Halterman, M.A.McEvoy, *J.Am.Chem.Soc*, 1990, **112**, 6690.

[22] J.S. Hyde, W. Froncisz, *Annual Review of Biophysics and Bioengineering*, 1982, **11**, 391.

[23] M.Valko, R.Klement, P.Pelikan, R.Boca, L.Dihan, A.Bottcher, H.Elias, L.Muller, *J.Phys.Chem*, 1995, **99**, 137.

[24] M.Valko, R.Boca, R.Klement, J.Kozisek, M.Mazur, P.Pelikan, H.Morris, H.Elias, L.Muller, *Polyhedron*, 1997, **16**, 903.

[25] H.R.Gersman, J.D.Swalen, *J.Chem.Phys*, 1962, **36**, 3221.

[26] S. Kita, M. Hashimoto, M. Iwaizumi, *Inorganic Chemistry*, 1979, **18**, 3432.

[27] A. Schweiger, *Structure and Bonding*, (Berlin), VCH Publishers, 1982, **51**, 1.

Chapter 8

General conclusions

8.0 General conclusions

In order to understand and elucidate the mechanistic pathways involved in a homogeneous catalytic reaction, key pieces of information are required ranging from the composition, structure and bonding of the active sites throughout the catalytic cycle, to the spatial arrangement of the ligands around the substrate-catalyst complex. For homogeneous catalysis involving a paramagnetic metal centre, such information can be obtained using the family of EMR techniques. The most commonly used of the EMR techniques is continuous wave (*cw*) EPR which provides information on the g factor, the central atom hyperfine, and the zero-field splitting interaction (for $S > ½$ systems). However, information on ligand identification, ligand conformation, bonding characteristics and the extent of spin delocalisation onto the surrounding ligands is usually derived from the interaction of the unpaired electron with nearby nuclear spins. This results in splittings that are usually too small to be resolved in the EPR spectrum. They can however be resolved by the related technique of *cw* ENDOR as demonstrated in this Thesis.

Two important advantages of ENDOR for structural analysis is the ability to provide unsurpassed detail on (a) location of various protons, and (b) the spin delocalisation over a paramagnetic site. Because of the abundance of protons in many chemically relevant systems, different regions of a functional site can be probed by mapping their ^{1}H hyperfine couplings. Although x-ray crystallography is by far the most established and effective method for determining three-dimensional structure, its resolution is limited with respect to proton positions. In a sense, ENDOR experiments on single crystals with known three-dimensional structures can be regarded as complementary proton crystallography. The position of the protons can also be determined more precisely by ENDOR compared to x-ray crystallography, and unlike neutron diffraction does not require deuterated samples. Also, in disordered systems, like polymers, glasses, frozen solutions, amorphous solids and microcrystalline powders, ENDOR can be used to study local structure (up to 0.5 nm) with a precision comparable to NMR and EXAFS which represent the main alternatives. ENDOR is therefore an important tool for the determination of geometrical structure for paramagnetic systems which cannot be crystallised nor investigated in solution.

All of these advantages of using ENDOR to determine structural parameters in frozen solution have been described in this Thesis, with specific reference to coordination chemistry and homogeneous catalysis. The approach used to extract the structural parameters was angular selective ENDOR, utilising a simulation programme developed in house. The work has demonstrated how subtle changes in the structure of a paramagnetic complexes in solution, as a result of changes in solvent or via interaction with small molecules, can be probed.

In the first system studied (chapter 5), the conformational changes of an oxo-vanadium (IV) complex in frozen solution [V^{IV}=O(acac)$_2$] was examined using a combination of ENDOR spectroscopy and DFT calculations. The complex was studied in both non-coordinating (dichloromethane-CD_2Cl_2) and coordinating solvents (pyridine). In the non-coordinating solvent the complex was found to adopt the expected square pyramidal structure. The vanadyl-proton coordinates obtained by DFT and ENDOR simulations were found to be in excellent agreement with each other and with this expected structure. Small variations in the VO...CH distances were ascribed to weak H-bonding interactions between CD_2Cl_2 and [V^{IV}=O(acac)$_2$], which were not accounted for in the DFT calculations. In the presence of pyridine and substituted pyridines, two different isomers of the resulting [V^{IV}=O(acac)$_2$(C_5D_5N)] adduct were identified by ENDOR. Owing to the small energy difference between the two isomers, both appear to co-exist in solution before freezing, with only a slight predominance of the *cis* structure over the *trans* structure in the frozen state. In the case of the 2-picoline adduct, [V^{IV}=O(acac)$_2$(C_6D_8N)], an equal ratio of *cis* and *trans* isomers was found This result demonstrates the power of combined ENDOR and DFT studies to discriminate subtle structural differences between coordination compounds, even when present as a mixture of isomers in frozen solution.

Upon completion of this study, slightly more complex ligand systems were investigated with respect to detecting the solvent induced changes to the ligand structure (chapter 6). Therefore the "solvatochromic" effects of a vanadyl salen complex [VO^{IV}(salen)] in frozen solution were studied by ENDOR and DFT calculations. In a non-coordinating solvent (dichloromethane), both ENDOR and DFT were in excellent agreement on the expected square pyramidal structure, where V^{IV}=O is positioned out of the equatorial ligand *xy* plane (as determined from calculated V...H distances). However, in a coordinating solvent

(dimethylformamide), a subtle perturbation from the square pyramidal structure was observed, suggesting that DMF coordinates *trans* to the vanadyl oxo-ligand, pulling V^{IV}=O back into the ligand plane. The axial coordination of DMF was confirmed by ENDOR and in the DFT optimised [VO^{IV}(salen)]-DMF complex. These differences in ligand structure (visualised through the VO....H_{lig} distances) were very subtle, but nevertheless such observations are extremely important in understanding weak interactions between complex and substrate, as in enantioselective homogeneous catalysis, in order to generate an accurate structural and electronic visualisations of catalyst-substrate interactions in the *solution* phase.

To explore these possibilities further, attempts were made to establish some mechanistic basis of the commercially important kinetic resolutions described by Jacobsen in chapters 7 and 8. These reactions, in which racemic epoxides are resolved via enantioselective ring opening attack by an appropriate nucleophile are catalysed by Co or Cr complexes of bulky chiral salen type ligands. Whilst chiral discrimination of enantiomers of the substrate by separate molecules of catalyst has been *implied* it has never been directly *observed.* In this Thesis evidence for this chiral interaction was presented for the first time. The ^{1}H ENDOR spectra of the *RR*-[VO(**11**)] dissolved in *R*-propylene oxide was identical to *SS*-[VO(**11**)] dissolved in *S*-propylene oxide, while *RR*-[VO(**11**)] dissolved in *S*-propylene oxide was identical to *SS*-[VO(**11**)] dissolved in *R*-propylene oxide. Finally examination of the ENDOR spectrum of *racemic*-[VO(**11**)] in *racemic*-propylene oxide revealed an identical ENDOR spectrum to the enantiomeric pair *RR*-[VO(**11**)] and *R*-propylene oxide and *SS*-[VO(**11**)] and *S*-propylene oxide. This result indicated not only binding of epoxide by [VO(**11**)] but also a high degree of enantiodiscrimination by *RR*-[VO(**11**)] for *R*-propylene oxide. It is important to note that the EPR spectra of such complexes displayed *no* differences when different pairs of diastereomeric combinations were compared. These results are all the more remarkable when one considers that an epoxide is an exceedingly poor donor and that five coordinate vanadyl complexes display significant pyramidalisation which raises the VO moiety ~0.5Å above the N_2O_2 plane of salen ligand backbone. This work not only demonstrates the feasibility of generating accurate, sterochemically detailed models for complex species in solution, but also highlights the sensitivity of the ENDOR technique in being able to detect and quantify very weak interactions. An analogous study was subsequently carried out using enantiomers of *RR*-, or *SS*-[Cu(**18**)] in *R*- and *S*- enantiomers of a

chiral amine. In this case only partial enantiodiscrimination of the complex with the substrate was detected in the ENDOR measurement. This was explained on the grounds that the copper-amine interaction was stronger, compared to the VO-epoxide interaction, so that the ability to detect differences in diastereomer energies is significantly reduced.

Overall the results presented in this thesis, have illustrated how ENDOR spectroscopy can be an effective tool in homogeneous catalysis research and coordination chemistry. Systems studied have ranged from observing weak diastereomeric effects in solution to conformational changes solvatochromic effects. It has also been demonstrated how ENDOR spectroscopy can be applied to various paramagnetic transition metal complexes to extract detailed information on the structural changes which evolve in frozen solution through the extraction of the proton coordinates.